

THE USE OF DIFFRACTION PEAK PROFILE ANALYSIS IN STUDYING THE PLASTIC DEFORMATION OF METALS

A thesis submitted to the University of Manchester for
the degree of

Doctor of Philosophy in the Faculty of Engineering and
Physical
Sciences

2012

THOMAS H. SIMM

School of Materials

Contents

List of Figures.....	8
List of Tables	24
Symbols	27
Abstract.....	29
1. Introduction	33
Aims and Objectives.....	34
2 Background and Literature Review	37
2.1 Deformation of metals	38
2.1.1 Plastic Deformation	38
2.1.2 Slip in FCC metals.....	39
2.1.3 Slip in HCP Metals	39
2.1.4 Additional modes of deformation.....	43
2.1.5 Work Hardening	47
2.1.6 Recovery.....	49
2.1.7 The Composite Model	59
2.1.8 Crystal Plasticity Models.....	61
2.2 Characterisation of the deformed state	65
2.3 Sources of radiation	69
2.3.1 Laboratory X-ray diffraction	69
2.3.2 Synchrotron X-ray Diffraction	70
2.3.3 Neutron Diffraction	71

2.4	Diffraction Peak Profile Analysis	72
2.4.1	Basic Principles.....	72
2.4.2	Integral Breadth methods	80
2.4.3	Fourier Methods.....	86
2.4.4	Variance Method.....	99
2.4.5	Dislocation Broadening.....	107
2.4.6	Planar Faults.....	116
2.4.7	Variation in the intergranular strains	120
2.4.8	Defects of the first class	122
2.4.9	Instrumental Considerations	122
2.4.10	The Application of DPPA methods	123
3	Materials and Method	125
3.1	Introduction.....	125
3.2	Materials.....	125
3.3	Mechanical Tests.....	128
3.4	Diffraction Measurements.....	129
3.4.1	Overview- Diffraction Measurements	129
3.4.2	Laboratory X-ray, Materials Science Centre	132
3.4.3	Synchrotron X-ray, ID31 ESRF.....	133
3.4.4	Neutron diffraction, HRPD ISIS	135
3.5	Microscopy.....	140
3.6	Hardness Tests	140
4	Results Overview	141
4		

5	Microscopy and Mechanical Properties	143
5.1	Microscopy	143
5.1.1	Starting Microstructure.....	143
5.1.2	Deformed Microstructure	146
5.2	Stress-Strain Curves	150
5.3	Hardness Tests	151
6	Implementation of Diffraction Peak Profile Analysis Methods	153
6.1	Introduction	153
6.2	Quantifying Errors	154
6.3	Preparation of Diffraction Data	156
6.4	Analytical Fit	158
6.5	Integral Breadth Method.....	159
6.6	Variance Methods	164
6.6.1	Variance-A, Analytical Approach	165
6.6.2	Variance-A, Errors and Best Practice.....	169
6.6.3	Variance-B, Analytical Approach	174
6.7	Contrast Factors	179
6.7.1	Contrast factor: FCC metals	179
6.7.2	Contrast factor: HCP metals	180
6.8	Williamson-Hall Methods	183
6.9	Fourier Methods	190
6.9.1	Fourier Methods, Preparing the Data	192
6.9.2	Fourier Methods, Analytical Approach	194

6.9.3 Fourier Method, Errors and Best Practice.....	200
6.10 Conclusion	207
7 Application of DPPA Methods	209
7.1 Introduction.....	209
7.2 Full-width Analysis Method	210
7.3 Size And Strain Broadening.....	213
7.3.1 Crystal Size in Nickel	215
7.3.2 Crystal Size in metals with low SFE.....	219
7.3.3 Micro-strain and Size Broadening	223
7.4 Components of Strain Broadening	229
7.4.1 Dislocation Density.....	229
7.4.2 The Arrangement of Dislocations	235
7.4.3 Dislocation Population and the Contrast Factor	239
7.4.4 Slip system population in FCC metals	239
7.4.5 Systematic Errors in the use of contrast factors for FCC metals	242
7.4.6 Conclusion: Contrast Factors in FCC alloys.....	247
7.4.7 Slip systems in Titanium alloys	247
7.4.8 Systematic Errors from the use of the contrast factor for titanium.	257
7.4.9 Contrast Factor in titanium: Conclusions.....	262
7.5 Comparison of Diffraction Sources	263
7.6 Conclusion	266
7.6.1 Crystal Size and Micro-strain	266

7.6.2	Comparison of methods that give crystal size and micro-strain values	267
7.6.3	Methods that give dislocation density values	269
7.6.4	The contrast factor	271
7.6.5	The full-width analysis methods.....	272
8	The use of polycrystal plasticity models to predict peak shape in different texture components.....	273
8.1	Introduction	273
8.2	Polycrystal Plasticity Modelling Approach	274
8.2.1	FCC: Polycrystal Plasticity Modelling Approach	274
8.2.2	Titanium: Polycrystal Plasticity Modelling Approach	275
8.3	Comparisons of Measured Broadening with Predicted Contrast Factor	
	280	
8.3.1	Modelling Approach.....	280
8.3.2	FCC Metals.....	281
8.3.3	Titanium.....	291
8.4	Additional Causes of Peak Broadening Heterogeneity	296
8.4.1	FCC Metals	296
8.4.2	Titanium.....	305
8.5	Twinning in titanium alloys.....	312
8.6	Conclusions	319
9	Conclusions	321
	Further Work	325
	References	327

List of Figures

Figure 2-1. FCC (left) and HCP (right) unit cells. For the FCC unit cell, one of the (111)[110] slip systems are shown. In HCP notation the a_1 , a_2 , a_3 axes are used and selected planes and Burgers vectors are shown. (Lutjering and Williams 2007).....	40
Figure 2-2. TEM micrograph of high pure titanium deformed to a strain 0.06 (Biswas 1973), showing dislocations close to the basal plane.....	42
Figure 2-3. TEM micrograph of a single-phase titanium alloy (left), showing long and straight $\langle a \rangle$ dislocations on the right and wavy $\langle c+a \rangle$ dislocations on the left. A TEM micrograph of a two-phase Ti-6Al-4V showing $\langle a \rangle$ dislocations (Zaefferer 2003).	42
Figure 2-4. Twin observed in Ti-6Al-4V (left) are often small (Yappici et al. 2006). Whereas, those in Ti-CP are larger often dominating a grain (Glavicic et al. 2004).....	45
Figure 2-5. Deformation twins in SS-316 at a strain of 10% (Byun et al. 2003) includes doses up to 0.05.	46
Figure 2-6. Transmission electron microscopy (TEM) of extended dislocations in a copper alloy (above) and a diagram representing the region highlighted in the TEM picture (below) (Hull and Bacon 2001).	47
Figure 2-7. The change in the square-root of the dislocation density with changes in the stress for copper samples measured by TEM and etch pit methods (Mecking and Kocks 1981).....	49
Figure 2-8. The different stages of recovery of a plastically deformed metal (Humphreys and Hatherly 2004).....	50
Figure 2-9. Dislocation structure of high purity nickel at 2.5% strain with a grain size of $36\mu\text{m}$ (left), 10% strain grain size ($g_s=200\mu\text{m}$) (middle) and 24% strain $g_s=200\mu\text{m}$ (right) from Keller and colleagues (2010).	53

Figure 2-10. The different types of dislocation arrangements in SS-316 from Feaugas (1999). In (a) are dislocation tangles, in (b) dislocation walls and in (c) dislocation cells. The evolution of these different dislocation types is shown in (d). In stage I, tangles and walls are active, in stage II tangles dominate and in stage III dislocation cells dominate.	54
Figure 2-11. Dislocation structures of deformed high purity titanium alloy, viewed by TEM micrographs (magnification 46,000x) showing a cell structure after a strain of 2.27 (227%) (Biswas 1973).	55
Figure 2-12. The variation in the cell boundary angle (middle) and cell size (bottom) with different orientations in iron (Dilamore et al. 1972). The variation in the Taylor factor is also shown (top).....	57
Figure 2-13. The different dislocation structures in aluminium identified by TEM (Hansen et al. 2006). The value of M increases from [100] to the outside of the stereographic triangle.....	58
Figure 2-14. The different cell structures observed in (a) polycrystal nickel with grain size $168\mu\text{m}$, (b) austenitic stainless steel and (c) polycrystal nickel with grain size $18\mu\text{m}$ (Feagus and Haddou 2007)	59
Figure 2-15. An asymmetric 002 diffraction peak measured in deformed single crystal copper (Ungar et al. 1984), The peak can be considered as the sum of a peak representing the cell walls I_w and the cell interior I_C	60
Figure 2-16. TEM micrograph (a) and an EBSD map (b) of an aluminium alloy, deformed by cold rolling to a strain of 0.2, displaying aligned low angle grain boundaries (Humphreys and Bate 2006).	68
Figure 2-17. Face-centred-cubic unit cell (left), the lattice parameters a , b , c are displayed. The hexagonal close packed unit cell (right) (Lutjering and Williams 2007). The lattice parameter a , is the distance between atoms on the perimeter, given by 0.295nm , and the c parameter perpendicular to this, given by 0.468nm , the values are those for a titanium alloy.	73

Figure 2-18. An example x-ray diffraction pattern for CdF₂(30) sample using a laboratory x-ray with copper radiation (Ribarik et al 2005). The measured data and the fit of this data are shown..... 73

Figure 2-19. An illustration of Braggs Law. A monochromatic beam is incident upon a perfect crystal with lattice spacing d, and produce a scattered beam at an angle θ . The angle θ given by Braggs law. 74

Figure 2-20. Gaussian (--) , Cauchy (-.-) analytical functions and the Voigt curve, which is a convolution of the two (Langford 1978)..... 77

Figure 2-21. An example Williamson-Hall plot of a 99.98% copper sample, showing broadening anisotropy, that is the broadening is not proportional to 'K' but is {hkl} dependent. Where, the full-width=ΔK, and g=K..... 83

Figure 2-22. An example modified Williamson-Hall plot of the same 99.98% copper sample as in Figure 2-21. The use of the contrast factor has accounted for the anisotropy so that broadening is proportional to $K\sqrt{C}$. Where, the full-width=ΔK, and g=K..... 84

Figure 2-23. A Cauchy function can be considered as a sum of harmonic terms. It is shown how the different harmonics of frequency 'n' add to produce a peak that is closer to the Cauchy as each additional harmonic is added. The magnitude of the peaks are normalised so that I=1 at x=0. 87

Figure 2-24. The Fourier coefficients of a Cauchy function..... 88

Figure 2-25. A crystal, or domain, within the measured sample can be considered as a number of columns of base $a_1 \times a_2$ (the size of the unit cell in these directions) and height given by the size of the domain in the direction g. The distance between unit cells in a column is L..... 90

Figure 2-26. Characteristic behaviour of second-order moments (left) and fourth-order moments divided by σ^2 (where q used in the figure is equivalent to σ). The samples shown are AlMg deformed at room temperature in compression and 400°C and an annealed iron powder. The iron powder shows behaviour characteristic of only size broadening, whereas the AlMg shows both size and strain broadening (Borbely and Groma 2001)..... 106

Figure 2-27. The axes used to define a dislocation, the direction ε_3 points in the direction of the dislocations slip line, ε_2 is normal to the slip plane, and b is the dislocations Burgers vector. The angle α gives the character of the dislocation, $\alpha=90^\circ$ is an edge and $\alpha=0^\circ$ is a screw dislocation.	108
Figure 2-28. The effect of the parameter M on the shape peaks, intensity against k is plotted (Wilkins 1970).	115
Figure 2-29. Planar Faults in FCC materials, (1) the regular fcc sequence, (2) a stacking fault and (3) a twin fault. Atoms can be in one of three positions, A, B or C, but cannot repeat the previous sequence, i.e. A cannot follow A....	116
Figure 2-30. How the different planar faults contribute to broadening, Balogh and colleagues (2006), (a), left, intrinsic stacking faults for the 311 plane, and (b), right, the types of fault for the 111 plane.....	120
Figure 3-1. Differences in the instrumental broadening of the three different diffraction sources. The results of the fit to the instrumental diffraction pattern are shown. The asymmetry component is the full-width of the right-hand-side divided by the full-width of the left. Values of full-width and k are in units of Å. These values are found by fitting the instrumental sample using a pseudo-Voigt curve.....	131
Figure 3-2. (a), left, Example x-ray diffraction pattern and the fit of the data for SS304 specimen with grain size 100 μm , 18% strain, (b), silicon standard instrumental profile showing the α_1 and α_2 components and the pseudo-Voigt fit.....	133
Figure 3-3. The experimental set-up at ID-31 (Frankel 2008).	135
Figure 3-4. Diffraction patterns produced at ID31, ESRF. (a), left, (b), LaB6 standard instrumental profile and the pseudo-Voigt fit of one of the peaks.	135
Figure 3-5. THE Schematic of HRPD set-up (left-top) (Ibberson et al. 1992), and the backscattered detector (middle-top). 2θ varies from 176° at the centre of the detector to 160° at the edge (in the left-right direction) and varies	

between a maximum of approximately $\pm 8^\circ$ in the up-down direction at the edges. Samples were placed in vanadium holders and rotated (right-top). The sample is rotated so that the angle between the tensile direction and the diffraction vector, α , varies between 0 and 90 degrees (bottom).....	137
Figure 3-6. Typical diffraction pattern using HRPD. For SS-316 compressed to 2%, measured at $\alpha=50^\circ$ and a beam current of $24\mu\text{m}$, the peaks shown are 111, 200, 222, 400.....	138
Figure 3-7. Example of the fits used for Ni compressed to 10%. The 222 peak fit using a split (left) and regular pseudo-Voigt (right).....	138
Figure 5-1. EBSD map of nickel samples. Left, at 0% strain showing IPF colouring using Channel 5 the lines represent boundaries more than 15° . Right, at 2% strain showing Euler colours using VMAP.....	144
Figure 5-2. EBSD maps of SS-304. Left, IPF map at 0% strain, using Channel 5 showing boundaries at 15° . Right, sample at 2% showing a Euler colour map using VMAP, with boundaries at 5°	144
Figure 5-3. EBSD maps of SS-316. Left, IPF colour maps using Channel 5, at 0% strain, lines show boundaries at 15° . Right, Euler colour map using VMMPA 0.5% strain.....	145
Figure 5-4. Optical microscope image of un-deformed Ti-CP sample.....	145
Figure 5-5. Optical microscope image of un-deformed Ti-6Al-4V sample.....	146
Figure 5-6. EBSD map of SS-316 at 10%. The map shows IPF colour using Channel 5, thick lines show misorientations more than 15° and thinner lines at 0.5° . The step size used was $0.07\mu\text{m}$	147
Figure 5-7. EBSD maps of SS-316 at 10% applied strain. Maps show Euler colour using VMAP. Deformations twins are highlighted.....	148
Figure 5-8. EBSD map Ni-200 at 10%. The main map (and map top right) shows IPF colour using Channel 5, thick lines show misorientations more than 15°	

and thinner lines at 1.5° . The step size used was $0.1\mu\text{m}$. Map bottom right shows relative Euler colours using VMAP.....	149
Figure 5-9. True Stress-true strain curve for the different metals studied.....	150
Figure 5-10. Strain-hardening rate versus true strain for the different metals studied.....	151
Figure 5-11. The Vickers Hardness values (HV) for the different metals studied using 0.5kg indent.....	152
Figure 6-1. An example of how errors in the results of a DPPA method are quantified. The results of a method are fitted to a polynomial against strain, the result at a particular strain (R_i) for a particular measurement point (i) then has a fitted value of P_i . The deviation (or indication of error) of point i, is then $ R_i - P_i $	155
Figure 6-2. An example x-ray diffraction pattern and the fit of a silicon standard instrumental profile showing the α_1 (large peak on left) and α_2 (smaller peak on right) components and the pseudo-Voigt fit.	156
Figure 6-3. The change in full-width with applied strain for nickel-200, SS-316 and Ti-6Al-4V. The lines represent a fit of the values to a 2 nd order polynomial (see text Section 6.2).	159
Figure 6-4. The root-mean-square-strain (top) and crystal size values in Å (top), for SS-316 found from different peaks, using the Integral Breadth method.	161
Figure 6-5. The root-mean-square-strain (top) and crystal size values in Å (top), for Ti-6Al-4V found from different peaks, using the Integral Breadth method. The lines represent a fit of the values to a 2 nd order polynomial (see text Section 6.2).	162
Figure 6-6. The change in root-mean-square-strain and crystal size, found using the integral breadth method, with applied strain for nickel-200, SS-316 and Ti-6Al-4V. The lines represent a fit of the values to a 2 nd order polynomial (see text Section 6.2).	164

Figure 6-7. Left (a) the change in the variance (M_2) with different background level, plotted against the difference from the Bragg angle in degrees 2θ . In the transverse direction, the variance values are for the measured intensity values. Right (b) variance values found using the background from the pseudo-Voigt and from reducing a σ^3 term. The diffraction peak is $(1 \bar{1}02)$ for Ti-CP samples.	168
Figure 6-8. Variance-A method results for Ti-6Al-4V data. The crystal size, in Å, (left) and RMS strain (right) values are shown.....	170
Figure 6-9. The change in root-mean-square-strain, found using the Variance-A Voigt (top) and pseudo-Voigt (bottom) method, with applied strain for nickel-200, SS-316 and Ti-6Al-4V. The lines represent a fit of the values to a 2 nd order polynomial (see text Section 6.2).....	172
Figure 6-10. The change in crystal size in Å, found using the Variance-A Voigt (top) and pseudo-Voigt (bottom) method, with applied strain for nickel-200, SS-316 and Ti-6Al-4V. The lines represent a fit of the values to a 2 nd order polynomial (see text Section 6.2).....	173
Figure 6-11. Examples of the fits for the variance method for the $\{01 \bar{1}0\}$ (top) and $\{11 \bar{2}2\}$ peaks (bottom). The M_2 variance is above the M_4 variance for fits with the same level of background and crystal size but the other parameters are different.	176
Figure 6-12. Results of the dislocation density from variance fits for the $\{ 11 \bar{2}2\}$ peak for Ti-6Al-4V in the axial direction. The results are shown for the M^2 and M^4 variances.....	177
Figure 6-13. The change in dislocation density and crystal size, found using the Variance-B method, with applied strain for the $\{01-10\}$ (shown as 010) and $\{11-22\}$ (shown as 112) planes in Ti-6Al-4V, measured in the transverse direction. The lines represent a fit of the values to a 2 nd order polynomial (see text Section 6.2).	178

Figure 6-14. The change in crystal size values (in Å), for the WH-1 (top) and mWH-3 (bottom) methods. The lines represent a fit of the values to a 2 nd order polynomial (see text Section 6.2).....	187
Figure 6-15. The change in strain term size, the rms-strain for the WH-1 method (top) and the strain component for the mWH-3 method (bottom). The lines represent a fit of the values to a 2 nd order polynomial (see text Section 6.2).	188
Figure 6-16. The change in the strain values found from different Williamson-Hall methods. The rms-strain is shown for the WH methods and the overall strain term for modified methods. The changes are shown for Nickel-200 (top left), SS-316 (top-right) and Ti6Al-4V (bottom). The lines represent a fit of the values to a 2 nd order polynomial (see text Section 6.2)......	189
Figure 6-17. The change in the crystal size values (in Å) found from different Williamson-Hall methods. The changes are shown for Nickel-200 (top left), SS-316 (top-right) and Ti6Al-4V (bottom). The lines represent a fit of the values to a 2 nd order polynomial (see text Section 6.2)......	190
Figure 6-18. The effect on the measured and real Fourier coefficients when the background level is changed. (a), left, an overestimation of the background and (b), right, an underestimation.....	193
Figure 6-19. Comparison of WA approaches, the WA plot for the log-INDI (left) and Fourier coefficients for log-ALL WA methods (right). A Ti-6Al-4V sample is used as an example. In the log-INDI method lines are fitted to the FCs at different n values, as shown on the left, where different lines represent different n or L values. Whereas in the log-ALL method the Fourier coefficients are fitted together over a range of n (or L) values as shown on the right.....	195
Figure 6-20. An example of the 'hook' effect for a Ti-6Al-4V sample using the Log-INDI method.	196

Figure 6-21. Example Krivoglaz-Wilkens plots, the log of the Fourier length against the strain coefficients. Top left for Log-INDI, top right for Lin-INDI and bottom for the alternative method, for the same Ti-6Al-4V sample..... 198

Figure 6-22. Krivoglaz-Wilkens plots for SS-316 at 10% applied strain found using the WA log-INDI method, with two different fits to the data, at different ranges of L values. The fit on the left, gives a dislocation density 60% higher and an M value 24% lower than the fit on the left. 198

Figure 6-23. An example of the change in the parameters obtained from a WA log-ALL analysis when the fitting range is changed. This is done for the same Ti-6Al-4V sample. 200

Figure 6-24. The change in crystal size values (in Å), for the log-INDI (top) and log-ALL (bottom) methods. The lines represent a fit of the values to a 2nd order polynomial (see text Section 6.2). 203

Figure 6-25. The change in dislocation density values, for the log-INDI (top) and log-ALL (bottom) methods. The lines represent a fit of the values to a 2nd order polynomial (see text Section 6.2). 204

Figure 6-26. The change in the crystal size values (in Å) found from different Fourier methods. The changes are shown for Nickel-200 (top left), SS-316 (top-right) and Ti6Al-4V (bottom). The lines represent a fit of the values to a 2nd order polynomial (see text Section 6.2). 205

Figure 6-27. The change in the dislocation density values found from different Fourier methods. The changes are shown for Nickel-200 (top left), SS-316 (top-right) and Ti6Al-4V (bottom). The lines represent a fit of the values to a 2nd order polynomial (see text Section 6.2). 206

Figure 7-1. The change in the full-width of the different metals with true strain. The lines represent a fit of the values to a 2nd order polynomial (see text Section 6.2). 211

Figure 7-2. The change in full-width of the different metals plotted against the flow stress. The lines represent a fit of the values to a 2nd order polynomial (see text Section 6.2). 213

Figure 7-3. The change in crystal size plotted against true strain for nickel and different methods. The lines represent a fit of the values to a 2 nd order polynomial (see text Section 6.2).	216
Figure 7-4. The change in crystal size (in Å) for nickel, plotted against work-hardening stress. The results are for the mWH-3 (top) and Integral Breadth (bottom) methods. The lines represent a fit of the values to a 2 nd order polynomial (see text Section 6.2).	221
Figure 7-5. The change in crystal size (in Å) for nickel, plotted against work-hardening stress. The results are for the WA log-INDI (top) and alternative (bottom) methods. The lines represent a fit of the values to a 2 nd order polynomial (see text Section 6.2).	222
Figure 7-6. The change in the relative size and strain broadening for the different metals using the standard (top) and modified (bottom) Williamson-Hall methods. Values are plotted against WH stress.	225
Figure 7-7. The change in the relative size and strain broadening for the different metals using the standard (top) and modified (bottom) Warren-Averbach methods. Values are plotted against WH stress.	226
Figure 7-8- The change in the relative size and strain broadening for the different metals using the integral breadth methods (top) and alternative method (bottom). Values are plotted against WH stress.	227
Figure 7-9. The change in the relative size and strain broadening for the different metals using the log-ALL (top) and lin-INDI (bottom) methods. Values are plotted against WH stress.	228
Figure 7-10. Fit of WA log-indi method dislocation density values against work-hardening stress used to determine α' (and in this case also the yield stress). The value $(\sigma - \sigma_0)/(GMb)$ is plotted against the square-root of the dislocation density. Where $\sigma - \sigma_0$ is the work-hardening stress, G the shear modulus, b the magnitude of the Burgers vector and M a constant equal to 3.	233
Figure 7-11. Results of the dipole character M, for the different Fourier methods applied to the different metals.	238

Figure 7-12. Results of the q-values for FCC samples found using the WA log-INDI method (a, top), mWH-3 method (b, middle), lin-INDI (c, bottom left) and log-ALL (d, bottom right). The lines represent a fit of the values to a 2nd order polynomial (see text Section 6.2). 241

Figure 7-13. Comparison of size and strain broadening for modified and standard approaches for different metals plotted against strain. The Williamson-Hall (top) and Warren-Averbach (bottom) methods are shown. 244

Figure 7-14. The change in the full-width of different FCC peaks for SS-316 with applied strain (left) and a modified WH plot at 27% strain (right). On the mWH plot the fit of the data is shown as well as fits when the q-values are set at edge and screw values. 246

Figure 7-15. The change in the full-width of different FCC peaks for SS-304 with applied strain (left) and a modified WH plot at 24% strain (right). On the mWH plot the fit of the data is shown as well as fits when the q-values are set at edge and screw values. 246

Figure 7-16. The change in the full-width of different FCC peaks for Ni-200 with applied strain (left) and a modified WH plot at 24% strain (right). On the mWH plot the fit of the data is shown as well as fits when the q-values are set at edge and screw values. 246

Figure 7-17. The q-value results from the mWH-1 method for Ti-6Al-4V. The results shown are for the fit of the first 15 and 20 HCP peaks measured in the axial and transverse direction..... 248

Figure 7-18. The change in the percentage of $\langle a \rangle$ (top), $\langle c+a \rangle$ (bottom left) and $\langle c \rangle$ (bottom right) slip systems, with different q-values, found using the Ungar-type method. 250

Figure 7-19. Inferred slip systems in Ti-6Al-4V using an Ungar-type method based on the q-values shown in Figure 7-17. The planes of the slip systems are given in Table 6.8..... 250

Figure 7-20. Results of the individual slip system predictions using the average $\langle c+a \rangle$ screw values for Ti-6Al-4V. For Pr $\langle a \rangle$, Py $\langle c+a \rangle$, Scr $\langle a \rangle$, Scr $\langle c+a \rangle$

(top left), Ba<a>, Pr<a>, Py<c+a>, Scr<a>, Scr<c+a> (top right) and Ba<a>, Py<a>, Pr<a>, Py<c+a>, Scr<a>, Scr<c+a> (bottom left). Found using q-values from Figure 7-17. 253

Figure 7-21. Results of the individual slip system predictions using the Py {10 $\bar{1}$ 1} <c+a> screw values, for Ti-6Al-4V. For Pr<a>, Py<c+a>, Scr<a>, Scr<c+a> (top left), Ba<a>, Pr<a>, Py<c+a>, Scr<a>, Scr<c+a> (top right) and Ba<a>, Py<a>, Pr<a>, Py<c+a>, Scr<a>, Scr<c+a> (bottom left). Found using q-values from Figure 7-17. 254

Figure 7-22. Predicted C_b^2 values calculated based on the different slip system predictions. 258

Figure 7-23. Comparison of size and strain broadening for modified and standard approaches of the Williamson-Hall method, for Ti-6Al-4V plotted against strain. Only the hkl indices of the hkil notation are shown. 260

Figure 7-24. Comparison of size and strain broadening for modified and standard approaches of the Williamson-Hall method, for Ti-6Al-4V plotted against strain. The strain values are adjusted by using the q-values found from the modified WH method, to adjust the contrast factor value. i.e. if a peak has a larger contrast factor then the strain broadening is reduced. Only the hkl indices of the hkil notation are shown. 260

Figure 7-25. Example modified Williamson-Hall plots for Ti-6Al-4V at a strain of 2% (left) and 8% (right). For the 8% mWH plot the change in $gC^{0.5}$ if all dislocations are Pr<a> is shown. 261

Figure 7-26. The change in the Full-width (average of first 5 peaks, with instrumental accounted for) found from laboratory x-ray and neutron sources (HRPD). The lines represent a fit of the values to a 2nd order polynomial (see text Section 6.2). 264

Figure 7-27. The change in the crystal size (left) and rms strain (right) found from laboratory x-ray and neutron sources (HRPD), using the PV Variance method. The lines represent a fit of the values to a 2nd order polynomial (see text Section 6.2). 264

Figure 7-28. The change in the crystal size (left) and rms strain (right) found from laboratory x-ray and neutron sources (HRPD), using the WH-2 method. The lines represent a fit of the values to a 2nd order polynomial (see text Section 6.2). 265

Figure 7-29. The change in the crystal size (left) and rms strain (right) found from laboratory x-ray and neutron sources (HRPD), using the mWH-3 method. The lines represent a fit of the values to a 2nd order polynomial (see text Section 6.2). 265

Figure 7-30. The change in the crystal size (left) and dislocation density (right) found from laboratory x-ray and neutron sources (HRPD), using the WA log-INDI method. The lines represent a fit of the values to a 2nd order polynomial (see text Section 6.2). 265

Figure 8-1. The slip activity of different slip systems, for different texture components. The slip systems are separated based on their contrast factor (See section 2.4.5) into three different values. The texture components represent the grains that correspond to the (111) reflection at the different angles between the loading and diffraction vectors. 275

Figure 8-2. Dislocation density predictions found using the Schmid model. Model A, left, and Model B, right. Model B has higher CRSS values for the secondary slip systems basal $\langle a \rangle$, pyramidal $\langle a \rangle$ and pyramidal $\langle c+a \rangle$. The two measurement directions transverse (Tr) and axial (Ax) are shown. 279

Figure 8-3. The changes in the predicted total dislocation density plotted against x for the two different models in the measurement directions..... 279

Figure 8-4. Measured and fitted full-width values divided by g ($g=1/d$) at different angles between the tensile direction and the diffraction vector. These measurements are for nickel-200 and stainless steel 316. The fatigue sample is from the work of Wang et al. (2005). 284

Figure 8-5. The full-width divided by g ($k=g=1/d$) predictions for uni-axial tension test. These values are found from the square root of the contrast factor, found the use of the Taylor model. The predictions on the left assume

all grains have the same dislocation density, and those on the right that the relative dislocation densities are given by the Taylor factor. 286

Figure 8-6. A comparison of measured (left) full-width (or integral breadth) divided by g results at different angles, and the corresponding best matched predictions. For stainless steel 10% (top), the results best match the edge predictions with equal dislocation density. For nickel 10%, the results best match the edge predictions with variable dislocation density. For stainless steel fatigue sample the results best match the 50:50 edge to screw, equal dislocation density predictions. 287

Figure 8-7. Measured and fitted full-width values divided by g ($g=1/d$) at different angles between the rolling direction and the diffraction vector (top). For RD-ND sample. These measurements are for nickel-200. The full-width divided by g predictions for this plane is shown for edge dislocations with equal (left bottom) and variable (right bottom) dislocation density in different grains.

..... 289

Figure 8-8. Measured and fitted full-width values divided by g ($=1/d$) at different angles between the rolling direction and the diffraction vector (top). For RD-TD samples. These measurements are for nickel-200 and stainless steel 304. The full-width divided by g predictions for this plane is shown for edge dislocations with equal (left bottom) and variable (right bottom) dislocation density in different grains. 290

Figure 8-9. The change of FW/g values at different x-values and at different strains, for axial (top) and transverse (bottom) directions. 293

Figure 8-10. Measured FW/g values data plotted against x, for 1% strain (top left) and 8% strain (top right) and the predicted FW/g values using Model A (bottom left) and Model B (bottom right). 295

Figure 8-11. Calculated average contrast factor values found using the program ANIZC (Borbely et al 2003), for the different slip systems used in the model. 295

Figure 8-12. The changes in the measured fitted pseudo-Voigt mixing parameter for deformed nickel at 2%, 10% and 30% (left) and stainless steel at 2%, 10% and 16% (right) measured at different angles between the tensile and diffraction vector. The values are the fitted values that are not corrected based on the instrumental broadening..... 298

Figure 8-13. Measured and fitted pseudo-Voigt mixing parameter values at different angles between the tensile direction (or rolling direction) and the diffraction vector. The values are the fitted values that are not corrected based on the instrumental broadening..... 299

Figure 8-14. The calculated pseudo-Voigt mixing parameter of diffraction peaks due to variations in the slip systems (a). The change in the Taylor factor for the grains contributing to the different orientations (b). The calculated shape of diffraction peaks due to a cell structure, where dislocation arrangement and crystal size are orientation dependent, for the full-width (c) and pseudo-Voigt mixing parameter (d)..... 301

Figure 8-15. Taylor factor for uni-axial tension (top) and rolling between the rolling and normal directions (bottom-left) and between rolling and transverse directions (bottom-right)..... 304

Figure 8-16. The measured pseudo-Voigt mixing parameter values for Ti-6Al-4V samples deformed to different applied strains. The values are plotted against x. The values are the fitted values that are not corrected based on the instrumental broadening..... 306

Figure 8-17. WA prediction of mixing parameter from model A..... 307

Figure 8-18. Warren-Averbach analysis results. The change in dislocation density assuming b and C are zero, which is actually $\rho b^2 \bar{C}$. The change in the reciprocal of the crystal size and the extent of the hook effect..... 309

Figure 8-19. Size Fourier coefficients at 8% strain. There is a clear hook effect for all planes, such that the size coefficients can be thought of consisting of two parts..... 309

Figure 8-20. Full-width divided by g plotted against x, for Ti-CP.....	317
Figure 8-21. PV mixing parameter values for Ti-CP. Values are the fitted values from the diffraction pattern.....	317
Figure 8-22. Full-width asymmetry, ASY, (see text for definition) of Ti-6Al-4V (top at 1% strain and middle at 2% and 8%) and Ti-CP (bottom) plotted against x.....	318
Figure 8-23. The predicted activity of (10.12) twins using the Schmid model presented in Section 8.2.2. The peaks See text for difference between twin and parent values.	319

List of Tables

Table 2-1. The value of the planar fault parameter W(g) in fcc crystals, for the first five planes from Warren (Warren 1969)	118
Table 3-1. Composition of the different metals studied.....	127
Table 3-2. The stacking fault energy (γ_{SFE}) of the metals used in this report and selective other alloys.....	128
Table 6-1. Errors associated with full-width values, for Ni, SS-316 and Ti-6Al-4V. The absolute and fractional deviation from a polynomial fit of the data, and the percentage of results that are used in this fit because they are assessed to be part of a trend.....	159
Table 6-2. Errors associated with size and strain values from the Integral Breadth method values, for Ni, SS-316 and Ti-6Al-4V. The absolute and fractional deviation from a polynomial fit of the data, and the percentage of results that are used in this fit because they are assessed to be part of a trend.....	163
Table 6-3. Results for crystal size (D) in Å and rms strain (multiplied by 10^{-3}) using the different single line methods, for Ti-6Al-4V at 8% strain measured in the transverse direction. The ‘good’ peaks are those without considerable overlap and are the (10.0), (10.2), (11.0), (10.4) and (20.3) peaks. The mean and standard deviation values are shown.....	170
Table 6-4. Errors associated with size and strain values from the Variance-A Voigt method, for Ni, SS-316 and Ti-6Al-4V. The absolute and fractional deviation from a polynomial fit of the data, and the percentage of results that are used in this fit because they are assessed to be part of a trend.....	174
Table 6-5. Errors associated with size and strain values from the Variance-A pseudo-Voigt method, for Ni, SS-316 and Ti-6Al-4V. The absolute and fractional deviation from a polynomial fit of the data, and the percentage of results that are used in this fit because they are assessed to be part of a trend.	174

Table 6-6. Errors associated with dislocation density and size values from the Variance-B method, for Ni, SS-316 and Ti-6Al-4V. The absolute and fractional deviation from a polynomial fit of the data, and the percentage of results that are used in this fit because they are assessed to be part of a trend.	179
Table 6-7. The elastic constants (c_{11} , c_{12} and c_{44}) and calculated C_{h00} and q values for nickel and stainless steel found using ANIZC (Borbely et al. 2003). The q -values for standard (111)[110] and partial dislocations (111)[$\bar{2}11$] with a 50:50 edge to screw ratio are shown.	180
Table 6-8. The parameters used to find the contrast factor for the eleven slip systems of titanium (Dragomir and Ungar 2002). The Py-Scr $\langle c+a \rangle$ values are calculated using ANIZC (Borbely et al. 2003) for a random texture and {10 $\bar{1}1$ } (Py4). All slip systems are for edge dislocations except those with 'Scr' that are screw dislocations.....	181
Table 6-9. A comparison of methods used to calculate slip system population from q -values in titanium. The q -values and the corresponding slip systems predictions from Ungar and colleagues (Ungar et al. 2007) are shown and the method used in this work.....	183
Table 6-10. Errors associated with strain and size values from the Williamson-Hall methods, for Ni-200 and Ti-6Al-4V. The fractional deviation from a polynomial fit of the data, and the percentage of results that are used in this fit, because they are assessed to be part of a trend, are shown.	189
Table 6-11. Errors associated with dislocation density and size values from the Warren-Averbach methods, for Ni, SS-316 and Ti-6Al-4V. The fractional deviation from a polynomial fit of the data, and the percentage of results that are used in this fit, because they are assessed to be part of a trend, are shown.	205
Table 7-1. The change in parameters K and m (found from fitting data to equation 7.2), used to show how the crystal size changes with flow stress, for different DPPA methods. These parameters are determined allowing both to change	

and only allowing K to change. The expected values are compared with TEM data on aluminium (Raj and Pharr 1986)* and nickel-200 (Mehta and Varma 1992)**.....	217
Table 7-2. The change in parameters α' and σ_0 (found from fitting data to equation 7.4), used to show how the dislocation density changes with flow stress, for different DPPA methods. These parameters are determined allowing both to change and only allowing α' to change. The expected values are compared with TEM data (details in body of text).....	234
Table 7-3. Contrast factor values for different FCC planes, for edge and screw dislocations, calculated for Nickel-200 and stainless steel.....	244
Table 7-4. The predicted slip systems for Ti-CP at 3.5% and Ti-6Al-4V at 2% and 5%. Results are based on the average q-values obtained from modified Williamson-Hall fits for the axial and transverse direction and using different peaks. For details of the methods see the body of the text. The planes of the slip systems are given in Table 6.8.	255
Table 7-5. The parameters used to find the contrast factor for the eleven slip systems of titanium (Dragomir and Ungar 2002). The planes of the slip systems are given in Table 6.8.....	258
Table 8-1. CRSS values for different slip systems in Ti-6Al-4V from literature [1]- Yapici et al. 2006, [2]- Fundenberger et al. 1997, [3]- Philippe et al. 1995 and those used in this work.....	277

Word Count 70 000

Symbols

ρ	- the dislocation density
σ	- the yield stress
σ_0	- the friction stress, or the yield stress of an annealed sample
G	- the shear modulus
M^T	- the Taylor factor (~3 for an un-textured sample)
α	- a constant dependent on the strain rate, temperature and dislocation arrangement
b	- the magnitude of the Burgers vector
τ^C	- the critically resolved shear stress
$\dot{\gamma}$	- the strain rate
θ	- half the angle between the incident and diffracted beam
λ	- the wavelength
d	- the lattice spacing
n	- an integer representing the order of a peak
g	- the reciprocal of the lattice spacing
k	- the value of g at a particular peaks centre
I_0	- a diffraction peaks maximum intensity
Γ	- the full-width of the peak at half its maximum height (full-width)
ω	- the complex error function
β	- the integral breadth

- β_G - the Gauss integral breadth
 β_c - the Lorentzian integral breadth
 η - the Lorentzian (Cauchy) fraction or the mixing parameter of a pseudo-Voigt function
 $\langle D \rangle_v$ - the volume weighted crystal size perpendicular to the given plane.
 K - the Scherrer constant
 β - is the integral breadth of a peak
 N - an ‘apparent’ strain
 ε - the root-mean-square-strain or micro-strain
 f_M - a parameter related to the parameter M
 $O(..)$ - a higher order term used in MWH equations that gives information about the dislocation arrangement
 C - the contrast factor
 A_n - symmetric Fourier coefficients
 B_n - asymmetric Fourier coefficients
 n - the Fourier frequency
 F - the structure factor
 I - the intensity of a peak
 L - the Fourier length
 \AA - a unit of length equal to 10^{-10}m

The use of Diffraction Peak Profile Analysis in studying the plastic deformation of metals

Abstract of thesis submitted by Thomas H. Simm to the School of Materials, University of Manchester, for the Degree of Doctor of Philosophy, 2013

Analysis of the shapes of diffraction peak profiles (DPPA) is a widely used method for characterising the microstructure of crystalline materials. The DPPA method can be used to determine details about a sample that include, the micro-strain, crystal size or dislocation cell size, dislocation density and arrangement, quantity of planar faults and dislocation slip system population.

The main aim of this thesis is to evaluate the use of DPPA in studying the deformation of metals. The alloys studied are uni-axially deformed samples of nickel alloy, nickel-200, 304 and 316 stainless steel alloys and titanium alloys, Ti-6Al-4V and grade 2 CP-titanium.

A number of DPPA methods were applied to these metals: a full-width method; a method that attributes size and strain broadening to the Lorentzian and Gaussian integral breadth of a Voigt; different forms of the variance method; the Williamson-Hall method; the alternative method; and variations of the Warren-Averbach method. It is found that in general the parameters calculated using the different methods qualitatively agree with the expectations and differences in the deformation of the different metals. For example, the dislocation density values found for all metals, are approximately the same as would be expected from TEM results on similar alloys. However, the meaning of the results are ambiguous, which makes it difficult to use them to characterise a metal. The most useful value that can be used to describe the state of a metal is the full-width. For a more detailed analysis the Warren-Averbach method in a particular form, the log format fitted to individual Fourier coefficients, is the most useful method.

It was found that the shape of different diffraction peaks change in different texture components. These changes were found to be different for the different metals. A method to calculate the shape of diffraction peaks, in different texture components, using a polycrystal plasticity models was investigated. It was found that for FCC metals, the use of a Taylor model was able to qualitatively predict the changes in the shape of diffraction peaks, measured in different texture components. Whereas, for titanium alloys, a model which used the Schmid factor was able to qualitatively explain the changes. The differences in the FCC alloys was attributed to being due to differences in the stacking fault energy of the alloys. For nickel, which develops a heterogeneous cell structure, an additional term describing changes in the crystal size in different orientations is required. The differences between the titanium alloys were shown to be due the presence of twinning in CP-titanium and not in Ti-6Al-4V. This difference was thought to cause an additional broadening due to variations in intergranular strains in twinned and non-twinned regions. The use of polycrystal plasticity models, to explain the shape of diffraction peaks, raises questions as to the validity of some of the fundamental assumptions made in the use of most DPPA methods.

Declaration

I declare that no portion of the work referred to in the thesis has been submitted in support of an application for another degree or qualification of this or any other university or other institute of learning.

Copyright Statement

- (i) The author of this thesis (including any appendices and/or schedules to this thesis) owns any copyright in it (the Copyright) and he has given The University of Manchester the right to use such Copyright for any administrative, promotional, educational and/or teaching purposes.
- (ii) Copies of this thesis, either in full or in extracts, may be made only in accordance with the regulations of the John Rylands University Library of Manchester. Details of these regulations may be obtained from the Librarian. This page must form part of any such copies made.
- (iii) The ownership of any patents, designs, trade marks and any and all other intellectual property rights except for the Copyright (the Intellectual Property Rights) and any reproductions of copyright works, for example graphs and tables (Reproductions), which may be described in this thesis, may not be owned by the author and may be owned by third parties. Such Intellectual Property Rights and Reproductions cannot and must not be made available for use without the prior written permission of the owner(s) of the relevant Intellectual Property Rights and/or Reproductions.
- (iv) Further information on the conditions under which disclosure, publication and exploitation of this thesis, the Copyright and any Intellectual Property Rights and/or Reproductions described in it may take place is available from the Head of School of Materials (or the Vice-President) and the Dean of the Faculty of Life Sciences, for Faculty of Life Sciences candidates.

1. Introduction

The study of the peaks produced by X-ray diffraction and their shapes is a well-developed and valuable method for the study of the microstructure of crystalline materials. This technique, which I refer to as Diffraction Peak Profile Analysis (DPPA), is principally used to find the crystal or subgrain size, the dislocation density and the slip systems present in a metal (Kuzel 2007, Ungar 2003, Warren 1969). DPPA is a statistical method, because it uses information from a single diffraction pattern, which consists of information from many grains. From this pattern a DPPA method quantifies the microstructure of a sample.

To be able to do this it is necessary to make approximations as to how the peaks should broaden by different defect microstructures. The accuracy of these approximations is fundamental as to whether the technique works. However, there is a difficulty in verifying the results by other methods, which means there is an inherent ambiguity in the results. The only parameters that are adequately measured by both DPPA and other methods are the dislocation density and the crystal size. For the dislocation density the results show agreement (Gubicza et al. 2006). Whereas for the crystal size, the values agree for un-deformed samples (Ungar 2003), but for deformed samples the values from DPPA are most often less than found by other methods (Ungar 2003, van Berkum et al. 1994, Kuzel 2007). This discrepancy in crystal size results has led some to believe (van Berkum et al. 1994) that the methods produce systematic errors because of the assumption in their mathematical equations.

One of the main assumptions made is that deformation is homogenous, which means that any differences in the deformation of a grain are random. In order to describe the different broadening of different diffraction peaks (with different hkl indices), an equation called the contrast factor of dislocation has been introduced (Ungar and Tichy 1999, Dragomir and Ungar 2002). This equation can then be used to find information about the dislocations present such as the quantity of edge dislocations, or the amount of a dislocation type (e.g. the amount of $\langle c+a \rangle$ dislocations). However, there are often systematic differences in the deformation of individual grains in a metal based on its orientation (Taylor 1934, Zaefferer 2003, Bridier et al 2005, Dilamore et al. 1972). A method developed by Borbely

and colleagues (Borbely et al. 2000) accounted for this heterogeneity by predicting the different slip systems active in different grains, and hence calculating the contrast factor. The approach has had no use to the author's knowledge, other than by Borbely and colleagues. Hence, further investigation of the approach is needed since it would lead to different results than the contrast factor equation.

Aims and Objectives

The aim of this thesis is to examine the use of Diffraction Peak Profile Analysis methods (in abbreviated terms DPPA) as a technique to characterise the deformed microstructure of metals. The aim is to understand what the results of different DPPA methods represent and to evaluate the use different methods.

The thesis takes a unique approach to evaluate the usefulness of DPPA methods. Five different metals, deformed by uni-axial tension and compression to various applied strains, are analysed by the different DPPA methods. In previous research, when DPPA has been used, in most cases only one metal was studied. In the cases when more metals are analysed, this is either only done at one strain value or for samples that are not plastically deformed. For my research, a number of metals are used. These different metals have been chosen to try to understand a number of factors: (a) the influence of stacking fault energy (SFE), (b) the differences caused by different crystal structures, (c) the influence of twinning. The metals used are nickel-200, stainless steel 316, stainless steel 304, Ti-6Al-4V and Ti-CP. The metals were also chosen because they had similar grain sizes (more than 20 μm) and a single (or dominant) crystal structure. These metals were deformed to a range of applied strains by uni-axial tension and compression, and by rolling, to help to show how the results of the methods change with the amount of imposed deformation. In addition, polycrystal plasticity models were used to try to understand the DPPA results.

The metals were measured by three different diffraction sources, to provide diffraction data to be analysed by the DPPA methods. Measurements were taken

using laboratory x-rays (Materials Science Centre, Manchester, UK), synchrotron x-rays (ID-31, ESRF, Grenoble, France) and neutrons (High Resolution Powder Diffractometer, ISIS, Oxfordshire, UK).

The overall structure of the thesis is as follows:

Chapter 2 provides a literature review and background information. The chapter is separated into sections on the deformation of metals, DPPA methods and other methods that can be used to characterise a deformed metal. In Chapter 3, details are provided of the materials used and how they were deformed, the experimental techniques used in this thesis and in particular the diffraction experiments performed. Chapter 4 introduces the results chapters. These consist of results of the mechanical tests carried out and microscopy of the metals, in Chapter 5. In Chapter 6, the way that the different DPPA methods are implemented are discussed, along with errors involved in their use. In Chapter 7, the different DPPA methods are applied to the different metals at different applied strains to understand the usefulness of the different methods. In Chapter 8, polycrystal plasticity models are combined with diffraction experiments that measure different texture components to understand why different diffraction peaks broaden. Finally, the results are concluded in Chapter 9, where details are provided of future research paths.

2 Background and Literature Review

The scope of this thesis is to understand the use of diffraction peak profile analysis (DPPA) in the field of studying plastic deformation. To do this it is necessary to introduce and discuss research in three key areas-

A. Deformation (Section 2.1)

In this section the current understanding of plastic deformation is presented. The focus is on features of plastic deformation that may be measured by DPPA, such as the deformation microstructure.

B. Techniques (Section 2.2)

In this section the thesis looks at the different techniques that can be used to understand a deformed metal.

C. Diffraction Peak Profile Analysis (Section 2.3 & 2.4)

The focus here is on a particular technique- diffraction peak profile analysis (DPPA)- the different methods of that analysis and different diffraction sources.

2.1 Deformation of metals

When a metal is deformed plastically, the state of the metal changes in a number of ways; shape changes occur at different scales from the macro scale to the grain scale, the texture (or preferred orientation) evolves, intergranular stresses and strains are generated, the flow stress (or ease with which it plastically deforms) usually increases and the microstructure changes with an increase in the distortion in the crystal lattice. The manner in which these different aspects change is difficult to understand, due to the complicated nature in which these changes occur on a number of different length scales. Instead, it is common to consider only part of the deformation, such as the texture evolution or development in the microstructure. Models that try to predict changes of the sample as a whole, such as its texture, its strength or the average stresses in the grains, often consider the grains as a continuum and ignore the microstructure (Taylor 1934, Bate 1999, Lebensohn and Tome 1993). Other models, called work hardening models, are primarily concerned with dislocations and their interactions with each other. These models may also predict macroscopic properties, often the yield strength, but do so by modelling how dislocations interact (Mughrabi 2006a & 2006b, Kocks 1966, Kuhlmann-Wilsdorf 1998, Kubin and Cannova 1992, Hahner 2002).

2.1.1 Plastic Deformation

The deformation of metals has two components, an elastic component and a plastic component. It will experience an elastic deformation as the atoms are pulled further apart and a plastic deformation, where the crystal structure is disturbed. In metals, the main process of plastic deformation involves the movement of planes of atoms across each other. This is called slip, and occurs with the movement of a defect in the crystal structure called a dislocation. The behaviour of dislocations is very important in being able to understand how a metal deforms. Three vectors define a dislocation: its Burgers vector, which is the distortion in the perfect lattice caused by the dislocation, the slip plane normal, a vector normal to the crystallographic plane that the dislocation glides along, and the dislocation line vector, a line or loop in the crystal defining the position of the dislocation. The direction of the dislocation line relative to the Burgers vector

affects the behaviour of the dislocation. When the vectors are parallel, called a screw dislocation, the dislocation can move onto other crystallographic planes, whereas when they are perpendicular, an edge dislocation, this is not possible. In most cases dislocations are a mixture of the two.

A dislocation is most likely to move on the slip plane on which atoms are most closely packed and with a Burgers vector in the direction that atoms are closest packed on this plane. To define how easy a particular slip system is to activate, a quantity called the critically resolved shear stress (CRSS) is used. The CRSS of a slip system is the resolved shear stress at which the system activates. Therefore in general, slip systems on the close packed planes and directions have the lowest CRSS.

Two different types of crystal structures are studied in this work, face-centred-cubic (FCC) and hexagonal-close-packed (HCP). The crystal's structure has a large influence on how a metal deforms.

2.1.2 Slip in FCC metals

For FCC metals, dislocations are only observed on the {111} slip planes and with [110] Burgers vectors (Figure 2-1). The exception to this is when the [110] dislocation dissociates, or splits, into two smaller dislocations with a defect called a stacking fault between them. These partials are still on the {111} plane but have a Burgers vector in the [112] directions.

2.1.3 Slip in HCP Metals

In metals with a hexagonal structure it is common in polycrystals to observe more than one type of dislocation. The close packed direction is in the set of [11 $\bar{2}$ 0] or $\langle a \rangle$ directions (see Figure 2-1). These dislocations have the lowest CRSS and are the most dominant. $\langle a \rangle$ dislocations have been observed on basal, prismatic and pyramidal planes (Yoo and Wei 1967). The ease with which slip can occur on these different slip systems is dependent on the c/a ratio (the ratio of the length of the unit cell in the \underline{c} and \underline{a} directions). For metals with high values of c/a , such as magnesium, the closest packed plane is the basal plane and slip on this plane

dominates. For metals with a smaller c/a ratio, such as in titanium, prismatic slip can become the dominant slip system. This is partly because the prismatic planes become more closely packed as the c/a ratio falls. However, the c/a ratio is not the only factor contributing to which slip system dominates. Slip on a particular system may be preferred if it is energetically favourable for a dislocation to dissociate and slip as a pair of partial dislocations.

Slip in the $\langle a \rangle$ directions is mostly preferred, but with just $\langle a \rangle$ type slip it is not possible to accommodate strain in the $\langle c \rangle$ direction. There are two main ways in which strain may be accommodated in the c-direction in HCP metals; $\langle c+a \rangle$ slip and twinning (twinning is discussed in more detail later). The quantity of $\langle c+a \rangle$ dislocations can be difficult to determine. This is due to the difficulty of using TEM to determine a dislocation type, but also because of the difficulty in separating a $\langle c+a \rangle$ dislocation from a twin (Zaefferer 2003).

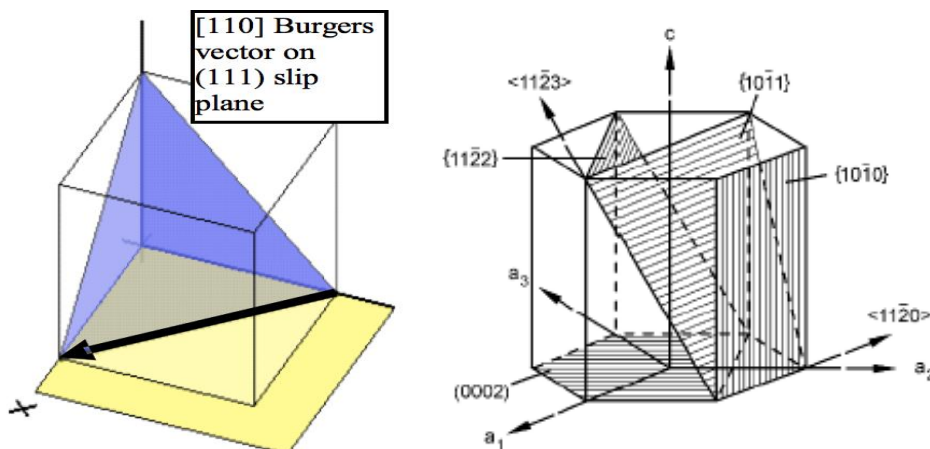


Figure 2-1. FCC (left) and HCP (right) unit cells. For the FCC unit cell, one of the $\{111\}[110]$ slip systems are shown. In HCP notation the a_1 , a_2 , a_3 axes are used and selected planes and Burgers vectors are shown. (Lutjering and Williams 2007)

The dominant slip systems in titanium are prismatic $\langle a \rangle$, basal $\langle a \rangle$, first order $\{10\bar{1}\bar{1}\}$ pyramidal $\langle a \rangle$ and $\langle c+a \rangle$ and second order $\{11\bar{2}\bar{2}\}$ pyramidal $\langle c+a \rangle$. However, the relative activities are dependent on the composition (Biswas 1973, Zaefferer 2003, Partridge 1967). For single crystals of high purity titanium (oxygen and nitrogen content less than 0.1 weight %) the dominant slip system

was found to be prismatic $\langle a \rangle$, with a CRSS a third of basal $\langle a \rangle$ (Biswas 1973). With increased oxygen, nitrogen (Biswas 1973) or aluminium content (Zaefferer 2003) the CRSS of the other $\langle a \rangle$ slip systems falls. In the case of Ti-6Al-4V, which is a two-phase alloy containing both HCP and body-centred-cubic (BCC) phases, Zaefferer (2003) believes the increased aluminium content has the effect of reducing the stacking fault energy on the basal plane and restricting the screw dislocations to this plane. The composition changes the relative activity and CRSS of the different $\langle a \rangle$ slip systems, but researchers report the same order of importance of prismatic and then basal and the pyramidal. In the majority of cases the $\langle c+a \rangle$ slip systems observed are either first or second order pyramidal planes (Zaefferer 2003, Gloaguen et al. 2002, Partridge 1967, Akhtar 1975). The most commonly observed plane is the first order $\{10\bar{1}1\}$ plane and $\langle c+a \rangle$ on $\{11\bar{2}2\}$ are much more rare.

In DPPA whether a dislocation is screw or edge, has important consequences to the results. This observation is found for titanium, for both commercially pure titanium (CP-Ti) (Conrad and Jones 1953, Biswas 1973, Zaefferer 2003) and for Ti-6Al-4V (Castany et al 2007, Zaefferer 2003). At low strains, dislocations are often found to be long, straight and close to screw dislocations, with debris of edge dislocations and prismatic loops (Figure 2-2 and Figure 2-3). However, the plane of these dislocations can be difficult to determine. Castany et al. (2007) suggests that in Ti-6Al-4V the screw dislocations lie on the prismatic, pyramidal and basal planes. In contrast Zaefferer (2003) believes screw dislocations are mainly restricted to the basal plane. The observation of screw dislocations being predominantly on the basal plane was also found by Biswas (1973). These screw dislocations often have debris of edge dipoles and prismatic loops, a result of dislocation interactions (Biswas 1970, Conrad 1981). The slip plane of edge dislocations is in most cases the prismatic plane (Biswas 1973, Zaefferer 2003). The ability of $\langle c+a \rangle$ dislocations to cross-slip is also dependent on the composition. It is possible for these dislocations to be short and straight or more wavy, as shown in Figure 2-3.

With increasing strain in high purity and commercially pure titanium (Biswas 1973) the number of these lines was found to increase. In addition, there was

found to be a more uniform distribution of dislocations along with more tangling of dislocations.

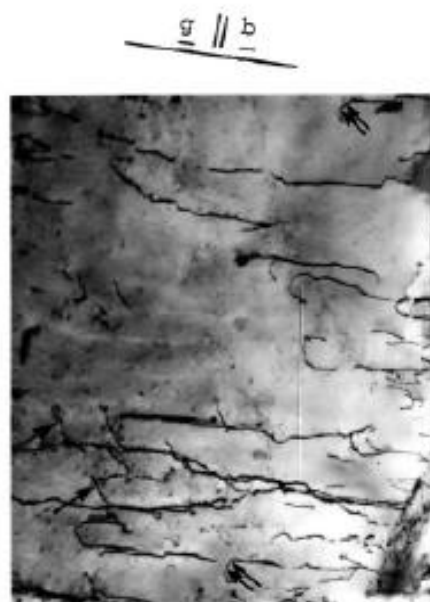


Figure 2-2. TEM micrograph of high pure titanium deformed to a strain 0.06 (Biswas 1973), showing dislocations close to the basal plane.

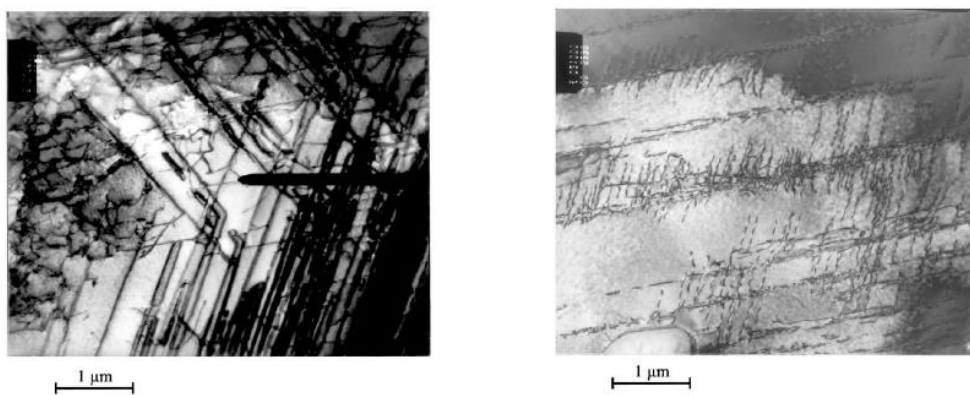


Figure 2-3. TEM micrograph of a single-phase titanium alloy (left), showing long and straight $\langle a \rangle$ dislocations on the right and wavy $\langle c+a \rangle$ dislocations on the left. A TEM micrograph of a two-phase Ti-6Al-4V showing $\langle a \rangle$ dislocations (Zaefferer 2003).

2.1.4 Additional modes of deformation

Slip is the dominant form of deformation in metals but is not the only one. For the metals studied here, additional modes of deformation also occur and some of these are presented below.

Deformation Twinning

Deformation twinning is a mode of deformation that causes a metal to undergo a sudden localised shear (Christian and Mahajan 1995, Honeycombe 1968). The process involves the co-operative movement of atoms within a small region, the twinned region, which shear and shuffle to produce a lattice, which is re-orientated with respect to the surrounding parent material. The likelihood of twinning occurring is dependent on the metal and the manner that the metal is deformed. In general twinning, is favoured at high strain rates and low temperatures (Honeycombe 1968, Christian and Mahajan 1995). For many metals these are the only conditions that twinning is expected to occur under. However, there are exceptions when twinning occurs at moderate strain rates and at room temperature. In FCC metals the activity of twinning is directly related to the stacking fault energy (SFE) of the metal (Hadji and Badji 2002). When this value is high such as in nickel, slip dominates and twinning is unlikely to occur. However, the lower the SFE the more important twinning is as a deformation mode. Another exception is in HCP metals. In these metals, twins can occur when the dominant $\langle a \rangle$ slip is unfavourably orientated or in order to accommodate shear in the c-direction (Honeycombe 1968, Christian and Mahajan 1995). However, the presence or otherwise is very dependent on the composition of the metal (Honeycombe 1968, Christian and Mahajan 1995).

Although the incorporation of twinning into polycrystal plasticity models has had some success for HCP metals (Philippe et al. 1995, Barnett 2003, Kiran Kumar et al. 2007) and FCC metals (van Houtte 1978), there are problems with doing so. Normally, twinning is incorporated into a model in the same way as a slip system (van Houtte 1978), but allowing for the fact that twinning is directional. A twin is directional because the activity of a twin is dependent on the angle between the planes and directions, which define the twin, and the applied deformation (Honeycombe 1968). This directionality is incorporated by giving different values

for the ease with which a twin can occur depending on the relationship between the twin and the applied deformation.

However, such an approach may be problematic because of the differences between slip and twinning. For example it has been suggested that a large quantity of twins occur as the result of nucleation at a grain boundary due to prismatic slip in a neighbouring grain (Wang et al. 2010). This would not be accounted for in standard polycrystal plasticity models. In addition to this it is debatable whether there is a CRSS for twinning in the same way as there is for slip (Christian and Mahajan 1995).

In HCP metals twins can occur but whether they do is very dependent on the alloying additions. The most common twins are {1122} and {10T1}, when the c-axis is in compression and {10T2} and {1121}, when the c-axis is in tension (Glavicic et al. 2004, Battaini et al. 2007, Bozzolo et al. 2010, Mullins and Patchett 1981). In CP-Ti, twinning is known to be an important deformation mode (Glavicic et al. 2004, Battaini et al. 2007, Bozzolo et al. 2010, Mullins and Patchett 1981). The twins vary in size, see Figure 2-4, and can grow to engulf the whole grain. In Ti-6Al-4V twinning is only expected under extreme conditions (Liu et al. 2003, Karaman et al. 2005, Yappici 2006). However, recent research (Prakash et al. 2010) has shown that twinning may be a significant contributor to deformation at low strain rates and at room temperature. In addition, some researchers have used twinning as a slip system in polycrystal plasticity models in order to explain experimental results (Philippe et al. 1995). The twins observed in Ti-6Al-4V are smaller than in Ti-CP (Liu et al. 2003, Prakash et al. 2010, Karaman et al. 2005, Yappici et al. 2006) and are less than $0.1\mu\text{m}$ in thickness. Prakash and colleagues (Prakash et al. 2010) also suggest that complete grain twinning may occur.

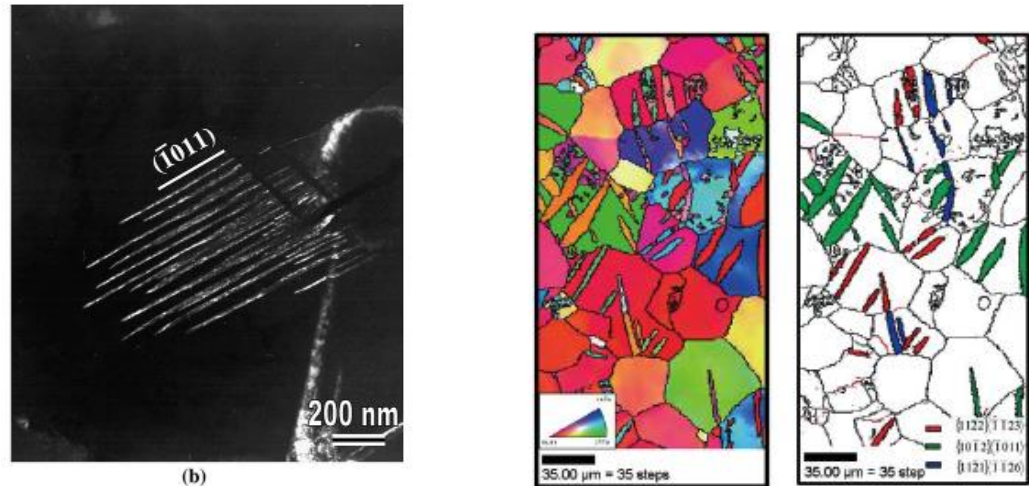


Figure 2-4. Twin observed in Ti-6Al-4V (left) are often small (Yappici et al. 2006). Whereas, those in Ti-CP are larger often dominating a grain (Glavicic et al. 2004).

In nickel, twins are not expected to occur unless at very low temperatures or high strain rates. However, the SFE of stainless steel is much lower and deformation twins are often observed. Unlike twins in HCP metals twins in FCC metals are all reported to occur on the (111) plane. The twins tend to occur as long bands, with a thickness of approximately $0.1\mu\text{m}$, smaller than the average twin in Ti-CP (Figure 2-5). These bands may also contain stacking faults, martensite and twins (Lee and Lin 2001). The occurrence of these twins may be related to the stress of the sample. Byun and colleagues (Byun et al. 2003, Byun et al. 2006) separated types of deformation modes into three groups depending on the stress in the stainless steel alloy, SS-316. Below 600MPa twinning is not thought to be significant but above 600MPa they describe deformation as being dominated by twins and large stacking faults. The results of Bocher et al. (2001) on SS-316 agree with this; below 550MPa twins occur in less than 5% of grains but at 600MPa around 20% of grains contain twins. The stainless steel alloy SS-304, has a lower SFE to SS-316 and so has a higher propensity to twin, but a similar behaviour to SS-316 is observed (Lee and Lin 2001). In stainless steel, annealing twins can be produced during grain growth (Vaughan 1970). These twins are similar to deformation twins and it can be difficult to separate the two (Capeletti et al. 1972).

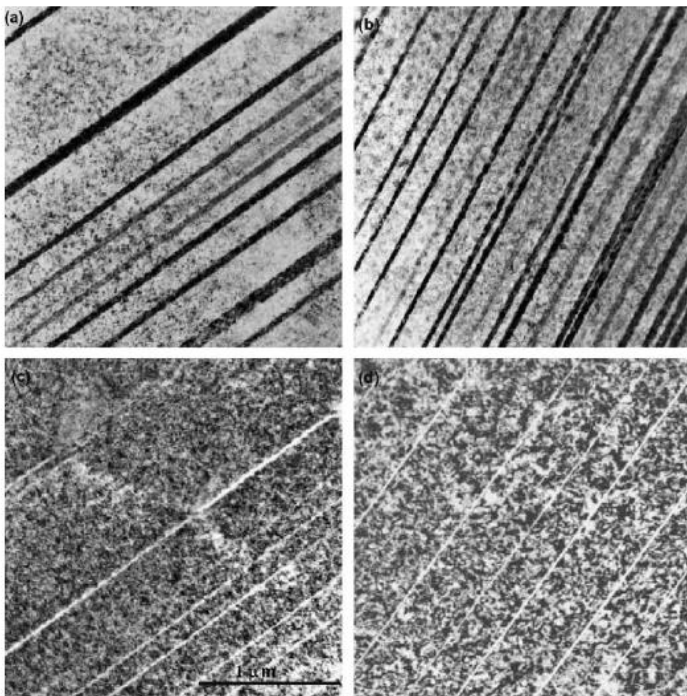


Figure 2-5. Deformation twins in SS-316 at a strain of 10% (Byun et al. 2003) includes doses up to 0.05.

Stacking Faults

A stacking fault is a planar fault, which causes the organised rearrangement of the position of atoms from the perfect crystal structure (Figure 2-6). Stacking faults can be produced during plastic deformation and play an important role in deformation (Hull and Bacon 2001).

An important way in which stacking faults can occur is by dissociation (splitting) of a dislocation into two smaller dislocations. These two dislocations become connected by an intrinsic stacking fault and may move more easily than the whole dislocation. The stacking fault energy (SFE) is the force per unit length of dislocation line that acts to pull a dislocation together. The value is inversely proportional to the equilibrium separation of the dislocations. The SFE is different for different metals, influenced by alloying, and has a large influence on the deformation microstructure. Stacking faults are more likely to have a larger separation, and hence more likely to be observed, when the SFE of a metal is high, and after the metal has been deformed to a greater extent. They are often observed in stainless steel alloys. Byun and colleagues (2006) showed that in

SS316 the separation of stacking faults increased from 30nm at 440MPa to 100nm at 550MPa.

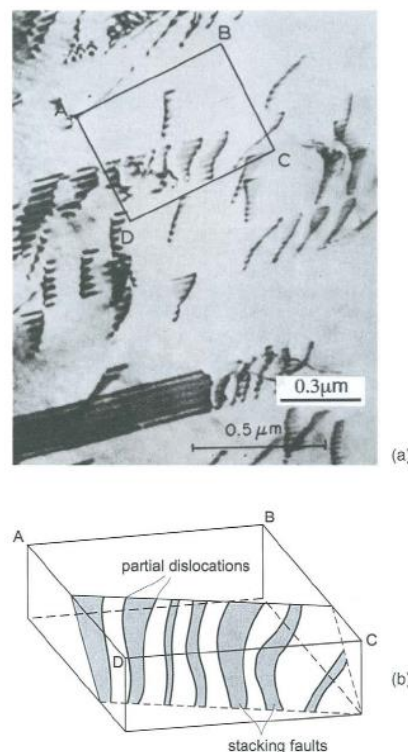


Figure 2-6. Transmission electron microscopy (TEM) of extended dislocations in a copper alloy (above) and a diagram representing the region highlighted in the TEM picture (below) (Hull and Bacon 2001).

2.1.5 Work Hardening

In most metals, with increasing amounts of plastic deformation, there is an increase in dislocation density. This causes an increase in flow stress with plastic deformation, called work hardening (Honeycombe 1968).

During plastic deformation dislocations move and interact with each other, with grain boundaries, with second phase particles and precipitates and with other defects of the perfect crystal structure. The dislocations can annihilate each other, new dislocations can be generated and dislocations can become trapped. When a metal work hardens the dislocation density increases, because of these interactions and this in turn causes an increase in the resistance of dislocations to glide.

Therefore, the stress needed for plastic deformation to occur increases with increasing amounts of plastic deformation.

The behaviour of many dislocations is difficult to understand. Some researchers try to model this by simulating the behaviour of dislocations, such as the dislocation pile-up (Hull and Bacon 2001) or more complicated models involving the interaction of many dislocations (Kubin and Canova 1992). Others consider groups of dislocations and try to model the behaviour of the groups (Holt 1970, Kocks 1966, Kuhlmann-Wilsdorf 1998). In both cases assumptions must be made and there are limitations with the predictions of the models.

Numerous experiments have shown that the flow stress (the stress needed to allow plastic deformation) is proportional to the square-root of the dislocation density (Figure 2-7). This relationship is also found to be independent of the dislocation structure or the crystal structure of the metal (Mecking and Kocks 1981, Conrad 1981). This relationship is called the Taylor equation and can be given by the following equation:

$$\sigma = \sigma_0 + \alpha M^T G b \sqrt{\rho} \quad (2.1)$$

Where, ρ is the dislocation density, σ is the yield stress, σ_0 the friction stress, or the yield stress of an annealed sample, G the shear modulus, M^T is the Taylor factor (~3 for an un-textured sample) and α is a constant dependent on the strain rate, temperature and dislocation arrangement.

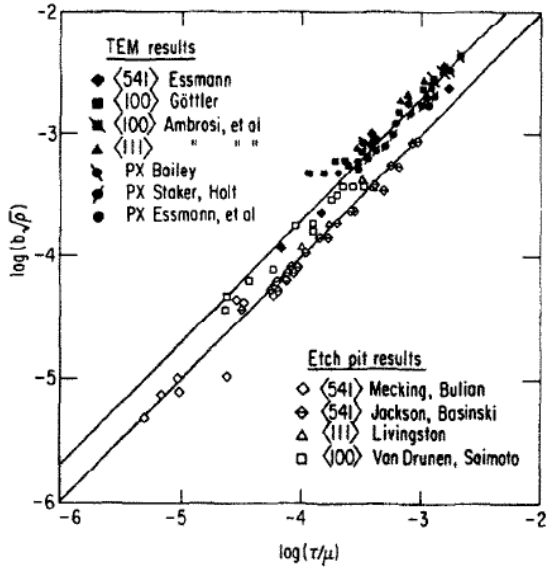


Figure 2-7. The change in the square-root of the dislocation density with changes in the stress for copper samples measured by TEM and etch pit methods (Mecking and Kocks 1981).

The value of α measured by different techniques has been found to vary between approximately 0.17 and 1. Mecking and Kocks (1981) showed that it varied between 0.5 and 1 for a number of different experiments on copper, the range being mainly due to measurement technique, for TEM it was approximately 0.5. Lee and Lin (2001) found the value of alpha to be approximately 0.17, and independent of strain rate, for stainless steel 304 samples using TEM. Conrad (1981) found the value to vary between 0.53 and 0.74 for different titanium alloys deformed at different temperatures. DPPA has been used to measure dislocation density for aluminium, copper and nickel (Gubicza et al. 2006) and IF steel (Sarkar et al. 2009). In both cases the value of alpha was found to be 0.33. The value of α is expected to change due to differences in the dislocation arrangement, but this change is expected to be by less than 10% (Kocks and Mecking 2003).

2.1.6 Recovery

Recovery is a series of micromechanisms that change the properties of a deformed material, most importantly the dislocation structure (Figure 2-8). Recovery begins with the development of dislocation cells, after this the misorientation across these cells increases and dislocations within are annihilated and finally these

dislocation structures can grow. There is a driving force for these changes because the dislocation structures with fewer more misorientated boundaries are more energetically favourable. For example, it can be shown (Humphreys and Hatherly 2004) for a particular type of boundary, a tilt boundary, that the energy of the boundary increases with increasing misorientation and the energy per dislocation decreases with increasing misorientation.

Recovery can occur during deformation, and is called dynamic recovery, or during annealing of a deformed metal. The extent to which recovery occurs depends on a number of factors including: the material, the strain and deformation temperature. The most favourable conditions being for high SFE metals with low solute content, large strains and high temperatures.

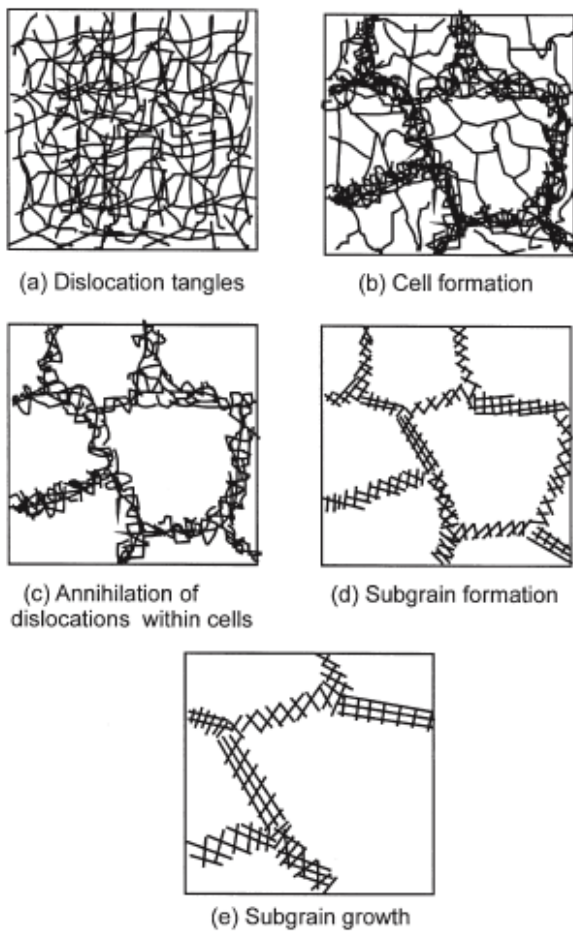


Figure 2-8. The different stages of recovery of a plastically deformed metal (Humphreys and Hatherly 2004).

Edge and screw dislocations behave in slightly different ways and these differences help determine how the dislocation microstructure develops. Edge dislocations have a much higher mobility than screw dislocations. For example edge dislocations have been shown to move 50 times faster than screw dislocations (Hull and Bacon 2001). Screw dislocations can cross-slip onto different slip planes, but edge dislocations may slip onto different planes at high temperatures by a process known as climb. This ability to cross-slip means that screw dislocations are more likely to attract and annihilate other screw dislocations, of opposite signs. However, this ability to cross-slip is not the same for all metals. The biggest factor that determines how easy it is for a metal to cross-slip is the stacking fault energy (SFE). Cross-slip is more difficult to occur when a dislocation has dissociated into partial dislocations, separated by a stacking fault. This separation is energetically favourable; hence energy is required to form a perfect dislocation. For metals with high SFE dislocations less energy is required to form perfect dislocations and they can cross slip easily, whereas when the SFE is low, the energy required is higher and dislocations tend to remain on the same plane.

These differences have important consequences to how the dislocation arrangement changes. This will be considered in terms of the distinct ‘stages’ of work-hardening, after Diehl (1956), that a metal experiences. It is thought that the features of these different stages are the same for all metals. However, depending on the metal and the conditions a particular stage may not occur.

In stage I primary dislocations, those with the highest resolved shear stress, are activated. In metals with high stacking fault energy, edge dislocation are dominant and screw dislocations are rarely seen as they attract and annihilate each other (Hull and Bacon 2001). However, when the SFE is low there is a dominance of screw dislocations, because of the greater mobility of edge dislocations and the difficulty of cross-slip by screw dislocations. In stage II there is the start of activity of secondary dislocations and the steepest rate of strain hardening, as secondary and primary dislocations interact. In stage III, dislocations cross-slip from their original slip planes. The screw dislocations are attracted to each other and annihilate and edge dislocations rearrange to form low-angle boundaries. This

process results in the reduction of the dislocation density and arrangement of dislocations into a cell structure and is called dynamic recovery. The onset of stage III is favoured at higher temperatures and for high SFE metals. If the stacking fault energy is low, dynamic recovery is restricted and may occur at a higher amount of deformation or not at all. In these cases dislocations can be restricted to planar slip, where large amounts of deformation are accommodated by the formation of deformation bands. In addition to this there can be additional active deformation modes. If instead the stacking fault energy is high then stage III will dominate and the other stage may not be visible.

In agreement with the high stacking fault energy (SFE) of nickel, dislocation cell structures are observed in nickel from the earliest stages of plastic deformation (Keller et al. 2010, Hansen & Ralph 1982 and Feaugas and Haddou 2007). An example of the dislocation structures present in nickel is shown in Figure 2-9.

Stainless steel has a lower SFE and consequently the dislocation arrangement was found to be different. The type of stainless steel has been found to be important in determining the nature of the deformation. For the two austenitic stainless steels that have been studied here, SS-304 has a lower SFE than SS-316. Both metals have been found to have a similar and varied defect microstructure. Dislocations have been observed in different arrangements, including planar slip, tangled random dislocations, dislocation arrays and dislocation cells. It has been found that the arrangement of the dislocations changes with increased amounts of deformation. With increased applied strain the dislocation arrangement changes from being dominated by planar slip, at low strain, to dislocation tangles then dislocation walls, at higher strains, and then dislocation cells at the highest strain (Lee and Lin 2001, Feaugas 1999 and Bocher et al. 2001). The relationship found by Feaugas (Feaugas 1999) is shown in Figure 2-10, for SS-316, but others find similar observations for SS-316 (Bocher et al. 2001) and SS-304 (Lee and Lin 2001). However, it can be seen that the dislocation cell structures in stainless steel are not as well developed as in nickel and their formation is delayed.

A dislocation cell structure can develop in some titanium alloys. However, this is only possible for alloys with a high SFE. Biswas (1973) found a cell structure developed in high purity titanium (Figure 2-11) but not for the other alloys measured. In particular in Ti-6Al-4V the high aluminium content is expected to lower the SFE and make the development of cell structures unlikely to occur (Zaefferer 2003, Prakash et al. 2010).

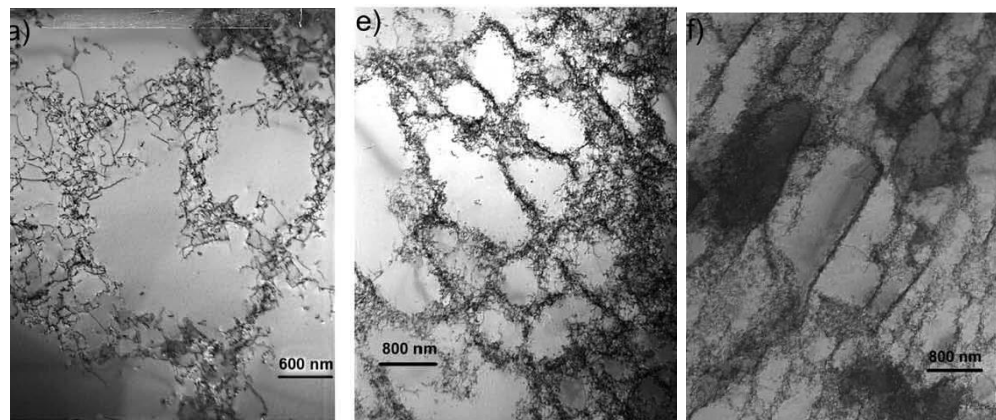


Figure 2-9. Dislocation structure of high purity nickel at 2.5% strain with a grain size of $36\mu\text{m}$ (left), 10% strain grain size ($\text{gs}=200\mu\text{m}$) (middle) and 24% strain $\text{gs}=200\mu\text{m}$ (right) from Keller and colleagues (2010).

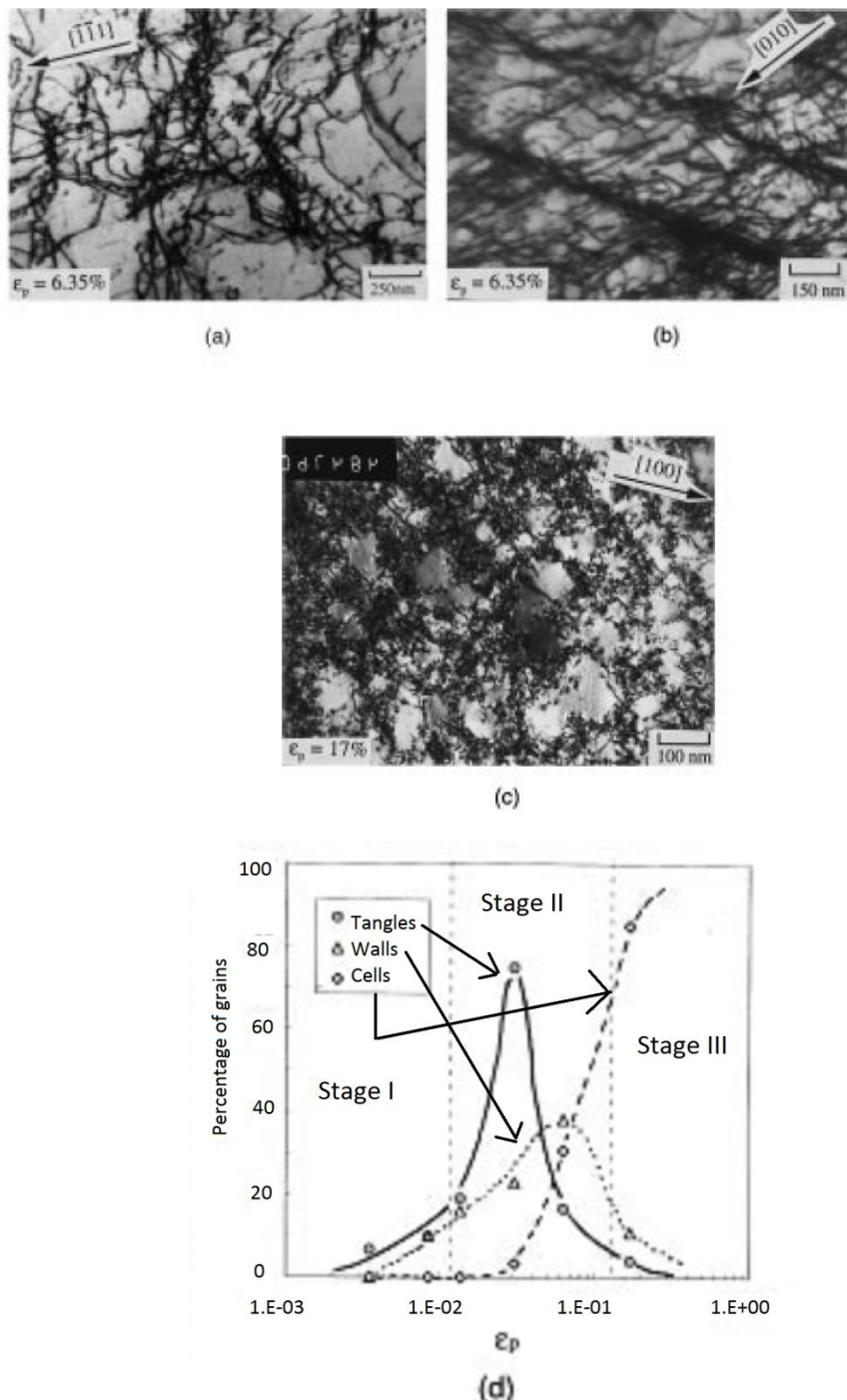


Figure 2-10. The different types of dislocation arrangements in SS-316 from Feaugas (1999). In (a) are dislocation tangles, in (b) dislocation walls and in (c) dislocation cells. The evolution of these different dislocation types is shown in (d). In stage I, tangles and walls are active, in stage II tangles dominate and in stage III dislocation cells dominate.

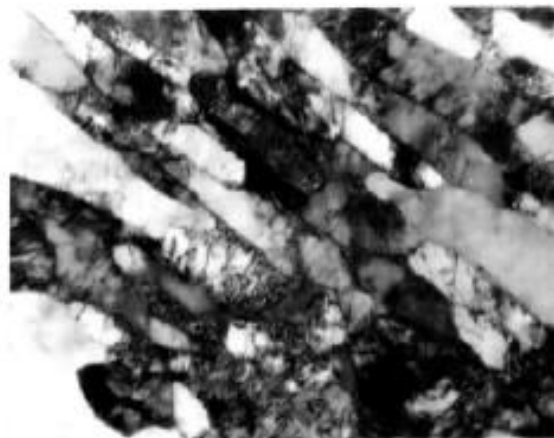


Figure 2-11. Dislocation structures of deformed high purity titanium alloy, viewed by TEM micrographs (magnification 46,000x) showing a cell structure after a strain of 2.27 (227%) (Biswas 1973).

The nature of the cell structure will change with increasing amounts of applied deformation. In particular it has been found, for a number of different metals, that the size of dislocation cells will fall and the misorientation across these cells will increase with applied strain (Sevillano et al. 1981), independent of the deformation mode. A number of researchers (Abson and Jonas 1972, Barrett et al. 1972, Lee and Lin 2001) have found that the dislocation cell size (D) falls approximately inversely proportional to the flow stress, this is equivalent to the cells behaving as grains and following a Hall-Petch relationship. However, Raj and Pharr (1986) did a compilation of the available data and found that a more accurate representation would be given by:

$$D = Kb \left(\frac{G}{\sigma} \right)^m \quad (2.2)$$

Where, b is the magnitude of the Burgers vector, m and K are constants that are approximately 1 and 10 respectively, G the shear modulus and σ the flow stress. Aluminium had values of m and K of 0.95 and 25, an aluminium-zinc alloy values of 1.05 and 20, and stainless steel had values of 1.5 and 0.6 (Raj and Pharr 1986).

It has been found that there is a heterogeneity to the dislocation structure. Dilamore and colleagues (1972) showed this in rolled iron (Figure 2-12) and

Hansen and colleagues (2006) in pure aluminium (Figure 2-13). These two observations suggest that there is a relationship between a quantity called the Taylor Factor and the dislocation structure. The Taylor factor is a quantity found from polycrystal plasticity models that is related to the orientation of a grain and how the sample is deformed. From Figure 2-12, it can be seen that with increasing values of M^T , the cells are smaller with a bigger misorientation across them, which is the same as the behaviour that happens with increased plastic deformation. This observation is similar to that of Hansen and colleagues (2006), because the regions with the highest Taylor factor have a cell-block structure with parallel planar GNBs, which they called type I cell structure. At the lowest values of M , there is type II structure with equiaxed dislocation cells, and the least misorientation across them. In between these two in terms of Taylor factor and dislocation structure is the type III structure. The relationship of Dilamore and colleagues (1972) and Hansen and colleagues (2006) are slightly different. For example, there are orientations where the Taylor factor of Type I and Type II are the same, in contrast to the results of Dilamore and colleagues. In addition, the results of Hansen and colleagues suggest that the types of dislocation structure are distinct, whereas the results of Dilamore and colleagues show a continuous change.

The behaviour observed by Hansen and colleagues (2006) was also observed by Feaugus and Haddou (2007) in nickel. However, for stainless steel 316, with a lower SFE, they found the position of type I and type III were switched, Figure 2-14.

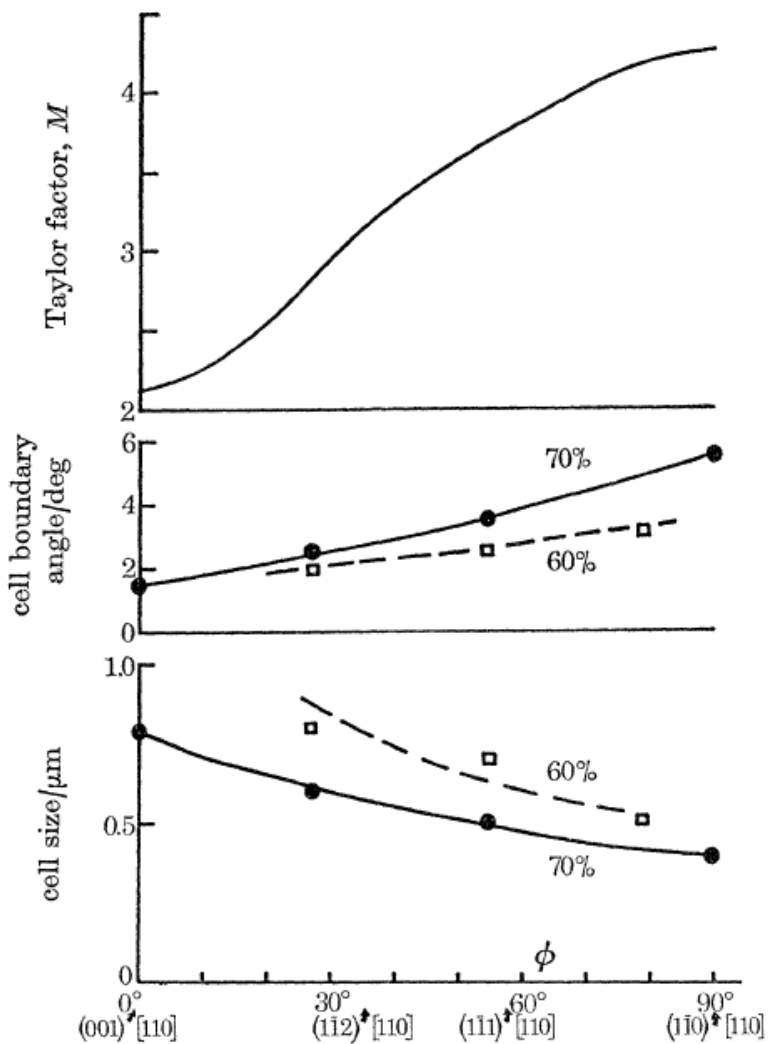


Figure 2-12. The variation in the cell boundary angle (middle) and cell size (bottom) with different orientations in iron (Dilamore et al. 1972). The variation in the Taylor factor is also shown (top).

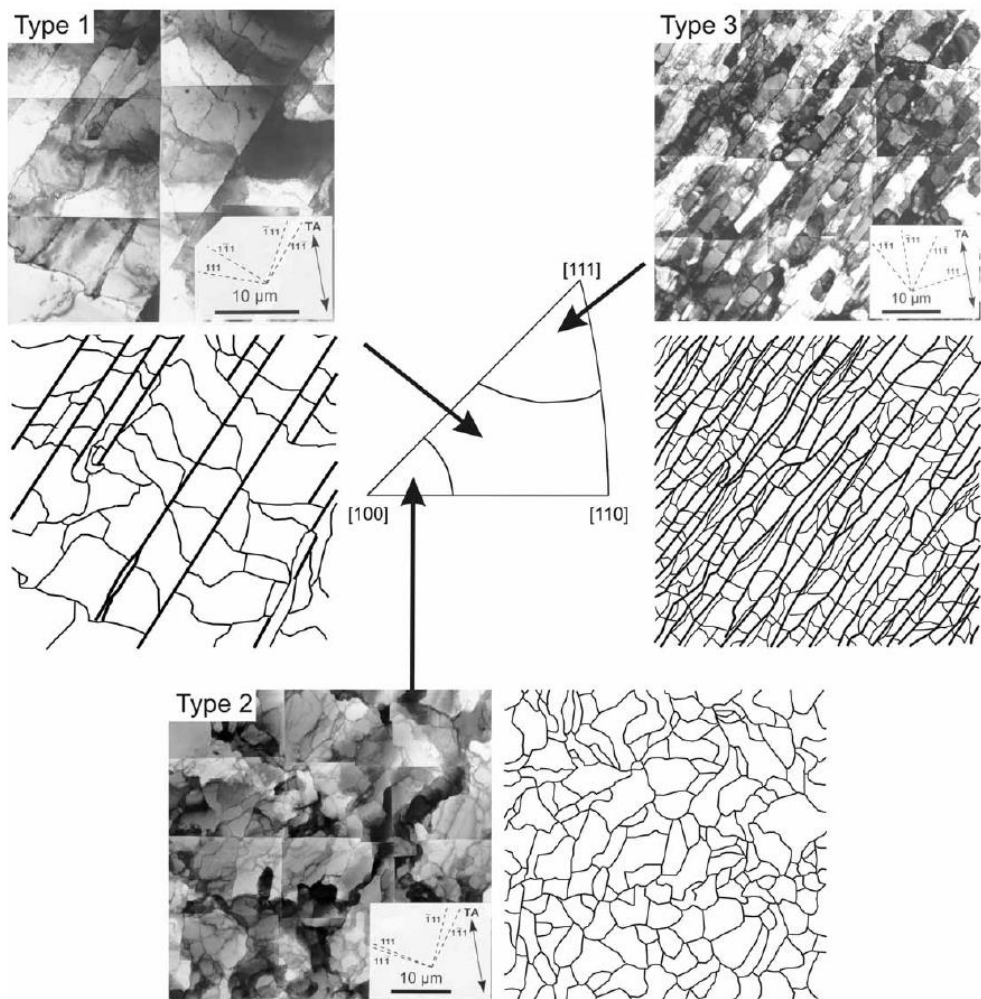


Figure 2-13. The different dislocation structures in aluminium identified by TEM (Hansen et al. 2006). The value of M increases from [100] to the outside of the stereographic triangle.

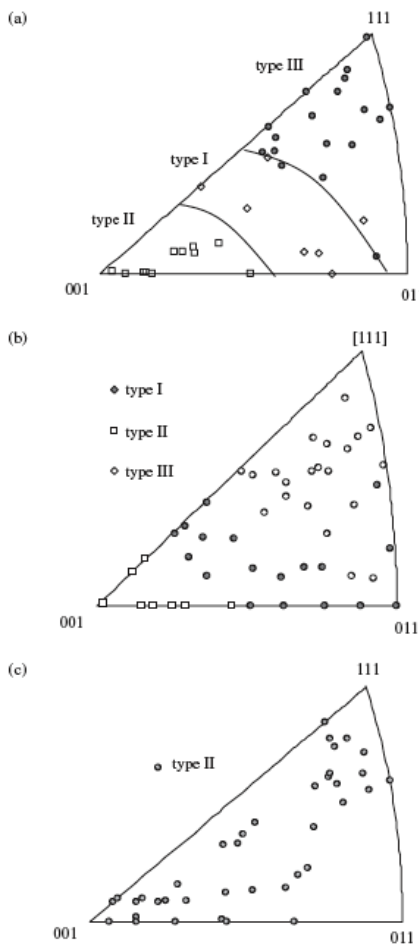


Figure 2-14. The different cell structures observed in (a) polycrystal nickel with grain size $168\mu\text{m}$, (b) austenitic stainless steel and (c) polycrystal nickel with grain size $18\mu\text{m}$ (Feagus and Haddou 2007)

2.1.7 The Composite Model

There are many work-hardening models that try to describe how a cell structure may develop and how it will behave. Mughrabi's Composite Model (Mughrabi 2006a and 2006b) has as a starting point that the cell structure exists and then tries to explain how the metal will behave. This model is important because it was able to explain observations about the peak shape from various X-ray measurements of high SFE metals (Ungar et al. 1984).

In Mughrabi's Composite Model the idea is that the cell-walls are harder than the cell-interior such that the deformation induces internal stresses of the same sign as the external stress in the cell walls, and of opposite sign (or 'back') in the cell interiors. A particular diffraction peak can be considered to consist of two peaks,

one from the cell interiors and the other from the cell walls. Since the cell interiors are larger in size, they have a greater intensity. In contrast, the cell walls have a larger dislocation density and consequently a bigger full-width, but because the two components are at different stresses the position of the two peaks are also different. Consequently, an asymmetric diffraction peaks is expected (Figure 2-15).

An experiment that verified this model was conducted by Ungar and colleagues (1984), on uni-axially deformed single crystal copper sample. In the experiment, he 200 diffraction peaks parallel and perpendicular to the tensile direction, was measured by x-ray diffraction. It was found that the peak was asymmetric (the width of the peak was different either side of its centre), and this asymmetry was reversed in the two directions.

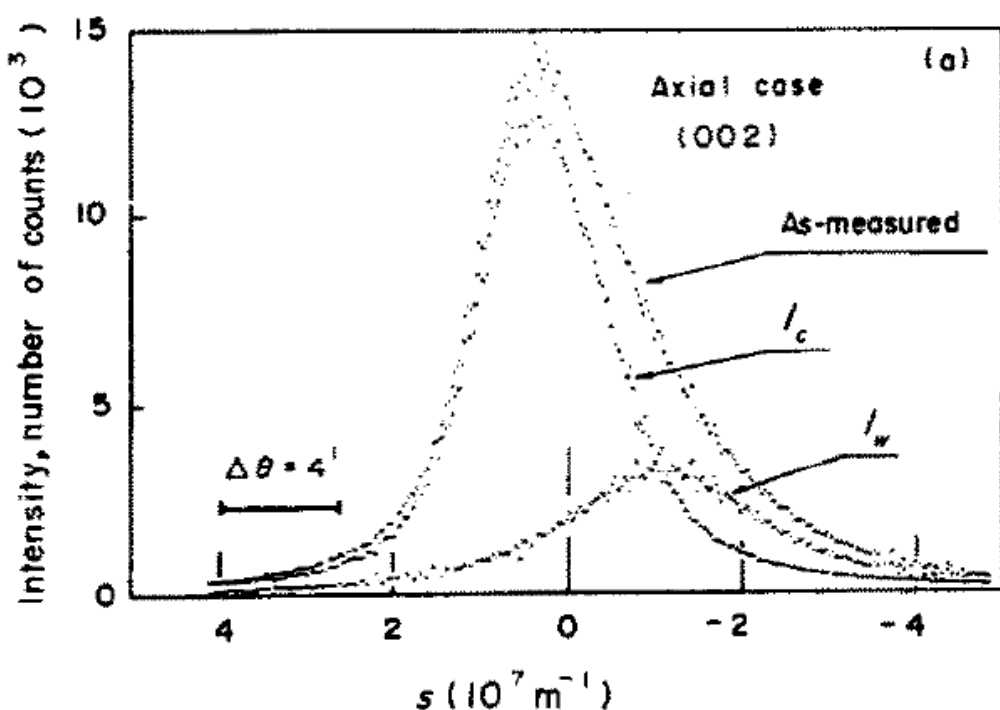


Figure 2-15. An asymmetric 002 diffraction peak measured in deformed single crystal copper (Ungar et al. 1984). The peak can be considered as the sum of a peak representing the cell walls I_w and the cell interior I_c .

2.1.8 Crystal Plasticity Models

In this section, the focus is shifted to models that try to understand deformation at the macroscopic scale, but ignore some of the properties of the microstructure, such as dislocations. These models are useful in providing information about macroscopic properties such as flow stress, texture evolution or average intergranular strains.

In the previous sections it was shown that a quantity found from a polycrystal plasticity models, called the Taylor factor, might be related to the deformation microstructure. This quantity will be explained in greater detail. In the final part of this section it will be shown how these models may be used to predict the dislocation population and how these may be compared to measurements.

For single crystal HCP metals deformed by uni-axial tension it has been found that the tensile yield stress (σ_0) can vary considerably depending on the orientation.

However, when this stress is resolved on to the dominant slip systems slip plane in the slip direction, called the critically resolved shear stress (τ_0) or CRSS, this stress is found to be independent of the orientation. This is referred to as Schmid's law (Honeycombe 1984):

$$\tau_0 = \sigma_0 \sin \chi_0 \cos \varpi_0 \quad (2.3)$$

Where, χ_0 is the angle between the slip plane and tension axis and ϖ_0 the angle between slip direction and tension axis and the product of the sin and cosine terms is the Schmid factor. For a given grain and slip system, the larger the Schmid factor the greater the resolved shear stress is and hence the easier a slip system is to operate. Hence, if it is assumed that all grains in a polycrystal have the same stress, and they can be treated as single crystals, then the activity of the slip systems could be given by the Schmid factor. In metals with different CRSS, this would in turn affect the activity of a slip system and would need to be accounted for. The Sachs model is a polycrystal plasticity model that uses the Schmid factor (Sachs 1928). In this model the active slip system(s) is the one with the highest

Schmid factor. The use of the Schmid factor to predict slip systems has been used by a number of researchers, with some success in HCP (Battaini et al. 2007, Zaefferer 2003, Bridier et al. 2005) and FCC metals (Liu and Hansen 1995, Winther 2001) metals. Generally, the approach is favourable at low strains and for metals, such as HCP metal, with less slip systems.

An alternative approach is instead of each grain having the same stress that they instead have the same strain which leads to another polycrystal model called the Taylor model (Taylor 1934). In the Taylor model, it is assumed that all grains, representing all possible orientations, plastically deform in the same manner with the applied load (the same strain tensor). One of the implications of this is that grain interactions are ignored. The active slip systems of a particular grain are calculated by finding the possible combinations of five slip systems that produce the same deformation as the applied deformation. From these different slip system combinations, it is assumed that the active combination is that for which the energy is minimised. The energy dissipated by a slip system is given by the multiple of its critically resolved shear stress and the activity of that slip system. When using the Taylor model for cubic materials with the twelve slip systems {111} [110], this leads to a number of solutions that have equivalent energy dissipation. One way this problem can be dealt with is by assuming all the combinations are active, hence take the average.

$$P = \sum_{s=1}^N \tau_s^c |\dot{\gamma}_s| = \min \quad (2.4)$$

Where, the active set of N (N=5) slip systems, s, are those that minimise the product of the critically resolved shear stress, τ^c , and the strain rate $\dot{\gamma}$ or the energy dissipated P (Bunge and Leffers 1971).

The assumption that all grains deform in the same way as the applied load may be modified by relaxing some of the constraints. These relaxed constraint models are mainly used when the amount of deformation is high such as in rolling.

The Taylor model is primarily used to predict the changes in texture of a metal due to plastic deformation. Although, the model is simple it has been shown to provide good agreement with measured data (Bunge and Leffers 1971, Dilamore and Katoh 1974, van Houtte 1978, Philippe et al. 1995, Barnett 2003), although there can be problems with the predictions. In FCC metals the SFE can have an influence on the texture but would not be included in the Taylor model. This problem was considered by van Houtte (1978), who showed that it could be explained by including twinning as a deformation mode in metals with a low SFE. When applied to HCP metals there can be problems, because of the assumption of all grains deforming in the same way may not be valid in anisotropic crystals. There are also problems with knowing which slip systems are active and what CRSS values they should have. However, the model has been used with some success in HCP metals (Philippe et al. 1995, Barnett 2003, Kad et al. 2002)

An alternative to the Taylor model, which also allows relaxation of the constraints, are self-consistent models. In these models, a grain is considered as an inclusion embedded in a medium representing the average property of all other grains. The medium may be considered as visco-plastic (Lebensohn and Tome et 1993), which is used to account for texture evolution and hardening, or elasto-plastic (Hill 1965) where the elastic strains are considered but cannot be used for texture development.

The problem with the above models is that they do not include grain-to-grain interactions, and they cannot be used individually to explain elastic strains, texture development and hardening. An alternative that does not have these drawbacks is the crystal plasticity finite element method (CPFEM) (Bate 1999). In this method, the microstructure is represented as a finite element mesh, where each grain is represented as one or more elements. Local constitutive laws, are then used to simulate the behaviour. The main problem with CPFEM is the increased computational time that is required.

The use of plasticity models to predict dislocation population

The models predict slip system activity, but it is not clear whether there is any relationship between these predictions and the deformation microstructure. The models predict increments of slip caused by different slip systems, but this is not the same as predicting how many dislocations of that slip system there are. The movement of a dislocation causes a shear and so it may be expected that there is a link between the two. The problem is that the behaviour of dislocations can be complicated. Dislocations interact with other dislocations, they can be created and annihilated, cross-slip onto other slip planes, can be trapped and groups of dislocations can organise into dislocation structures (Hull and Bacon 2001, Humphreys and Hatherly 2004). A method to convert the shears into dislocation densities is given by the Orowan equation (equation 2.5). In this the dislocations are separated into two types, mobile dislocations and non-mobile or forest dislocations. The first provide the shear and the second are the result of dislocation interactions. Where, for a given slip system, l , the average shear, γ , is equal to the dislocation density of mobile dislocations on that slip system, ρ_m , multiplied by its Burgers vector, b , and the dislocations velocity, V (Franciosi 1985).

$$\dot{\gamma}^l = \rho_m^l b^l V^l \quad (2.5)$$

In order to be able to verify whether a plasticity model can predict the quantity of different dislocation types, they need to be validated by experimental evidence.

TEM is the most used method to study the deformation microstructure. However, it can be very difficult to use it to determine the slip system population. It can be very difficult to quantify the density of dislocations on the different slip systems.

For FCC metals with twelve possible slip systems, the difference between modelling predictions of the slip system population in different grains is small. The predicted differences could only be validated by measuring the dislocation population in many grains. This would be very difficult to do using TEM.

For HCP metals with less symmetry and slip systems with different planes and Burgers vectors, a comparison between the predictions of a model and TEM results can be easier. Zaefferer (2003) did a TEM study of different types of

titanium metals to determine the activity of different slip and twinning systems. They were able to qualitatively determine the activity of different deformation systems by quantifying whether they were active or not in a grain. Their measurements of samples deformed by up to 5% by uniaxial or biaxial tension showed some correlation with Schmid factor predictions of slip activity but not a Taylor approach.

It is therefore very difficult to determine whether the predictions of a plasticity model have any relation to the deformation microstructure by actually observing the dislocations, such as done when using TEM. However, Borbely and colleagues (Borbely et al. 2000) developed a method that made a comparison possible. The model supposes that the mobile dislocation density of a particular slip system can be given by the Orowan equation (Franciosi 1985) using the shears calculated by a polycrystal plasticity model. The contribution of an individual dislocation to the full-width is found by calculating its contrast factor using the program ANIZC (Borbely et al. 2003). The full-width can then be predicted based on the summation of the contributions from the different dislocations in the different grains contributing to a peak. They found some agreement between their predictions and the results. However, the method worked better for some texture components and worked poorly for others. They also found that different texture components had different dislocation densities. No correlation was made between the different dislocation densities and the models predictions, suggesting a limitation to the method.

2.2 Characterisation of the deformed state

When investigating the deformation of metals there are various techniques that can be used. DPPA provides information of the deformation microstructure at a scale from μm (10^{-6}m) to \AA (10^{-10}m). In this section techniques that can be used to study similar features of deformation are considered.

There are a number of methods used to observe dislocations. Surface dislocations can be revealed by etching a sample (Hull and Bacon 2001). The region around a
65

dislocation is susceptible to removal of atoms and so an etched sample the dislocations can be revealed as etch pits. The technique can be useful but is limited in what can be observed and to samples with low dislocation density.

The most common method used to observe dislocations is transmission electron microscopy, TEM (Williams and Carter 2009). In TEM, electrons are fired at a thin foil, less than 100nm thick, of the chosen metal. The electrons interact with the foil as they pass through it and an image of the specimen can be formed. The contrast of the image is due to a variety of different causes including thickness variations, bends in the sample, compositional differences and the presence of defects in the crystal structure. It is possible to enhance the visibility of defects such as dislocations by adopting the correct imaging conditions. From TEM it is possible to determine the dislocation density, the types of dislocations (their Burgers vector and slip plane) and how they are arranged and the presence and arrangement of other defects.

However, there are a number of problem with TEM, most of which are due to the small sample size. The samples are difficult to prepare and dislocations can be introduced or reduced during the preparation (Hull and Bacon 2001, pg. 35). The small size also means that in order to study many grains a large number of samples has to be prepared, for the results to be representative of the material. There are also problems with making the measurements. The technique works best when the amount of deformation and dislocation density is not too high (Rohatgi et al 2001, Gutierrez-Urrutia and Raabe 2012, Kocks and Mecking 2003). The field of view is often quite small, limited by lattice bending and twisting and variations in the sample thickness. This can mean microstructural changes that occur over larger distances are difficult to study and make quantification of the microstructure difficult (Mughrabi 2006b, Zaehlerer 2003). There can be problems in characterising a TEM sample because identification of different defects can be difficult. This is particularly a problem in HCP metals, because of dislocations with different Burgers vectors (Zaehlerer 2003), or when identifying the presence of twins (Prakash et al 2010, Byun et al 2006) This has meant that there still remains uncertainty as to the dislocation population in particular HCP metals (Zaehlerer 2003). A method used to reduce these problems

is to combine images from computer models of dislocations and the measured image (Hull and Bacon 2001 Section 2.7).

In a scanning electron microscope electrons are fired at a sample, which interact with the metal and electrons, X-rays and light are emitted from the sample (Chescoe and Goodhew 1990). The most important of these are secondary electrons, whose signal are mainly due to changes in the surface topography, and backscattered electrons (BSE), the strength of the signal being mainly due to the atomic number of the material studied. These two signals may be used in the same way as an optical microscope to provide an image of the sample.

Alternatively, variations in the BSEs can be used to provide additional information by two different techniques electron channeling contrast imaging (ECCI) (Joy et al 1982, Wilkinson et al 1993, Gutierrez-Urrutia and Raabe 2012) and electron backscatter diffraction (EBSD) (Humphreys 2001).

When the sample is orientated at a particular angle, close to the Bragg angle of a particular plane, changes in orientation cause rapid changes in the BSE. Crystal defects such as twins or dislocations cause local orientation changes. A dislocation cause local bending of crystallographic lattice and twins a bending of the lattice and an organised local orientation change. These attributes are used for imaging in ECCI. The advantage of ECCI is that details of the deformation microstructure can be found for bulk sample and with easier sample preparation than TEM. The method is mainly used to image defects (Prakash et al 2010), but can be used for calculation of dislocation density (Gutierrez-Urrutia and Raabe 2012).

In EBSD the variation in the intensity of the BSE intensity is used in a different manner. BSEs from the sample interfere to produce a diffraction pattern; this diffraction pattern can then be used to determine the crystal orientation at a particular point on the surface of the metal. A phosphor screen is used to detect the diffraction pattern and a computer program can be used to determine the orientation. A sample can be scanned to produce a crystal orientation map. When

a metal is plastically deformed there is an overall orientation change, and an increase in the spread of the orientations in a grain. The overall change is much easier to understand than the local. Kamaya et al. (2005) and Lehockey et al. (2000) showed that the local variation in orientation could be used to quantify the amount of plastic deformation of a metal. However, the relationship between the local orientation and plastic strain is also dependent on the metal and the SEM used. The EBSD maps can be used to show dislocation cell structures as shown in Figure 2-16, or to determine the type of a twin (Battaini et al. 2007). However, the spatial and angular resolution can limit the characterisation of dislocation structures.

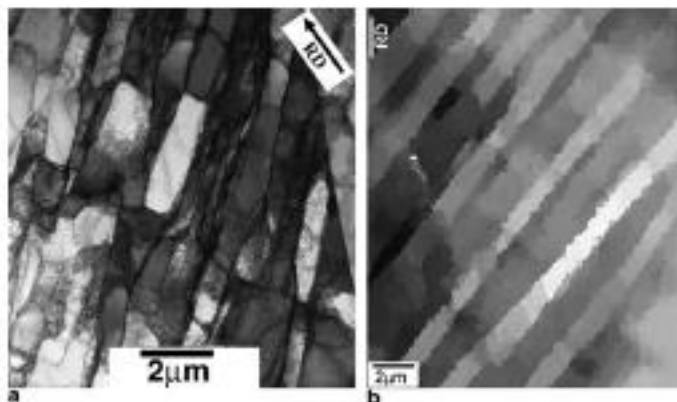


Figure 2-16. TEM micrograph (a) and an EBSD map (b) of an aluminium alloy, deformed by cold rolling to a strain of 0.2, displaying aligned low angle grain boundaries (Humphreys and Bate 2006).

Most techniques to assess the state of a metal are more indirect and often based on a model of how the metal will behave when deformed. The strength of a sample is an important parameter on its own, but can also be used to find the dislocation density of a sample. There are two main methods that can be used as a measure of strength. Tensile samples can be made from the sample and the yield strength measured and the samples hardness can be measured. Both are changed by the amount of plastic deformation but are also changed by additional factors. Therefore, to use these techniques the different parameters must be separated.

Calorimetry, electrical resistivity and magnetic properties have been used to gain information about the quantity of defects within a sample. The problem with these

methods is that they can not easily differentiate dislocations from other defects. The intergranular strains and texture changes of a metal have been used to provide useful information of the plastic deformation. These measurements are mainly used to compare with polycrystal plasticity models to gain an understanding of the sample. Instead of the overall texture change, the variation of orientations can instead be used as a parameter of plastic deformation. This can be done using EBSD or diffraction. The method is limited because it can be difficult to relate the quantify the variations in orientation or to relate these to features of the microstructure.

2.3 Sources of radiation

The three most commonly used sources of radiation when using DPPA techniques are laboratory X-rays, neutron diffraction and synchrotron X-ray diffraction. These different sources are discussed in the following sections.

2.3.1 Laboratory X-ray diffraction

The most commonly used source are laboratory X-rays. They are the most widely used source because they are relatively simple, cheap, small and easy to gain access to. However, they have a relatively high beam divergence and low brightness (Langford and Louer 1996).

The x-rays are produced when electrons are accelerated against a metal anode within an evacuated tube (Cullity 1978). This produces two types of radiation; white radiation over a range of wavelengths and more intense radiation at a number of characteristic wavelengths. The most common wavelengths are produced by $K\alpha$ and $K\beta$ radiation. A filter is often used to reduce the intensity produced by the $K\beta$ wavelength, so that the X-rays reaching the sample are an almost monochromatic source of $K\alpha$ X-rays. The wavelength of $K\alpha$ is dependent on the choice of the metal used for the anode. $K\alpha$ radiation is not purely monochromatic but instead consists of a number of wavelengths. The most important of these are the doublet $K\alpha_1$ and $K\alpha_2$ (it has been suggested that these

components may be divided further (Holzer et al. 1997). The α_1 component has an intensity that is approximately twice that of α_2 , this exact ratio being dependent on the diffractometer and its settings. In some diffractometers the α_2 component is removed, although this can be difficult to achieve effectively (Ladell et al. 1975). Otherwise there are different methods that can be used to separate the two.

There are methods that assume α_1 and α_2 have the same shape (for example full-width and mixing parameter for a pseudo-Voigt) but different wavelengths and intensities. This is the method used in one of the earliest and most popular methods the Rachinger correction (Rachinger 1948). The method is very simple; it works in removing most of the α_2 component but often leaves unreasonable values around where the α_2 was. However, it has been suggested that are problems with the approximation that the two peaks are similar (Bearden and Shaw 1935, Allison 1933). Instead, Ladell et al. (1975) proposed an algorithm to separate the components using the shape of measured diffraction peaks.

2.3.2 Synchrotron X-ray Diffraction

Synchrotron x-ray radiation has the advantage over lab x-ray of a higher intensity, several orders of magnitude higher (Langford and Louer 1996), and a much more parallel beam, meaning the resolution is much higher.

Synchrotron x-ray radiation is produced when electrons are accelerated along a curved path at high speed by magnetic fields (Fitch 2004). The radiation produced is of a very high energy and is over a continuous spectrum of wavelengths. It is possible to use this white beam radiation or to select a narrow band of wavelengths using a monochromator.

The wavelength (λ) is inversely proportional to its energy in KeV (E) and given by $\lambda = \frac{12.3975}{E}$. The energy (and hence wavelength) can be changed depending on the particular experiment (Langford and Louer 1996).

An analyzer crystal, which is placed in the diffracted beam, is sometimes used with synchrotron diffraction. The analyser crystal enables the diffracted beam to

be correctly positioned in the detector. In addition, the analyser crystal reduces problems that are caused by the shape of the specimen, such as changes in the peak position due to the position in the sample that the diffracted beam is from (Hutchings et al. 2005). However, it has the disadvantage that it reduces the intensity of the diffracted radiation. Hence, an analyser crystal is only used when the diffracted intensity is sufficiently high; hence it is not used with other diffraction sources, such as neutron diffraction, because of its lower diffracted intensity.

2.3.3 Neutron Diffraction

Neutrons can be produced in two main ways, at a reactor source by controlled fission (e.g. the Institut Laue-Langevin (ILL) in Grenoble, France), or in a spallation source by the collision of high-energy particles with a metal target (e.g. ISIS facility in Didcot, Oxford, UK). The two sources produce a range of wavelengths, which are around the same magnitude as the atomic spacing of metals. There are also two approaches that can be taken, either by 2θ scanning as is done with x-ray sources (called a continuous source) or by time of flight (Withers and Bhadeshia 2001, Langford and Louer 1996). An advantage of neutrons in comparison to other methods is the greater penetration depth, in comparison to x-ray sources. For example, for aluminium the penetration depth in aluminium is less than 50 μm for lab x-rays, 50-150mm for synchrotron x-rays and 200mm for neutrons (Withers and Bhadeshia 2001). However, this advantage means that neutron sources have a low diffracted intensity in comparison to other sources. A further advantage of neutrons is that the scattering cross-section does not vary with d (Langford and Louer 1996).

It is believed (Withers and Bhadeshia 2001) that a continuous source is advantageous when only part of a diffraction pattern is required, whereas time-of-flight is advantageous when the whole diffraction pattern is needed. Time-of-flight also has the advantage that resolution ($\Delta d/d$) is constant with the d -spacing of a peak (d), whereas for the continuous approach (and for x-rays) resolution is lower for low d (Langford and Louer 1996).

In a time-of-flight source, the neutron source consists of range of energies and consequently wavelengths, which are separated into a series of pulses. The time a neutron takes to travel from the source to the detector is different depending on the wavelength of a neutron. For a particular pulse, a fixed detector measures the time that the diffracted beam reaches the detector, to produce a diffraction pattern of intensity against time of flight. A series of these diffraction patterns for numerous pulses are added together to produce the diffraction pattern. The time of flight can then be converted to a d or g ($=1/d$).

2.4 Diffraction Peak Profile Analysis

This section describes the most important DPPA methods. The way in which the methods work is described and the results that can be obtained including what assumptions are used and the limitations of their use.

2.4.1 Basic Principles

Crystal Lattice

In an ideal crystal structure, atoms are arranged in a periodically repeating sequence. The arrangement of the atoms can be defined by their unit cell (Figure 2-17). In an ideal crystal the crystal structure consists of the repeated stacking of this unit cell.

The unit cell defines the crystal structure of the material. The most commonly observed crystal structures in metals are face-centred-cubic (FCC e.g. aluminium), body-centred-cubic (BCC e.g. iron) and hexagonal-close-packed (HCP e.g. titanium).

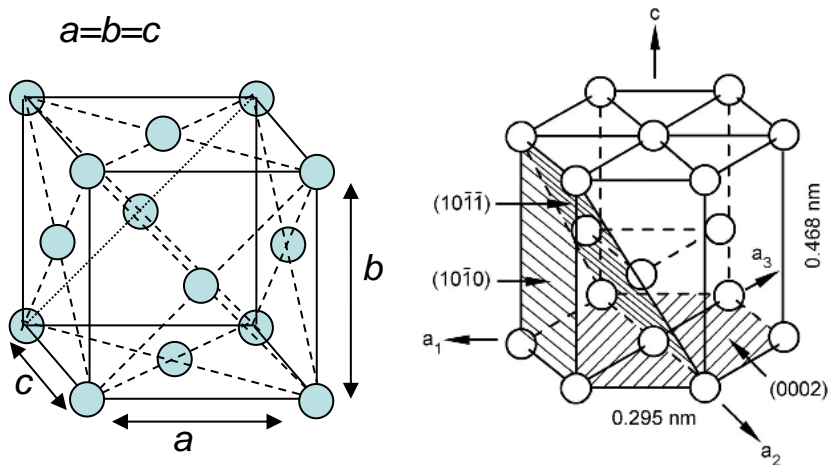


Figure 2-17. Face-centred-cubic unit cell (left), the lattice parameters a , b , c are displayed. The hexagonal close packed unit cell (right) (Lutjering and Williams 2007). The lattice parameter a , is the distance between atoms on the perimeter, given by 0.295nm, and the c parameter perpendicular to this, given by 0.468nm, the values are those for a titanium alloy.

Bragg's Law

When an x-ray beam of a single wavelength is incident upon a crystalline material, a diffraction pattern is produced (Figure 2-18). The peaks in this diffraction pattern correspond to different crystallographic planes and from the positions of these peaks it is possible to identify the crystal structure. The position of the peaks can provide information on the strain of the metal. This is done by measuring how far a peak has moved from the un-deformed position and from this the strain and stress of a sample can be found.

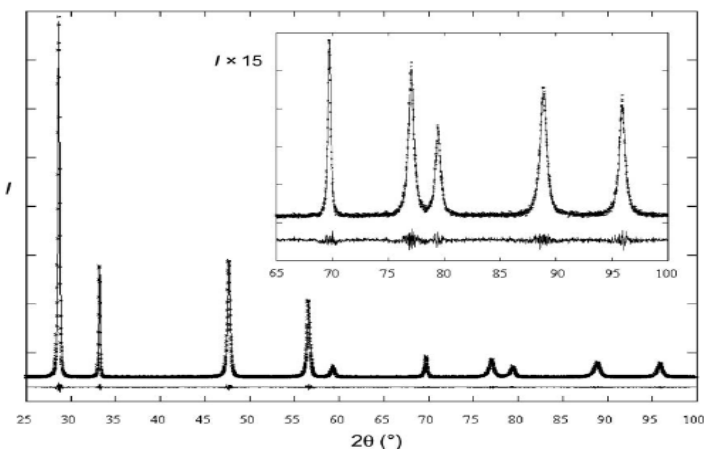


Figure 2-18. An example x-ray diffraction pattern for $\text{CdF}_2(30)$ sample using a laboratory x-ray with copper radiation (Ribarik et al 2005). The measured data and the fit of this data are shown.

An illustration of why these diffraction peaks are formed is given in Figure 2-19. When an incident beam gets close to an atom it may either be absorbed by the atom or be scattered elastically or inelastically. The elastic scattering is important because it is coherent and may interfere with other elastically scattered beams. The elastically scattered beam is scattered at all angles. However, it is only at a particular angle that the scattered beam (from all the atoms in the crystal) does not cancel out. This angle is given by Braggs Law.

$$2d \sin \theta = n\lambda . \quad (2.6)$$

Where, 2θ is the angle between the incident and diffracted beam, λ is the wavelength, d is the lattice spacing and n an integer representing the order of a peak.

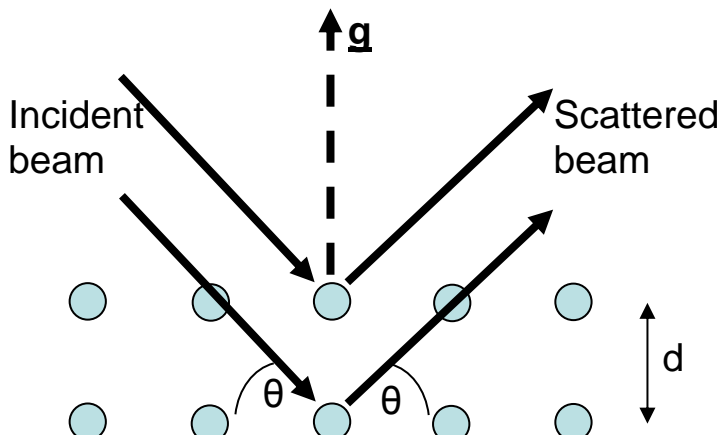


Figure 2-19. An illustration of Braggs Law. A monochromatic beam is incident upon a perfect crystal with lattice spacing d , and produce a scattered beam at an angle θ . The angle θ given by Braggs law.

Non-Perfect Crystals

If the instrument used to measure the diffraction pattern is perfect (ignoring instrumental effects) and the crystal being measured is also perfect then the shape of the diffraction peaks will be given by the delta function. In this situation, the peaks will be very narrow, and the intensity will only be significant at the Bragg

angles. However, ‘real’ crystals contain imperfections that cause the peaks to broaden, become asymmetric and move from the Bragg position.

The peak shape due to an imperfect crystal is often separated into three groups; ‘size’, ‘strain’ and ‘fault’.

The ‘size’ part is due to the finite size of the crystal but the definition of size, as given by the Warren Averbach analysis (Warren 1959), and indeed most other x-ray profile methods, is different from the size obtained by using other forms of measurement. The crystal size measured is called the domain size. This is the length of a region, perpendicular to the plane being viewed, in the metal that diffracts incoherently (or diffracts independently) with respect to all other regions. The phase difference between the diffraction from one domain to any other has an equal probability of being between 0 and 2π , hence they diffract incoherently. This issue will be returned to later when discussing the size coefficients in Fourier methods. The size broadening occurs as a result of the coherent region being finite. The result of this is that there are not enough scattered beams to cancel out all scattered beams around the Bragg angle (Cullity 1978).

The ‘strain’ part is due to variations in the lattice spacing, and is often called the micro-strain to distinguish it from macro-strains (or intergranular strains), which are concerned with the movement of the diffraction peaks. The micro-strain may be divided into the variations of the lattice spacing within a grain and variations in the lattice spacing in different grains. The two cannot be separated easily, and the former is often treated exclusively as its effect is believed to be the greater in most situations (Kuzel 2007).

The ‘fault’ part is due to faults such as planar faults, including stacking faults and twins. These affect the crystal structure between layers of atoms.

In addition to these effects, the instrument is never perfect and hence contributes to the shape and broadening of the peaks.

The measured intensity profile (I) may be given as the convolution of these parts (Klug and Alexander 1974), or similarly the product of the Fourier coefficients (A) (described later):

$$I_{\text{meas}} = I_{\text{size}} * I_{\text{strain}} * I_{\text{fault}} * I_{\text{instr}}$$

$$\ln(A_n^{\text{meas}}) = \ln(A_n^{\text{size}}) + \ln(A_n^{\text{strain}}) + \ln(A_n^{\text{fault}}) + \ln(A_n^{\text{instr}}) \quad (2.7)$$

In the next section, it will be shown what these peaks look like and some functions that may be used to describe their shape.

Fitting diffraction peaks

An analytical function is a function chosen to best fit the diffraction peaks. Its use can be very helpful in the analysis of diffraction patterns. They are especially useful if the quality of the peaks is low (due to say low counting statistics) or if peaks overlap. Their use can be a part of a method that uses the full-width (integral breadth methods) or they can also be used as part of a Fourier analysis (Balzar and Ledbetter 1993). When plotting diffraction profiles there are a number of different scales that can be used. It is most common to measure in constant steps of 2θ and this is the most common scale used. However, there are advantages of using a d-scale or g scale, where $g=1/d$, particularly because the scale is independent of the wavelength of radiation used.

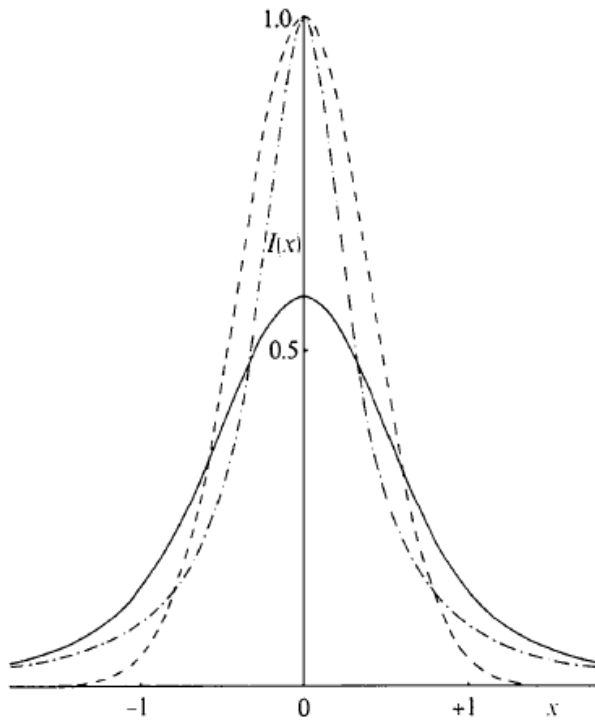


Figure 2-20. Gaussian (--) and Cauchy (-.-) analytical functions and the Voigt curve, which is a convolution of the two (Langford 1978).

The earliest functions used to describe the diffraction peaks were Gaussian and Cauchy (or Lorentzian) functions (Figure 2-20). The Gaussian (equation 2.8) and the Cauchy function (equation 2.9) are given by the following.

$$I_G(x) = I_0 \exp \left[-2 \left(\frac{x - x_0}{\Gamma \sqrt{\ln 2}} \right)^2 \right] \quad (2.8)$$

$$I_C(x) = \frac{I_0}{\left(1 + 2 \left(\frac{x - x_0}{\Gamma} \right)^2 \right)} \quad (2.9)$$

Where, I_0 is the peaks maximum intensity, x_0 the position of x (normally either g or 2θ) at the peaks maximum height, Γ the full-width of the peak at half its maximum height (full-width).

However, it was found that diffraction peaks of measured samples are never exactly described by either function, but are instead often somewhere between the two. A number of different functions may instead be used that provide a better approximation. One of the most popular of these is the Voigt function. The Voigt function (equation 2.10) is a convolution of a Gaussian and Cauchy functions (Langford 1978).

$$I(x) = \text{Re} \left\{ \beta_C I_C(0) I_G(0) \omega \left[\frac{\sqrt{\pi}x}{\beta_G} + ik \right] \right\} \quad (2.10)$$

$$\omega(z) = \exp(-z^2) \left[1 + \frac{i2}{\sqrt{\pi}} \int_0^z \exp(t^2) dt \right] \quad k = \beta_C / (\sqrt{\pi} \beta_G)$$

Where, ω is the complex error function, β_G and β_c the Gauss and Cauchy integral breadth, x is 2θ or g depending on units used, $I_C(0)$ and $I_G(0)$ are the intensities of the Gauss and Cauchy parts at $x=0$.

The reason why a Voigt curve, in particular, is helpful for peak profile analysis is that the convolution of two Voigt curves is another Voigt. This makes it easier to separate instrumental broadening from physical broadening and separate size from strain, because of equation 2.7.

An alternative to the Voigt function is the pseudo-Voigt function (equation 2.11), which is the sum of a Gauss and a Cauchy function (Wertheim et al. 1974).

$$I(x) = \frac{\eta}{\left(1 + 2 \left(\frac{x - x_0}{\Gamma} \right)^2 \right)} + (1 - \eta) \exp \left[-2 \left(\frac{x - x_0}{\sqrt{\ln 2\Gamma}} \right)^2 \right] \quad (2.11)$$

Where, η is the Cauchy (Cauchy) fraction or the mixing parameter, Γ the full-width, x_0 the value of x at the centre of the peak.

A pseudo-Voigt function is similar to a Voigt function. Unlike a Voigt, the convolution of two pseudo-Voigt curves is not another pseudo-Voigt. This means that the removal of the instrumental broadening is not as straightforward as it is

for a Voigt. However, the pseudo-Voigt does have the advantage that the tails of a the function may be more pronounced than a Cauchy by allowing η to be more than 1, this is described as a super-Cauchy. The function is also computationally quicker, because it does not involve the complex error function. It is possible to convert between a pseudo-Voigt and a Voigt (equation 2.12) (Dong and Scardi 2000 and Delhez et al. 1982).

$$\begin{aligned}\beta_{\text{pv}} &= 0.5\Gamma[(1-\eta)\sqrt{(\pi/\ln 2)} + \eta\pi] \\ \frac{\beta_c}{\beta} &\approx 2.0207 - 0.4803\left(\frac{\Gamma}{\beta}\right) - 1.7756\left(\frac{\Gamma}{\beta}\right)^2 \\ \frac{\beta_g}{\beta} &\approx 0.6420 + 1.4187\sqrt{\left(\frac{\Gamma}{\beta} - \frac{2}{\pi}\right)} - 2.2043\left(\frac{\Gamma}{\beta}\right) + 1.8706\left(\frac{\Gamma}{\beta}\right)^2\end{aligned}\quad (2.12)$$

The integral breadth, β , of a peak is the area under a diffraction peak, excluding the background divided by the peaks height.

Numerous studies have shown that if a diffraction peak is symmetric it can in most cases be described with some accuracy by a Voigt, a pseudo-Voigt, or one of the similar functions like the Pearson VII (Soleimanian and Aghdaee 2008). However, diffraction peaks are not always symmetric. To account for this the previous functions can be modified or one can use an entirely different function.

The easiest way to modify the above functions is to split them about their maximum intensity, so that all its parameters are the same on both sides except the full-width. The amount of asymmetry can then be expressed as the ratio of the full-width on the low side to the full-width on the high side. This is called a split function (Balzar 1999).

Different DPPA Methods

In order to use the shape of a peak to determine useful information of the material three different methods have been developed concurrently. These methods consist of those that use the normalised area under a peak (integral breadth) or its width at

half its maximum height (full-width), those that use the Fourier coefficients of the peak and those that use the intensity values of the peaks to find the restricted moments. Each method is based on the kinematical theory of diffraction, which is believed to be the best method to use for a distorted crystal. Although, all the methods are derived from a similar base their inherent different assumptions means they will give different results. In the next three sections these methods are discussed separately, starting with those using the analytical function just described.

2.4.2 Integral Breadth methods

The Scherer Equation

One of the earlier DPPA methods was introduced by Scherrer (1918). Scherer showed that if broadening is due to the crystal size alone, then the integral breadth of a peak is proportional to the inverse of the crystal size, at a given angle. The relation (equation 2.13) can be derived from the kinematical theory of diffraction (Warren 1969).

$$\langle D \rangle_v = \frac{K\lambda}{\beta(2\theta)\cos\theta} = \frac{K}{\beta(g)} \quad (2.13)$$

Where, g is the reciprocal of the lattice spacing at the Bragg angle, $\beta(g)$ and $\beta(2\theta)$ are the integral breadth of the broadened peak without instrumental broadening on a 2θ and g scale respectively, θ the measured diffraction angle (both $\beta(2\theta)$ and θ are in radians), K the Scherrer constant ~ 0.9 , λ the wavelength of the X-rays, and $\langle D \rangle_v$ the volume weighted crystal size perpendicular to the given plane.

In order to convert between values on the two scales, θ in radians and g , the following equation (equation 2.14) and equation 2.6 are used:

$$\Delta\theta = \frac{\Delta d}{d} \tan\theta = \frac{\Delta g}{g} \tan\theta = \frac{\Delta g}{2} \frac{\lambda}{\cos\theta} \quad (2.14)$$

The Scherrer equation is only expected to be significant for determining size for crystals less than 1000Å (Warren 1969). It is often thought as a qualitative

description and is rarely used (Langford 1999). A problem the method has is it ignores the distribution in sizes and the shape of crystals.

The Stokes and Wilson equation

In a similar manner, Stokes and Wilson (1944) were able to describe the broadening solely in terms of the micro-strain present. They defined an ‘apparent’ strain (N), and considered how different distributions of strain would affect the integral breadth (β). If all values of strain between zero and a maximum were equally likely, then this would give an upper bound for the micro-strain (ε_{\max}) given by eq. 2.15.

$$\varepsilon_{\max} = \frac{\beta(2\theta)\cot\theta}{4} = \frac{\beta(g)}{2g} = \frac{N}{4} \quad (2.15)$$

However, this strain distribution is unlikely to be observed in a real material. A more probable strain distribution is the Gaussian distribution, which Stokes and Wilson (Stokes and Wilson 1944) showed would give the following formula if the standard deviation of the strain is ε_{rms} .

$$\varepsilon_{\text{rms}} = \frac{\beta(2\theta)\cot\theta}{2\sqrt{2\pi}} = \frac{\beta(g)}{g\sqrt{2\pi}} = \frac{N}{2\sqrt{2\pi}} \quad (2.16)$$

The Scherer and Stokes and Wilson equation are useful equations and provided major advances in the understanding of the broadening of diffraction peaks. However, they are both not useful if size broadening and strain broadening are both present and they are both only valid for given distributions of crystal size and strain.

The Williamson-Hall method

The Williamson-Hall method tries to solve the first of these problems by making an approximation as to how the two effects combine. This method takes both

equations and combines them. There are two forms to the equations, depending on how the shape of peaks caused by size and strain broadening are assumed to be.

If both are assumed to be Cauchy, the parts are added together, whereas if they are assumed to be Gaussian, the squares of the parts are added together (eq. 2.17).

$$\begin{aligned}\beta(g) &= \beta_S + \beta_D = K/\langle D \rangle_V + 2g\varepsilon_{\max} \\ \beta^2(g) &= \beta^2_S + \beta^2_D = K/\langle D \rangle_V^2 + 2g^2\varepsilon_{\max}^2\end{aligned}\quad (2.17)$$

Where, the subscripts S and D represent the size and strain components respectively. If the peaks are Voigtian, then one could use both equations with the appropriate Gauss and Cauchy integral breadths.

The Williamson-Hall method works by fitting a straight line to the integral breadths, on a g or g^2 scale, and the intercept and gradient are used to determine the size and strain components (Figure 2-21).

Modified Williamson-Hall Method

For most materials, and in particular for those with anisotropic elastic constants, the different diffraction peaks broaden by different amounts, and the broadening does not increase linearly with g (or g^2). This broadening anisotropy is very common and it means that the Williamson-Hall or Warren-Averbach method (discussed later) can only really be used on one type of diffraction peak but of different orders, e.g. 111 and 222. In most DPPA methods this anisotropy is accounted for by the contrast factor, C. The contrast factor is the only parameter that is dependent on the {hkl} indices of a peak. In a later section, greater detail of the contrast factor is provided for situations where it is assumed that dislocations account for the anisotropy. Although, this does not need to be the case if there is another cause of broadening that is different for the different planes (Leineweber and Mittemeijer 2006).

In the modified Williamson-Hall method (Ungar et al. 1996) g is replaced with gC . This approach is also applicable for the Warren-Averbach methods (discussed later). Figure 2-22 shows how the method works to remove the anisotropy of

broadening seen in Figure 2-21. The contrast factor is a function of the indices of a peak and other parameters that relate to why the anisotropy occurs. In Figure 2-22 the contrast factor for each peak is found by varying the anisotropy parameter to obtain a best fit to a particular modified Williamson-Hall method (mWH).

There are three different mWH equations that can be used. If equations 2.17 are modified this leads to the two modified versions:

$$\beta(g) = K / \langle D \rangle_V + f_M g \sqrt{(\rho \bar{C}_{hkl})} + O(g^2 \bar{C}_{hkl}) \quad \text{mWH-1} \quad (2.18)$$

$$\beta^2(g) = K / \langle D \rangle_V^2 + f_M^2 g^2 (\rho \bar{C}_{hkl}) + O(g^4 \bar{C}_{hkl}^2) \quad \text{mWH-2} \quad (2.19)$$

Where, f_M is related to the parameter M (discussed later) and gives information about the dislocation structure, K is the Scherer constant often set at 0.9 and O(..) is a function that is dependent on the dislocation arrangement.

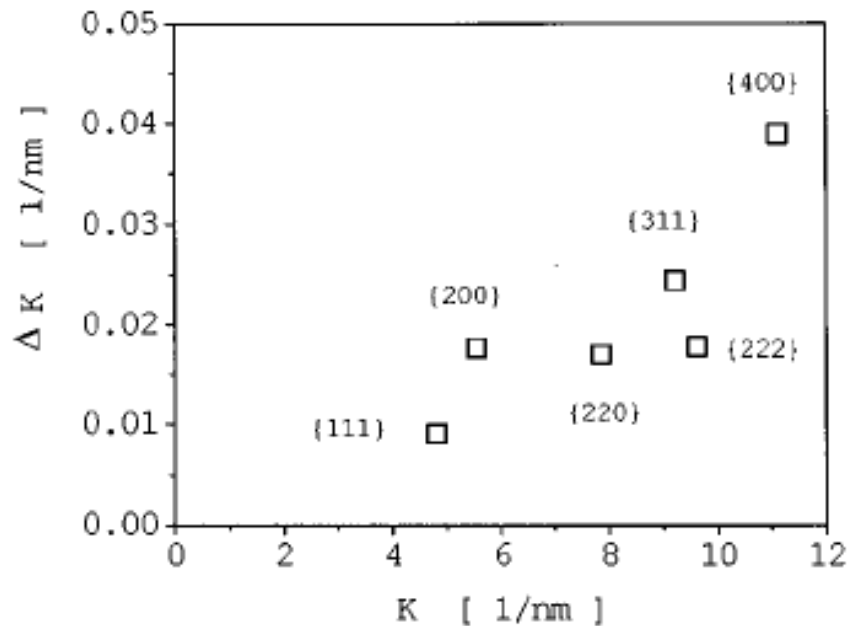


Figure 2-21. An example Williamson-Hall plot of a 99.98% copper sample, showing broadening anisotropy, that is the broadening is not proportional to 'K' but is {hkl} dependent. Where, the full-width=ΔK, and g=K.

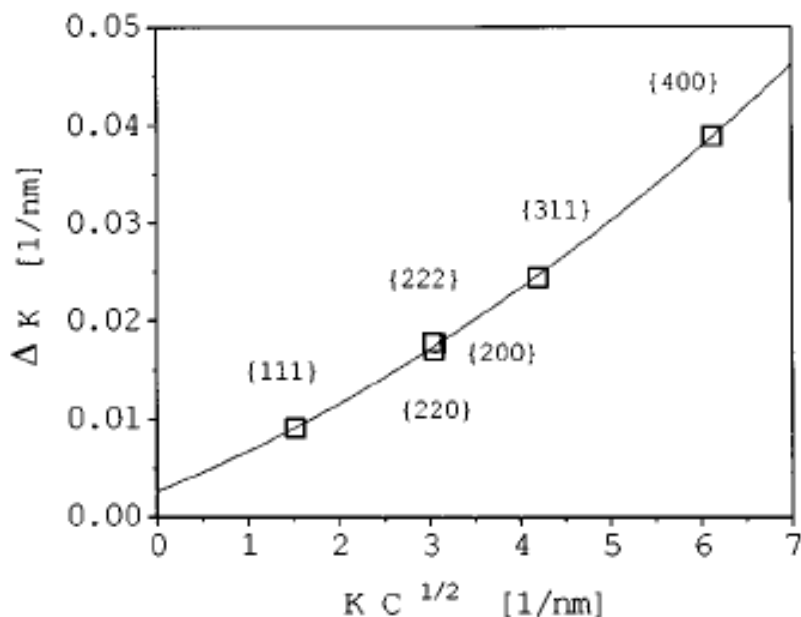


Figure 2-22. An example modified Williamson-Hall plot of the same 99.98% copper sample as in Figure 2-21. The use of the contrast factor has accounted for the anisotropy so that broadening is proportional to $K\sqrt{C}$. Where, the full-width= ΔK , and $g=K$.

Furthermore, a further equation (equation 2.20) has been suggested that when broadening is principally due to dislocations (Ungar, Gubicza et al. 2001).

$$\beta(g) = K / \langle D \rangle_V + \sqrt{\rho} f_M^2 g^2 \bar{C}_{hkl} + O(g^4 \bar{C}_{hkl}^2) \quad \text{mWH-3} \quad (2.20)$$

Where, the constant f_M is related to the arrangement of the dislocations. Ungar et al. (Ungar et al. 2001) showed that the expression can be described approximately by equation 2.21.

$$f_M^2 \approx \left(\frac{\pi M^2 b^2}{2} \right) \quad (2.21)$$

Wu et al. (Wu et al. 1998a and Wu et al. 1998b) has provided an expression for the term f_M , describing the arrangement of dislocations, with Burgers vector of magnitude b , using the notation of Glavicic and Semiatin (Glavicic and Semiatin 2006). The expression can be given as:

$$f_M^2 = b^2 \{ a_0 \ln(M+1) + b_0 \ln^2(M+1) + c_0 \ln^3(M+1) + d_0 \ln^4(M+1) \}$$

with $a_0 = -0.173$ $b_0 = 7.797$ $c_0 = -4.818$ $d_0 = 0.911$

(2.22)

The different WH equations are not equivalent and will give different results, and if the full-widths are used instead of the integral breadths, this will also provide different results. This modified form is useful as it allows the Williamson-Hall method to be used with more diffraction peaks and in addition can also be used to provide information about the dislocation population (see Section 2.3.5) giving information of the cause of the anisotropy.

Single Peak Methods

In certain circumstances, it may not be possible to obtain more than one diffraction peak. In these situations, it is beneficial to be able to quantify the causes of broadening from one peak.

The majority of single peak methods are based on simplifying assumptions of the size and strain distribution, and Delhez and colleagues (1982) provide a review of some of these methods. The principal behind most of these methods is that the strain distribution can be described by a Gauss function and that the size profile is approximately described by the Cauchy function.

As with the multiple line methods, these simple single line methods can be expressed in terms of the Fourier coefficients or the intensity values. The most popular method is to assume that for a peak consisting of a Cauchy and a Gauss component, such as a Voigt peak, the Cauchy component is solely due to size broadening and the Gaussian solely due to strain broadening. This method has been adopted by a number of different researchers (Delhez et al. 1982, de Keijser et al. 1982). The easiest and most common approach is to use a Voigt curve and the Cauchy component (β_C) is used to find the size (β^S) and the Gauss component

(β_G) the strain (β^D), using the Scherer and Stokes-Wilson equations to find the values.

$$\beta^S = \beta_G \quad \beta^D = \beta_C \quad (2.23)$$

These equations can be related to the size and strain components using the Scherrer equation and Stokes and Wilson equation. There is some justification for these methods, the different components can describe the shape of size and strain broadened profiles and Fourier coefficients and give values similar to multiple line methods (Halder & Wagner 1966, Gupta and Anantharaman 1971, Nandi & Sen Gupta, 1978). Another single peak method, the Variance method is described later.

2.4.3 Fourier Methods

Fourier methods are more detailed than integral breadth methods. Instead of using one parameter to define a particular diffraction peak, they use the whole of the peak. They still contain some of the problems that were encountered in the integral breadth methods, such as the separation of different causes of broadening. However, with increases in the computational power of computers, along with the more detailed information they can provide, these methods have gained in popularity.

In this section, the main kinematical diffraction equations that are used, will be considered along with how different methods use these equations to quantify the state of a material. Before this can be done it will first be shown how the Fourier coefficients of a diffraction peak can be found and what these Fourier coefficients mean.

Fourier Coefficients

A non-periodic function, such as a diffraction peak, can be expressed in terms of harmonic (sine or cosine) functions of different frequencies and amplitudes, thus

making the function easier to analyse. The function ($I(x)$) is then given in terms of these harmonics (equation 2.24 and Figure 2-23).

$$I(x) = \sum_{n=-\infty}^{\infty} A_n \cos(2\pi n x) + B_n \sin(2\pi n x) \quad (2.24)$$

Where, the amplitude of a particular harmonic, with frequency n , is given by its symmetric and asymmetric Fourier coefficients A_n and B_n . The Fourier coefficients can be found by the inverse relationships.

$$A(n) = \sum_{x=-\infty}^{\infty} I(x) \cos(-2\pi n x) \quad (2.25)$$

$$B(n) = \sum_{x=-\infty}^{\infty} I(x) \sin(-2\pi n x)$$

In Figure 2-23, a Cauchy function is shown in terms of its symmetric cosine harmonics. With the addition of each harmonic, the total gets closer to describing the shape of the Cauchy. In Figure 2-24 the amplitudes of these harmonics, or the cosine Fourier coefficients, are shown.

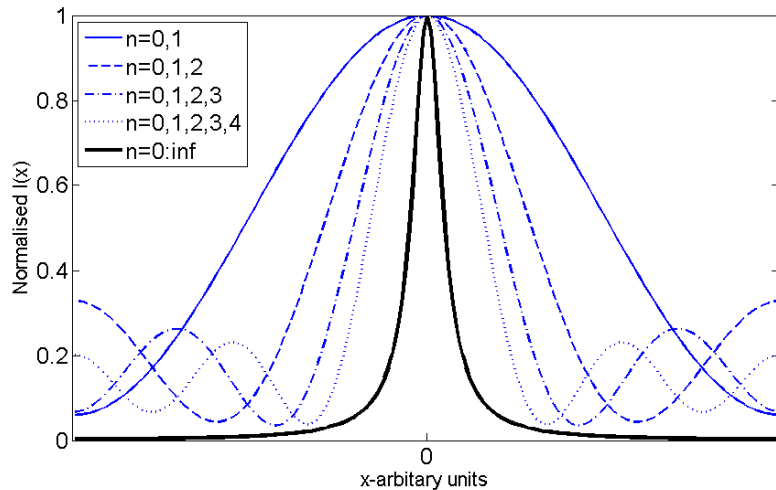


Figure 2-23. A Cauchy function can be considered as a sum of harmonic terms. It is shown how the different harmonics of frequency ‘ n ’ add to produce a peak that is closer to the Cauchy as each additional harmonic is added. The magnitude of the peaks are normalised so that $I=1$ at $x=0$.

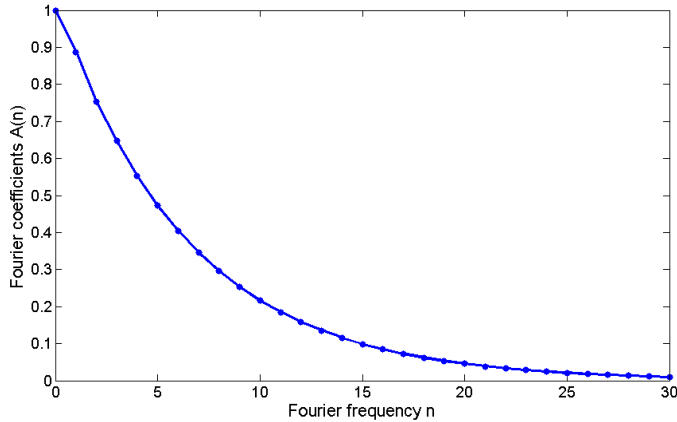


Figure 2-24. The Fourier coefficients of a Cauchy function.

Kinematical Theory of Diffraction

The kinematical theory of diffraction is the main diffraction theory used to describe imperfect crystals. From this theory it is possible to describe the Fourier coefficients in terms of the size and strain present in a material. The details are only described briefly; a more complete description is given by Warren (1969).

If we consider an un-polarized monochromatic beam of wavelength, λ , incident on a sample, whose dimensions are small in comparison to the distance from the sample to detector. Then the intensity, I , is given by the kinematic equation 2.26.

$$I = F^2 \sum_m \sum_{m'} \exp \left[\left(2\pi i / \lambda \right) (\vec{g}) \cdot (\vec{R}_m - \vec{R}_{m'}) \right] \quad (2.26)$$

Where, m and m' represent the different number of positions that can be occupied by the atoms with position given by R , g is the diffraction vector and F the structure factor. This can be expressed in terms of the Fourier coefficients (Warren 1969) by equations 2.27 and 2.28. This equation introduces some new terms that are described later.

$$P'(2\theta) = K(\theta)N \sum_{n=-\infty}^{+\infty} [A_n \cos(2\pi gL) + B_n \sin(2\pi gL)] \quad (2.27)$$

$$A_n = \frac{N_n}{N_3} \langle \cos(2\pi L g \varepsilon_L) \rangle \quad B_n = -\frac{N_n}{N_3} \langle \sin(2\pi L g \varepsilon_L) \rangle \quad (2.28)$$

Where, $P'(2\theta)$ is the intensity measured, $K(\theta)$ is a function which for a given diffraction peak slowly varies with 2θ , K is dependent on a number of factors including the structure factor, angle, wavelength and distance to the sample.

The significance of this equation is that it allows the measured diffraction peak to be compared directly with the structure of a material. The ratio N_n / N_3 are often called the size Fourier coefficients, and are due to the finite size of the crystals within the sample, and $\langle \cos(2\pi L g \varepsilon_L) \rangle$ are the strain Fourier coefficients, due to the distortion within the crystals, or put another way, the variations in the d-spacing.

The cosine coefficients are most often used exclusively. This is because they are in most cases larger than the sine coefficients and the sine coefficients are more difficult to interpret. It is also possible to normalise the cosine coefficients, since when $n=0$ the strain coefficients equal one and the size coefficients equal one, since by definition (see below) $N_{n=0}=N_3$.

It is assumed that the distortion within a unit cell can be ignored and that a particular measurement geometry has been used. Some of these assumptions will be considered later.

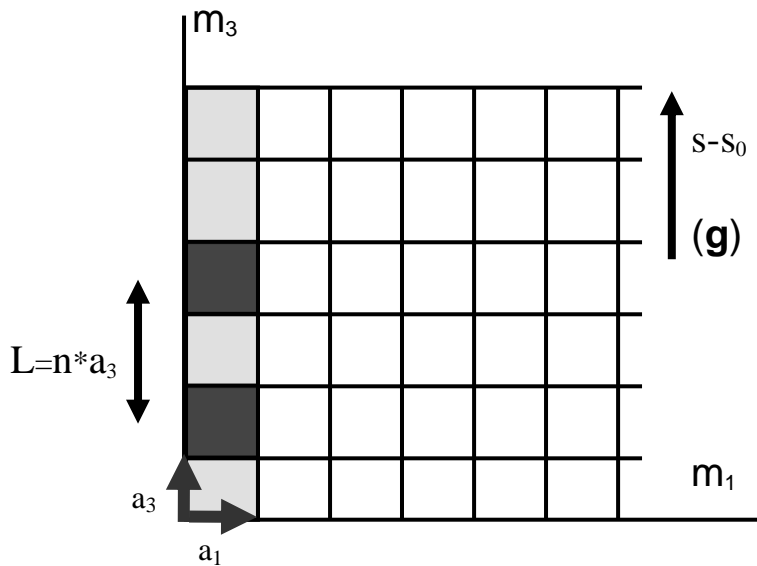


Figure 2-25. A crystal, or domain, within the measured sample can be considered as a number of columns of base $a_1 \times a_2$ (the size of the unit cell in these directions) and height given by the size of the domain in the direction g . The distance between unit cells in a column is L .

The other terms in equation 2.27 and equation 2.28 (L , ϵ , N) can be understood if we consider a crystal within the sample to consist of an array of periodically repeating unit cells (Figure 2-25). The position of a particular unit cell can be given by the vector R_m

$$\begin{aligned}\hat{R}_m &= m_1 \hat{a}_1 + m_2 \hat{a}_2 + m_3 \hat{a}_3 + \hat{\delta}(m_1 m_2 m_3) \\ \hat{\delta}_m &= X_m \hat{a}_1 + Y_m \hat{a}_2 + Z_m \hat{a}_3\end{aligned}\quad (2.29)$$

Where, $\delta(m)$ gives the distortion, or difference from the perfect crystal, of the specified unit cell with position m , if we ignore any distortion within the unit cells. The vectors $\hat{a}_{1,2,3}$ give the dimension of the unit cell.

If we consider a diffraction peak from the 001 plane, then we can make the approximation $\hat{\delta}_m \approx Z_m \hat{a}_3$, and the crystal can be thought of as consisting of a number of columns with base dimensions \hat{a}_1, \hat{a}_2 and height given by the size of

the crystal. The diffraction peak consists of the sum of the contributions from these different columns.

The kinematical diffraction equations can be simplified by the introduction of the variable ‘n’ (Bertaut 1949), where ‘n’ is the separation of two unit cells in the same column $n = m_3' - m_3$. The variable ‘L’ gives the distance between these unit cells.

The terms describing the number of cells in the sample can then be given by the following definitions. N is the number of cells in the crystal, N_n is the average number of cells with an nth neighbour in the same column and N_3 is the average number of cells per column. If the sample is a polycrystal then these values are averages of the different crystals that contribute to the diffraction peak. The size Fourier coefficients are therefore the ratio of a quantity indicating the distribution of the crystal size (N_n) and the average crystal size (N_3).

The difference in distortion between two unit cells is given by $Z_n = Z(m_3') - Z(m_3)$. This distortion is over a distance L and it causes L to change by $\Delta L = a_3 Z_n$. So that the strain over the distance L is ε_L and given by:

$$\varepsilon_L = \frac{\Delta L}{L} = \frac{Z_n}{n} \quad (2.30)$$

The value of ε_L (and Z_n) is the average value for all columns within the crystal, and for all crystals that contribute to the diffraction peak.

In the equations above, it has been assumed that the Fourier coefficients of a {00l} peak have been found between $l-0.5$ to $l+0.5$ (on a 1/d scale). However, in general the range over which the Fourier coefficients are found will be chosen to be lower, due to the overlapping of other peaks. It is then necessary to introduce

the fictitious quantities n' & a_3' , to allow conversion to the ‘real’ quantities. The relations between these quantities and L are given by:

$$a_3' = \frac{\lambda}{4(\sin \theta_2 - \sin \theta_0)} = \frac{1}{2\left(\frac{1}{d_2} - \frac{1}{d_0}\right)}$$

$$L = n \times a_3 = n' \times a_3' \quad (2.31)$$

Where, θ_0 and d_0 are the values at the Bragg angle, θ_2 and d_2 are the maximum and minimum values the Fourier coefficients are found between. The distance between d_2 and d_0 is kept constant for the different peaks.

Although equation 2.27 and 2.28, are useful equations that relate the structure of a material to its diffraction peaks, they are difficult to deal with. In order to use the equations it is necessary to make assumptions as to the distribution of size and strain and convert the strain coefficients from an average of a cosine function to an average of a strain term. The next two parts of this section consider how this can be achieved.

Size Fourier Coefficients

To find the mean size it is necessary to make an approximation as to the size distribution. This is because the size coefficients ($\frac{N_n}{N_3}$) provide information about both the mean size and its distribution.

If $p(i)$ is the fraction of columns of length ‘i’, then the average number of n pairs in a column (N_n), is given by the following sum and integral (since $i \gg 1$):

$$N_n = \sum_{i=|n|}^{\infty} (i - |n|) p(i) \approx \int_{i=|n|}^{\infty} (i - |n|) p(i) di \quad (2.32)$$

By differentiating with respect to n , we obtain a term describing the derivative of the Fourier coefficients:

$$\frac{dA_n^s}{dn} = -\frac{1}{N_3} \int_{i=|n|}^{\infty} p(i) di \approx \left[-\frac{1}{N_3} \right]_{n \rightarrow 0} \quad (2.33)$$

Equation 2.33 provides a simple method to obtain the mean size of the crystals within a sample. In this method, the gradient of the size Fourier Coefficients is found for low n (and L) values, and the reciprocal of this value gives the mean crystal size N_3 .

In practise, it is difficult to measure the gradient at a sufficiently small enough value of n for the distribution to be ignored. This is because of random errors and fluctuations in the Fourier coefficients and the increased unreliability of the Fourier coefficients at low n , mainly due to the estimation of the background level.

A different but analogous approach adopted to find the size of domains is to make an assumption as to the distribution $p(i)$. It is then possible to fit this distribution to the size Fourier coefficients.

A number of functions can be used to approximate the size distribution found in measured materials (Scardi and Leoni 2001). The most popular of these is the lognormal distribution, because the lognormal distribution has been shown through various measurements (Ungar 2003) to be a good approximation to the size distribution found in materials.

The lognormal grain size distribution, g_s , is given by:

$$g_s(D) = \frac{1}{D\omega(2\pi)^{0.5}} \exp\left[\frac{(\ln D - \gamma)^2}{2\omega^2}\right]$$

$$m = \exp(\gamma + 0.5\omega^2) \quad v = \exp(2\gamma + \omega^2) \exp(\omega^2 - 1) \quad (2.34)$$

Where, ω and γ are the lognormal standard deviation and mean and m and v the mean and variance of the distribution.

The size Fourier coefficients for this function, for spherical crystals, has been shown (Scardi and Leoni 2001) to be given by the following function.

$$A_{\text{lognorm}}^s = \sum_{n=0}^3 H_n^c \frac{M_{l,3-n}}{2M_{l,3}} \operatorname{erfc} \left[\frac{\ln(K^c L - \gamma - (3-n)\omega^2)}{2^{0.5}\omega} \right] L^n \quad (2.35)$$

$$M_{l,n} = \exp[n\gamma + 0.5(n\omega)^2]$$

Where, for spherical crystals H and K are variables given by $K^c = 1$, $H_0^c = 1$, $H_1^c = -3/2$, $H_2^c = 0$, $H_3^c = 1/2$. L is the Fourier length and erfc is the complementary error function.

The size distribution of a particular material can be found by fitting equation 2.35 to the measured size coefficients, by allowing the variables ω and γ to change.

In some cases, the shape of the crystals may be aligned in such a way that the sizes are different for the different diffraction peaks, with different $\{hkl\}$ indices. If this is the case, Ribarik and colleagues (2001) provided a description of how this dependence could be introduced into the size Fourier coefficients.

The size value from Fourier methods are called the area-weighted values, whereas those using the Scherer or WH methods is called the volume-weighted value. If the distribution is given by a lognormal distribution these can be related to each other and the arithmetic average by the following equation (Ungar 2003).

$$\langle x \rangle_j = m \exp(kv^2) \quad (2.36)$$

Where, j represents the different averages, the arithmetic, area and volume weighted averages. The value of k= 0.5, 2.5 and 3.5 for the different values. From this it is found that the volume weighted average is always more than or equal to the area weighted value.

If the derivative of the size coefficients (equation 2.33) is differentiated, the second derivative of the size coefficients is given by:

$$\frac{d^2 A_n^S}{dn^2} = \frac{p_n}{N_3} \quad (2.37)$$

In theory, this equation could be used to find the distribution of sizes. However, in practise, this is not possible, as the second derivative of any raw size coefficient data is too noisy.

The importance of this equation is its use in assessing the accuracy of the measured size coefficients. The size distribution p or the crystal size N₃ can never be negative, hence neither can the second derivative of the size coefficients. When the second derivative of the size coefficients are negative the magnitude of the gradient of the size coefficients increases with increasing L values. This is particularly common at low values of L and is known as the ‘hook effect’. The ‘hook effect’ is often observed in measured size coefficients and its presence is mainly thought to be due to overestimation of the background level or poor quality data (Langford and Louer 1996). This effect can be corrected for by extrapolating the size Fourier coefficients, with a positive second derivative, to zero L, and then renormalizing the size coefficients to make A_S(0) =1.

Wilkins (1979) showed that the ‘hook effect’ might not just be a feature of the accuracy of the coefficients, but may instead be caused by the presence of small-angle grain boundaries. Wilkins assumed a periodic distribution of edge dislocations in an elastically isotropic and infinitely extended crystal. Wilkins calculated the displacement field and size and strain Fourier coefficients using a method called the Warren-Averbach method (or the log Warren-Averbach method discussed later). The results show that the small-angle boundaries produce a

‘hook-effect’ and cause a size broadening that is approximately equivalent to the separation of the defects, D, in the direction of g.

There is also a disagreement on whether a dislocation cell wall, with a very small misorientation across it, contributes to size broadening. Ungar (2006), believes that they contribute to size broadening, due to a phase shift across dipolar dislocation walls even when the misorientation is zero. However, others, such as van Berkum and colleagues (1994), believe that these types of boundaries should only contribute to strain broadening and not size broadening, since any misorientation is small.

The measurement of fine sized crystals (in powders with submicron grain size or metals with nanocrystals), where strain broadening is a small factor, has shown to give comparable results between Fourier methods and other measurement methods (Ungar 2003). It is the belief of some (Kuzel 2007) that the current description of size broadening is satisfactory. However, the same could not be said when both size and strain are present, as is normally the case when strain is present. In this situation there is the additional problem of the separation of size and strain. The mathematics behind any separation of the two is only an approximation and as such, this adds uncertainty to the size results one obtains. It is argued by van Berkum and colleagues (1994) that any discrepancy is a consequence of the size and strain separation method used, which can also be seen from the predictions of Wilkens. In the next section, these approaches to separate the size and strain components will be discussed, along with how the strain components are used.

Strain Fourier Coefficients

As with the size coefficients, the current form of the strain coefficients is difficult to deal with. This is because it is beneficial to be able to describe the Fourier coefficients in terms of a strain term and not a cosine of one. In order to do this it is possible to write the strain coefficients in terms of the probability ($P(Z_n)$) that the distortion Z_n is between Z_n and Z_n+dZ_n , which leads to:

$$A_n^D = \langle \cos(2\pi g L \varepsilon_L) \rangle = \int P(Z_n) \cos 2\pi g L \varepsilon_L d\varepsilon_L \quad (2.38)$$

In order to evaluate this integral certain approximations must be made. The most common approach is to expand the cosine parts as a Taylor series (van Berkum et al. 1994). The Fourier coefficients of a broadened peak are the product of the size and strain coefficients (Warren 1969). This may be expressed in terms of the logarithm as:

$$\ln(A_n) = \ln(A_n^S) + \ln(A_n^D) \quad (2.39)$$

If the logarithm of the strain coefficients are expanded and terms with higher order than g^2 are ignored, this leads to the standard Warren-Averbach formula, or the log-WA method:

$$\ln(A_L) = +\ln(A_L^S) - 2\pi^2 g^2 L^2 \langle \varepsilon_L^2 \rangle \quad (2.40)$$

If the strain coefficients are expanded by a Taylor series and limiting to lower order terms gives the linear WA method:

$$A_L = A_L^S \left(1 - 2\pi^2 g^2 L^2 \langle \varepsilon_L^2 \rangle \right) \quad (2.41)$$

The assumptions made in the log WA method are that g and L are small and that the strain function is physically realistic. The separation is achieved at $g=0$ and for a limited number of increasing L values. Therefore, as long as the L values are not too large and a linear curve can be fitted as $g \rightarrow 0$, the assumptions are met. If the strain distribution, $P(Z)$, is Gaussian the log WA method leads to exact results for the coefficients over all g and L . The separation of size and strain is then achieved by plotting g^2 against $\ln A$. The size coefficients are given by the intercept of the plot and the gradient gives the strain coefficients.

In the linear WA method, there is no strain distribution, which would give the exact values for the Fourier coefficients (1994). Delhez and colleagues (1982), believes that this method should be preferred to that of the log WA method, because it is not as limited in its assumptions about the strain distribution. Van Berkum (.1994) believes there are more systematic errors in the linear method, but less random errors, compared to the log WA method.

The separation of size and strain is then achieved by plotting g^2 against A. The size coefficients are given by the intercept of the plot and the strain coefficients can be determined from the gradient.

Van Berkum and colleagues (1994) suggested a different approach, the ‘alternative method’, which they believed offered advantages over the WA method. The alternative method of van Berkum (1994) is also based on an approximation of the Taylor series of the strain Fourier coefficients. The main assumption in deriving the alternative method is that strain gradients within domains are not important and that for large values of L the displacement of the cells are large and random, such that the average local strain and its derivatives are negligibly small (over this distance). This is known as the Stokes-Wilson approximation (Stokes and Wilson 1944). In particular, the method is most applicable when strain is uniform or varies slowly within a domain. If the local strain ϵ_0 , for a given position, varies slowly in space, then the derivatives of the strain are small. The extreme case of this is when there is no distortion within grains, but there is a variation in the intergranular strain in different grains (van Berkum et al. 1994).

If it is assumed that $L/\langle D \rangle$ is small and the distribution of grain sizes is not far from an exponential distribution, then the strain Fourier coefficients are found to be independent of both L and g, and are given as:

$$A^D(L_i, g_i) = A^D(L_1, g_1) \quad \text{with} \quad L_i = (g_1 / g_i)L_1 \quad (2.42)$$

The full expression of the Fourier coefficients is then:

$$\ln[A(L_i, g_i)] = \ln[A^D(L_1, g_1)] + (g_1 / g_i) \ln[A_s(L_1)] \quad (2.43)$$

Similar to the log WA method, plots of $1/g$ (instead of g^2) against the log of the Fourier coefficients, remembering L_i and not L are used, give the size and strain components. Although, the size obtained from the alternative method can be compared directly with the WA method the strain component gives the local strain, rather than the average strain between cells a distance L apart as obtained

from WA. The method can though be used in conjunction with the description of dislocation broadening of Wilkens, or other descriptions.

Any approach to separating the size and strain broadening is based on a number of assumptions. Therefore, the accuracy of the results is dependent on how close the assumptions are to the actual structure of a particular sample. The log WA method is best used for strain distributions that are Gaussian and where there are gradients in strain among a domain, and it is suggested to be better for broadening due to size (van Berkum et al. 1994). In contrast, the alternative method is less dependent on the strain distribution. The alternative method is best used when the strain is uniform within a domain. In addition the main limitation for all methods is that they are only valid for small values of L and g

The WA method, and in particular the log-WA form, is the most widely used method to evaluate the integral but it is not without fault. The alternative method, on the other hand, has only been used by van Berkum who also developed it.

2.4.4 Variance Method

The variance method is a single line method to evaluate the contribution of size and strain broadening. The method was first suggested by Tournarie (1956), and then developed by Wilson (1962a). There are two approaches that can be taken with the Variance method, depending on how the strain component is treated. The first works by using a general description of strain and the second uses the strain from dislocations. The general description of strain is discussed first, then the dislocation description.

The variance method is based on the restricted moments of a diffraction peak, also known as its moments or variance. These moments are, in a similar manner to the

Fourier coefficients, a way to quantify the shape of a peak. They are found using the intensity values of a single peak using the following formula:

$$M_\kappa(\sigma_k') = \frac{\int_{-\sigma'}^{\sigma'} \sigma_k^\kappa I(\sigma_k) d\sigma_k}{\int_{-\infty}^{\infty} I(\sigma_k) d\sigma_k} \quad (2.44)$$

Where, σ is the difference from the Bragg angle in units of $1/d$, $M_\kappa(\sigma')$ are the restricted moments of the κ^{th} order at different values of σ and the intensity, I , is normalised to be one at its maximum. The variance are the 2nd order restricted moments, that is $\kappa=2$.

Wilson (Wilson 1962b) showed that if broadening is due to size broadening alone then the variance, M_2 , is given by:

$$M_{2,S}(\sigma_\theta) = \frac{\lambda K \sigma_\theta}{\pi^2 \cos \theta_0 \langle D \rangle} - \frac{\pi^2 L^2 (\chi)^2}{4K^2}$$

Where,

$$\chi = \frac{\lambda K}{\pi^2 \cos \theta_0 \langle D \rangle} \quad (2.45)$$

Where, L is the taper parameter and K the Scherer constant, which for spherical crystals $L=0$ and $K=1.2090$ (Langford and Wilson 1978). θ_0 is the position of the peak in radians, λ the wavelength and σ is the distance from the Bragg angle in units of θ in radians.

In the same manner, if the broadening is due to strain alone then the variance is given by (Wilson 1963a):

$$M_{2,D}(\sigma_\theta) = 4 \langle e^2 \rangle \tan^2 \theta_0 \quad (2.46)$$

If a measured line profile $H(\sigma)$ is composed of two components, the instrumental line profile (G) and the real line profile due to the material (F), such that

$H(\sigma)=F(\sigma)*G(\sigma)$ (* represents a convolution), then variance of the measured line profile is the sum of the variances (Mitra and Giri 1987),

$$M_H = M_F + M_G \quad (2.47)$$

The variance method therefore provides an easy method to separate the instrumental broadening from the material related broadening because the instrumental moments can be subtracted from the measured to get the real. It also makes it easier to separate size and strain broadening because only the size term has a σ term. The variance due to broadening by size and strain is the sum of the terms, which can be expressed in terms of a straight line with gradient k_f and intercept W_f ,

$$M_2(\sigma_\theta') = W_f + k_f \sigma_\theta \quad (2.48)$$

The components are given by,

$$W_0 = 4\langle e^2 \rangle \tan^2 \theta_0 - \frac{\pi^2 L^2 (\chi_f)^2}{4K^2}$$

$$k_f = \frac{\lambda K}{\pi^2 \cos \theta_0 \langle D \rangle} \quad (2.49)$$

There is experimental validity to these equations, because it has been shown that the second-order restricted moments are in most cases linear with σ (Langford 1982). The components W_f and k are found by fitting a straight line to the linear region of the restricted moments, to the material broadened peak.

Corrections to the Variance Method

Depending on the procedure taken errors can be introduced. In this section some of the corrections that may be taken are detailed.

The variance function is slightly curved (Wilson 1962a) and would include extra terms:

$$M(\sigma) = W + k\sigma + c\sigma^{-1} + \dots \quad (2.50)$$

If straight lines are fitted to the measured broadening and instrumental broadening (g) then we must take account of a non-additive term. This non-additive term is the result of the curvature of the measured and instrumental profiles (c and higher order terms in equation 2.50). Hence, if a straight line is fitted without accounting for the additional terms there is an error. This changes the real variance gradient by a value depending on the gradient of the measured and instrumental profiles (Edwards and Tomen 1971a),

$$W_f = W_h - W_g + \frac{1}{2} \pi^2 k_g (k_h - k_g) \quad (2.51)$$

The additional terms in equation 2.50 ($c\sigma^{-1} + \dots$) are negligible for large σ , but for the range of values most often used with this method, can have a significant influence, particularly on the strain term. It is possible to interpret this in terms of theoretical considerations if broadening is due to small size alone. This was done by Edwards and Toman (1971a) who derived terms for the correction in the intercept for different shapes of crystals.

Edwards and Toman (1971a) derived a formula to give the correction to the intercept and gradient due to curvature. The adjustment to the intercept between two points σ_1 and σ_2 is given by adding W_{cu} in equation 2.52 to the W value obtained, the correction for the gradient is often negligible.

$$W_{cu} = \frac{f(q)}{\sigma_2} \left[3W_g k_f - \frac{3\pi^2}{4} k_g \left(\frac{L}{K} \right)^2 k_f^2 - \frac{\pi^2 M k_f^3}{4K^3} \right] \quad (2.52)$$

$$f(q) = \frac{2}{(1+q)} \left\{ 1 - \frac{4(1-q^3)}{(1-q)^3} \left[1 + \frac{1}{2} \frac{(1+q)}{(1-q)} \log q \right] \right\} \quad q = \sigma_1 / \sigma_2$$

In all practical cases the Variance is taken from a truncated peak over a range $\pm\sigma_{\max}$. The denominator in equation 2.44 will instead be $\int_{-\sigma_{\max}}^{\sigma_{\max}} I(\sigma)d\sigma$ and the experimental variance will differ from the theoretical value by the ratio of the two denominators. The corrections to the intercept and slope can be adjusted by subtracting the following values from those measured (Langford 1982),

$$\begin{aligned}\Delta W &\approx W_{\sigma_{\max}} k / \sigma_{\max} \\ \Delta k &\approx k^2 / \sigma_{\max}\end{aligned}\tag{2.53}$$

Alternatively, if the peak to background level is low, or there is overlapping of profile tails, Langford (1981) and Langford and Wilson (1963) suggest using a different form of the variance with a different denominator.

The choice of the level of the background is important because it affects both the intercept and gradient and is not as easily to correct for as the other sources of error. Edwards and Toman (1971b) make two assumptions in order to calculate the background level. They assume that if the background is set correctly the variance will be linear for large values of σ and if not it will give rise to a σ^3 term. A function of the form given by equation 2.54, can then be fitted to the data, adjusting the background so that a_3 is minimised.

$$M_2 = W + k\sigma + a_3\sigma^3\tag{2.54}$$

A problem with this is that if the curvature term $c\sigma^{-1}$ (equation 2.50) is negative and not negligible it will lead to the background level being set too high. Edwards and Toman (1971a) instead take the average of the corrected background and the original level.

The use of analytical functions with the variance method

An alternative method for background determination is to use the result of a fit of an analytical function. There are three different ways that this method can be used

to determine the variance gradient and intercept. The fit of an analytical function (and background) can be used just for determining the level of the background.

Alternatively, the analytical function can be used directly either by linear fit to the variance of the analytical function or from expressions for the variance parameters that have been derived from the analytical function. The last two of these methods are useful because it is not necessary to correct for truncation of the profile or curvature of the variance and it allows the method to be used when there is overlapping of peaks.

Sanchez-Bajo and Cembrera (1997) derived an expression relating the components of a pseudo-Voigt to the variance using equation 2.48 and 2.49, to obtain relations for the variance gradient and intercept.

$$W = \frac{(0.5fw)^3}{\beta} \left(0.5\sqrt{\pi}[1-\eta]\ln 2^{-\frac{3}{2}} - \eta\pi \right) \quad (2.55)$$

$$k = \frac{2\eta(0.5fw)^2}{\beta}$$

$$\beta = 0.5fw \left(\pi\eta + [1-\eta]\sqrt{\frac{\pi}{\ln 2}} \right)$$

Where, fw is the full-width at half maximum intensity of a peak in radians on a 2θ scale, η the pseudo-Voigt mixing parameter and β the integral breadth in radians.

Sanchez-Bajo and colleagues (2006) derived similar relations for a Voigt function:

$$W = \frac{\beta_G^2}{2\pi} - \frac{\beta_C^2}{\pi^2} \quad (2.56)$$

$$k = \frac{2\beta_C}{\pi^2}$$

Where, β_C and β_G are the Cauchy and Gaussian integral breadths respectively, in radians.

The variance function and dislocation broadening

Wilson (1963c) showed that if broadening is due to dislocations then the assumptions made in the derivation of equation 2.46, for $M_{2,D}$, are invalid. This is because those equations are based on a different description of strain. Instead, he derived an equation with an additional $\log(\sigma)$ term, by assuming each crystal contained a single screw dislocation. Groma (1998) expanded this description for a non-uniform dislocation distribution. It is based on straight dislocations, but unlike Wilkens theory, no assumption is made as to the dislocation distribution. Borbely and colleagues (Borbely and Groma 2001, Borbely et al. 2006) developed the model to include the effect of small crystals. The method was applied to a cold and hot deformed Al-Mg alloy and on a nanocrystalline iron powder, to show how the method can be used. The method is based on behaviour of the second- and fourth-order restricted moments. These are found to be related to the dislocation density ρ , the average column length $\langle D_f \rangle$ by equation 2.57 (Borbely and Groma 2001).

$$M_2(\sigma_k) = \frac{\sigma_k}{\pi^2 \langle D_f \rangle} - \frac{L}{4\pi^2 K^2 \langle D_f^2 \rangle} + \frac{\Lambda \langle \sigma \rangle \ln(\sigma_k / q_0)}{2\pi^2} \quad (2.57a)$$

$$\frac{M_4(\sigma_k)}{\sigma_k^2} = \frac{\sigma_k}{3\pi^2 \langle D_f \rangle} + \frac{\Lambda \langle \rho \rangle}{4\pi^2} + \frac{3\Lambda^2 \langle \rho^2 \rangle}{(2\pi)^2} \frac{\ln^2(\sigma_k / q_1)}{\sigma_k^2} \quad (2.57b)$$

Where, K the Scherer constant, Λ is related to the contrast factor and L is the Taper constant describing the shape of the grains. In this case σ is in units of $1/d$. Borbely and colleagues (2006) modified the fourth order moments to:

$$\frac{M_4(\sigma_k)}{\sigma_k^2} = \frac{\sigma_k}{3\pi^2 \langle D_f \rangle} + \frac{\Lambda \langle \rho \rangle}{4\pi^2} + \frac{3\Lambda \langle \rho \rangle}{(2\pi)^4 \langle D_f \rangle} \frac{\ln(\sigma_k / q_1)}{\sigma_k} \quad (2.58)$$

The variables q_1 and q_0 are fitting parameters.

Borbely and colleagues suggest that if the two moments are linear at large q then size broadening is dominant and we are left with the first description. If instead, the curves are not linear but their rate falls at high q , strain broadening is

dominant. They recommend the determination of the level of the background by finding the value that gives the same particle size for both the fourth and second order moments. Characteristic behaviour of the different moments is shown in Figure 2-26.

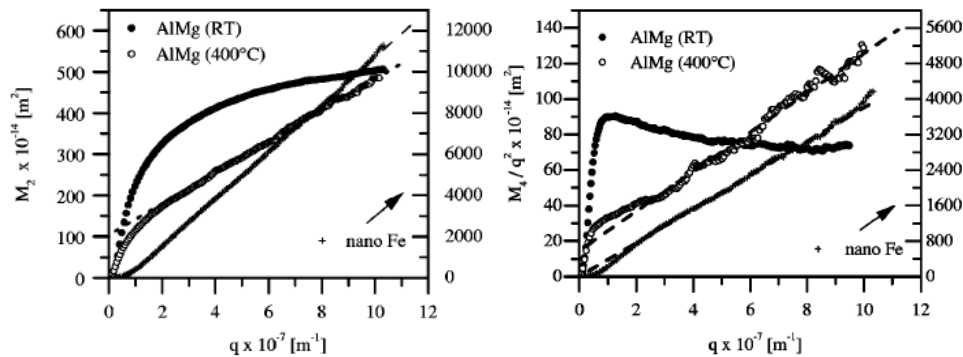


Figure 2-26. Characteristic behaviour of second-order moments (left) and fourth-order moments divided by σ^2 (where q used in the figure is equivalent to σ). The samples shown are AlMg deformed at room temperature in compression and 400°C and an annealed iron powder. The iron powder shows behaviour characteristic of only size broadening, whereas the AlMg shows both size and strain broadening (Borbely and Groma 2001).

2.4.5 Dislocation Broadening

Dislocations are a type of defect in the crystal structure of a material. In plastically deformed metals, dislocations are in most cases the most important cause of broadening. This is because they are the main contributor to strain broadening and to size broadening. In later sections, other types of factors affecting the shape of diffraction peaks will be considered. In the first part of this section, the effect of the broadening of a single dislocation will be considered. It will be shown that a dislocation can broaden different peaks by different amounts and this can be used to explain broadening anisotropy through the contrast factor term (introduced earlier). However, in order to understand the shape of a diffraction peak it is not sufficient to consider only one dislocation, but it is instead necessary to consider the contribution from all dislocations. The second part of this section will focus on how it is possible to approximate the arrangement of dislocations to explain the shape of a diffraction peak in terms of dislocations.

Contrast Factor of Individual Dislocations

Dislocations contribute to the broadening of a particular peak in a similar way that dislocations are observed in transmission electron microscopy (TEM); broadening, or visibility, is dependent on the vectors defining the dislocation and the elastic constants of the material. This visibility is quantified by what is known as the contrast (or orientation) factor.

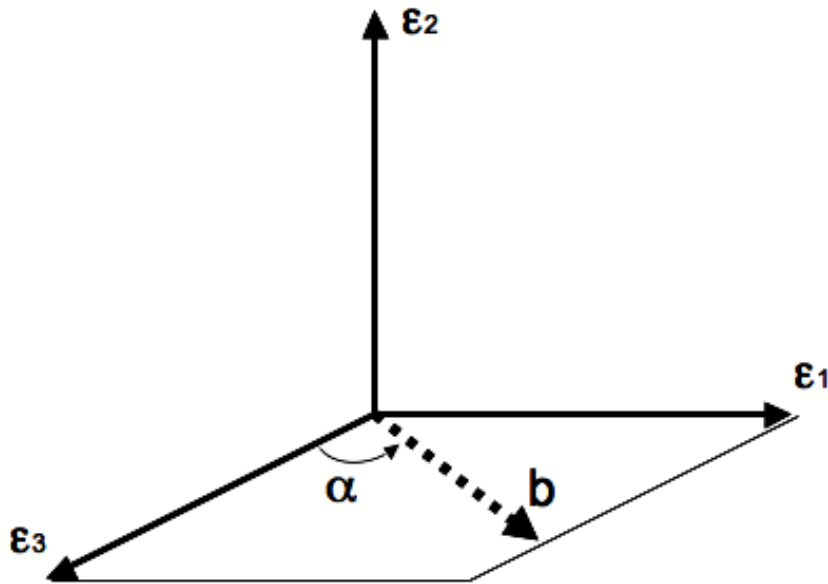


Figure 2-27. The axes used to define a dislocation, the direction ϵ_3 points in the direction of the dislocations slip line, ϵ_2 is normal to the slip plane, and b is the dislocations Burgers vector. The angle α gives the character of the dislocation, $\alpha=90^\circ$ is an edge and $\alpha=0^\circ$ is a screw dislocation.

The contrast factor can be found by calculating the displacement field of a dislocation. Borbely and colleagues (2003), showed how this might be done and created a program to calculate the contrast factors for different dislocations. The contrast factor of an individual dislocation is given by the following formula, according to Wilkens (1987), Groma and colleagues (1988) and Klimanek and Kuzel (1988),

$$C = \frac{1}{\pi} \int_0^{2\pi} F^2(\varphi) d\varphi \quad (2.59)$$

The function $F(\varphi)$, is related to the diffraction vector g and the distortion tensor β_{ij} , in terms of the polar angle φ .

$$F(\varphi) = \sum_{i=1}^3 \sum_{j=1}^2 \gamma_i \gamma_j \beta_{ij}(\varphi) \quad (2.60)$$

Where, γ_i and γ_j are the direction cosines of the diffraction vector relative to the axes defined in Figure 2-27. The angular part of the distortion tensor $\beta_{ij}(\varphi)$ is

found from the gradient of the displacement field u and is given by Klimanek and Kuzel (1988), as:

$$\beta_{ij}(\varphi) = \frac{2\pi r}{b} \frac{\partial u_i}{\partial x_j} \quad (2.61)$$

Where, b is the Burgers vector of the dislocation, r is the polar distance to the origin, u is the displacement field of the dislocation and x the direction, the indices i and j represent the different directions given by Figure 2-27.

Borbely and colleagues (2003) solved these equations in the program ANIZC, which calculates the contrast factor of an individual dislocation given its associated vectors, the elastic constants of the material and the particular diffraction peak being observed, or for different values of g . The contrast factor is highest when the angle between the Burgers vector and the diffraction vector is close to zero for edge dislocations. However, for screw dislocations the contrast factor is highest when this angle is 45 degrees. This difference of contrast factor for edge and screw dislocations is often used to explain differences in broadening anisotropy.

Using the Contrast Factor with Powder Diffraction Patterns

In a powder diffraction pattern, a particular peak consists of the sum of diffraction peaks from different crystals, which contain a number of different types of dislocations. Therefore, in order to calculate the contrast factor for different peaks it is necessary to make assumptions as to the type of dislocations present. The type of dislocations present within a sample, given by the Burgers vector and slip plane, is defined as the dislocation population.

If it is assumed that, the sample has a random texture (no preferred orientation) and that slip systems, with a given Burgers vector and slip plane, are equally populated, this leads to a description for the contrast factor for a cubic material (Ungar and Tichy 1999), given as:

$$\bar{C} = C_{h00} (1 - qH^2)$$

$$H^2 = \frac{h^2 k^2 + h^2 l^2 + k^2 l^2}{(h^2 + k^2 + l^2)^2} \quad (2.62)$$

Where, C_{h00} and q are constants that are dependent on the elastic constants of the material and the dislocations present and h, k, l are the indices of the diffraction peak. When fitting to measured diffraction data, the constant q is allowed to vary to provide the best fit, to the model being used e.g. the Williamson-Hall method.

There are two main ways that equation 2.62 can be used to evaluate the type of dislocations present in a measured sample. The equation can be used to find the fraction of edge and screw dislocations or the fraction of different types of slip system groups. The second of these can be used to provide information on the fraction of partial dislocations or the fraction of different slip system types, e.g. in body centred cubic materials two different slip system groups are often observed. It is only possible to find one of these fractions, so assumptions must be made as to the quantity of the other values.

The calculation of the fraction can be expressed as:

$$F_{para1} = \frac{|q_{meas} - q_{para1}|}{|q_{para2} - q_{para1}|} \quad (2.63)$$

Where, F_{para1} is the fraction of parameter 1 (e.g. edge dislocations), q_{meas} the q -value found from fitting the data, q_{para1} and q_{para2} the calculated q values of parameter 1 and 2. For this equation to work, the measured q value must be restricted between the two calculated values.

Once the value of q is found, from fitting to the data, it is used to find one of these fractions and this information is used to evaluate the constant C_{h00} . In practise this may not be necessary as C_{h00} may only change by a small amount for differences in q (and hence the fractions), which may be less than other errors.

In a similar manner, Dragomir and Ungar (2002) give the contrast factor for HCP metals for equally populated slip systems as:

$$\bar{C}_{hk,l} = \bar{C}_{hk,0} (1 + q_1 x + q_2 x^2) \quad (2.64)$$

$$x = \frac{2l^2}{3(ga)^2}$$

Where, $g=1/d$, l is the 3rd hkl index, and ‘a’ one of the lattice parameters (the HCP notation {hkil} is used but ignoring the ‘i’ index). In this case q_1 and q_2 are used as fitting parameters to the appropriate function.

The interpretation of equation 2.64 is the same as that of equation 2.62. However, in this case, two fitting parameters are used and the equation cannot be used simply to find the fraction of edge and screw dislocations present with any accuracy, due to the different type of slip systems observed in HCP metals. Instead, Dragomir and Ungar (2002) used the equation to find the quantity of the different dislocation burgers vectors found in HCP metals, $\langle a \rangle$, $\langle c \rangle$ and $\langle c+a \rangle$. In this method the different types of dislocations are split into eleven slip system families, which have different slip planes, Burgers vectors and character of screw or edge (e.g. edge basal $\langle a \rangle$, edge prismatic $\langle c+a \rangle$, screw $\langle a \rangle$ etc). The calculated q and $\bar{C}_{hk,0}$, values of these slip families are found by assuming that the dislocations are randomly (or equally) populated for these families within all grains, for different HCP metals (Dragomir and Ungar 2002). It is assumed that a slip family is either active, with a fraction of $f = 1/N$ where N is the number of slip families active, or not active with a fraction zero. These values are compared with the measured values and if they are within set tolerances of the values are used to calculate the fraction of $\langle a \rangle$, $\langle c \rangle$ and $\langle c+a \rangle$. This is done by finding the centre of a histogram of a frequency distribution of the different fractions of the three Burgers vector types, which have met the tolerances.

The problem with these approaches is the assumption that all slip systems are equally populated. However, deformation is in most cases anisotropic meaning that this assumption would be invalid. This will in turn lead to bigger

discrepancies when using for HCP metals than for metals with a cubic crystal structure.

Dislocation Arrangement

The earliest models of how dislocations contribute to the broadening of a diffraction peak were based on the strain-field caused by a single dislocation.

Krivoglaz (1969) recognised that it was insufficient to consider individual dislocations and that it was necessary to account for the combined effect of dislocation strain fields.

Krivoglaz (1969) developed a model of how dislocations were arranged. In this model it is assumed that each crystal contained a set of straight and parallel dislocations that were arranged within each crystal completely randomly. The model of Krivoglaz accounted for the infinite singularities of dislocations at large and small distances by including a logarithmic term in which the singularity at large distances was accounted for by the size of the crystal. Wilkens (1970) expanded the theory of Krivoglaz, to include a more realistic distribution of dislocations, in which dislocations were assumed to be arranged in a restrictedly random distribution. The theory also replaced the size of the crystal with the outer cut-off radius of dislocations. This being the shortest distance over which the interaction energy of dislocations becomes vanishing. The model divides a crystal into a number of cylinders, which are parallel to each other and divide the whole of the crystal. Each cylinder consists of parallel screw dislocation distributed randomly parallel to the length of the cylinder, whose radius is approximately equal to the effective outer-cut off radius of the dislocations. Although developed with the restriction of screw dislocations it was later shown that the model should also be applicable to dislocations of other character (Wilkens 1976).

The theory of Wilkens leads to the following expression for the strain Fourier coefficients, caused by dislocations:

$$\ln A_D(L) = -\rho BL^2 \left(\frac{1}{d^2} \bar{C} \right) f \left(\frac{L}{R_e^*} \right) \quad (2.65)$$

$$R_e = 0.5 \exp(-0.25) \exp(2) R_e^*$$

Where, A_D are the distortion Fourier coefficients, ρ the dislocation density, C the contrast factor, L the Fourier length, and R_e the outer cut-off radius.

The term on the right is called the Wilkens function (Wilkens 1970) and is given approximately by (Scardi and Leoni 2001):

$$f^*(x) = \begin{cases} -\ln x + 7/4 - \ln 2 + \frac{x^2}{6} - \frac{32x^3}{225\pi} & \text{for } x \leq 1 \\ \frac{256}{45\pi x} - \left(\frac{11}{24} + \frac{\ln 2x}{4}\right)x^{-2} & \text{for } x > 1 \end{cases} \quad (2.66)$$

Others have derived similar descriptions of the strain term by following slightly different derivations, but all have a leading logarithm term. For example, Groma and colleagues (Groma et al. 1988, Groma 1998) developed a more general description of the broadening of diffraction peaks by dislocations. The method is advantageous in that it not only describes the peak shapes but it does not assume any distribution of dislocations, as is the case with the restrictedly random distribution of Wilkens. However, the use of this expression in its full form is limited because of the increased number of fitting parameters and it is only valid for a limited number of Fourier coefficients. This description leads to the following strain Fourier coefficients:

$$\ln A_D(L) = -\rho BL^2 \ln\left(\frac{R_e}{L}\right) \left(\frac{1}{d^2} \bar{C}\right) + QB^2 L^4 \ln\left(\frac{R_1}{L}\right) \ln\left(\frac{R_2}{L}\right) \left(\frac{1}{d^2} \bar{C}\right)^2 \pm O(L^6)$$

$$B = \pi b^2/2 \quad (2.67)$$

Where, b is the burgers vector of the dislocations, and the other terms relate to the dislocation arrangement and character.

The problem with using equation 2.67 is that the strain coefficients start to increase at large values of L (Scardi and Leoni 2002). The Wilkens function avoids this divergence and is therefore more useful in whole pattern fitting.

However, the Wilkens function reduces the physical meaning of the outer cut-off radius, to merely a length parameter and it can result in different results when fitting.

The dipole character of dislocations

The arrangement of a group of dislocations is called the dipole character and given by the dimensionless value M.

$$M = R_e \sqrt{\rho} \quad (2.68)$$

Wilkens (1976) described how the parameter M, is related to the arrangement of dislocations.

If $M \gg 1$, then dislocations are not screened by neighbouring dislocations.

If $M \approx 1$, dislocations are just screened by their neighbours

and if $M \ll 1$, then the dislocations are arranged into dipole arrangements.

If broadening is due to dislocations alone, the shape of the peak is dependent on the parameter M. For a particular peak and constant values of the contrast factor and M, the peak width is proportional to the root of the dislocation density. The shape of a particular peak, and in particular the tails, is strongly dependent on M (Figure 2-28). The tails of the profile will follow a k^{-3} (where $k=1/d$) relationship, but this is only possible to detect if M is small. Hence, for $M \gg 1$, the peaks will have a Gaussian type shape, whereas for smaller M values the peak will be more Cauchy in shape.

If M is constant then the screening of dislocations scale with the distance between them, and different levels of deformation, would be similar. This is known as the principle of similitude. However, it has been shown that M often changes with increasing strain and may be used to show a change in the stage of work-hardening (Schafler et al. 2005 and Zehetbauer et al. 1999). The value of M may be expected to fall if dislocations become more organised and screen each other

more (Schaeffler et al. 2005). However, the dipole character M, is also expected to increase with increased values of dislocation density (Zehetbauer et al. 1999). This is because regions with low and high dislocation density will develop and this can occur throughout all stages of deformation.

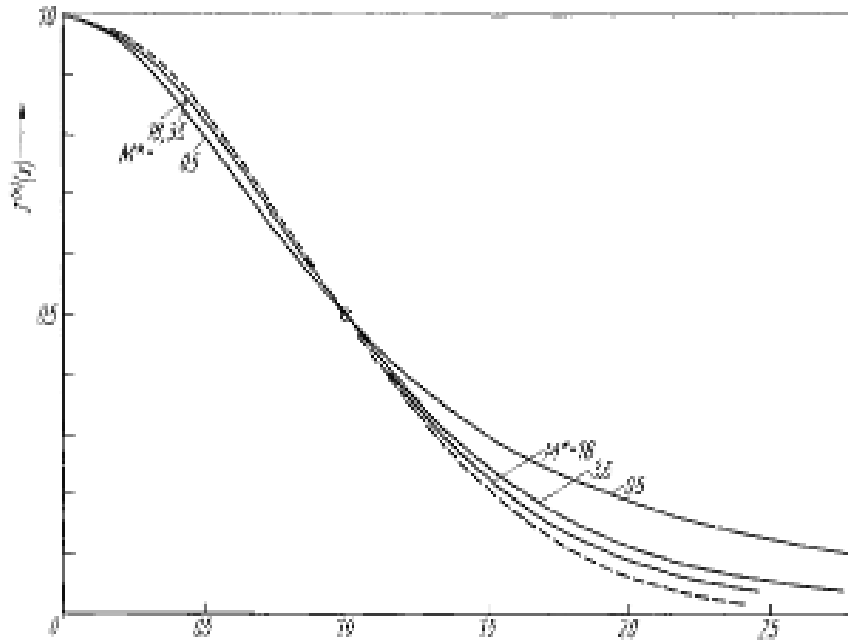


Figure 2-28. The effect of the parameter M on the shape peaks, intensity against k is plotted (Wilkins 1970).

The models of Wilkins, provides the most used method to quantify the dislocation density and arrangement, in deformed metals by x-ray diffraction. It has been shown by various experiments that this approach gives values of dislocation density and arrangement that are consistent with that observed by other methods (Gubicza et al. 2006). However, there are problems with this description. The description of a restrictedly random distribution of dislocations is an approximation and such a distribution may not actually exist in any metal (Borbely et al. 2006). From the derivation the approach would also only be valid if the radius of the dislocations were larger than the reciprocal of the square root of the dislocation density.

2.4.6 Planar Faults

Planar faults are caused when the regular stacking of atoms is interrupted. The quantity of faults present in a material is due to many factors, including the atomic interactions, and any mechanical work the material has undergone. For example, whereas in clay materials faults are very common and can be considered as the main defect, in metals they are less common and other defects such as dislocations are more important.

Planar faults may be separated into two main types, called stacking faults and twin faults. The difference in these types of planar faults can best be described for face-centred-cubic (fcc) materials. The position of an atom (or a layer of atoms) may take one of three positions (Figure 2-29), which we label A, B or C. In the normal fcc structure the layers are arranged in the order ABCABC etc. A stacking fault causes a jog in the sequence, with the result that some of the layers have a HCP structure, CACA in Figure 2-29. There are two types of stacking faults, called intrinsic and extrinsic stacking faults, which depend on the change in the sequence of layers. A twin fault causes the order to reverse at the twin fault, although the crystal structure is the same either side of the twin (it is still fcc).

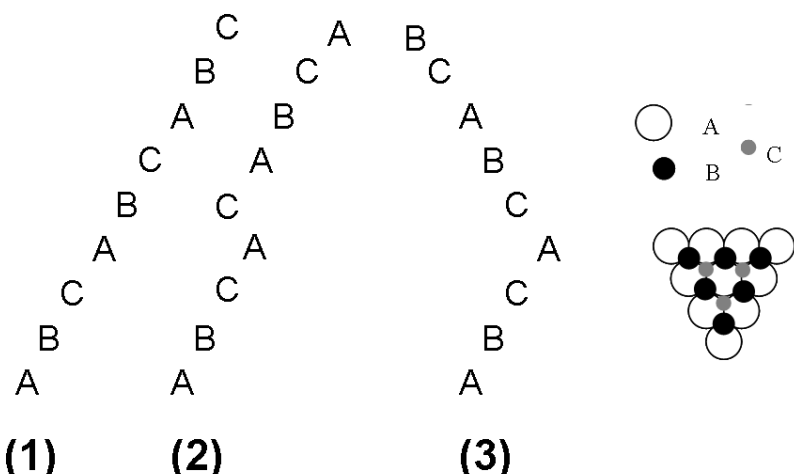


Figure 2-29. Planar Faults in FCC materials, (1) the regular fcc sequence, (2) a stacking fault and (3) a twin fault. Atoms can be in one of three positions, A, B or C, but cannot repeat the previous sequence, i.e. A cannot follow A.

A number of different authors have attempted to explain how the diffraction peaks are changed by the presence of planar faults (Landau 1937, Lifshitz 1937, Wilson 1942, 1943). The most widely used approach is the difference equation method that was developed by Warren (1959, 1969). The method is useful, but it has two main problems. The equations do not describe completely how planar faults change the shape of diffraction peaks and the assumptions inherent in calculating how planar faults cause broadening are simplistic. Others have provided a more general treatment, including Hendricks and Teller (1942) and Cowley (1981). The different methods are related (Kakinoki and Tomura 1965) but have slightly different mathematical approaches and how to deal with a statistical ensemble of faults.

The remainder of this section will consider faults in FCC metals, as this is one of the more common crystal structures in metals and is a simple structure, which means the mathematics, is easier to solve.

Warrens Difference Equation Method

By using the kinematic approximation and considering how atoms at a planar fault are displaced in respect to the perfect lattice it is possible to derive a kinematic equation for planar faults (Warren 1969).

A method to solve this equation was provided by Warren (1959 and 1969) who did so by making various assumptions. He assumed that the probability of a layer having a stacking fault (α), or a twin fault (β), was small. He also assumed that the probability of a fault occurring on a particular plane was dependent on the probability that it had occurred on a previous layer, with the average number of layers between faults given by $1/\alpha$ and $1/\beta$. It is also assumed that faults occur independently of each other and randomly (or equally) on the different planes. Warren found how planar faults affect the broadening of diffraction peaks for face-centred-cubic, body-centred-cubic and hexagonal crystal structures. He was able to show that stacking faults broaden a diffraction peak in proportion to the quantity of faults. The proportionality constant was found to be dependent on the particular {hkl} plane but independent of the order of that plane. Faults were

therefore shown to be similar to size broadening. This theory modifies the Warren Averbach and Williamson-Hall method in the following ways:

$$\begin{aligned}\ln A(L) &\Rightarrow \ln A(L) + L\beta'W(g) \\ \Delta K &\Rightarrow \Delta K - \beta'W(g)\end{aligned}\tag{2.69}$$

Where, the apparent planar fault density (β') is given as:

$$\beta' = \frac{(1.5\alpha + \beta)}{a}\tag{2.70}$$

Where, α is the density of stacking fault boundaries, β the density of twin boundaries and 'a' the lattice spacing. The constant $W(g)$, is given for face-centred-cubic by the following equation, and table 1.1, as:

$$W(g) = \frac{\sum_b |L_0|}{h_0(u+b)}\tag{2.71}$$

Where, $L_0 = 3l - (h+k+l)$ and the sum is taken over different hkl combinations of the measured diffraction peak (given by g) that broaden; $h_0^2 = h^2 + k^2 + l^2$; u is the number of components un-broadened by faulting and b the number broadened. Table 2-1, gives the values of $W(g)$, for different planes in an FCC from Warren (Warren 1969).

Table 2-1. The value of the planar fault parameter $W(g)$ in fcc crystals, for the first five planes from Warren (Warren 1969)

g	{111}	{200}	{220}	{311}
W(g)	0.43	1	0.71	0.45

The Shape of Peaks Broadened by Faults

The method of Warren (Warren 1969) provides a useful approach to incorporate faults into x-ray diffraction broadening methods, but it does not provide a detailed description of the shape of the peaks. Balogh and colleagues (2006) applied the

program DIFFAX (Treacy et al. 1991) to explain the overall shape of fault broadened peaks in face-centred-cubic metals. They were able to show that a broadened diffraction peak could be considered as the sum of Cauchy peaks, with full-width and position given by the quantity of faults. These different peaks correspond to the different relations between the diffraction vector and the plane of the fault.

In a statistically random crystal the probability of planar fault occurring on the different $\{111\}$ planes (e.g. (111), (1-11) etc) will be the same. However, these different planes will shift and broaden the diffraction peak by different amounts depending on the dot product $|\bar{g} \bullet \bar{\delta}|$. Balogh and colleagues (2006) showed that the intensity of a diffraction peak, broadened by planar faults in a FCC metal, could be given as the sum of profiles from the different $\{111\}$ planar faults:

$$I_{hkl}^{PF}(g) = w_\delta I_{hkl}^\delta(g) + \sum_{j=1}^4 w_L^j I_{L,hkl}^j(g) \quad (2.72)$$

Where, $I_{hkl}^\delta(g)$ is a delta peak (very narrow) when for a (hkl) plane $|h+k+l|=3n$ is satisfied and w_δ is its weight. $I_{L,hkl}^j(g)$ and w_L^j are the corresponding values for those planar faults where the condition is not met. The shape of $I_{L,hkl}^j(g)$ was found to be given approximately by the Cauchy function (hence the index L), which has full-widths and positions that depend on the quantity and type (e.g. twin) of planar faults and the relation between the diffraction vector and the displacement caused by the planar fault. The shape and position of the Cauchy are given as fifth order polynomials, where the constants can be found in Balogh and colleagues (2006):

$$\begin{aligned} FWHM^{Lj}(hkl, \alpha) &= \sum a_n^{(j,hkl)} \alpha^n \\ shift^{Lj}(hkl, \alpha) &= \sum b_n^{(j,hkl)} \alpha^n \end{aligned} \quad (2.73)$$

The calculations of Balogh and colleagues (2006) showed that, twinning faults produced broadened peaks that are approximately symmetrical, whereas intrinsic and extrinsic stacking faults produced broadening that is not symmetric (Figure 2-30). They also showed that for a (111) planar fault in a given crystal, with a diffraction vector (hkl) normal to the reflecting plane, the diffraction peak will broaden and shift in proportion to the magnitude of the sum $h + k + l$.

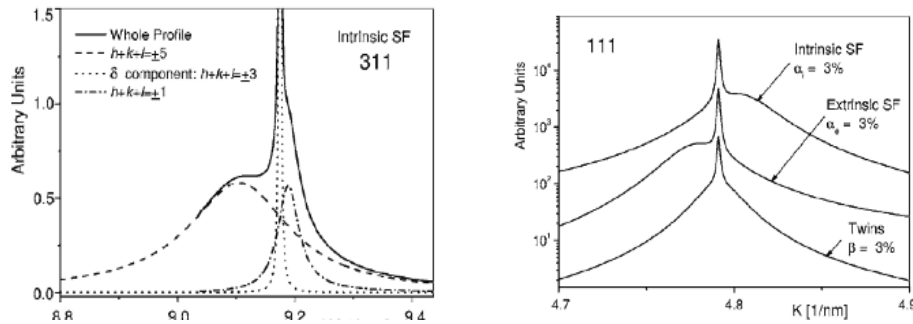


Figure 2-30. How the different planar faults contribute to broadening, Balogh and colleagues (2006), (a), left, intrinsic stacking faults for the 311 plane, and (b), right, the types of fault for the 111 plane.

The treatment of planar faults is similar to dislocations in that it is assumed that they are equally populated in all grains and on all planes. However, as with dislocations planar faults may not be equally populated, especially if they are formed by plastic deformation. Twinning is dealt with as a change in the order of planes, but the daughter twin may be different from the parent grain, with different intergranular strains and dislocation densities. These secondary effects may be larger if the size of the twin is large, as is often the case in HCP metals.

2.4.7 Variation in the intergranular strains

The broadening by defects has received a lot of attention, whereas that of strain broadening due to differences in the lattice spacing in different grains (2nd kind stresses or intergranular strains), but the same within a grain, is often ignored. This section will provide a brief review of this area and try to quantify how this type of strain changes the shape of peaks.

Generally, the broadening by variations in intergranular strains is only accounted for in situations where it is the only (or main) cause of broadening (Leineweber and Mittemeijer 2006). When other causes of broadening have a similar magnitude this type of broadening is more difficult to deal with. This is because broadening by intergranular strains has a very similar affect as broadening by micro-strain within a grain. If it is assumed that the strain distribution is Gaussian, then the integral breadths are given by the Stokes and Wilson equation (equation 2.16) and the Fourier coefficients by the following term (Kuzel 2007):

$$A^{D,2nd} = \exp\left(-2\pi^2 g^2 L^2 \langle \varepsilon_{hkl}^2 \rangle\right) \quad (2.74)$$

Where, $\langle \varepsilon_{hkl}^2 \rangle$ is the mean square strain (or the square of ε_{mss} in equation 2.16).

The overall strain term is then the product of the dislocation strain Fourier coefficient term and the above term.

However, the intergranular strain distribution may not necessarily be Gaussian, which would mean the equations would be incorrect. A possible indicator as to whether broadening is due to intergranular strains may be that there is no size

broadening, higher than expected values of M or $\frac{\ln A^D}{L^2}$ not being proportional to the log of L, which would all be expected for dislocation broadening.

The reason that it is often ignored is because the variation in the strain would have to be close to the magnitude of the actual strain in most metals for it to be observed. In metals that are highly anisotropic such as HCP metals, the variation in the intergranular strains may be large enough for this effect to be significant. Brown and colleagues (2005) suggest that twinning in HCP magnesium may play a significant role in peak broadening, due to the intergranular strain effects. They suggest that the strains in newly formed twins are lower than in those formed earlier. Their results show the broadening of those grains that have twinned only increases in the region where the twins are active, and that the stress-strain curves suggest little plastic deformation in the twin grains.

2.4.8 Defects of the first class

Krivoglaz (1996) distinguished different types of defects based on whether they would cause broadening of peaks into two groups, defects of the first and second class. Krivoglaz showed mathematically how the different types of defect would contribute to the broadening of a diffraction peak. He showed that defects of the first kind do not cause broadening. They include point defects, second phase particles and other defects whose strain field falls off with distance at a higher rate than r^{-2} . Defects of the first class cause reduction in intensity of the peaks and their shift. They are difficult to quantify since they do not broaden the peaks.

Although a method to do so was suggested by Ungar (2006), who used the ratio of background level and the integrated intensity of the peaks to describe their presence, in particular that of point defects.

Defects of the second-class cause broadening and the main defects in this class are dislocations and planar faults, i.e. stacking or twin faults. It is possible that defects of one class can become defects of the alternative category depending on how they are arranged. In general, though it is not expected by Krivoglaz that defects of the second class will be arranged appropriately in enough proportion that they need to be considered in the shape of the peaks in metals.

2.4.9 Instrumental Considerations

To remove the broadening caused by the instrument from the measured diffraction peaks it is necessary to measure the diffraction pattern from a sample that displays very little broadening of its own. It is normal to use either a LaB₆ or a silicon standard for this and the instrumental peak used for each measured peak is the one that is the closest (on a 2θ or k scale).

If one of the integral breadth methods is being used then either of the WH equations (equations 2.17) may be used to remove the instrumental broadening. However, both equations are only an approximation and therefore both will introduce errors. Alternatively, if the Cauchy and Gauss integral breadths are known, either by using the Voigt function or from converting a pseudo-Voigt function to a Voigt, then both equations can be used with more accuracy. In

theory, this approach should be more accurate in removing the instrumental broadening, however it does rely on accurate knowledge of the shape of the peaks and the assumption that the peaks are represented by these equations.

When using Fourier coefficients the instrumental broadening can be removed using the Stokes correction (Stokes 1944):

$$A^M(x) = A^P A^I \quad (2.75)$$

Where, the physically broadened Fourier coefficients (A^P) are found by dividing the Fourier coefficients of the measured profile (A^M) by the Fourier coefficients of the instrumental profile (A^I). Although the equation applies to the cosine Fourier coefficients, it can be used for both the cosine and sine coefficients if required. The method is very useful in removing instrumental broadening; however, it can on some occasions either fail completely or become unstable. This is especially the case if instrumental broadening is large in comparison to the physical broadening.

2.4.10 The Application of DPPA methods

DPPA methods have been applied to a variety of different metals, with different microstructures and having been subject to different types of deformation.

Various researchers have applied DPPA techniques to understand the development of deformation. Zehetbauer and colleagues (1999) used a Warren-Averbach method to the deformation of copper polycrystals and was able to conclude that the results from the different parameters found by the method were consistent with expectations. Various other have applied DPPA to deformed metals; the majority of researchers use the Warren-Averbach method. Most early measurements were made on high stacking fault energy cubic metals, such as copper and aluminium, and consequently there has been less research on other types of metal. Examples of the use of different metals include; Zirconium alloys (Sarkar et al. 2008, Kapoor et al. 2004), IF steel (Sarkar et al. 2009), austenitic stainless steel (Kesavan Nair and Vasudevan 1977), silver alloys (De and Sen Gupta 1970), titanium alloys (Dragomir et al. 2005, Glavicic and Semiatin 2006).

It is rare that the different DPPA techniques or different metals are compared. In most cases where it is, the approach used does not enable a detailed understanding of the usefulness of DPPA applied to understanding deformation. Balzar et al. (Balzar et al 2004) and Soleimanian and Aghdaee (Soleimanian and Aghdaee 2008) compared different DPPA methods and instruments, however they both only used one sample with minimal strain broadening.

In some cases different DPPA techniques are compared to introduce a new method. Examples of this include the work of Borbely and colleagues (Borbely and Groma 2001, Borbely et al. 2006), and van Berkum and colleagues (1994 and 1996) both compared the Warren-Averbach method to their own method and to different metals. These are more useful as they give practical examples of the comparison of two methods, which exhibit size and strain broadening. However, it is still not clear what are the benefits of each method mainly because of the limited examples they both present and any partiality they may possess. Different researchers have instead compared two different metals. The approach often taken is to use the method to gain an understanding about something that may otherwise be difficult to measure. An example of this is the work of Gubicza et al. (2006), who compared different metals and processing by equal channel angular pressing, which can be difficult to quantify by TEM because of the high dislocation density.

3 Materials and Method

3.1 Introduction

The overall aim of this thesis is to investigate the usefulness of the application of diffraction peak profile analysis (DPPA) in the study of the deformation of metals. In this chapter the methodology chosen to achieve this aim is provided.

The chapter is separated into four parts. In the first part, the particular alloys used and the reasons that they were chosen are provided. The scope of the thesis is the study of the deformed microstructure of metals, and in the next part the mechanical tests that were conducted to deform the metals is detailed. In the third part of this section, the details of the diffraction experiments that were performed on these metals are provided. The measurements from the diffraction experiments are the main focus of the thesis, and it is these measurements that are used to perform the DPPA methods, discussed in Chapters 6-8. In the final part of this chapter, details are provided of how hardness tests and microscopy measurements were taken, the results of which are given in Chapter 5.

3.2 Materials

There is a difficulty in assessing the usefulness of diffraction peak profile analysis (DPPA) methods, because the results these methods provide are in many cases not directly comparable by other measurement techniques (for example TEM or EBSD). In addition to this, there is an ambiguity in what the results of DPPA methods, actually mean. In order to address these issues a number of alloys have been studied. The alloys used were chosen because they had a relatively simple microstructure. All samples consist of a single phase, or a dominant phase for Ti-6Al-4V, with a relatively large grain size, $\sim 30\mu\text{m}$, and a near random texture. Different alloys were chosen because of the differences in the way they deform.

As discussed in Section 2.1.6, the stacking fault energy (SFE) of a metal has a large influence on the deformed microstructure. DPPA methods provide information about the deformed microstructure, so the results of DPPA methods should be different for metals with different SFE. To investigate this a commercially pure nickel alloy, Ni-200, and two stainless steel alloys, SS-304 and SS-316, were chosen (with composition give in Table 3-1). These alloys were chosen for their differences in SFE (see Table 3.2), but also because of their similarities in other regards. They all have a face-centred-cubic (FCC) crystal structure, a similar grain size, they all work-harden and have similar elastic constants (Ledbetter 1984). Two different types of stainless steel were used because they are expected to have similar deformation microstructures (Section 2.1), and this similarity is used to help evaluate the methods.

Two titanium alloys are also investigated to investigate the influence of a HCP crystal structure on the results of the DPPA methods, and the difference between an alloy that is expected to twin and one that doesn't. There are two ways in which a HCP crystal structure can influence the results of DPPA methods. Firstly, different equations are used for HCP metals in DPPA methods and secondly these metals deform in a different manner to FCC metals because of their crystal structure (as discussed in section 2.4.5). The two titanium alloys are Ti-6Al-4V, a two-phase alloy which consists of a majority HCP phase, and a commercially pure titanium alloy Ti-CP, which has a single phase HCP structure (the composition of these alloys is shown in Table 3.1).

The alloys were all annealed to produce grains with minimal residual stresses (between different grains and within grains) and contained minimal defects, such as dislocations. The two titanium alloys were supplied in annealed conditions and not further heat-treated. The stainless steel and nickel alloys were annealed by heating to 1050°C and held in an inert argon atmosphere for 2 hours and then air-cooled. The Ti-6Al-4V, Ti-CP, SS-316 and nickel alloys were supplied as bars and the SS-304 was a sheet. The details of the starting microstructure are provided in Section 5.1, from optical microscopy and EBSD.

An additional reason for the choice of these metals is that their deformation microstructure has been well researched. The focus of the thesis is on application of different DPPA methods, to the data provided by diffraction experiments, rather than other techniques. To assess these results the research that has been done on these, and similar, alloys is used. This may not be ideal because there will be differences in composition, microstructure and deformation conditions between the samples used in this study and those used by others. However, in order to gain useful qualitative and in particular quantitative information about the deformation microstructure of a sample requires considerable effort. TEM is the main method that can be used to provide this information and to use this technique would require the study of many samples and different grains, across different strains for each of the samples studied. In general, it is found that numerous researchers find the same features of the deformation microstructure for the different metals (Section 5.1.2).

Table 3-1. Composition of the different metals studied.

SS-304H
18.2 Cr, 8.6 Ni, 0.45 Si, 1.4 Mn, 0.05 C, 0.005 S, 0.038 N, Fe Bal.
SS-316
18.1 Cr, 12.2 Ni, 3.0 Mo, Fe Bal.
Ni-200
0.2 Cu, 0.2 Fe, 0.2 Mn, 0.1 C, 0.2 Si, Ni Bal.
Ti-CP Grade 2
N 0.03, C 0.1, H 0.015, Fe 0.3, O 0.25, Ti Bal.
Ti-6Al-4V
6.0 Al, 4.0 V, 0.2 Fe, 0.1 O, Ti Bal.

Table 3-2. The stacking fault energy (γ_{SFE}) of the metals used in this report and selective other alloys.

Metal/Alloy	γ_{SFE} (mJm ⁻²)	Reference
SS-304	21	Murr 1975, Hadji and Badji 2002
SS-316	42	Hadji and Badji 2002
Nickel	128	Murr 1975
Titanium	15	Conrad 1981
Aluminium	166	Murr 1975
Zirconium	240	Murr 1975

3.3 Mechanical Tests

The different alloys detailed in Section 3.2, were all deformed by either uni-axial compression or tension to a range of applied strains at room temperature, the results of which are shown in Chapter 6, 7 and 8. The tests were carried out using Instron 5569, for the tensile tests, and Instron 5885H, for the compression tests. The tests were conducted with a constant cross-head speed. The initial strain rate was 0.1mm/min for SS-304, 2mm/min for SS-316 and Ni-200, 1mm/min for the titanium alloys.

The nickel-200 and SS-316 alloys were deformed by uni-axial compression. The compression samples were cylinders with diameter of 20mm and length 20mm. A graphite-based lubricant was used to minimise frictional effects. The SS-304, Ti-6Al-4V and Ti-CP samples were deformed by uni-axial tension. The SS-304 had a gauge diameter of 6mm and parallel length of 35mm, and the titanium alloys, a gauge diameter of 8mm and a parallel length of 48mm.

Nickel-200 and SS-304 samples were deformed by rolling at room temperature, the results of which are in Chapter 8. For nickel-200, a nickel bar with a diameter of 20mm was used and was rolled to an engineering strain of 30%, by 8 steps, along its length. The dimensions of the rolled sample were not ideal because the

small width of the sample relative to height (the same before the 1st pass) meant that the change in dimension of the width was significant. The SS-304 alloy was rolled from a sheet of 8cm to an engineering strain of 25% by steps of approximately 2mm.

3.4 Diffraction Measurements

In this section the details of the experiments undertaken and why the particular approach was taken will be discussed. These experiments are used to provide the main results of this thesis. In the first part of this section, an overview is provided as to why the different diffraction sources were used, and the differences between them. The second part of the section details the experimental procedures used for the different diffraction sources.

3.4.1 Overview- Diffraction Measurements

Measurements were taken using three different types of diffraction sources: laboratory x-ray, synchrotron x-ray and neutrons. The laboratory x-rays were used to measure FCC samples of nickel and stainless steel alloys at different applied strains, the results of which are presented in Chapters 6 and 7. The neutron diffraction source was used to measure diffraction patterns in different texture components, which are presented in Chapter 8. The results of the neutron diffraction experiment are also used in Chapter 6, to investigate the influence of the diffraction source on DPPA results, by comparing the results with those found from the lab x-ray source. The synchrotron x-ray diffraction source was used to measure the two different titanium alloys at different applied strain in two measurement directions, the results of which are used for Chapters 6, 7 and 8.

The titanium samples were measured using the synchrotron x-ray diffraction source at the ID-31 beamline at the ESRF in Grenoble, France. The reason that this was chosen was because it has one of the highest resolution and minimum instrumental broadening of possible diffraction sources. Ideally both titanium and FCC metals would have been measured by this source. However, a lack of beam

time at ID31 meant this was not possible. This does add an uncertainty when comparing the FCC and titanium results as the differences may be in part due to the different instrument used. Instead, two sources were used for the FCC samples. For the results of Chapter 6 and 7, a Philips X-pert x-ray diffractometer with Co-K α radiation in Bragg-Brentano geometry, was used, because of its convenience and because it is the most common source available for most researchers. In Chapter 8, we consider how the broadening of peaks and their shapes change in different texture components. These measurements could not be performed accurately, or easily by the laboratory x-ray diffractometer. Instead the measurements were taken using neutron diffraction at the High Resolution Powder Diffraction (HRPD) source at ISIS, Oxfordshire. HRPD was used because it made it possible to measure many diffraction patterns for different texture components in a short time, with large samples so that many grains could be sampled and at a high resolution. It was not possible to measure the titanium samples at HRPD because the scattered intensity was too low and the peak shape could not be measured with enough accuracy. Instead, the ID31 synchrotron x-ray results are used in Chapter 8. The consequence of this is that the approach taken for FCC and titanium samples in Chapter 8 is slightly different.

A comparison of the instrumental broadening from these sources is shown in

Figure 3-1. Synchrotron diffraction at ID31, gives very low instrumental broadening, high resolution and a high flux, allowing diffraction patterns to be measured quickly. The experimental set-up was chosen to maximize the quality of these peaks. However, a consequence of this is the small sample size, which could mean that additional deformation may be introduced when the samples are made (by for example cutting or grinding the samples) or the sample may not be characteristic of the bulk. Neutron diffraction does not have this problem, as the sample size is much larger. The volume of sample that is being measured is different for the three sources. The lab x-ray source has the smallest volume at around 0.02mm³. The synchrotron x-ray samples have a larger volume of around 15mm³. The neutron samples have the largest volume at around 1 000mm³.

The acquisition time with neutron diffraction is of a similar order to the synchrotron measurements, and so is the range of k values (or the possible amount of peaks that can be measured for a given sample). However, even though HRPD is one of the highest resolution neutron sources in the world, the quality of the peaks are much lower than for synchrotron. For example the instrumental broadening is approximately five times higher. Laboratory X-rays have similar instrumental broadening to neutrons but can have a higher resolution. For example a step size of half the resolution of HRPD was used for the lab x-rays. However, lab x-rays also had the disadvantage of much slower acquisition times and a much smaller diffracting volume.

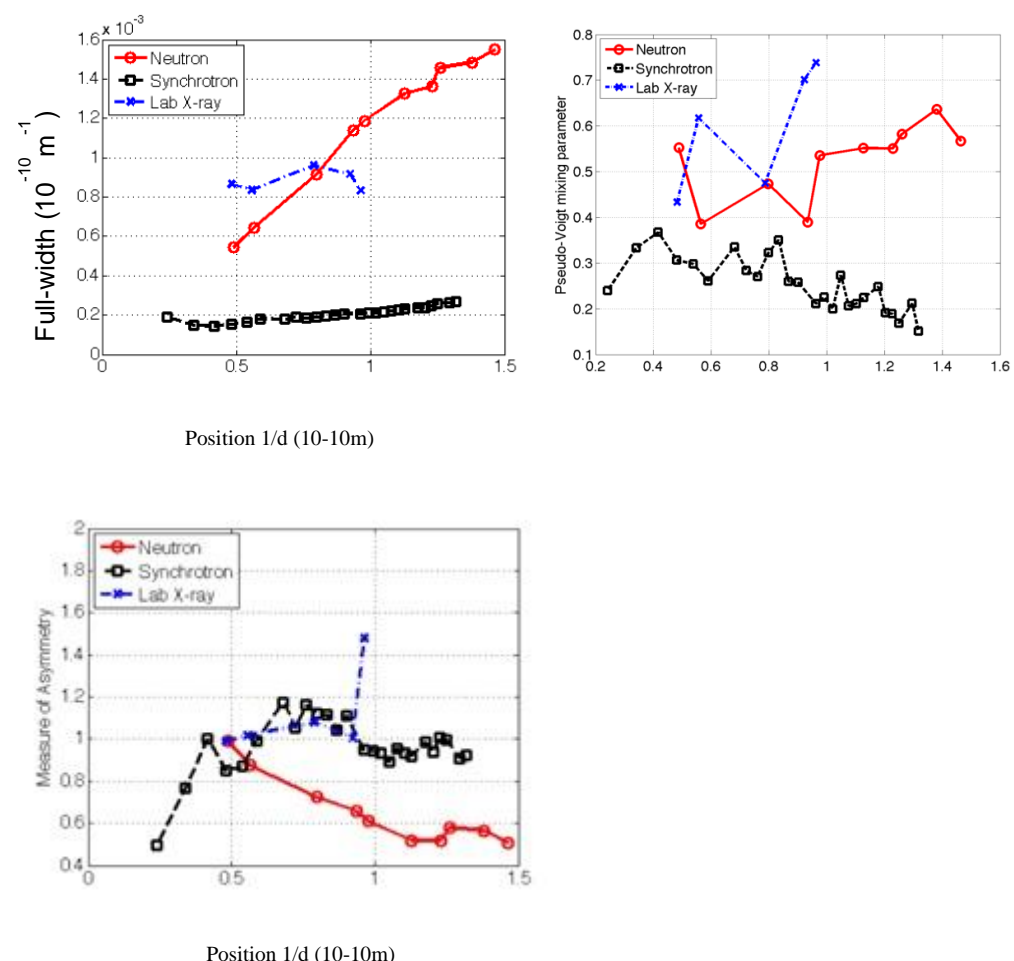


Figure 3-1. Differences in the instrumental broadening of the three different diffraction sources. The results of the fit to the instrumental diffraction pattern are shown. The asymmetry component is the full-width of the right-hand-side divided by the full-width of the left. Values of full-width and k are in units of Å. These values are found by fitting the instrumental sample using a pseudo-Voigt curve.

3.4.2 Laboratory X-ray, Materials Science Centre

In this section details of the experimental set-up taken when using the laboratory x-ray are provided.

Materials Preparation

The metals used were stainless steel 304, stainless steel 316 and nickel-200. Details of these metals are provided in Section 3.2. They were deformed by uniaxial tension and compression (Section 3.3) and then cut to be measured by laboratory X-rays. Flat square samples with length of approximately 15mm and around 5mm in depth were prepared from the SS-316 and Ni bars and slightly smaller samples, 6mm², for SS-304. They were cut so that the measured plane was from the centre of the gauge volume, to best avoid deformation gradients. For the SS-316 and Ni samples the plane normal was parallel to the tensile direction, the axial direction, whereas for the SS-304 samples the plane normal was perpendicular to the tensile direction, transverse. The reason for this difference was due to the smaller size of the SS-304 samples. Samples were prepared by cutting, grinding using 400, 600 and 1200 SiC-paper, polished by diamond paste on a woven polishing cloth and finally polished with OPS. No difference was noticed between this method and by electropolishing, in terms of full-width, so any additional plastic deformation from the cutting or grinding is expected to be minimal.

Experimental X-ray Set-up

X-ray diffraction from a Philips X-pert x-ray diffractometer with Co-K α radiation in Bragg-Brentano geometry was used. The cobalt tube was chosen instead of copper because it did not cause fluorescence in steel samples. The particular diffractometer was chosen because it had the lowest instrumental broadening and allowed the most peaks to be measured.

The diffracting volume is approximately 0.05mm in the plane of the instrument (the plane that the sample moves with 2 θ), and 10mm perpendicular to this (Langford and Louer 1996). The penetration depth of lab x-rays, is approximately 132

of $20 \times 10^{-6} \mu\text{m}$ (from Withers and Bhadeshia 2001). Hence, the diffracting volume is around 0.02 mm^3 .

The diffractometer was set-up to scan between angles of 40° and 130° in 2θ and take measurements at distinct values. The time of a measurement was set at 20 seconds and the step size was set at two values of 2θ of 0.5° ($k = 0.005 \text{ \AA}$) and 0.015° ($k = 1.7 \times 10^{-4} \text{ \AA}$). The smaller step time being around the FCC diffraction peaks, with a range approximately $\pm 5^\circ$ in 2θ ($k = 0.05 \text{ \AA}$) from the peak centre. This set-up was chosen as it provides the best compromise between the quality of the data and time, and takes approximately 24 hours for one complete diffraction pattern. The diffractometer allowed five FCC peaks to be measured 111, 200, 220, 311 and 222 (Figure 3-2a). A close up of the 311 peak for a SS304 sample is shown in Figure 3-2b. The peak consists of two components, α_1 and α_2 , but there is also an additional much smaller peak on the low 2θ (or low K) side of the peak. The lower intensity peak may have the effect of making peaks more Cauchy in shape, because of how it changes the tail of the higher intensity peak.

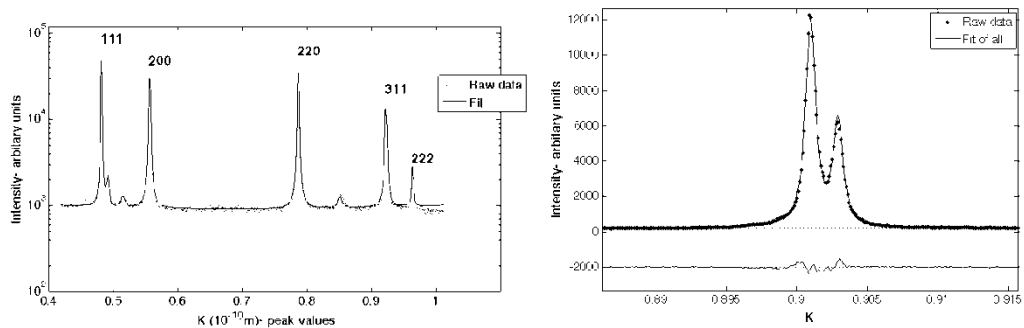


Figure 3-2. (a), left, Example x-ray diffraction pattern and the fit of the data for SS304 specimen with grain size $100 \mu\text{m}$, 18% strain, (b), silicon standard instrumental profile showing the α_1 and α_2 components and the pseudo-Voigt fit.

3.4.3 Synchrotron X-ray, ID31 ESRF

In this experiment two different titanium alloys were tested, Ti-6Al-4V and commercially pure titanium grade 2 (Ti-CP), see section 3.2. Square rods of 0.8 mm wide and 30mm long were prepared parallel to the tensile axis. These rods were cut from the centre of the gauge volume, then ground down using 400, 600

and 1200 SiC-paper. They were finally prepared by wet etching with hydrochloric acid, hydrofluoric acid, nitric acid, water solution in ratios 30:10:10:50. This was used to remove approximately 0.1mm from each side. These steps were taken to minimise any deformation that may be introduced by making the rods. The rods were placed in glass capillaries for use with the ID31 beamline.

Experimental x-ray set-up

Synchrotron diffraction measurements were obtained from the ID31 beamline at ESRF, Grenoble, France. This beamline was chosen because it is primarily designed to be a high-resolution powder diffractometer. The experimental set-up is shown in Figure 3-3. The beam energy used was 31.1keV and this gave a wavelength of 0.39827 Å. All 8 available detectors were used. The beam size was set to be slightly larger than the sample in both direction, and the sample was moved to obtain the maximum diffracted intensity. The values of 2θ was scanned between 0° ($k=0$) and 38° ($k=1.63\text{Å}$), with steps of 0.003° in 2θ ($k=1.3 \times 10^{-5}\text{Å}$). This allowed the assessment of the first 27 hexagonal peaks for titanium, although more reflections could have been fitted. These were chosen because of the reduced accuracy and greater overlapping of the later peaks. A LaB₆ instrumental sample with dimensions similar to the titanium samples was also measured but with a lower step size of 0.001° in 2θ . The diffraction pattern and example diffraction peak are shown in Figure 3-4.

The same samples were used to acquire diffraction patterns for the two different directions, axial and transverse. The transverse direction is when the diffraction vector is perpendicular to the tensile direction and the axial direction is when they are parallel. For the axial samples the samples were placed vertical and moved up and down so that more peaks could be included in the diffraction pattern. For the transverse direction the samples were placed horizontal and both rotated and moved parallel to their length.

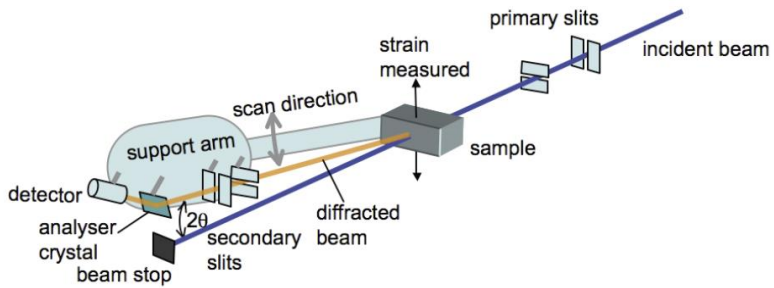


Figure 3-3. The experimental set-up at ID-31 (Frankel 2008).

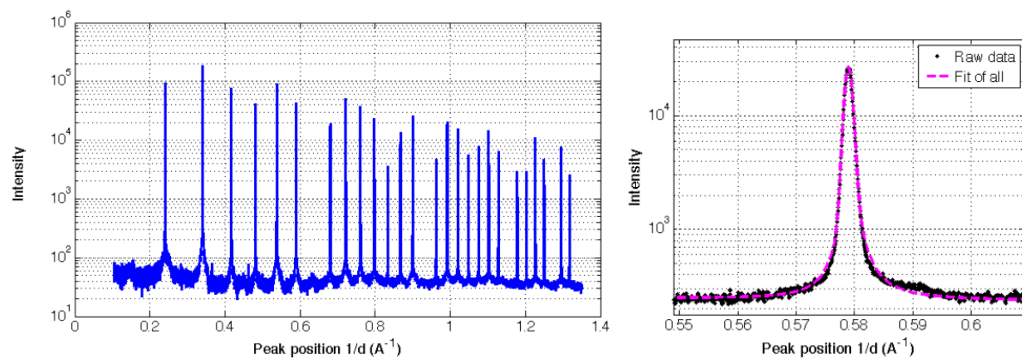


Figure 3-4. Diffraction patterns produced at ID31, ESRF. (a), left, (b), LaB6 standard instrumental profile and the pseudo-Voigt fit of one of the peaks.

3.4.4 Neutron diffraction, HRPD ISIS

The metals used in this experiment were SS-316 and Ni-200. The samples are the same FCC compression samples use for the lab x-ray measurements.

Measurements were also made on rolled nickel.

Square samples with sides of ~10mm were machined from the centre of the gauge volume and ground using 120, 400, 600 and 1200 SiC-paper. The square samples were cut so that the plane normal were either parallel or perpendicular to the tensile direction, for the compression samples. Alternatively, they were cut so the plane normal were parallel to either the rolling, normal or transverse directions for the rolled samples.

Neutron diffraction measurements were obtained using time-of-flight diffraction from the high-resolution powder diffractometer (HRPD) at ISIS, Chilton, Didcot,

UK. This allowed many grains to be measured quickly at a high resolution ($\delta d/d \sim 4 \times 10^{-4}$) compared to other neutron sources (Ibberson et al. 1992).

The beam size was set to be slightly larger than the sample in both directions. The diffracted beam is detected at two different fixed angle banks, a backscattered detector, and two side detectors (see Figure 3-5). The backscattered detector consists of eight octants of ZnS scintillator, which are separated into 60 radial strips and a range in 2θ values between 160 and 176°. Only two of these octants were used. The two side detectors have a lower resolution, and hence larger instrumental broadening. The side detector consists of 396 elements at a constant radius from the sample. The range in 2θ values for the side detectors is between 87 and 93°. The measurements from the different elements were combined to provide four diffraction patterns, two backscattered patterns (1 and 2 in Figure 3-5) and two from the two side detectors. The data from the side detectors is not used for the diffraction peak profile analysis results because of their lower resolution, but were used to confirm the results from the backscattered detectors.

The data was converted between time of flight (L) and d-spacing (d), is found using the following formula (Ibberson et al. 1992).

$$d_{hkl} = \frac{t_{hkl}}{505.55685 L \sin \theta_0} \quad (3.1)$$

Where, L is the flight path to the detector (in metres), t the time of flight of the neutrons (in seconds), θ_0 the Bragg angle (in radians) and d the d-spacing in Å.

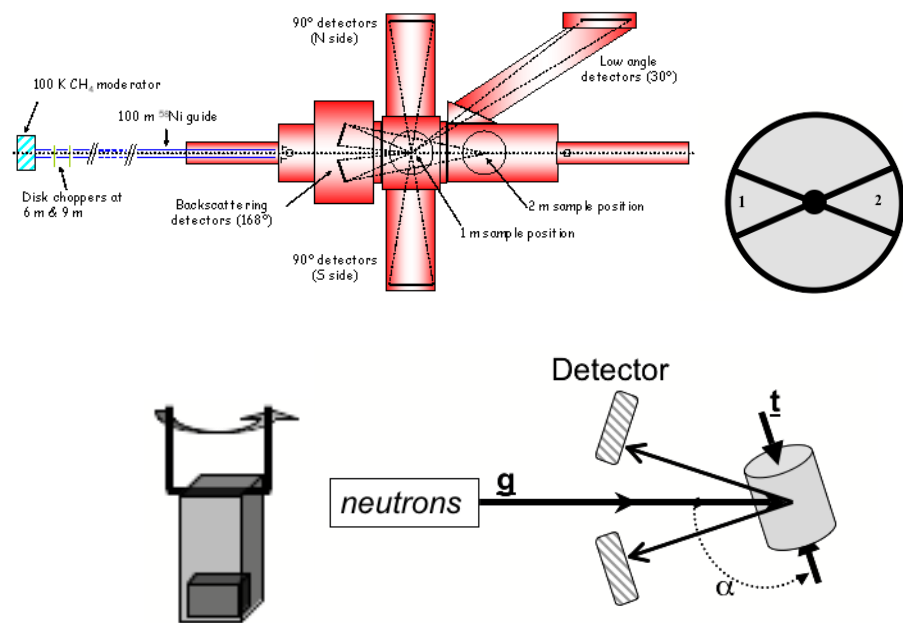


Figure 3-5. THE Schematic of HRPD set-up (left-top) (Ibberson et al. 1992), and the backscattered detector (middle-top). 2θ varies from 176° at the centre of the detector to 160° at the edge (in the left-right direction) and varies between a maximum of approximately $\pm 8^\circ$ in the up-down direction at the edges. Samples were placed in vanadium holders and rotated (right-top). The sample is rotated so that the angle between the tensile direction and the diffraction vector, α , varies between 0 and 90 degrees (bottom).

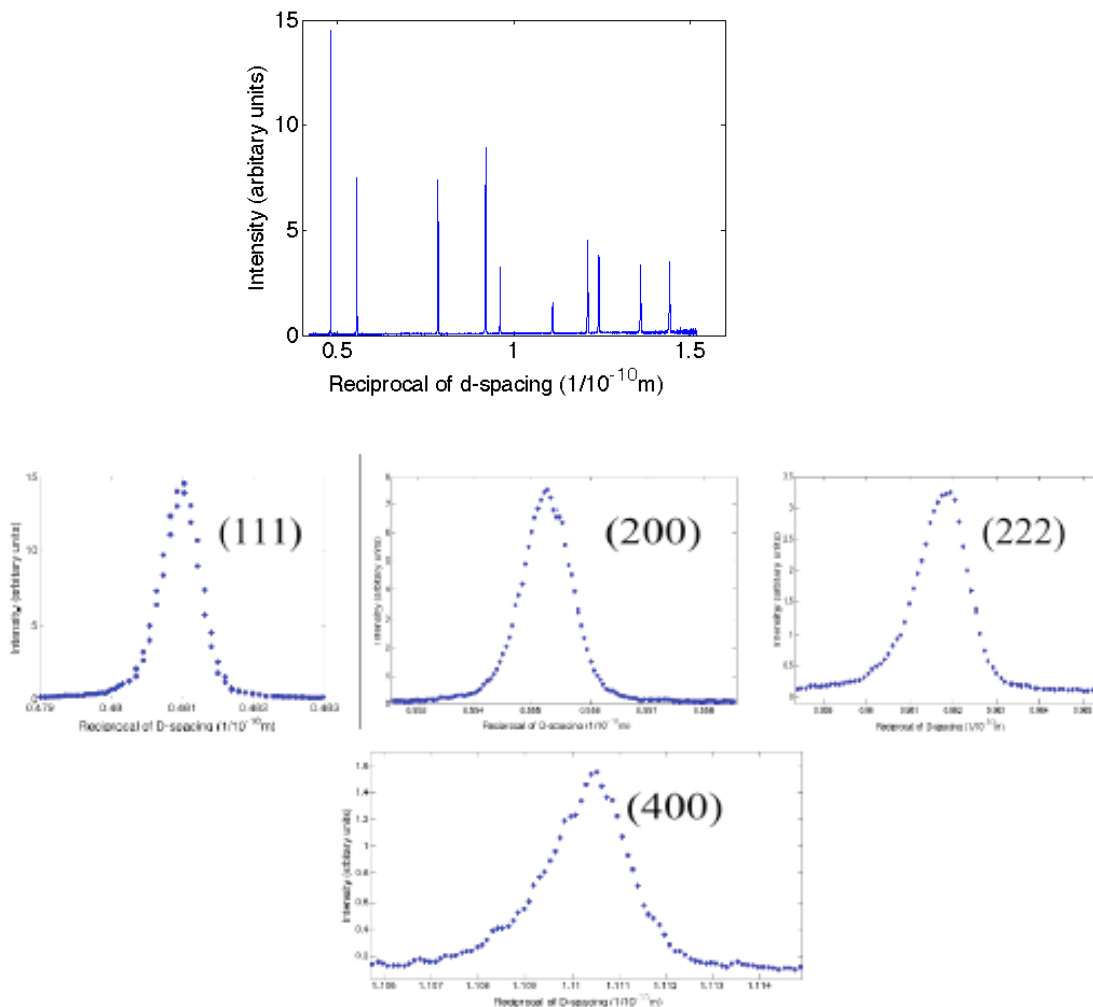


Figure 3-6. Typical diffraction pattern using HRPD. For SS-316 compressed to 2%, measured at $\alpha=50^\circ$ and a beam current of $24\mu\text{m}$, the peaks shown are {111}, {200}, {222}, {400}.

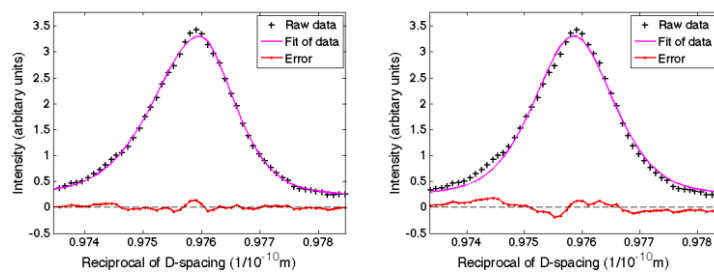


Figure 3-7. Example of the fits used for Ni compressed to 10%. The {222} peak fit using a split (left) and regular pseudo-Voigt (right).

The samples were placed in a vanadium holder, which was then placed in the beam. The samples were rotated about an axis perpendicular to the beam direction, on the same plane as the two side detectors and the two backscattered detectors octants used. The samples were placed such that the angle, α , between the tensile, or the rolling direction for rolled samples, was parallel to the beam (or the diffraction vector \mathbf{g}) for the first measurements. They were then rotated to distinct values of α and a set of diffraction patterns for each detector was obtained. For most samples, measurements were taken at steps of 10° and each measurement took approximately 20 minutes. Different integrated beam currents were investigated and it was found that above the value of $12\mu\text{A}$ (taking approximately 20 minutes), used for most samples, the increase in the quality of diffraction pattern was small relative to the increase in time. An alternative post processing of the data was attempted in which the two backscattered octants were divided into two, one near the centre and one on the outside. However, the quality of the peaks was lower and consequently this data was not used.

The use of a vanadium holder had the problem that it was not possible to know if the sample was rotating exactly in the centre of the beam or if the non-spherical shape of the sample had an influence. However, any systematic errors caused by this would be expected to be gradual and change all peaks. It was thought that any systematic errors were small because the $\{311\}$ full-width were for most samples almost constant and the same trends could be observed in all four detectors.

A typical diffraction pattern is shown in Figure 3-6. The peaks were asymmetric (as expected for time-of-flight data) and the quality of the fit was less than for other methods (Figure 3-7). There were, however, cases where the peak appeared to consist of the sum of two peaks, one with a large and one with a smaller full-width. The changes that we were looking for were of a similar magnitude to the errors in the fit of the peaks. This was particularly the case for the shape of the peaks, given by the mixing parameter. To account for this, the data from the two backscattered detectors was averaged and only the results of the first 6 diffraction peaks are used; $\{111\}$, $\{200\}$, $\{220\}$, $\{311\}$, $\{222\}$ and $\{400\}$.

3.5 Microscopy

The different alloys were characterised by optical microscopy and EBSD (results of which are provided in Section 5.1). To prepare the samples for these microscopy measurements, samples were cut from the un-deformed material and from the centre of the gauge volume of the tensile and compression samples. They were then wet ground with SiC paper, first with 800 and then with 1200 paper. This was followed by diamond polishing with $6\mu\text{m}$, $1\mu\text{m}$ and $\frac{1}{4}\mu\text{m}$ polishing paste and finally polished with OPS. The two titanium alloys were etched with Krolls reagent (Distilled water 92%, Nitric acid 6%, Hydrofluoric acid 2%), to reveal the microstructure.

EBSD measurements were taken using a CamScan 2040S Scanning Electron Microscope. The EBSD data was acquired and processed using HKL Channel 5 software packages, and VMAP software kindly provided by Professor Humphreys.

3.6 Hardness Tests

A Vickers micro-hardness testing machine was used to determine the hardness of the surface of the different alloys. The samples were prepared in the same way as the optical microscopy and EBSD samples (Section 3.5), but without the use of OPS or etchants. The results for a particular sample are the average of approximately 10 different measurements taken at different points on the surface of samples cut from the centre of the sample. A force of 0.5kg was used for all samples at all strains.

4 Results Overview

The overall aim of this thesis is to analyse the usefulness of Diffraction Peak Profile Analysis (DDPA) as a technique to understand the deformed state of a metal. To achieve this aim four different metals were chosen- nickel 200, stainless steel 304 and 316 (SS-304 and SS-316), and the titanium alloys Ti-6Al-4V and Ti-CP- (details of these metals are given in section 3.2).

These metals were then deformed by uni-axial tension and compression and by rolling (see Section 3.3). The deformed metals were measured using different diffraction sources (Section 3.4); these measurements provide the main results for the following results chapters. The measurements are then analysed by the different DPPA methods to determine the usefulness of DPPA as a tool to understand deformation.

In Chapter 5, the microstructure and mechanical properties of the metals are detailed. The microstructure of the metals is found from optical microscopy and EBSD measurements (Section 5.1). The mechanical properties of the metals are shown from the stress-strain curves and hardness measurements (see Section 5.2 and 5.3).

In the remaining results sections, diffraction peak profile analysis methods are applied to the measurements obtained from the diffraction experiments.

In Chapter 6, the main aim is to introduce the different DPPA methods that are used, how they work and how they are implemented. In this chapter, I also quantify the errors associated in their use, and provide recommendations on best practice.

In Chapter 7, the aim is to understand whether the values obtained from DPPA methods, such as crystal size or dislocation density, represent the samples being studied. This is done by comparing the DPPA results of the metals, with measurements on similar metals. The results of which were found by using different experimental techniques (e.g. TEM). In this chapter I will also show how systematic errors can be introduced.

In the final results, Chapter 8, polycrystal plasticity models are used in combination with DPPA methods. The reason for this approach–

- 1) it allows a better understanding of DPPA methods and the parameters obtained and
- 2) it helps understand how errors can be introduced.

In addition, I believe that the approach taken in this chapter could prove to be a valuable method that could be used to validate polycrystal plasticity models. The main advantage being that it allows modelling of microstructural details of bulk specimens, in a way that is not possible by other methods or approaches.

5 Microscopy and Mechanical Properties

This chapter provides results that are found by methods other than diffraction peak profile analysis (DPPA). It is divided into two parts –

Firstly, in 5.1 details of the microstructure, from microscopy measurements, of the starting and deformed alloys are shown and

Secondly, in 5.2 and 5.3 the mechanical properties of the alloys are detailed – from the stress-strain curves and micro-hardness tests.

Details of the alloys are provided in Section 3.2, and details of how the uni-axial tension and compression tests and hardness tests were conducted, are in Section 3.3 and Section 3.6.

5.1 *Microscopy*

Optical microscopy and EBSD measurements were made on the un-deformed and deformed alloys. Details of the sample preparation and how the EBSD measurements were made are provided in Section 3.5.

5.1.1 Starting Microstructure

The microstructure of the FCC samples are shown in Figure 5-1 for nickel, in Figure 5-2 for stainless steel 304, and in Figure 5-4 for stainless steel 316. The metals are all single phase FCC before they are deformed. The stainless steel samples have an additional martensite phase after deformation, which increases with applied strain. At a true strain of 0.2 the intensity of martensite diffractions peaks are less than 4% the size of austenite peaks. The grain size of the FCC samples are approximately 30 μm .

The un-deformed microstructure of the commercially pure titanium (Ti-CP) metal is shown in Figure 5-4. The crystal structure is a single phase HCP structure, with a crystal size of approximately 30 μm .

The Ti-6Al-4V starting microstructure is more complicated than the other metals (Figure 5-5). It consists of a majority α hexagonal phase and a cubic β phase of less than 10% (Lutjering and Williams 2007). The α phase is separated into a primary and secondary phases. The primary α phase has acicular grains of approximately 15 μm , whereas, the secondary phase are needles of around 1 μm thickness. The secondary α and β phase are situated around the secondary α grain boundaries.

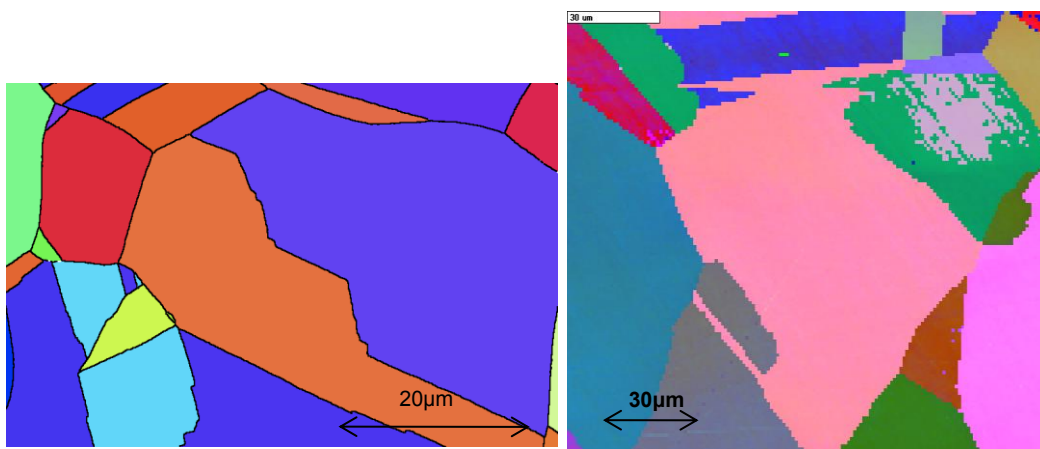


Figure 5-1. EBSD map of nickel samples. Left, at 0% strain showing IPF colouring using Channel 5 the lines represent boundaries more than 15°. Right, at 2% strain showing Euler colours using VMAP.

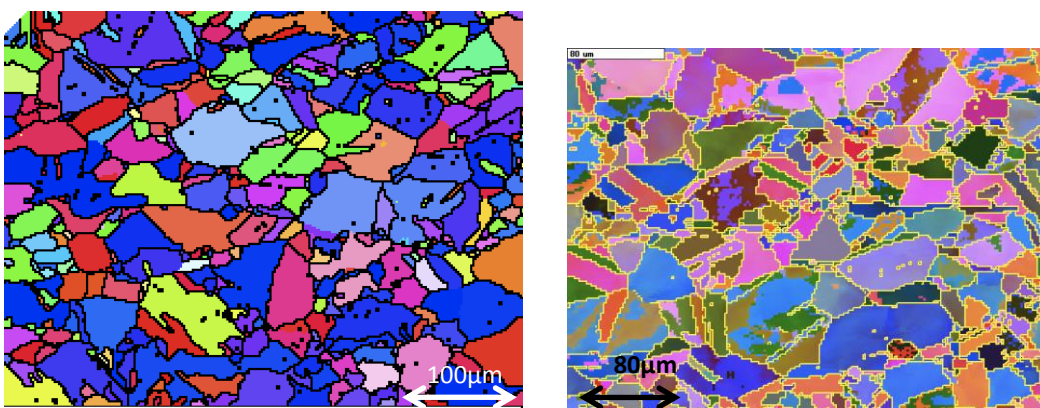


Figure 5-2. EBSD maps of SS-304. Left, IPF map at 0% strain, using Channel 5 showing boundaries at 15°. Right, sample at 2% showing a Euler colour map using VMAP, with boundaries at 5°.

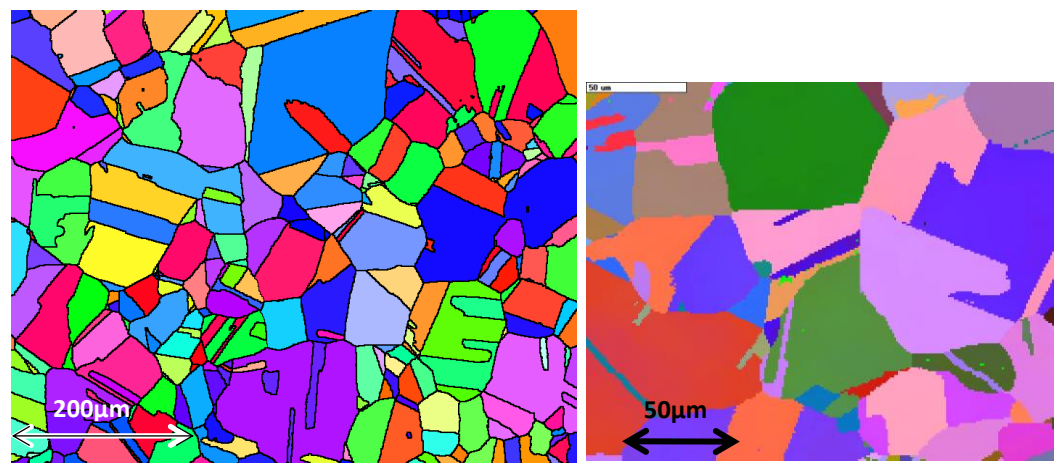


Figure 5-3. EBSD maps of SS-316. Left, IPF colour maps using Channel 5, at 0% strain, lines show boundaries at 15°. Right, Euler colour map using VMPA 0.5% strain.

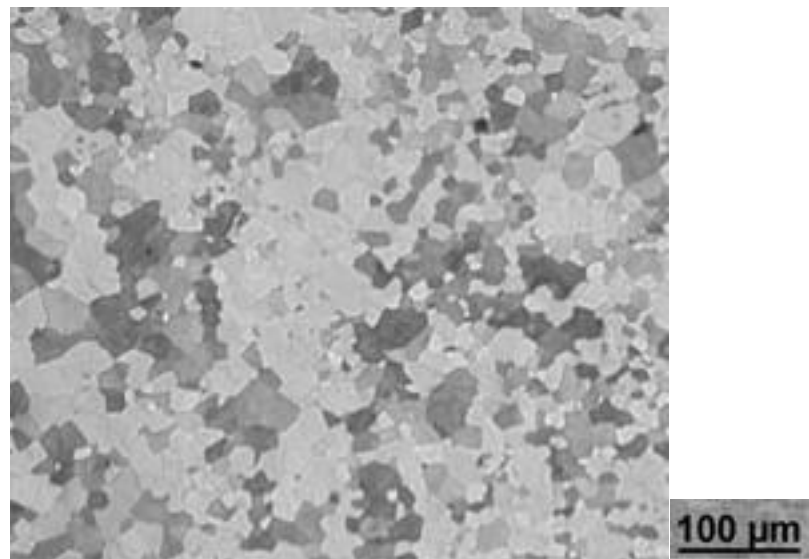


Figure 5-4. Optical microscope image of un-deformed Ti-CP sample.

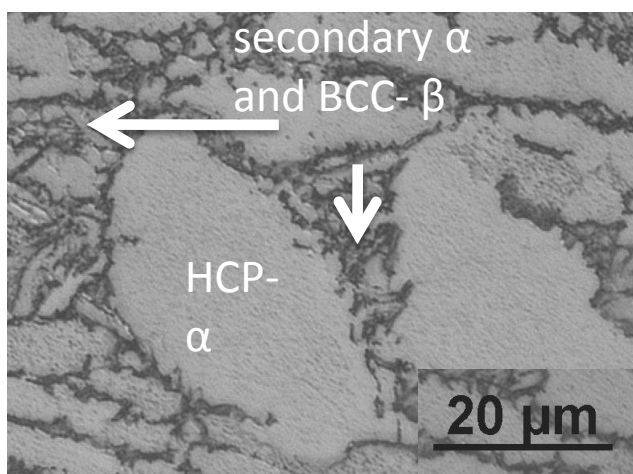
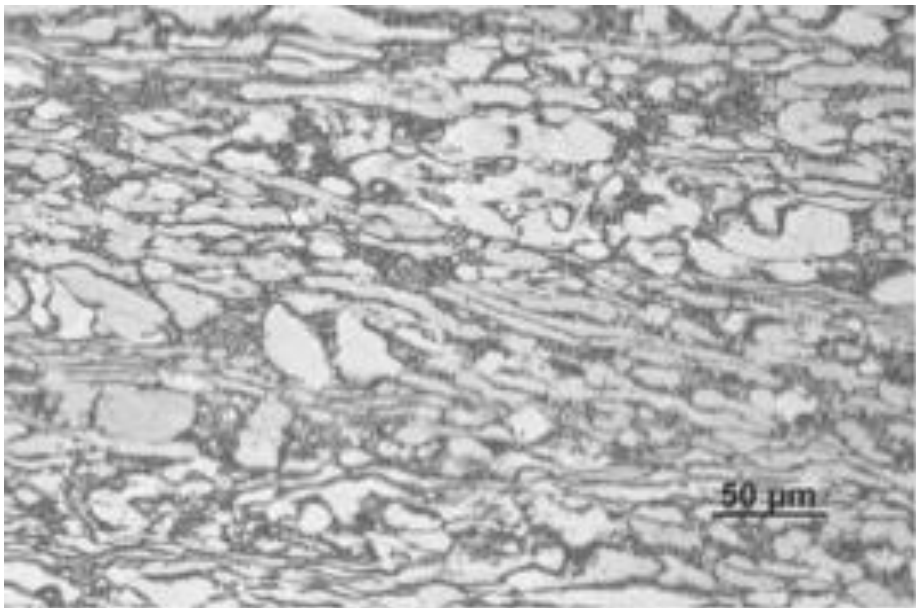


Figure 5-5. Optical microscope image of un-deformed Ti-6Al-4V sample.

5.1.2 Deformed Microstructure

The deformed microstructure of the FCC alloys has been studied by EBSD. Each point on an EBSD map shows the orientation of that point (Humphreys 2001). The maps can be used to show the presence of twins (Jorge-Badiola et al. 2009, Battaini 2007) and dislocation cell structures (Humphreys and Bate 2006).

EBSD maps of the stainless steel alloy, SS-316, are shown in Figure 5-6 and Figure 5-7. In these figures, twins can be observed in some of the grains. The twins are identified based on the misorientation across the boundary between the twin and the surrounding grain. These are likely to be deformation twins, as

opposed to annealing twins, because of their long and thin needle-like shape (Byun et al. 2003, Lee and Lin 2001). As shown in Figure 5-7, the deformed grains have a spread in misorientation, and do not show a break-up of the grains by recovery, and the formation of a dislocation cell structure with small angle grain boundaries.

An EBSD map of deformed nickel-200 is shown in Figure 5-8. The deformed nickel does not display any small twins, as was found for the stainless steel samples. Unlike the stainless steel samples, the samples display a dislocation structure. The grains (bounded by high angle grain boundaries) are broken up into smaller crystals separated by small angle boundaries.

The EBSD maps, and the deformed microstructure shown in this section, are consistent with other research (Section B.1) that has been carried out on deformed stainless steel (Byun et al. 2003, Lee and Lin 2001) and nickel (Keller et al. 2010, Hansen & Ralph 1982 and Feaugas and Haddou 2007).

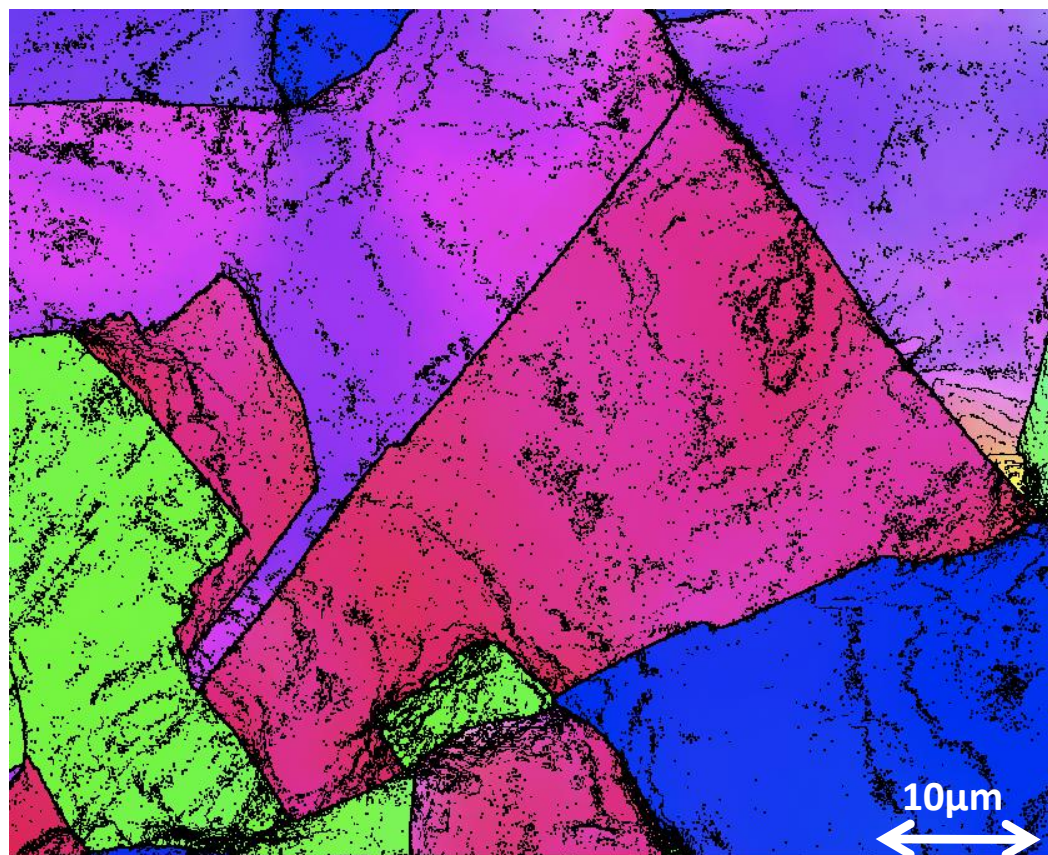


Figure 5-6. EBSD map of SS-316 at 10%. The map shows IPF colour using Channel 5, thick lines show misorientations more than 15° and thinner lines at 0.5° . The step size used was $0.07\mu\text{m}$.



Figure 5-7. EBSD maps of SS-316 at 10% applied strain. Maps show Euler colour using VMAP. Deformations twins are highlighted.

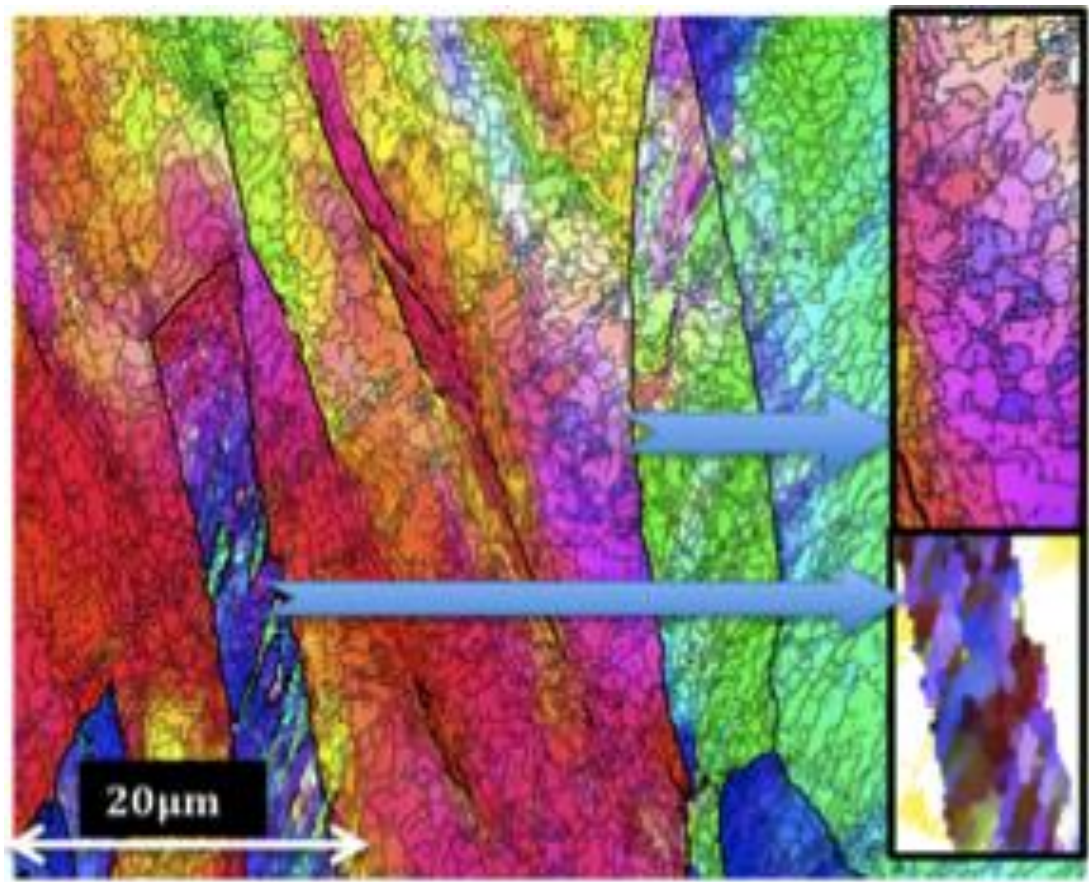


Figure 5-8. EBSD map Ni-200 at 10%. The main map (and map top right) shows IPF colour using Channel 5, thick lines show misorientations more than 15° and thinner lines at 1.5° . The step size used was $0.1\mu\text{m}$. Map bottom right shows relative Euler colours using VMAP.

5.2 Stress-Strain Curves

All alloys were deformed by uni-axial compression (SS-316 and nickel-200) or uni-axial tension (SS-304, Ti-6Al-4V, Ti-CP). Details of these measurements are provided in Section 3.3.

Stress-strain curves tests provide information about the mechanical properties of a metal. Stress-strain curves can be used to provide a variety of different information about a sample, including: the dislocation density (Mecking and Kocks 1981, Conrad 1981), the dislocation cell size (Raj and Pharr 1986), the deformation mechanisms present (Barnett et al. 2004, Agnew and Duygulu 2005), the dislocation interactions, such as the amount of recovery (Zehetbauer and Seumer 1993, Kuhlmann-Wilsdorf 1998) and the presence of recrystallisation (Humphreys and Hatherly 2004).

The stress-strain curves for the different metals are shown in Figure 5-9 and the strain-hardening rate in Figure 5-10. All the metals work-harden, and hence an increase in dislocation density would be expected for all alloys. There are differences in the yield stress and the rate of hardening for the different alloys.

These stress-strain curves are used in Chapter 7, when trying to understand the results of the diffraction peak profile analysis methods.

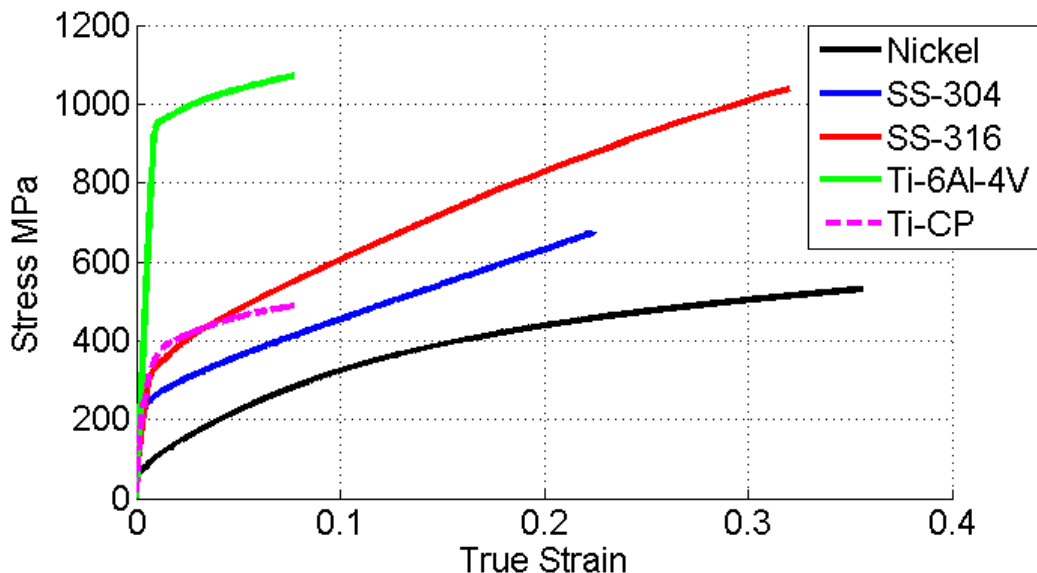


Figure 5-9. True Stress-true strain curve for the different metals studied.

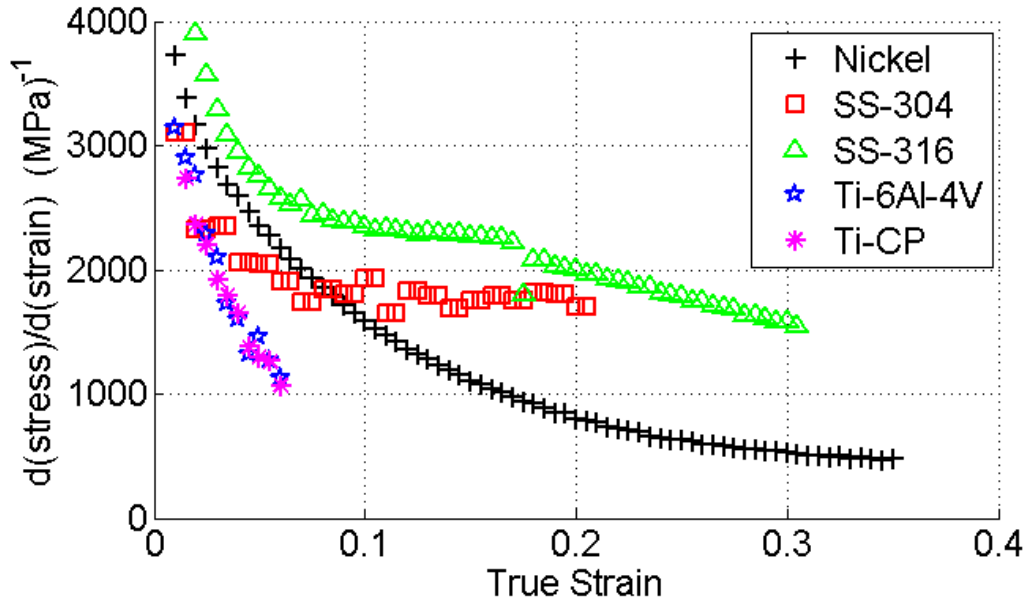


Figure 5-10. Strain-hardening rate versus true strain for the different metals studied.

5.3 Hardness Tests

A hardness test measures the localised resistance to plastic deformation. In a Vickers hardness test a small diamond indenter is forced into the surface and the size of the resulting indent is measured. This is then converted to a hardness value. Details of the hardness test are found in Section 3.6.

The hardness measurement of a metal has been shown to be proportional to the flow stress for different metals (Callister 2000). This may be expected because they are both a measure of the resistance of the movement of dislocations. Hence, hardness measurements are a useful technique in characterising the state of a metal.

The Vickers hardness values of the different metals is shown in Figure 5-11. As expected there is a relationship between the stress-strain curve and the hardness values, which is approximately linear. However, for Ti-6Al-4V the hardness does not change with increasing applied strain, over the range measured.

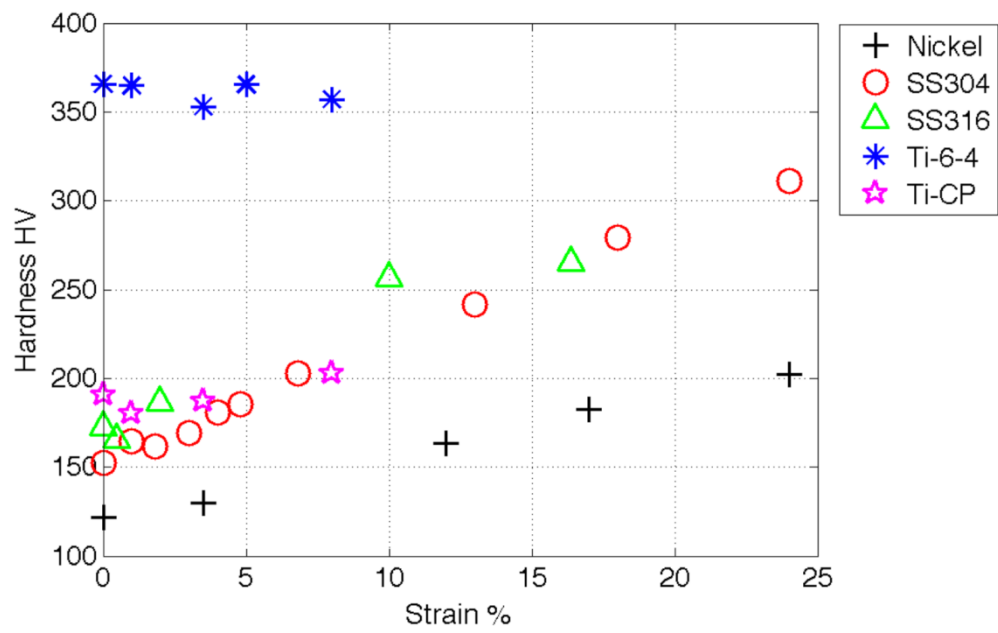


Figure 5-11. The Vickers Hardness values (HV) for the different metals studied using 0.5kg indent.

6 Implementation of Diffraction Peak Profile Analysis Methods

6.1 *Introduction*

The main aim of this chapter is to introduce the different diffraction peak profile analysis methods (DPPA) used in this thesis, and to show how they are implemented. In addition to this, the errors associated with the different methods are discussed, along with recommendations on the best practice when using them.

The DPPA methods that are considered in this chapter are:

1. Full-width (Section 6.4)
2. Integral breadth method (Section 6.5)
3. Variance method, in two different forms (Section 6.6)
4. Williamson-Hall method (Section 6.8)
5. Warren-Averbach method (Section 6.9)
6. The alternative method (Section 6.9)

The contrast factor (Section 6.7) is used in conjunction with the Williamson-Hall and Warren-Averbach method, and the manner that this is implemented is also discussed.

The different DPPA methods are applied to metals (details in Section 3.2) deformed by uni-axial compression (details in Section 3.3), on measured diffraction data found using laboratory x-ray, for the FCC metals, and synchrotron x-ray, for the titanium alloys, diffraction sources, details of which are found in Section 3.4.

6.2 Quantifying Errors

When using DPPA methods, errors can be introduced in a number of different ways. They can be introduced by approximations in the mathematics of a method, the application of the methods to experimental data and when obtaining the experimental peak profiles. For this reason, it can be difficult to determine the usefulness of the results obtained from a particular method, to study the deformation of a metal. However, to determine the usefulness two factors need consideration:

1. The way different methods work and what sort of errors are involved in their use and
2. Whether a particular method provides results that describe the sample being studied

The aim of this chapter is to try to understand the first of these factors, whilst subsequent chapters will consider the second point.

To understand the errors in the results of a DPPA method is not straightforward. The main approaches that may be used to assess the error in a measurement are either, to compare the measurement to a known value, or to repeat the measurement and determine how much the measurements deviate. However, neither method would be completely valid for assessing the errors in the results of a DPPA method. In many cases the results of a DPPA method are not directly comparable with another method, which effectively rules out this approach. Although, in some cases they are comparable and it is these situations that are considered in Chapter 7.

The second approach is impractical, mainly for the additional time needed, especially as it would not be sufficient to just repeat the measurement for one sample at a particular strain. Therefore, to make an assessment of the errors involved in a method a different approach is taken.

It is assumed that the results of a method should change smoothly with strain for a particular metal, and a second order polynomial (with three fitting values) is fitted to the results against applied strain. The deviation of the results from this

polynomial fit is then used to give an indication of the errors involved in a method. An example of how this approach works is shown in Figure 6-1. If a particular DPPA method is applied to a particular metal and gives a result R_i at a particular strain value (where i represents a particular measurement and N the total number of measurements) and the polynomial fit is P_i at the same value, then two error values can be defined. The ‘deviation’ is the average absolute deviation of a value from the polynomial fit. The ‘deviation ratio’ is the average of the deviation from the fit divided by the result at that value. The deviation ratio is more useful as it allows the errors from results with different absolute values to be compared.

$$\text{deviation} = \frac{1}{N} \sum_i^N |R_i - P_i|$$

$$\text{deviation ratio} = \frac{1}{N} \sum_i^N \frac{|R_i - P_i|}{R_i} \quad (6.1)$$

The deviation and, in particular, the deviation ratio will be used throughout this chapter to quantify the errors involved in a particular DPPA method.

An additional parameter will be used to define the errors in a method. If a particular result does not follow the general trend of the other results, or has an unrealistic value (e.g. it is negative), then this result is said to be an unreliable result.

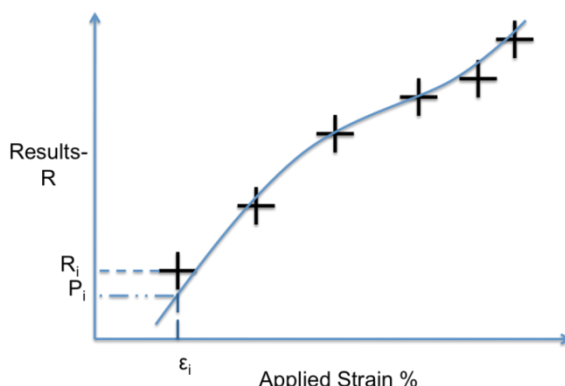


Figure 6-1. An example of how errors in the results of a DPPA method are quantified. The results of a method are fitted to a polynomial against strain, the result at a particular strain (R_i) for a particular measurement point (i) then has a fitted value of P_i . The deviation (or indication of error) of point i , is then $|R_i - P_i|$.

6.3 Preparation of Diffraction Data

In order to use the different DPPA methods, the measured diffraction data must be processed so that it is in the correct form to be analysed. This processing procedure, described in this chapter, is very important and not always straightforward but must be done correctly for a valid analysis.

The first step in processing the diffraction data was to convert it from measurements at constant values of 2θ , to constant values of k ($=1/d=2\sin\theta/\lambda$). This is done because data on a constant k -scale is more useful: it makes it easier to eliminate α_2 (the lower intensity component of the laboratory x-ray K- α radiation, see Section 3.4.2 and Figure 6-2) and to use the different broadening techniques. Consequently, the data was interpolated so that it would have a constant step size on a k -scale, with an appropriate step size so that a minimal amount of data is ‘created’ or, more importantly, ‘lost’.

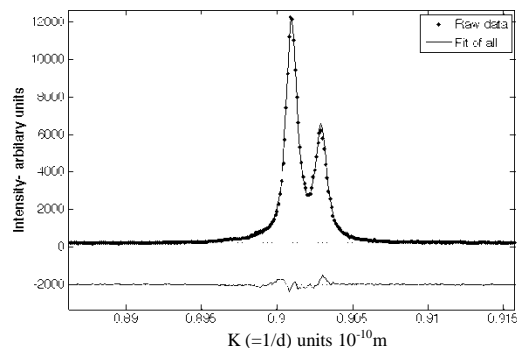


Figure 6-2. An example x-ray diffraction pattern and the fit of a silicon standard instrumental profile showing the α_1 (large peak on left) and α_2 (smaller peak on right) components and the pseudo-Voigt fit.

For all DPPA methods used, it is beneficial to fit the whole diffraction pattern, including all peaks. For some of the DPPA methods, the results of the fit (the full-width or integral breadths of the peaks) are used directly in the analysis. However, a fit is also important for the other DPPA methods, because it is used to accurately identify the position of the diffraction peaks, account for overlapping peaks and help in elimination of the α_2 radiation.

The measured diffraction patterns were fitted, using a split pseudo-Voigt (Wertheim et al. 1974) curve to fit each of the diffraction peaks and a quadratic polynomial for the background. The pseudo-Voigt (pV) curve (Equation 2.11) was used with boundaries for the mixing parameter (η) of 0 and 1.2, allowing the possibility of super-Cauchy (or super-Lorentzian when $\eta>1$). As can be seen in Figure 3.2, Figure 3.4, Figure 3.7 and Figure 6-2, this provides a good fit to the data in most cases; however, in some instances the background around a peak is not adequately fitted. In these cases, an additional fit of the data around a peak was performed with a linear background term. In a split pV full-width and mixing parameter are different either side of the peak, to account for asymmetry.

For the laboratory X-ray results described in Section 3.4.2, the K- α radiation consists of two main components, known as α_1 and α_2 . The method adopted to account for this is to assume the α_1 and α_2 have the same shape and to fit each peak with the sum of the two pV curves. This fitting method provides a good fit (Figure 6-2), but it often underestimates the tail on the low angle side; this occurs on the silicon standard, along with some of the FCC samples.

To allow the different methods to be used for {hkl} peaks, other than those of the same type (e.g. {111} and {222}), the contrast factor (C) was used. Equations 2.62 and 2.64, describing the contrast factor in FCC and HCP metals, were used. More details of this are provided in Section 2.4.5.

The instrumental broadening was removed from the measured broadening. For the titanium samples, which are measured at the ESRF, a LaB₆ sample was measured and used as an instrumental calibration sample, and for the FCC samples a silicon standard is used. For the full-width and Williamson-Hall methods the instrumental is accounted for using the equation, $\beta_M(g) = \beta_i + \beta_p$ where the full-width is used for β and the measured peak (M) is the sum of the instrumental (i) and physically broadened (P) peaks. This equation is correct if the peaks are Cauchy (Klug & Alexander 1974). However, the peaks are not necessarily Cauchy, or even Voigt, so there is some uncertainty introduced by this approximation (Scardi et al. 2004). For the Integral breadth and Variance methods, the pseudo-Voigt peaks are converted to Voigt functions. The Cauchy (using the superscript C) integral breadth is found using the following equation (Klug & Alexander, 1974):

$$\beta_M^C(g) = \beta_i^C + \beta_P^C \quad (6.2a)$$

The Gaussian integral breadths (using the superscript G) is found from the following equation (Klug & Alexander 1974):

$$(\beta_M^G(g))^2 = (\beta_i^G)^2 + (\beta_P^G)^2 \quad (6.2b)$$

6.4 Analytical Fit

The simplest of the DPPA method considered, is to use the full-width at half-maximum of a peak (full-width), fitted using an analytical function. It is found that with increasing applied strain, different peaks of a metal broaden by different amounts and in some instances some narrow when others broaden (see Section 7.4.5 and 8.3.3). This behaviour is more pronounced for Ti-6Al-4V in comparison to the FCC samples. Hence, it is recommended that when using this method more than one peak should be used and peaks that are not well fitted (for example because of overlap with other peaks or because they have lower intensity) be avoided.

For the FCC samples data the average of the first five peaks is used and for the titanium samples data, the average of the first 10 peaks was used. In Figure 6-3 and Table 6-1., the change in the average full-width for the different metals with different applied strains, and the deviation from the polynomial fits, are shown. The changes in full-width values change gradually with applied strain, and no values deviate significantly from these trends. The deviation of the full-width values from the trend is less than 5%.

The error values from the analytical fit will be used for comparison with other methods.

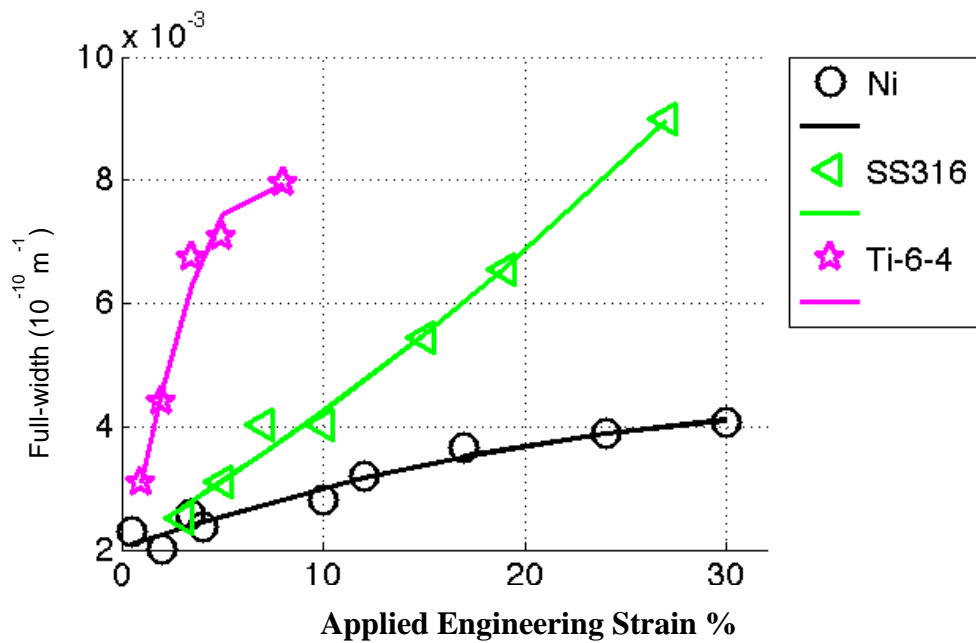


Figure 6-3. The change in full-width with applied strain for nickel-200, SS-316 and Ti-6Al-4V. The lines represent a fit of the values to a 2nd order polynomial (see text Section 6.2).

Table 6-1. Errors associated with full-width values, for Ni, SS-316 and Ti-6Al-4V. The absolute and fractional deviation from a polynomial fit of the data, and the percentage of results that are used in this fit because they are assessed to be part of a trend.

FW	Ni	SS316	Ti-6-4
Deviation (10^{-10}m^{-1})	0.12	0.14	0.20
Deviation ratio	0.048	0.039	0.032
% Points Reliable	100	100	100

6.5 Integral Breadth Method

This is a single line method where it is assumed that the Gaussian and Cauchy (Lorentzian) integral breadth of a Voigt can be represented as the strain and size

components, respectively. This method has been used by a number of different researchers (Delhez et al. 1982, de Keijser et al. 1982).

The method was applied by converting the fitted pseudo-Voigt curves to Voigt curves. Examples of the differences in the results for different peaks in Ti-6Al-4V (Figure 6-4) and SS-316 (Figure 6-5) are shown for the strain and size values, all five FCC peaks are shown and the HCP peaks with least overlap. There are variations in the results for the different peaks. As is evident from Figure 6-4 and Figure 6-5, the variation is largest for the SS-316 root-mean-square (rms) strain results, and the same is the case for the other FCC metals. Some of the peaks give zero or imaginary values for the Gaussian integral breadth. This does not occur for the titanium data and therefore probably arises because of the high instrumental broadening of the X-ray diffractometer measurements used for the FCC metals. The difficulties fitting to the shape of the peaks due to the different components of the α characteristic radiation is also a factor.

To understand the influence of instrumental broadening, it is worthwhile to consider the broadening, and shape, of the measured and instrumental peaks. For the FCC samples, the instrumental sample has mixing parameter values between 0.4 and 0.75 (where 1 represents a Cauchy and 0 a Gaussian peak). The mixing parameter is larger for deformed samples and increases with applied strain and with 2θ and g . To separate the instrumental broadening from the measured broadening, equations 6.1 and 6.2 are used. The problem that occurs is that the full-width of the deformed samples does not increase enough relative to the increase of the mixing parameter, such that the peaks Gaussian integral breadth is in many cases smaller than the instrumental samples Gaussian integral breadth. In some cases the measured samples have mixing parameter values of 1 or higher, which would represent the peak having no Gaussian integral breadth.

The most reliable peaks were found to be {200} and {311}, across all FCC metals, because they had the lowest deviation values found from the fit of the data. For the FCC metals only the {200} peak is used, because it gave the most

reliable results for this method and the analytical variance method (see Figure 6-4). The quality of the peaks is much higher in Ti-6Al-4V as shown in Section 3.4; therefore a large part of the scatter may be expected to be due to actual differences in the shape of the peaks due to the different texture components that the peaks represent, these differences are considered in more detail in later chapters. The titanium results obtained by using this method are the average of the five peaks with least overlap {10T0}, {10T2}, {11T0}, {10T4} and {20T3}.

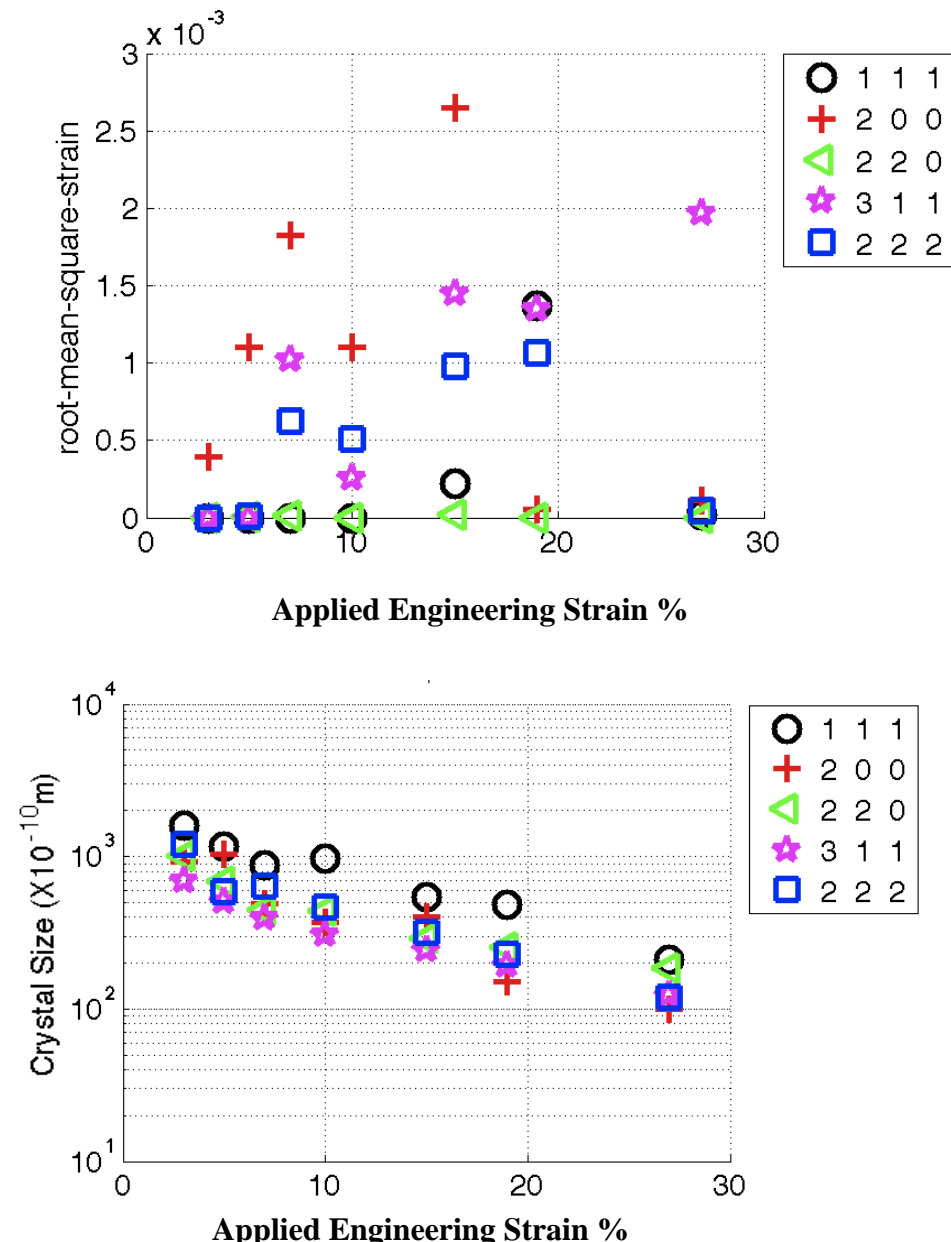


Figure 6-4. The root-mean-square-strain (top) and crystal size values in Å (bottom), for SS-316 found from different peaks, using the Integral Breadth method.

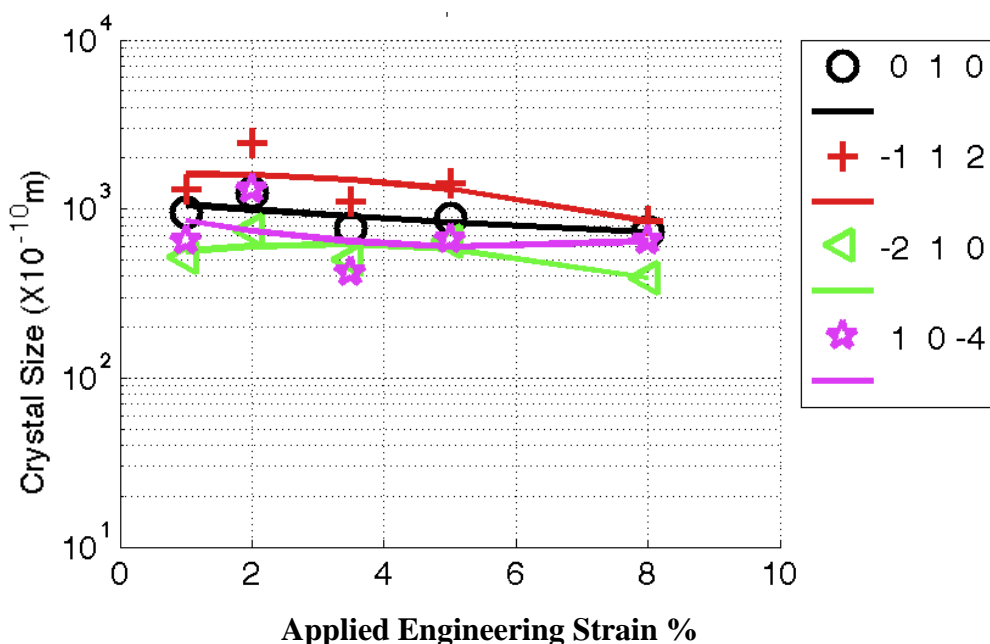
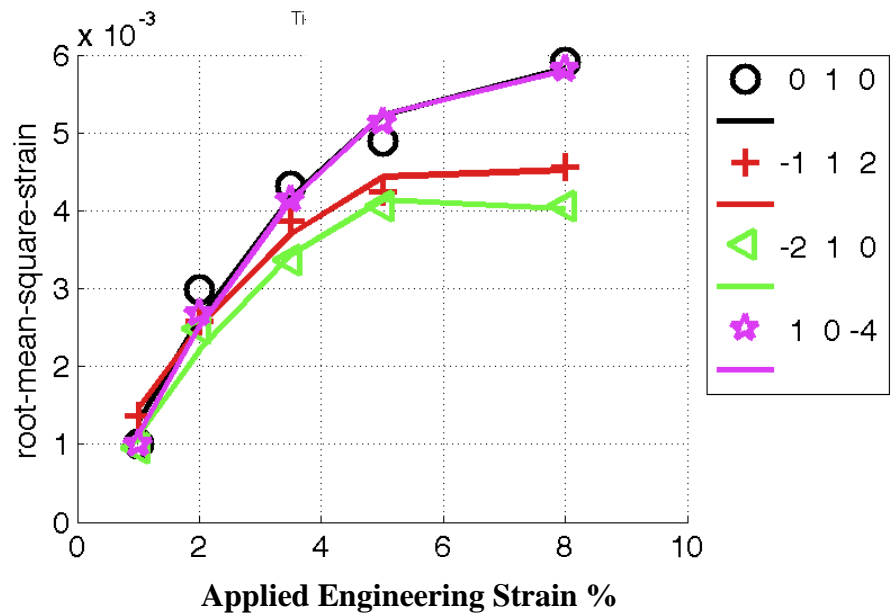


Figure 6-5. The root-mean-square-strain (top) and crystal size values in \AA (bottom), for Ti-6Al-4V found from different peaks, using the Integral Breadth method. The lines represent a fit of the values to a 2nd order polynomial (see text Section 6.2).

The changes in the size and strain values with applied strain, fitted to a polynomial to help understand the errors in the IB method, are shown in Figure 6-6. The errors determined from these figures are shown in Table 6-2. For the FCC metals the errors are approximately 4 to 5 times higher than found using the

full-width. For Ti-6Al-4V the error in the strain is close to that obtained for the full-width but for the size values the error is around 7 times higher.

I recommend that this method be avoided when the peak quality is poor, or when instrumental broadening is high, especially when the instrumental peak profile is close to being a Cauchy. When used ideally more than one peak should be used and if possible using more than one diffraction pattern (at a different part of the sample).

Table 6-2. Errors associated with size and strain values from the Integral Breadth method values, for Ni, SS-316 and Ti-6Al-4V. The absolute and fractional deviation from a polynomial fit of the data, and the percentage of results that are used in this fit because they are assessed to be part of a trend.

Strain	Ni	SS-316	Ti-6-4	Size	Ni	SS-316	Ti-6-4
Deviation x1e-3	0.19	0.35	0.12	Deviation x 10^{-10} m	710	97	210
Deviation ratio	0.20	0.29	0.05	Deviation ratio	0.28	0.21	0.24
% Points Reliable	100	71	100	% Reliable	100	100	100

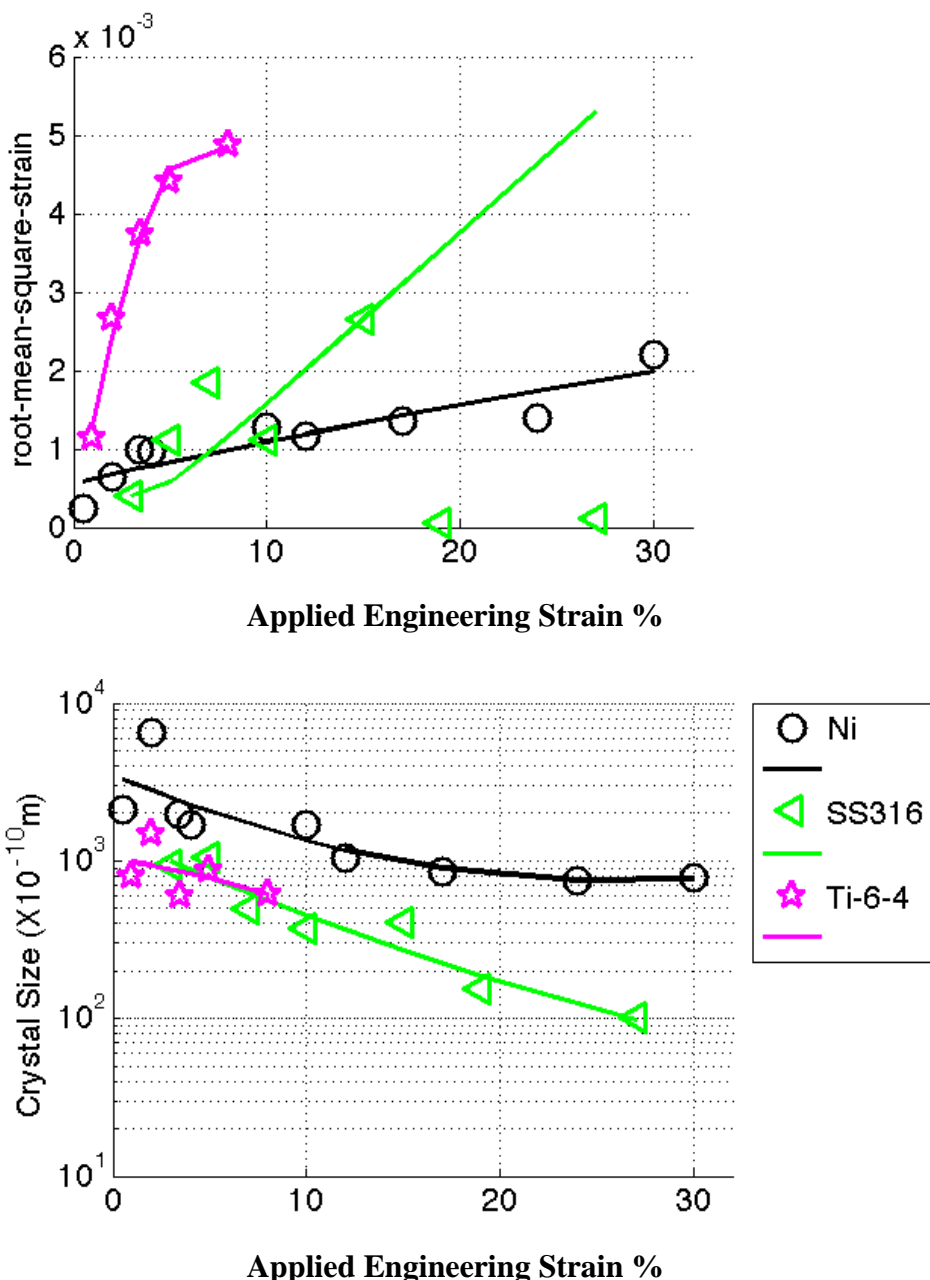


Figure 6-6. The change in root-mean-square-strain and crystal size, found using the integral breadth method, with applied strain for nickel-200, SS-316 and Ti-6Al-4V. The lines represent a fit of the values to a 2nd order polynomial (see text Section 6.2).

6.6 Variance Methods

The variance method is a single line method that uses the shape of all of a peak from its restricted moments or variance (Klugg and Alexander 1974) and has been used by a number of different researchers to study the study the microstructure of a material (Soleimanian and Aghdaee 2008, Borbely and Groma 2001, Borbely et

al. 2006, Sarkar et al. 2009, Kesavan and Vasudevan 1977). By using the kinematical theory of diffraction, equations have been derived that define these moments in terms of the microstructure of a sample (Tournarie 1956, Wilson 1962a, Borbely and Groma 2001). As detailed in Section 2.4.4, for the variance method there are two different approaches. A method to separate size and strain based on an assumed strain distribution, normally done by fitting a straight line to the variance values, which will be called the Variance-A method (described in Klugg and Alexander 1974). The second method determines the crystal size and dislocation density by fitting a function to the variance values that describes how dislocations contribute to broadening, which will be called the Variance-B method (Wilson 1963c, Groma 1998, Borbely and Groma 2001). The approach taken in the two methods is different, but there is some crossover. The implementation of Variance-A method is considered first, although some of the steps used are also used for Variance-B method.

6.6.1 Variance-A, Analytical Approach

Within the Variance-A method four different approaches are taken (these are detailed below), which are all based on the same formulae relating size and strain components to the variance. Two use the analytical fits of the peak, using pseudo-Voigt and Voigt curves, and formulas derived to relate the parameters of these curves to the strain and size components. For the final two approaches, straight lines are fitted to the variance values, the difference is how the background is determined.

The reason that these four different methods are used is twofold. Firstly the shapes of the peaks are not necessarily given by analytical functions (Voigt and pseudo-Voigt) and the aim is to test the validity of the formulas derived by Sanchez-Bajo and colleagues (Sanchez-Bajo and Cumbre 1997, Sanchez-Bajo et al. 2006) that use the parameters of the analytical functions. Secondly, the aim is to understand the importance the level of the background has on the results. The choice of background has a large influence on the shape of the variance, see Figure 6-7. However, the exact level that the background should be set at is not obvious.

The four different methods are:

- Analytical methods
 - Variance PV – formula derived (Sanchez-Bajo and Cumbre 1997) to relate the parameters of a pseudo-Voigt with the size and strain (equation 2.55).
 - Variance V – formula derived (Sanchez-Bajo et al. 2006) to relate the parameters of a Voigt with the size and strain (equation 2.56).
- Line methods (both using equation 2.47 and 2.48)
 - Linear PV background- size and strain found by fitting a straight line to the variance, the background level is obtained by using the pseudo-Voigt fit.
 - Linear σ^3 background- size and strain are found by fitting a straight line to the variance, the background level is obtained by a method that assumes the variance has a particular shape (described later with the use of equation 6.3).

The analytical methods use the analytical fits of the peaks, using the conversion of a pseudo-Voigt to Voigt given by equation 2.12.

The analytical methods have the advantage that they are fairly simple to implement, the variance values do not need to be calculated and issues surrounding finding the background and fitting the data are ignored. However, to choose the level of the background from the analytical fit is an arbitrary choice and it is not clear whether there is any justification for this. In addition the peaks may not be well described by the analytical function.

The linear methods work by finding the variance values of a peak and fitting a straight line to it, to determine the crystal size and strain. The intensity values of a peak were found by fitting the entire diffraction pattern. This fit was then used to eliminate all other peaks, except the one under consideration, and determine the level of the background. The variance values were obtained from the intensity profiles on a 2θ scale over a range 0 to 0.5° .

Two methods are adopted to find the level of the background. The first is that given by the fit of the peak. The raw data and not the pseudo-Voigt of a peak is then used, but otherwise the method of background determination is the same as given in the analytical methods. The alternative choice of background is made by making assumptions as to how the variance values should change. From derivations, using the kinematical theory, it is known that the moments are expected to change linearly with the difference from the Bragg angle (σ), and these can be used to help determine the background (Langford 1982). The most used approach is to fit the variance to an equation of the form of Equation 6.3, and assume the variance is linear for large values of σ and there is no σ^3 term.

$$M_2 = W + k\sigma + a_3\sigma^3 \quad (6.3)$$

Where, M_2 is the 2nd order variance (or moments), σ is the difference from the Bragg angle in 2θ and k and a_3 are constants.

It can be seen from Figure 6-7, that when the background is set too low there is clearly a σ^3 term to the variance (the variance increases rapidly with σ). However, when the background is set too high the variance becomes negative, which would not be possible. I believe this was caused by not being able to measure the variance values accurately enough at larger σ values. Therefore, there is a balance between these two factors and in all cases considered it was found that both conditions could not be met simultaneously. Hence, the range of σ -values used to fit the background was limited to values that were thought to be reliable. From Figure 6-7a, it can be seen that this is around 0.3° , because at this value the variance values change significantly and start to fall. To determine the background, equation 6.3 was fitted to the variance values, for values of σ up to 0.3. The chosen background was the one that had a positive value of the variance, M_2 , at $\sigma=0.3$, and the minimum value of a_3 .

A comparison of the variance found by this method (σ^3 background) and given from the pseudo-Voigt fit of the data is shown in Figure 6-7b. The variance from the pseudo-Voigt fit in many cases gave values, which were expected to be incorrect.

From these two different ways of finding the background level, crystal size and RMS strain values were obtained. Straight lines were fitted to the variance data, over a range of 0.1 to 0.2°, to determine size and strain values. The range was chosen because it was the most linear region.

For the analytical method, both FCC and titanium sample data are analysed, whereas for the line methods only the Ti-6Al-4V data is considered. This is because of the lower quality of the peaks in the FCC data.

For the FCC data the peaks used are {111}, {200} and {220}, whereas for the titanium {10T0}, {10T2}, {1120}, {10T4} and {2023} are used. The FCC peaks were chosen because they were thought to be the most reliable, and the titanium because they had the least overlap of the first 15 peaks. For the titanium data the results are also the average of the two measurement directions.

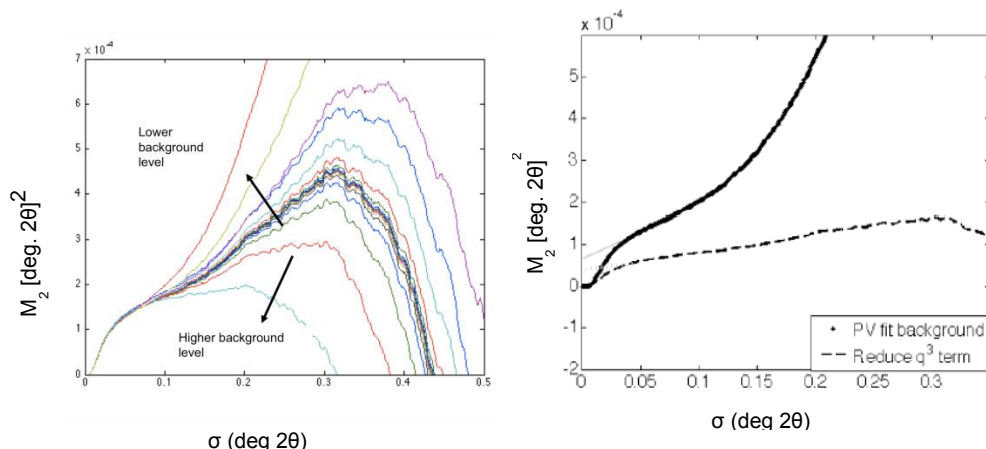


Figure 6-7. Left (a) the change in the variance (M_2) with different background level, plotted against the difference from the Bragg angle in degrees 2θ . In the transverse direction, the variance values are for the measured intensity values. Right (b) variance values found using the background from the pseudo-Voigt and from reducing a σ^3 term. The diffraction peak is (1 $\bar{1}$ 02) for Ti-CP samples.

6.6.2 Variance-A, Errors and Best Practice

All four of the Variance-A methods listed in Section 6.6.1, were applied to different peaks in Ti-6Al-4V samples, and the results are shown in Figure 6-8 and in Table 6-3. The results in the table are separated into two groups, all peaks between 1 and 15 and those 5 peaks with minimal overlapping peaks (good peaks). The mean and standard deviation of these different sets of peaks are shown.

It is evident that the values given by the methods vary considerably. The difference between the maximum size and strain values is approximately 2 to 3 times higher than the corresponding minimum values. The standard deviation in the values is also considerable, varying between close to the mean to less than a third of the mean. The table also shows the standard deviation in the integral breadth method are around the same magnitude as the variance values, although the values are higher.

The difference observed in Figure 6-8 and in Table 6-3, between the two line-methods shows the influence the choice of background level can have on the results. Although, the micro-strain values are close, the crystal size values are systematically different at all strains, by a factor of around 2. The only difference between the two analytical approaches should be due to the conversion of a pseudo-Voigt to a Voigt curve. However, the differences are significant, as can be seen in Figure 6-8, the Variance Voigt method has a micro-strain value more than 3 times higher and a crystal size almost half that of the pseudo-Voigt method.

Soleimanian and Aghdaee (2008) found differences in the results of the variance method by three different methods; using Voigt and pseudo-Voigt curves and the equations used here, and a line method using a Pearson VII function. They found the Voigt method gave the largest RMS strain value, which was over three times higher than the line method, and the pseudo-Voigt result was in between the other two values. However, the difference they found in RMS strain values between Voigt and pseudo-Voigt methods may be attributed to their use of an incorrect formula, missing a $\pi^{1/2}$ term, for the RMS strain Voigt values. They found that the

difference in the crystal size values for the three methods were closer; Voigt method gave the largest crystal size, the pseudo-Voigt and line methods gave lower values, which were approximately 20% lower than the Voigt method. The results found in this report show some agreement with the results of Soleimanian & Aghdaee (2008). The Voigt method gives the highest RMS strain values, and there is less variation between the samples in the size values than the strain values. However, the difference that we observed between Voigt and pseudo-Voigt, in Figure 6-8, is not expected. This may be due to the conversion of a pseudo-Voigt to a Voigt used in this work.

Table 6-3. Results for crystal size (D) in Å and rms strain (multiplied by 10^{-3}) using the different single line methods, for Ti-6Al-4V at 8% strain measured in the transverse direction. The ‘good’ peaks are those without considerable overlap and are the (10.0), (10.2), (11.0), (10.4) and (20.3) peaks. The mean and standard deviation values are shown.

	Mean rmss (good peaks)	St dev. rmss (good peaks)	Mean rmss (first 15 peaks)	St dev. rmss (first 15 peaks)	Mean D (good peaks)	St dev. (D good peaks)	Mean D (first 15 peaks)	St dev. (first 15 peaks)
Variance PV	0.49	0.39	0.47	0.49	650	260	960	2100
Variance V	1.77	0.49	1.52	0.94	360	130	390	500
Linear PV bcg	0.61	0.43	1.15	2.14	410	270	520	1300
Linear q3 bcg	0.73	0.42			850	1000		
IB method	4.94	1.00	5.02	1.18	570	210	680	1100

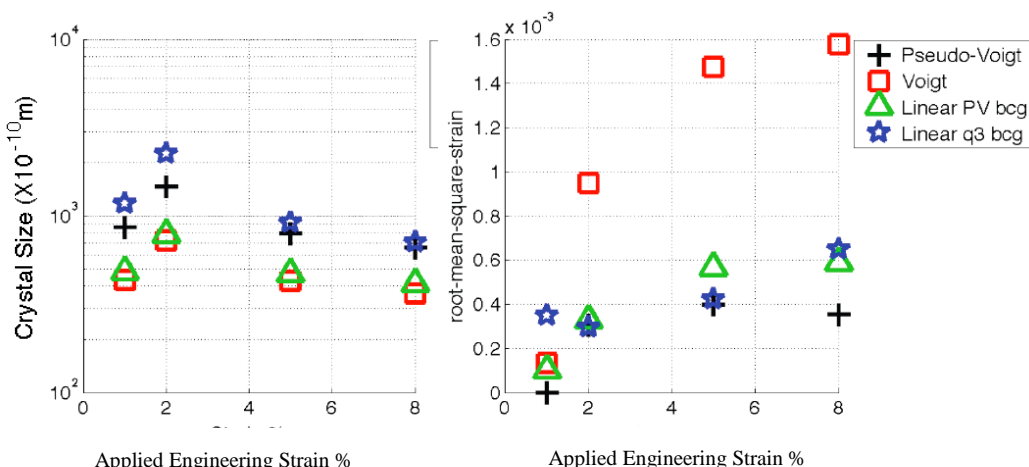


Figure 6-8. Variance-A method results for Ti-6Al-4V data. The crystal size, in Å, (left) and RMS strain (right) values are shown.

The changes in the crystal size and micro-strain values with applied strain are shown in Figure 6-9 and Figure 6-10. The values are fitted to a polynomial to help understand the errors in the Variance-A analytical methods and the errors are given in Table 6-4 and Table 6-5. For the FCC metals the strain values are all found to have unrealistic imaginary values, to display this the square of the root-mean-square strain is shown. For both FCC metals the square of the rms strain increases with applied strain, and is much larger in magnitude for SS-316. These problems are not found with the titanium samples, and are probably a result of the larger instrumental broadening for the FCC metals and the instrumental peak being close to Cauchy. This was found with the IB method too, but the results suggest its influence is larger for the variance-A method. The same problems are not found with the size values. The reason for the behaviour is the same as observed for the IB method, which is the measured peaks are more Cauchy than the instrumental and the physically broadened Gaussian integral breadth is often very low or negative. The strain values have problems because they are more dependent on the Gaussian component than the Cauchy component of the integral breadth. For example for the Voigt formulation the size value does not include the Gaussian integral breadth but the strain value does.

The errors determined from Figure 6-9 and Figure 6-10 show that the scatter is considerably larger than found with the full-width method, shown in Table 6-4 and Table 6-5. For Ti-6Al-4V, the micro-strain values have an error approximately a factor of ten higher than for the full-width, and size values with an error of around five times higher. For the FCC metals the error in the size values varies from being around 1.5 to 5 times higher than the full-width, and considerably lower using the Voigt analytical method.

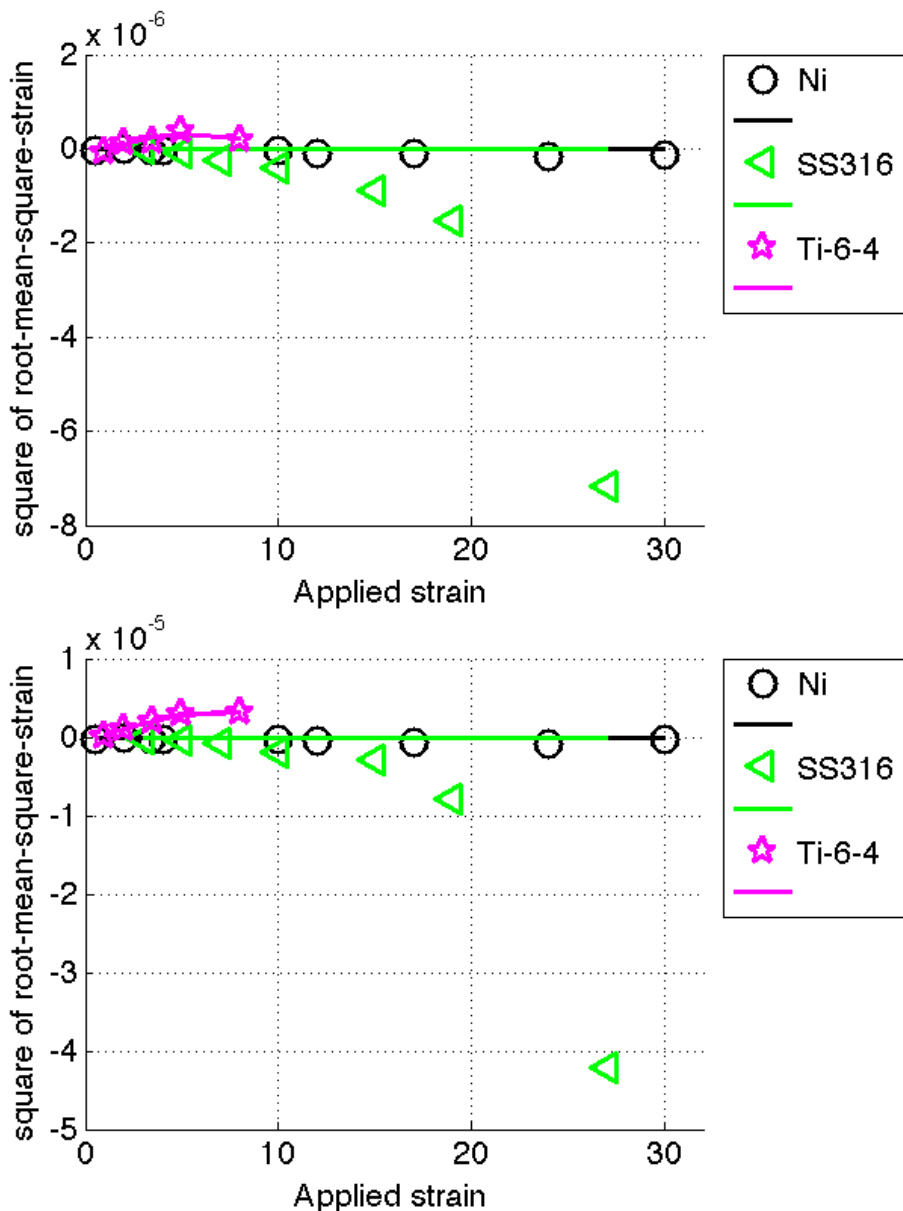


Figure 6-9. The change in root-mean-square-strain, found using the Variance-A Voigt (top) and pseudo-Voigt (bottom) method, with applied strain for nickel-200, SS-316 and Ti-6Al-4V. The lines represent a fit of the values to a 2nd order polynomial (see text Section 6.2).

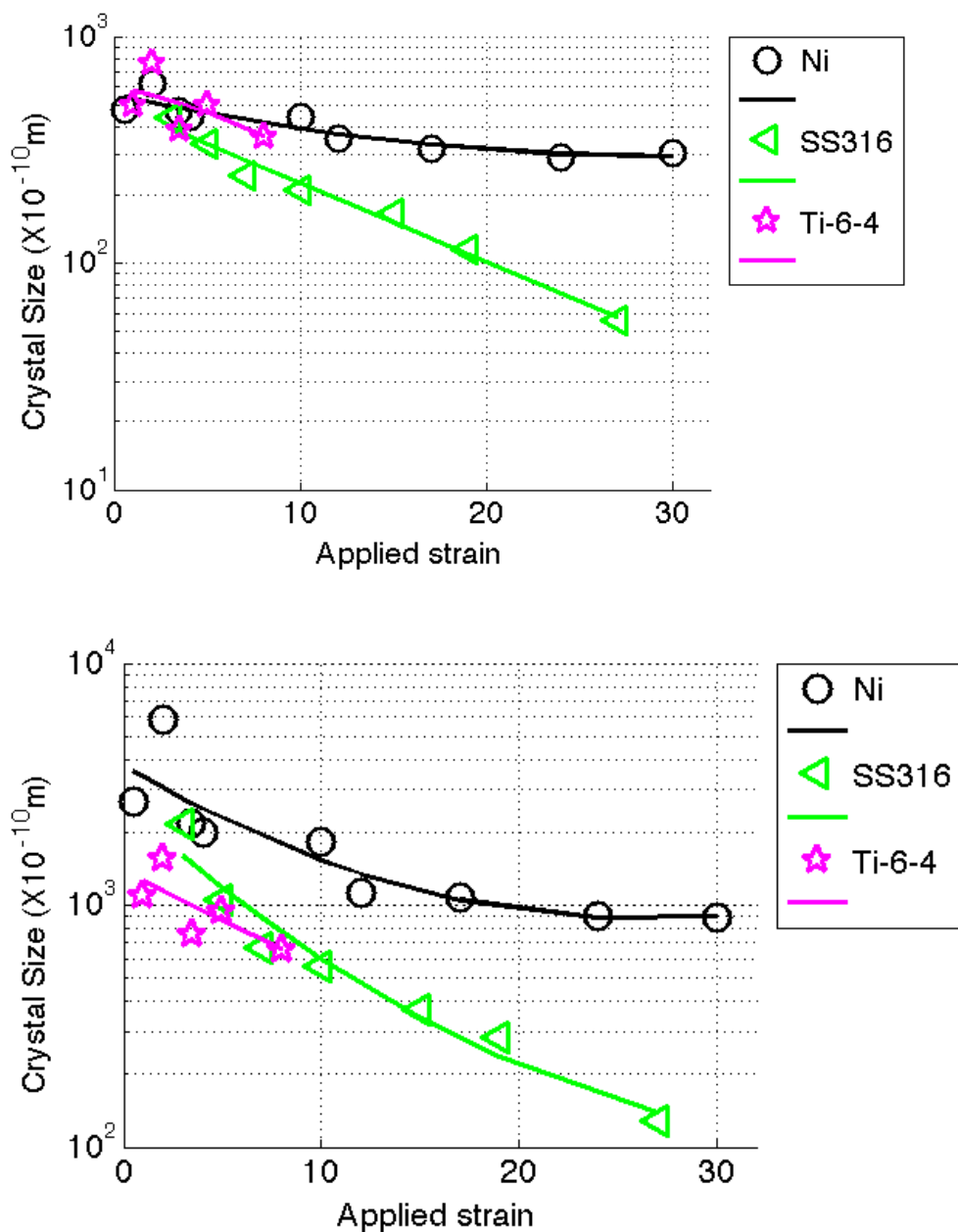


Figure 6-10. The change in crystal size in Å, found using the Variance-A Voigt (top) and pseudo-Voigt (bottom) method, with applied strain for nickel-200, SS-316 and Ti-6Al-4V. The lines represent a fit of the values to a 2nd order polynomial (see text Section 6.2).

Table 6-4. Errors associated with size and strain values from the Variance-A Voigt method, for Ni, SS-316 and Ti-6Al-4V. The absolute and fractional deviation from a polynomial fit of the data, and the percentage of results that are used in this fit because they are assessed to be part of a trend.

Var. Voigt- Strain	Ni	SS-316	Ti-6-4	Var. PV	Ni	SS-316	Ti-6-4
Deviation	-	-	8E-8		-	-	7E-08
Deviation ratio	-	-	0.26		-	-	0.33
% Points Reliable	0	0	100		0	0	80

Table 6-5. Errors associated with size and strain values from the Variance-A pseudo-Voigt method, for Ni, SS-316 and Ti-6Al-4V. The absolute and fractional deviation from a polynomial fit of the data, and the percentage of results that are used in this fit because they are assessed to be part of a trend.

Var. Voigt- Size	Ni	SS-	Ti-6-	Var. PV-	Ni	SS-316	Ti-6-4
Deviation $\times 10^{-10}$ m	35	18	89		580	150	180
Deviation ratio	0.08	0.07	0.17		0.22	0.17	0.16
% Points Reliable	100	100	100		100	100	100

6.6.3 Variance-B, Analytical Approach

The Variance-B method was originally developed by Wilson (Wilson 1963c), by assuming strain was due to dislocations, but was subsequently modified by Borbely and colleagues (Borbely and Groma 2001, Borbely et al. 2006). This form of the variance method has become more popular following the work of Borbely and colleagues.

In the Variance-B method, instead of obtaining crystal size and strain values, crystal size and dislocation density values are obtained. The method also uses the M_4 moments, and the standard variance values (used in Variance-A method), the M_2 moments.

The variance values are determined in the same manner as in the Variance-A method, but are found on a k-scale, over the range $\sigma=0$ and 0.015\AA , instead of on 174

a 2θ scale. The σ^3 background determination was used (described in the previous section), but was done so for both the M_2 and M_4 values as a starting level for the background.

The two Variance functions have many parameters, some of which cause similar changes in the moments. When fitting to these functions Borbely and Groma (Borbely and Groma 2001) recommends that the background level also be allowed to change. The correct level of background being, that which gives the same crystal size for the two equations. Hence, the fitting method used in this work involved changing both the background level and the crystal size between distinct values. For each particular set of background level and crystal size the second and fourth order variance values, M_2 and M_4 , were fit to the corresponding equations (equation 2.57, taken from Borbely and Groma 2001) separately to obtain the best fit. The background level was allowed to change by $\pm 5 \times 10^{-2}$ % of its maximum intensity and the crystal size between $0.01 \mu\text{m}$ and $1 \times 10^6 \mu\text{m}$. The fits are taken over the range 0.007\AA to 0.09\AA , in the value of σ (the difference from the Bragg angle on a k-scale). The results that are used are from the set of background levels that give the same crystal size for both M_2 and M_4 and also provide a good fit. The average of these values was taken. This method of fitting was found to be very slow (using Matlab on an iMac "Core 2 Duo" computer); each peak takes more than 30 minutes, and requires the fits to be manually checked. However, it was the only method that was found that could give reliable fitting and results.

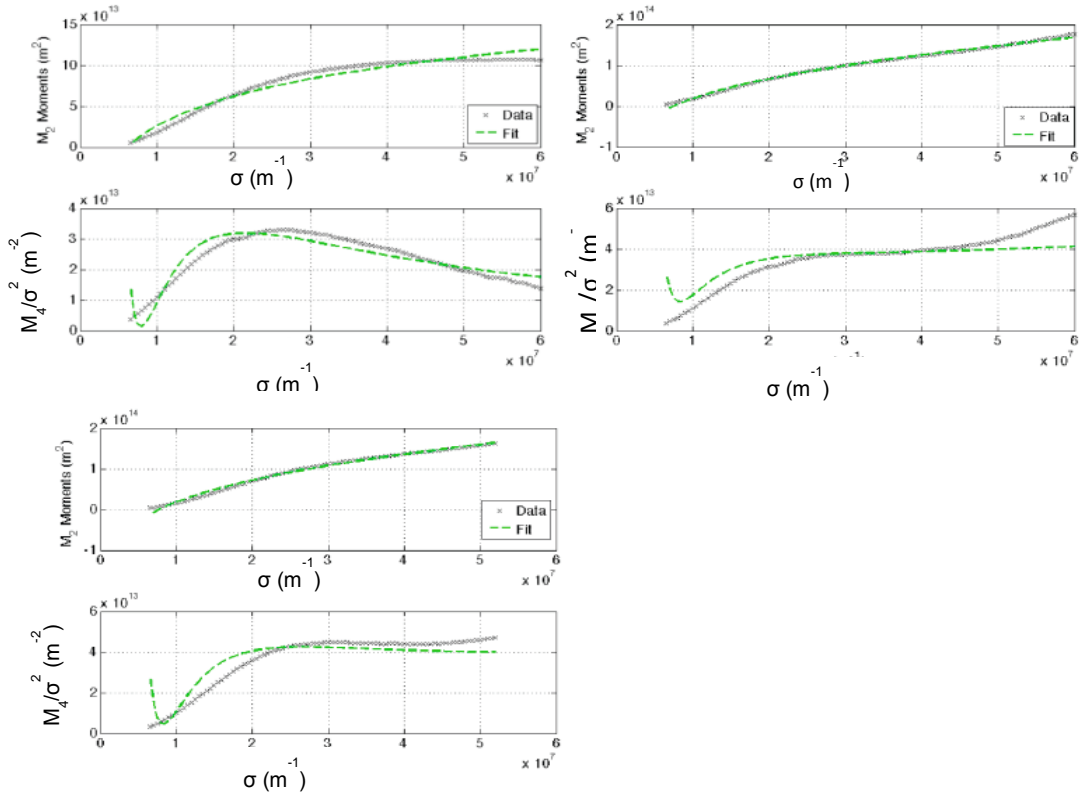


Figure 6-11. Examples of the fits for the variance method for the $\{01 \bar{1}0\}$ (top) and $\{11 \bar{2}2\}$ peaks (bottom). The M_2 variance is above the M_4 variance for fits with the same level of background and crystal size but the other parameters are different.

The method was only used on Ti-6Al-4V and only on the $\{01 \bar{1}0\}$ and $\{11 \bar{2}2\}$ peaks, because these were the only ones that were fit reliably (Figure 6-11). In the other peaks the M_4 moments are not fitted well in most cases. This is mainly because the shape of the M_4 variance of these peaks does not match the functions well.

The range that is chosen to fit the variances is important to the results obtained. The M_2 and M_4 functions increase to infinity at low values of σ . Therefore, it is not possible to fit from zero or too low a value of σ . However, in our results most of the M_2 and M_4 variances have a significant curve at low σ . If this region is not included then the results obtained are different than if it were included. There is also a point for most of the variances, for the different peaks, after which the data appears to become less reliable. This is because there is a sudden increase or decrease in M_2 or M_4 that would not be expected from the equations being used to

fit. Hence, the choice of the range of values of σ to fit over can have a significant influence.

For the Variance-B analysis only the crystal size and dislocation density values will be presented in this chapter and Chapter 7, as the other values don't have any physical meaning. The results of the dislocation density for the $\{11\bar{2}2\}$ peak in the axial direction is shown in Figure 6-12. In most cases the dislocation density values are different depending on which moments are used, M_2 or M_4 . On average the dislocation density value for M_4 (using equation 2.57a) is lower by around a quarter to a tenth of the value found with M_2 (using equation 2.57b). These findings are inconsistent with that of Borbely and Groma (2001) who found that when size broadening is low, as we observe here, M_2 and M_4 should give the same dislocation densities. In many cases the use of M_4 , at different background levels, gives dislocation density values that are at two very different values. In some cases when the fit is good, the values of M_4 and M_2 can be the same. When this did occur it did so at values closer to the average values found for M_2 . In general the values of M_4 also have a greater scatter. This adds an ambiguity to the M_4 values. Given these observations, it is suggested that the dislocation density values with M_2 are more reliable.

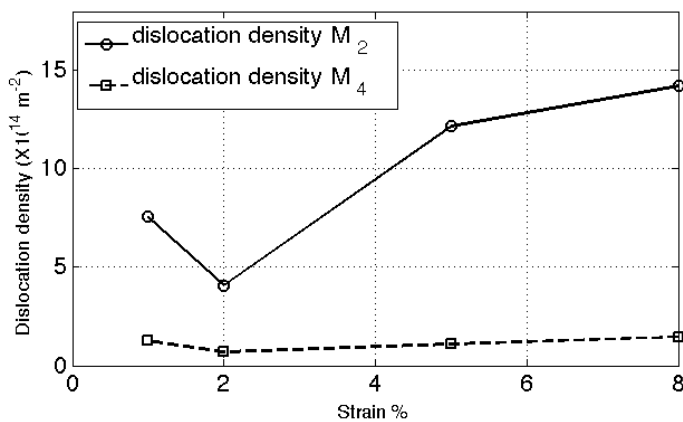


Figure 6-12. Results of the dislocation density from variance fits for the $\{11\bar{2}2\}$ peak for Ti-6Al-4V in the axial direction. The results are shown for the M^2 and M^4 variances.

The changes in the size and strain values with applied strain, fitted to a polynomial to help understand the errors in the Variance-B methods, are shown in Figure 6-13 and the errors in Table 6-6. The errors in the dislocation density values are higher than found for the full-width method (2-4 times higher) but lower than the strain values from Variance-A method (2-5 times lower). The way size was found means the method is not very sensitive to changes in size values. Hence, the error in the size is more difficult to interpret. If accurate size values are needed from this method, then I recommend that a different approach to that taken here is adopted.

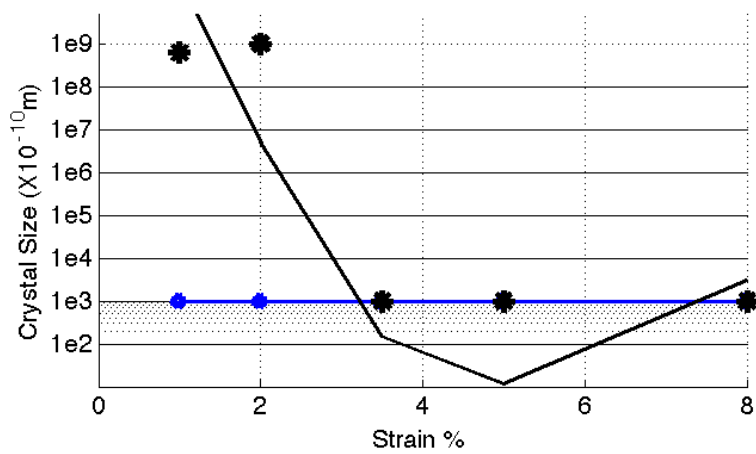
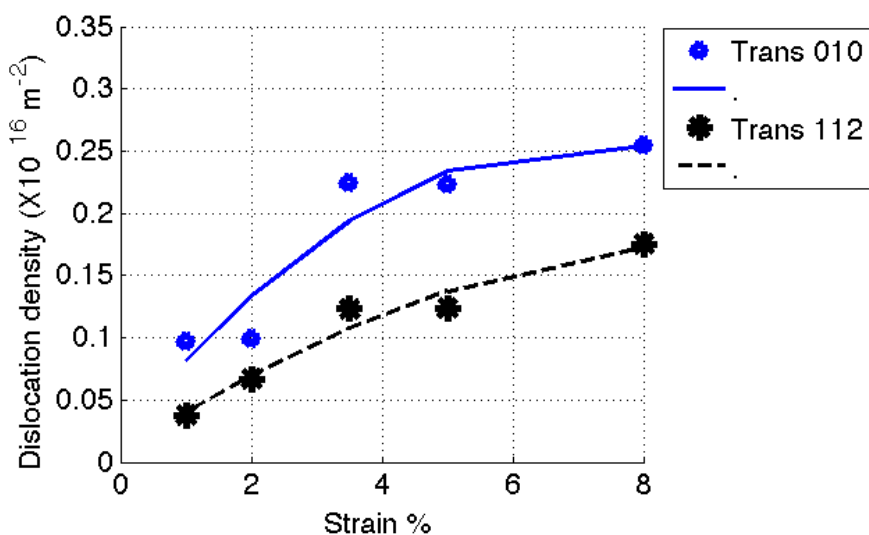


Figure 6-13. The change in dislocation density and crystal size, found using the Variance-B method, with applied strain for the {01-10} (shown as 010) and {11-22} (shown as 112) planes in Ti-6Al-4V, measured in the transverse direction. The lines represent a fit of the values to a 2nd order polynomial (see text Section 6.2).

Table 6-6. Errors associated with dislocation density and size values from the Variance-B method, for Ni, SS-316 and Ti-6Al-4V. The absolute and fractional deviation from a polynomial fit of the data, and the percentage of results that are used in this fit because they are assessed to be part of a trend.

Var- dislocation	Ti-6-4 {1-100}	Ti-6-4 {1-102}	Var- size	Ti-6-4 {1-100}	Ti-6-4 {1-102}
Deviation x1E13m ⁻²	18	7	x10 ⁻¹⁰ m	0	6E09
Deviation ratio	0.13	0.07		0	58
% Points Reliable	100	100		100	100

6.7 Contrast Factors

The contrast factor (see Section 2.4.5) is important because it allows the use of multiple peaks in DPPA for anisotropic metals where broadening is not just a function of its position but is also dependent on the hkl indices of the peak. The aim of this section is to show how the contrast factor has been implemented for use in Williamson-Hall and Warren-Averbach methods, which are discussed in the next two sections and in Chapter 7.

6.7.1 Contrast factor: FCC metals

As described in Section 2.4.5, for FCC metals the heterogeneity of broadening is incorporated into DPPA methods by the inclusion of the contrast factor term given in equation 6.4 (Ungar and Tichy 1999). When using this equation, the q value is allowed to vary to best fit the experimental results to the appropriate DPPA method.

$$\bar{C} = C_{h00}(1 - qH^2)$$

$$H^2 = \frac{h^2k^2 + h^2l^2 + k^2l^2}{(h^2 + k^2 + l^2)^2} \quad (6.4)$$

Where, C_{h00} and q are constants that are dependent on the elastic constants of the material and the dislocations present and h , k and l are the indices of the diffraction peak. The values of q and C_{200} for stainless steel 304 and nickel for edge and screw dislocations, calculated using ANIZC (Borbely et al. 2003) are 179

shown in Table 6-7. Based on these values, upper and lower fitting boundaries of q-values were selected to be just above the q-screw value and just below the q-edge value. From the values in Table 6-7, the value of C_{200} changes by less than 5% between the value for edge and screw dislocations. The average of the screw and edge C_{200} values is used. This may introduce a slight systematic error, if the q-value does represent the quantity of edge and screw dislocations. However, since the accuracy of determining q-values is low and these values may not represent edge and screw dislocations, this approach was taken.

Table 6-7. The elastic constants (c_{11} , c_{12} and c_{44}) and calculated C_{h00} and q values for nickel and stainless steel found using ANIZC (Borbely et al. 2003). The q-values for standard (111)[110] and partial dislocations (111)[$\bar{2}11$] with a 50:50 edge to screw ratio are shown.

Metal	C_{200} edge	C_{200} screw	q edge	q screw	c_{11}	c_{12}	c_{44}
Nickel	0.279	0.289	1.515	2.333	238	144	141
St. Steel	0.310	0.324	1.718	2.470	204.6	137.7	126.2
			q 50:50 edge to screw	q 50:50 partials			
St. Steel			2.09	1.69			

6.7.2 Contrast factor: HCP metals

In HCP metals, the contrast factor is given by equation 6.5 (Dragomir and Ungar 2002).

$$\bar{C}_{hk,l} = \bar{C}_{hk,0} (1 + q_1 x + q_2 x^2)$$

$$x = \frac{2l^2}{3(ga)^2} \quad (6.5)$$

Where, $g=1/d$, l is the 3rd hkl index, and ‘a’ one of the lattice parameters (the HCP notation {hkil} is used but ignoring the ‘i’ index).

The interpretation of the q-values is more complicated for HCP metals. Instead of one q value there are two and instead of one slip system there are many. In this part, the way in which the contrast factor is implemented in the results that follow

is discussed. In Chapter 7, a slightly different method is discussed to the method shown here.

The different slip systems that will be used, because they are the most commonly observed in HCP metals (Dragomir 2002, Honeycombe 1968), are listed in Table 6-8 along with the notation that will be used to describe them throughout the rest of this and the next chapters.

The q values are allowed to vary to best fit the experimental results to the appropriate equation. The lower and upper boundaries used are -2 and 2 respectively, for both q-values. These values are used based on the possible q-values for different slip systems shown in Table 6-8.

Depending on the slip systems present, the value of $C_{hk0}b^2$ varies considerably, as shown in Table 6-8. Therefore, the simplification used for FCC metals, that the fit of the contrast factor only changes the value of q, is not possible. To determine these values the slip systems present must be known. Since the different slip systems have different q values it is possible to make estimates as to the slip systems present.

Table 6-8. The parameters used to find the contrast factor for the eleven slip systems of titanium (Dragomir and Ungar 2002). The Py-Scr <c+a> values are calculated using ANIZC (Borbely et al. 2003) for a random texture and {10 11} (Py4). All slip systems are for edge dislocations except those with ‘Scr’ that are screw dislocations.

	Ba[a]	Pr[a]	Pr[c]	Pr [c+a]	Py[a]	Py2 [c+a]	Py3 [c+a]	Py4 [c+a]	Scr[a]	Scr [c+a]	Py-Scr [c+a]	Scr[c]
Burgers vector Slip plane		<2110> <2110> <0001> <2113> <2110> <2113> <2113> <2113> <2113> <2110> <2113> <2113> <0001>										
	(0001)	(0110)	(0110)	(0110)	(1011)	(2112)	(1121)	(1011)				(1011)
q1	-0.101	-1.193	3.616	2.017	-0.894	1.299	1.894	1.527	0.595	1.257	-0.574	1.7E+05
q2	-0.103	0.356	1.226	-0.617	0.183	0.397	-0.366	0.146	-0.710	-0.940	0.353	-9.9E+04
C_{hk0}	0.202	0.354	0.049	0.102	0.312	0.092	0.098	0.093	0.144	0.419	0.160	3.6E-06

Analytical Procedure to determine Contrast Factor for Titanium

A method similar to that used by Ungar and colleagues (2007) was used to find the slip systems. In this method a slip system can either be active or not. If it is active it has a probability of h, where h=1/N and N=number of active slip systems. The values of q are calculated for all the possible combinations of active

slip systems and given by $q^{(eff)}$. A particular slip system combination is considered active if it meets certain tolerances. The tolerances used are the same as used by Ungar and colleagues (2007), without the third condition, for a measured set of q-values $q^{(m)}$ a particular set of slip systems, with a calculate q value of $q^{(eff)}$, are considered active if:

If $|q_{1,2}^{(m)}| < 1$, the slip system combination is valid if

$$|q_{1,2}^{(m)} - q_{1,2}^{(eff)}| < \Delta q^{(abs)}$$

If $|q_{1,2}^{(m)}| \geq 1$, the slip system combination is valid if

$$1 - \Delta q^{(rel)} < \left(\frac{q_{1,2}^{(eff)}}{q_{1,2}^{(m)}} \right) < 1 + \Delta q^{(rel)}$$

To find the activity of the different slip systems for a given diffraction pattern, the average is taken for all the combinations that meet the tolerances. This is slightly different to the method of Ungar and colleagues (2007), which uses a histogram. The main difference between the method used and that of Ungar and colleagues (2007) is that there is no dividing of the slip systems into different dislocation types, when calculating the active slip systems. There are differences in the results between the method and that of Ungar and colleagues (2007), these can be seen in Table 6-9. The difference between the methods is around 11% with a standard deviation of around 8%. The biggest difference is found when the q-values are either very small or large, such as grains 4 and 8. The method I have developed (and will use in this chapter and Chapter 7) attributes the value to the slip system with the closest q-values, whereas the method of Ungar and colleagues gives a mix of slip systems.

It can be beneficial to know which slip systems are contributing to a particular result, to understand how a method works and systematic errors that may result from its use, although because there are 11 slip systems and only two parameters (the q-values) used to determine them, these fractions are not reliable. When the numbers of types of slip systems are reduced their fractions become more reliable,

which is the reason Ungar and colleagues (2007) split the slip systems into dislocation types, $\langle a \rangle$, $\langle c+a \rangle$ and $\langle c \rangle$.

Table 6-9. A comparison of methods used to calculate slip system population from q-values in titanium. The q-values and the corresponding slip systems predictions from Ungar and colleagues (Ungar et al. 2007) are shown and the method used in this work.

Grain	q ₁	q ₂	This work			Ungar et al. 2007			Deviation
			$\langle a \rangle$	$\langle c \rangle$	$\langle c+a \rangle$	$\langle a \rangle$	$\langle c \rangle$	$\langle c+a \rangle$	
1	0.94	-0.53	42	9	49	48	14	38	6, 5, -11
2	3.2	-3.8	50	50	0	43	32	25	-7, -18, 25
3	0.29	-0.54	75	0	25	67	12	21	-8, 12, -4
4	-3.9	3.7	100	0	0	67	17	16	-33, 17, 16
8	-4	2.6	100	0	0	68	17	15	-32, 17, 15
9	0.51	-0.1	54	7	40	52	17	31	-2, 10, -9
12	-0.61	0.041	100	0	0	76	18	6	-24, 18, 6
13	0.42	-0.46	65	3	32	60	14	26	-5, 11, -6
14	1.5	-0.84	34	20	46	40	14	46	6, -6, 0
18	0.49	-0.45	60	3	37	60	12	28	0, 9, -8
23	1.2	-0.91	41	17	42	54	13	33	13, -4, -9

6.8 Williamson-Hall Methods

The Williamson-Hall method is one of the most popular methods used to determine size and strain values (Scardi et al. 2004, Soleimanian and Aghdaee 2008, Ungar et al. 1998, Balzar et al. 2004). The method is a multiple peak method that is used to separate size and strain contributions. The method works by fitting straight lines to plots of the full-width (or integral breadth) of different peaks, against the reciprocal of the lattice spacing, the gradient is used to find the strain and the intercept the size. Different methods can be used depending on the separation of size and strain and the use of the contrast factor (Scardi et al. 2004).

Williamson-Hall methods, which are only used on peaks from the same family:

$$\beta(g) = \beta_S + \beta_D = K/\langle D \rangle_V + 2g\epsilon_{\max} \quad \text{WH-1}$$

$$\beta^2(g) = \beta^2_S + \beta^2_D = K/\langle D \rangle_V^2 + 2g^2\epsilon_{\max}^2 \quad \text{WH-2}$$

$$e_{rms} = \frac{2\epsilon_{\max}}{(2\pi)^{0.5}} \quad (6.6)$$

Where, $\beta(g)$ is the full-width of a particular peak with a reciprocal d-spacing of g .

The subscripts S and D represent size and strain components, K is a constant

(K=0.9), $\langle D \rangle$ is the crystal size and ϵ_{\max} is the upper bound of the microstrain.

Modified methods, which use the contrast factor and allow peaks from different families:

$$\beta(g) = K/\langle D \rangle_V + f_M g \sqrt{(\rho \bar{C}_{hkl})} + O(g^2 \bar{C}_{hkl}) \quad \text{mWH-1}$$

$$\beta^2(g) = K/\langle D \rangle_V^2 + f_M^2 g^2 (\rho \bar{C}_{hkl}) + O(g^4 \bar{C}_{hkl}^2) \quad \text{mWH-2}$$

$$\beta(g) = K/\langle D \rangle_V + \sqrt{\rho} f_M g^2 \bar{C}_{hkl} + O(g^4 \bar{C}_{hkl}^2) \quad \text{mWH-3} \quad (6.7)$$

Where, f_M is related to the parameter M (discussed later) and gives information about the dislocation structure, ρ is the dislocation density, $O(..)$ gives information about the dislocation arrangement and for simplicity is ignored.

For the WH approach, the FCC metals use the {111} and {222} peaks, and the HCP metals use the average of the results from the following families of peaks, (a) {10T0}, {20T0}, {30T0}, (b) {0002}, {0004}, (c) {10T1}, {20T2}. The mWH results use the first five diffraction peaks for FCC samples and the first 15 peaks for titanium samples.

The changes in the size and strain values with applied strain, fitted to a polynomial to help understand the errors in the WH-1 methods, are shown in Figure 6-14 and Figure 6-15 and the errors for WH-1 and WH-2 methods in Table 6-10. In general, the errors in the WH methods (Table 6-10) are larger than for the full-width method (Table 6-1.). However, there are variations based on the

different method used, the errors varying from around 10 times to approximately the same as the full-width method.

Overall, the micro-strain values have lower errors than the crystal size values. This can be seen both in the number of data points that are reliable, follow the trend of the majority of other points and are not unrealistic negative values, and the deviation of these reliable points from the fitted trend. The difference between errors in the strain values obtained using the standard and modified approaches, is mainly due to differences in the amount of reliable points. The deviation from the fitted trend does not change much between standard and modified approaches.

The micro-strain values of the two standard approaches are similar within the error of the methods. The strain values for the different modified approaches cannot be directly compared with the standard methods without an assumption about the dislocation arrangement (or density). However, it can be seen, in Figure 6-16 that the different methods show similar trends for the different metals.

The size values are much less reliable than the strain values, as indicated by the difference in reliable points in Table 6-10. For the standard method negative values are often observed and for the modified approaches large size values that do not fit with the trend of the other results are found. The reason for this difference is that in the modified approach a fitting boundary is used to stop negative size values, whereas this is not done in the standard approaches. As is found with the strain values from the fit does not change significantly between the standard and modified approaches. The lowest deviation values are the WH-2, for the standard approach, and mWH-3, for the modified approaches.

Unlike the strain values, the size values can be compared with each other. There are systematic differences between the methods, but these differences are different depending on the metal (Figure 6-17). For example, the WH-1 method gives higher values than WH-2, for Ni-200, but lower for Ti-6Al-4V. The differences between the modified approaches, for different metals, are clearer. The mWH-3, consistently gives the lowest size values and mWH-1 and mWH-2 give similar values. When comparing standard and modified approaches the difference

between FCC metals and titanium is particularly noticeable. For FCC metals the mWH-3 method best matches WH-2 method, the more reliable of the standard approaches. Whereas, for Ti-6Al-4V there is a large difference between the results of these two metals.

The main difference between standard and modified approaches is the greater amount of systematic errors, or unreliable results, found with the standard approaches. The use of the standard approach is advantageous to the modified approach because it requires fewer peaks and doesn't introduce additional systematic errors from the use of the contrast factor. To reduce these errors, the following recommendations are suggested by me:

- WH-2 method should be used instead of WH-1. Similar values are obtained but WH-2 has less systematic errors.
- Both WH-1 and WH-2 methods can be used to verify how reliable a size and strain value obtained is. The results of the methods can also be combined, if the values are close, to reduce random errors.
- To reduce systematic errors in the size component, it is recommended that size values above 10^6 and less than 0, should be ignored and the measurement repeated with more accuracy or at a different part of the sample (sampling different grains).
- The modified approach (either mWH-1 or mWH-2) could be used on some data to verify the size values.

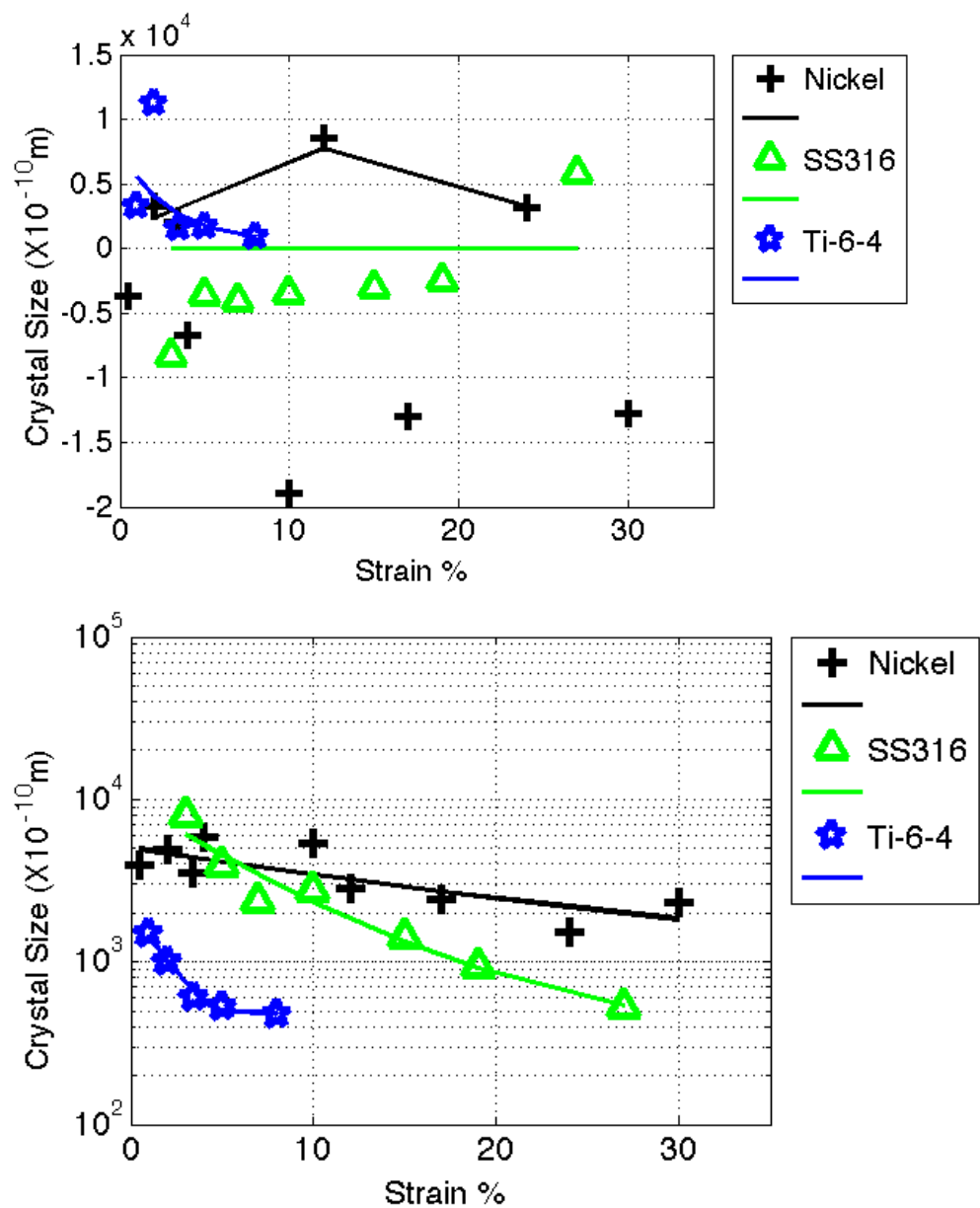


Figure 6-14. The change in crystal size values (in \AA), for the WH-1 (top) and mWH-3 (bottom) methods. The lines represent a fit of the values to a 2nd order polynomial (see text Section 6.2).

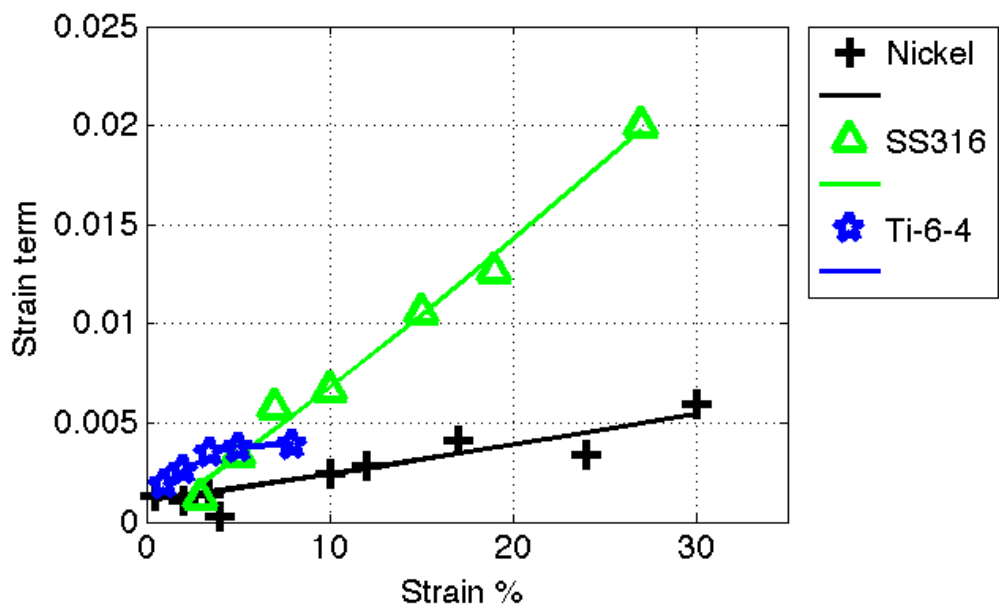
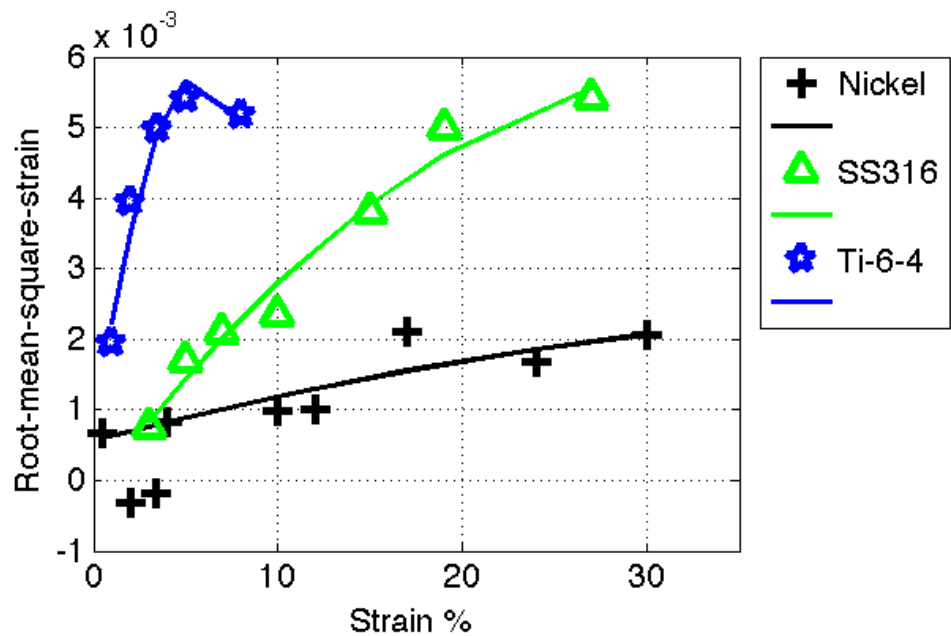


Figure 6-15. The change in strain term size, the rms-strain for the WH-1 method (top) and the strain component for the mWH-3 method (bottom). The lines represent a fit of the values to a 2nd order polynomial (see text Section 6.2).

Table 6-10. Errors associated with strain and size values from the Williamson-Hall methods, for Ni-200 and Ti-6Al-4V. The fractional deviation from a polynomial fit of the data, and the percentage of results that are used in this fit, because they are assessed to be part of a trend, are shown.

	WH-1	WH-2	mWH-1	mWH-2	mWH-3
Size- Ni	0.22	0.21	0.29	0.35	0.24
Size- SS-316	-	0.15	0.25	0.18	0.15
Size- Ti	0.54	0.35	0.23	0.66	0.037
Size % Reliable FCC	29	83	85	73	100
Strain- Ni	0.14	0.22	0.21	0.18	0.21
Strain- SS-316	0.085	0.089	0.16	0.082	0.10
Strain- Ti	0.062	0.052	0.034	0.021	0.018
Strain % Reliable FCC	89	95	100	100	100

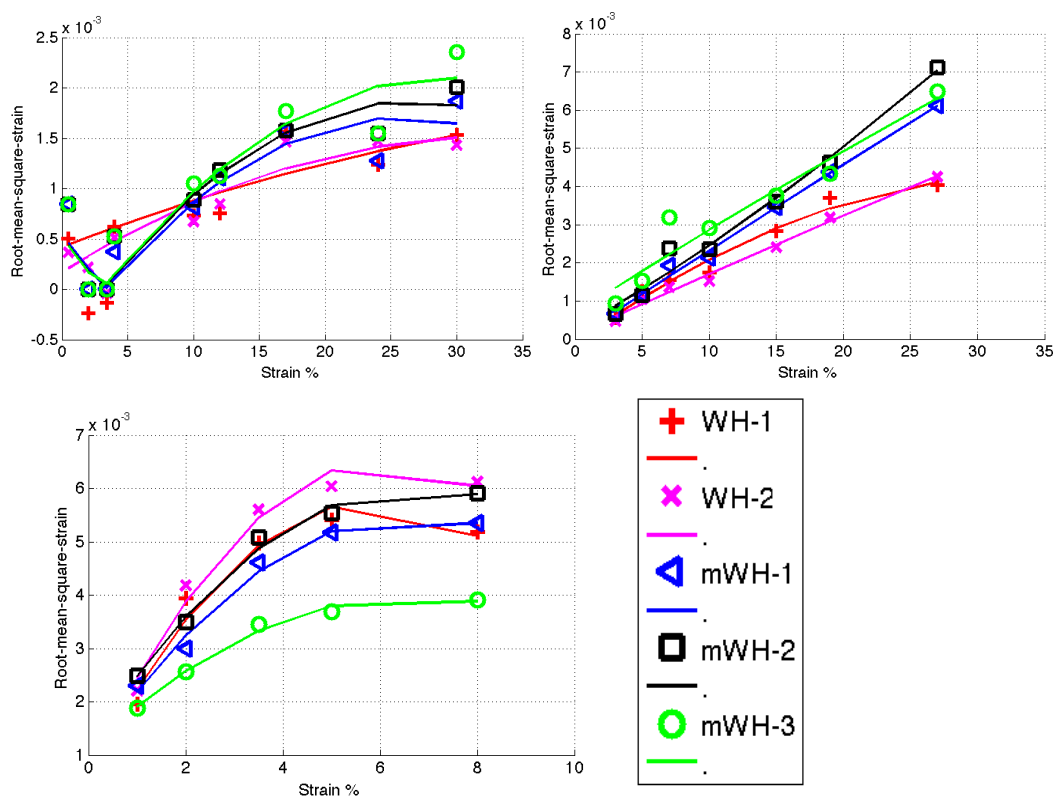


Figure 6-16. The change in the strain values found from different Williamson-Hall methods. The rms-strain is shown for the WH methods and the overall strain term for modified methods. The changes are shown for Nickel-200 (top left), SS-316 (top-right) and Ti6Al-4V (bottom). The lines represent a fit of the values to a 2nd order polynomial (see text Section 6.2).

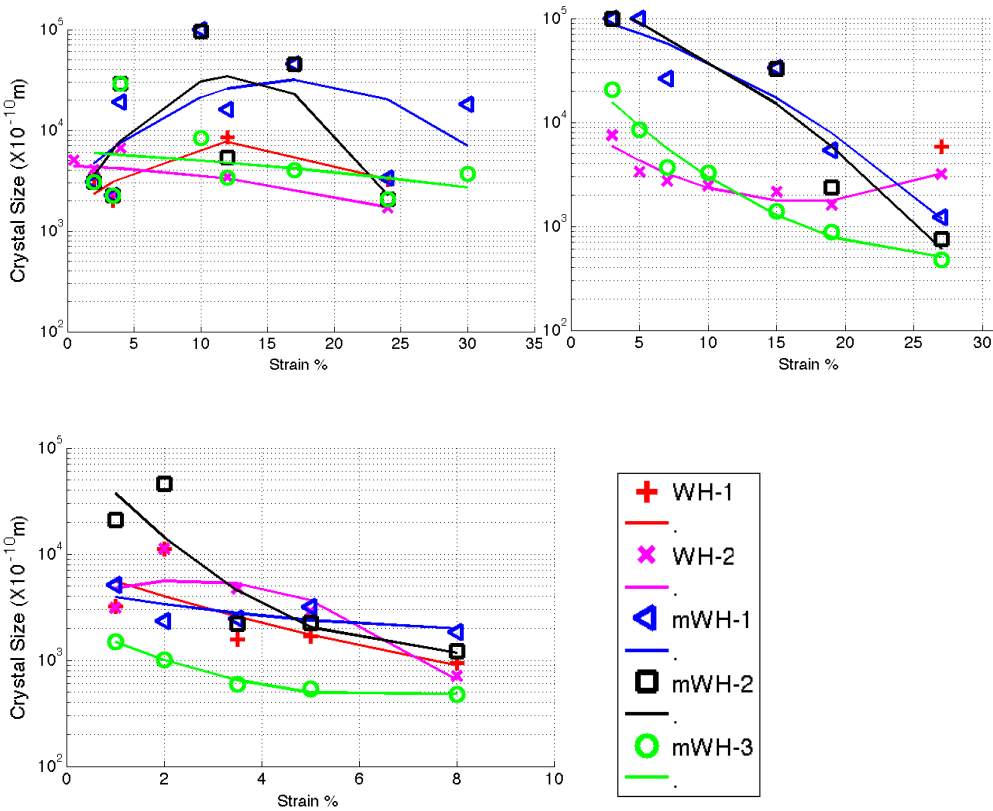


Figure 6-17. The change in the crystal size values (in \AA) found from different Williamson-Hall methods. The changes are shown for Nickel-200 (top left), SS-316 (top-right) and Ti6Al-4V (bottom). The lines represent a fit of the values to a 2nd order polynomial (see text Section 6.2).

6.9 Fourier Methods

In this section, the implementation of the different Fourier methods, used in this thesis, are discussed. More details of the Fourier methods can be found in Section 2.4.3. The Warren-Averbach method is the most used method when obtaining a more detailed description of the microstructure than just size and strain. However, there are various approaches that can be taken when using this method. There are two different equations that can be used, known as the ‘log’ and ‘linear’ versions (van Berkum et al. 1994). There are also different ways in which these methods can be fitted to the data. The difference in these approaches will be investigated. A Fourier method that is rarely used is the alternative method (van Berkum et al. 1994). It is based on a similar derivation to the Warren-Averbach but with different assumptions. The usefulness of this method is also investigated.

The different methods that are investigated are:

•log-INDI-

- uses the log form of the Warren-Averbach method (equation 2.40) and Fourier coefficients with distinct values of L are fitted separately

•log-ALL-

- uses the log form of the Warren-Averbach method (equation 2.40) and all the Fourier coefficients are fitted together

•lin-INDI-

- uses the linear form of the Warren-Averbach method (equation 2.41) and Fourier coefficients with distinct values of L are fitted separately

•lin-ALL-

- uses the linear form of the Warren-Averbach method (equation 2.41) and all the Fourier coefficients are fitted together

•individual-

- the same as log-INDI but peaks of the same family are used and the contrast factor is not used

•alternative-

- uses the alternative method (equation 2.42 and equation 2.43), peaks of the same family are used and the contrast factor is not used

The Fourier methods that use the contrast factor results use the first five diffraction peaks for FCC samples and the first 15 peaks for titanium samples. For the individual and alternative methods, the FCC metals use the {111} and {222} peaks, and the HCP metals use the average of the results from the following families of peaks, (a) {10T0}, {20T0}, {30T0}, (b) {0002}, {0004}, (c) {10T1}, {20T2}.

These methods and how they are applied are explained first and then in the next part results of these methods and errors.

6.9.1 Fourier Methods, Preparing the Data

After fitting the diffraction profile, using the method described previously, there are a few more processing procedures to follow before the different Fourier techniques can be used.

The intensity values are dependent on a smoothly varying function, known as the Lorentz-Polarisation factor (Warren 1969). However, the correction for this function was neglected since it has a small effect unless the peaks are very wide.

To obtain the Fourier coefficients it is necessary to find the intensity values of each of the diffraction peaks between a constant separation (ΔK), with the peak centre in the middle. The separation chosen was $\Delta K = 0.04(10^{-10} m)$, which gave enough information on the peak shape without being too big to be affected significantly by the overlapping of other peaks. To remove the instrumental broadening Stokes correction (Stokes and Wilson 1944) was used. The method was found to be very useful in removing instrumental broadening; however, it can on some occasions become unstable. This is especially the case if instrumental broadening is large in comparison to the physical broadening, which can be the case in the FCC samples deformed to low amounts of strain measured using the lab x-ray. It is normal to use either a LaB₆ or a silicon standard, chosen because it displays very little physical broadening. The instrumental peak used for each measured peak being the one that is the closest in reciprocal space. This was the method used for the titanium samples, where an instrumental sample of LaB₆ was used.

A different approach is to use the same material that is measured. It was found that heat-treated and annealed samples of SS-304 displayed similar broadening to a silicon standard. The results obtained with the different instrumentals were similar to each other but those using the stainless steel samples had less random error. The stainless steel instrumental sample has peaks at approximately the same angle as both the stainless steel and nickel samples, whereas the silicon standard

did not. This meant it was not necessary to remove the α_2 component of the peak before the removal of the instrumental broadening. For these reasons an annealed stainless steel 304 sample is used as an instrumental, for the FCC analysis.

The level of the background has an important influence on the Fourier coefficients, particularly at low Fourier lengths. Incorrect estimation of this level will produce incorrect results, including the forbidden ‘hook-effect’ of size Fourier coefficients. The problem is that there is no way of determining beforehand what the level should be, although there are instances when it is obvious that the background level is either under or overestimated (Figure 6-18). The most complete method to deal with this is to use the background level of all measured and instrumental peaks as a fitting parameter in the different Fourier methods. However, this can increase computational time considerably and would be difficult to incorporate effectively. Instead, a simpler method was adopted. The method tries to fit a straight line to the first few Fourier coefficients of the measured, instrumental and physically broadened peaks, the background level that is used is when these straight lines best fit the data. If this gives results that are inconsistent with other results and expectations (e.g. the ‘hook-effect’ or unrealistic values), the procedure can be repeated by adjusting the background manually then repeating.

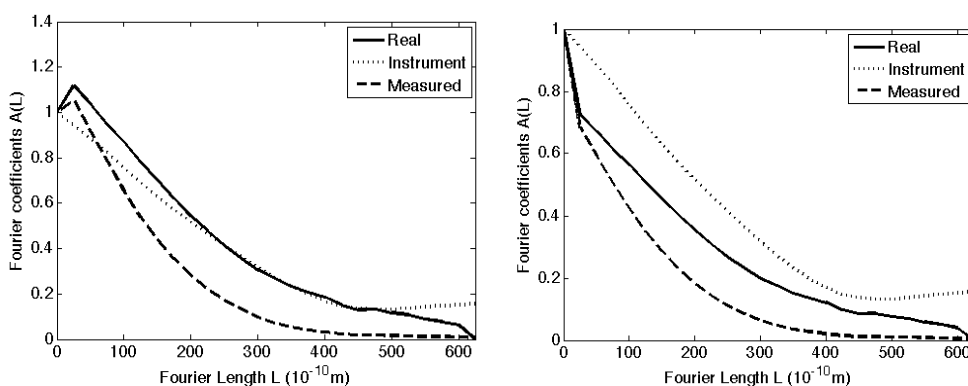


Figure 6-18. The effect on the measured and real Fourier coefficients when the background level is changed. (a), left, an overestimation of the background and (b), right, an underestimation.

6.9.2 Fourier Methods, Analytical Approach

In this section the details of how the different Fourier methods have been applied are given. The originally method to separate the size and strain coefficients was done by fitting the Fourier coefficients with different n (or L) separately or individually. However, it has become popular (Ribarik et al. 2001, Scardi and Leoni 2002) to fit to all the Fourier coefficients together, or even to the intensity values by using the relation between the Fourier coefficients and the intensity. Both of these approaches are investigated, and an example of the two methods for the log-WA method is shown in Figure 6-19. When using the different approaches slightly different equations describing the size and strain are used.

6.9.2.1 The INDI method of fitting

For the first approach, ‘INDI’, the size Fourier coefficients are given by the simpler size description (equation 4.6) and the Groma and colleagues (Groma et al. 1988) description of the strain Fourier coefficients (equation 2.67).

Other than the ‘individual’ methods and the alternative method all methods are used with the contrast factor. Equation 2.62 and 2.64 are used to describe the contrast factor in FCC and HCP metals, respectively. As described before the q-values are allowed to change to obtain the best fit. The q-values for the FCC analysis were obtained from a preliminary ‘ALL’ fit of the Fourier coefficients, for both ‘ALL’ and ‘INDI’ methods. Whereas, for the titanium data the q-values used were obtained from the mWH-1 method.

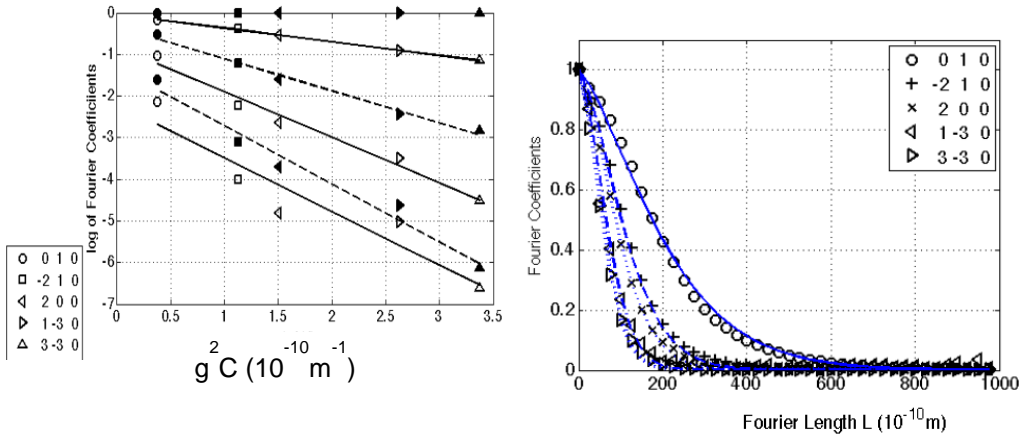


Figure 6-19. Comparison of WA approaches, the WA plot for the log-INDI (left) and Fourier coefficients for log-ALL WA methods (right). A Ti-6Al-4V sample is used as an example. In the log-INDI method lines are fitted to the FCs at different n values, as shown on the left, where different lines represent different n or L values. Whereas in the log-ALL method the Fourier coefficients are fitted together over a range of n (or L) values as shown on the right.

Size Coefficients

When using the ‘INDI’ methods and the alternative method, the size coefficients were fitted to the following equation:

$$A_L^S = \exp(-L/D) \quad (6.8)$$

This is a simplification that has been used by others (de Keijser et al. 1982) but can lead to errors in size and even strain values, depending on the fitting method (Houska C R, Kuzel 1999). The coefficients were not determined with enough accuracy to use a log-normal distribution and adequately determine the difference between the variance and mean. This was particularly the case with the laboratory X-ray samples, where in some cases the size coefficients could not be adequately determined at higher L values, when the size coefficients had fallen to values lower than 0.5. This makes evaluation difficult as it would not include most of the shape of the size coefficients, since they fall from 1 to 0 at a decreasing rate (see Figure 6-20).

In some of the specimens deformed at low strains the forbidden ‘hook-effect’ (Warren 1959, 1969) of the size coefficients was observed, irrespective of the 195

background level, such as seen in Figure 6-20a. This was corrected for by fitting a curve to the coefficients in the non-hooked region, extrapolating this to the y-axis and then normalising. The extent of the ‘hook-effect’ was larger for the titanium samples than the FCC samples. It is not clear whether this is because of the different diffraction source used or differences in the state of the metals. It is possible that the effect is a result of specific arrangement of dislocations, in the form of a small angle grain boundaries or a high value of the dipole character parameter M (Wilkens 1979). In this regard the results may suggest a tendency for the dislocations in titanium to arrange in low angle boundaries or with high values of M. The ‘hook-effect’ was different depending on the method used (Figure 6-20). In particular it was found to be larger when using the ‘log-INDI’ compared with the ‘lin-INDI’ method, for the Ti-6Al-4V data.

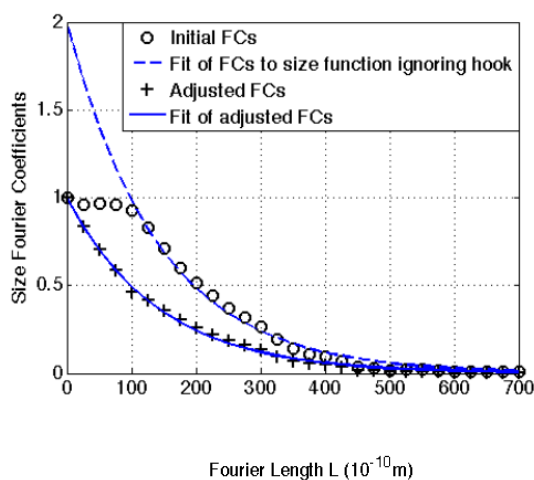


Figure 6-20. An example of the 'hook' effect for a Ti-6Al-4V sample using the Log-INDI method.

Strain Coefficients

The strain coefficients were fitted using the description of Groma et al. (1998), over the range of the Fourier length (L) of $100\text{-}300\text{\AA}$ for most of the data, since this is the region least affected by background (low L) or instrumental effects and limitations of the method (high L). The dislocation density was separated from the dipole character, M, by fitting straight lines to the log of the strain coefficients ($\ln A_D$) against the log of the Fourier length (L), which is called the Krivoglaz-

Wilkins plot (Kuzel 2007). The dislocation density (ρ) is found from the gradient, the dipole character (M) is found from the intercept. The relationship is found by re-arranging equation 2.67, and is shown below:

$$\frac{\ln A_D(L)}{L^2} = \rho \bar{C} B \ln(R_e) - \rho \bar{C} B \ln(L)$$

$$B = \pi b^2/2, M = R_e \sqrt{\rho} \quad (6.9)$$

In some cases the data in the Krivoglaz-Wilkins plot (K-W plot Figure 6-21) was curved. This was particularly the case for the lin-INDI method, which was often considerably curved, whereas the K-W plot for the log-INDI WA method in most cases showed a linear relationship. In Figure 6-22, there is an example how the separation of the dislocation density and dipole character can produce systematic errors. The K-W plot in this figure is curved; the dislocation density and M results vary significantly depending on what part is fitted, a lower gradient corresponds to a lower dislocation density and a higher dipole character. In the example shown the differences in results are significant, the dislocation density is 60% higher and M 24% lower, when fit to the low L values.

Hence, there is the possibility for systematic errors to be introduced by the choice of where to fit the straight line in the K-W plot. To reduce these errors the line was fitted to the 100-300 Å regions when possible. If the data points in this region were not in a straight line the procedure was to try to find another region where they were. The new region would be used if it had Fourier length values (L) which corresponded to Fourier coefficients of the different peaks, between 0.2 and 0.8. These values were set to avoid high and low L values, which can be problematic.

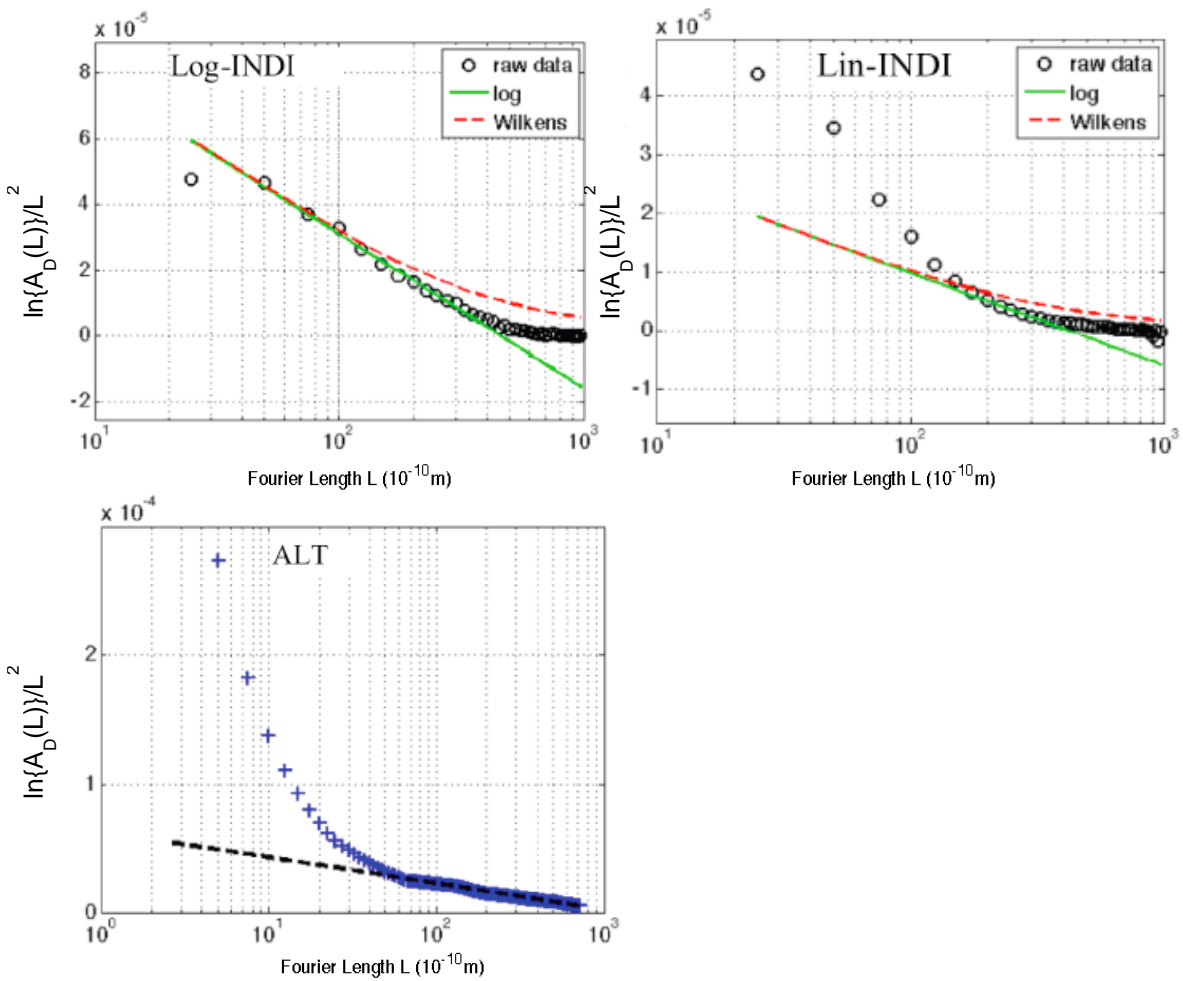


Figure 6-21. Example Krivoglaz-Wilkens plots, the log of the Fourier length against the strain coefficients. Top left for Log-INDI, top right for Lin-INDI and bottom for the alternative method, for the same Ti-6Al-4V sample.

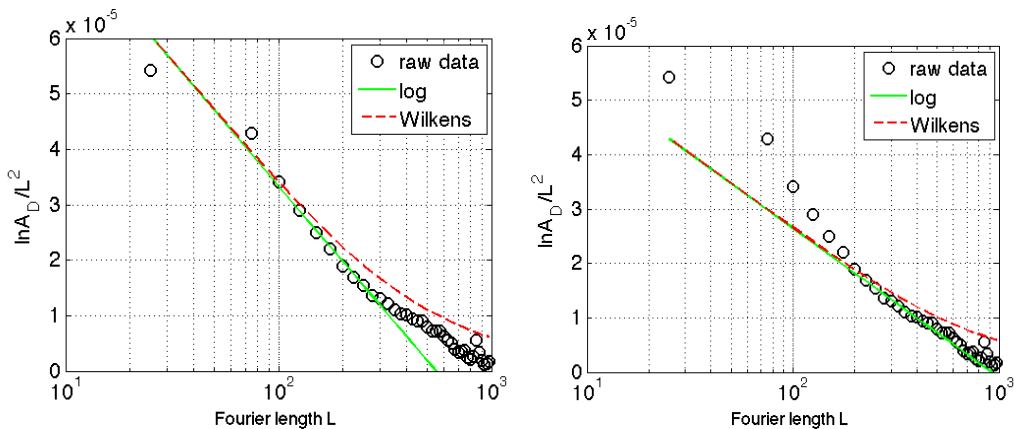


Figure 6-22. Krivoglaz-Wilkens plots for SS-316 at 10% applied strain found using the WA log-INDI method, with two different fits to the data, at different ranges of L values. The fit on the left, gives a dislocation density 60% higher and an M value 24% lower than the fit on the left.

6.9.2.2 The ALL Methods of fitting

In the INDI method of fitting the distinct Fourier coefficients, with particular L values, of different peaks are fitted separately. However, in the ALL method all the Fourier coefficients of all peaks, within a set range of L values, are fitted together. To do this the Fourier coefficients must be fitted to a function that describes both the size and strain distribution. These functions must also be valid over the whole range of L used. This means that the Wilkens function must be used instead of Groma's description, because it doesn't increase at high values of L and therefore better describes the strain coefficients over the whole range of L. The log-normal description of size is also used to avoid the simplifications of the equation used in the 'INDI' method, which in this case would also effect the strain parameters.

When fitting to the log of the Fourier coefficients it was found that the separation of the dislocation density from the dipole character was problematic and in some cases the values of the dipole character found were very low and the value of the dislocation density very high (this was especially the case for nickel). To try to reduce this error a lower fitting boundary was introduced to the dipole character. However, this did not remove the error and the results when this occurred were unreliable.

When adopting the ALL approach the choice of range that the Fourier coefficients are fitted over, has an influence on the results obtained. In principle, this would be done over the entire length of the Fourier coefficients, or at some point after all the coefficients are sufficiently close to zero. However, in practice this was not possible without adversely affecting the results, because the Fourier coefficients often became unreliable at a certain values of L. This was particularly evident for the lab x-ray samples. This is possibly due to poor sampling, deconvolution or other instrumental effects. Therefore, the coefficients had to be fitted to the largest range possible that was thought to be reliable. The effect of the fitting range is shown in Figure 6-23, for a Ti-6Al-4V sample. If the range selected is so that the peak with the slowest decay has Fourier coefficients less than around 0.1, the values are almost constant. For ranges below this the values change, the crystal

size and dislocation density increase and the dipole character falls. This behaviour may explain the systematic error that is sometimes observed in the FCC samples, where the dipole character goes to lower values and the dislocation density to high values. This behaviour is the same that was shown in Figure 6-22, for the log-INDI method.

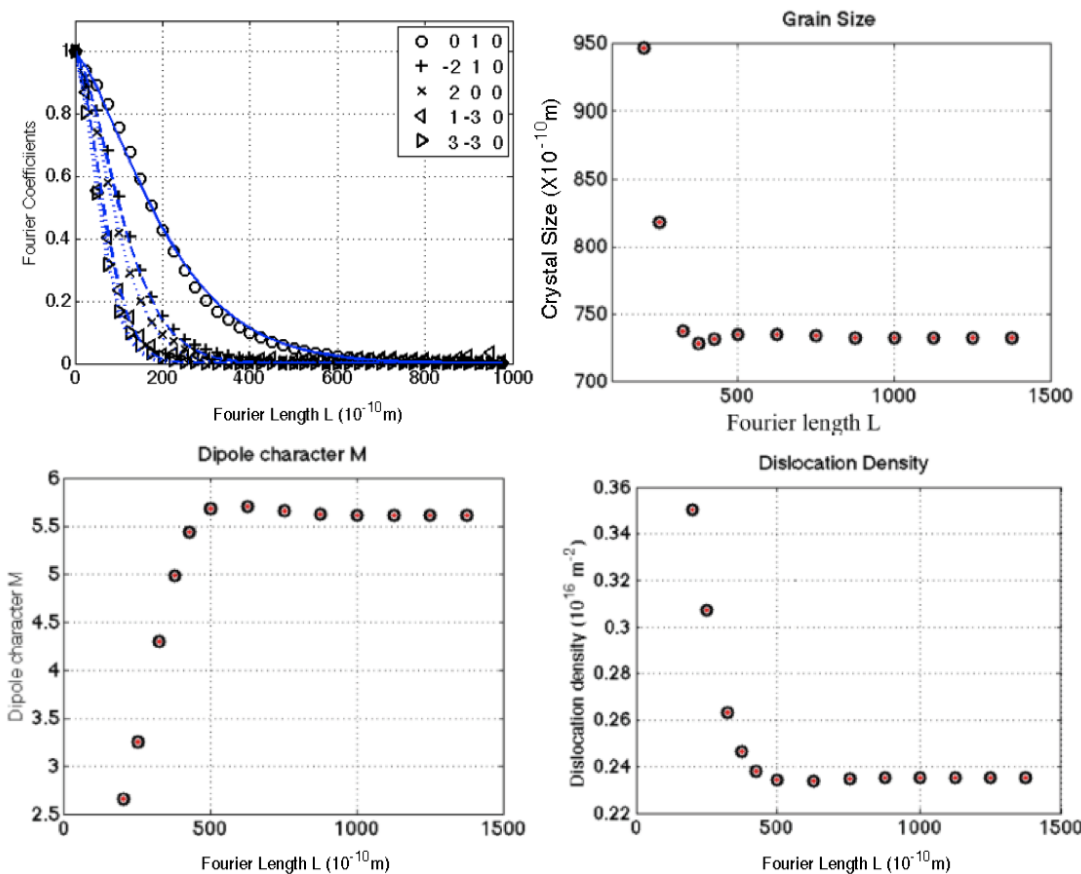


Figure 6-23. An example of the change in the parameters obtained from a WA log-ALL analysis when the fitting range is changed. This is done for the same Ti-6Al-4V sample.

6.9.3 Fourier Method, Errors and Best Practice

The changes in the dislocation density and size values with applied strain, fitted to a polynomial to help understand the errors in the different Fourier methods, are shown for the log-INDI and log-ALL methods in Figure 6-25 and Figure 6-24, and the errors for all Fourier methods in Table 6-11.

There is a significant variation in the errors from the different methods. For the dislocation density values the INDI methods have the lowest deviation from the fit. The log-INDI method has the lowest error, for the FCC metals the deviation is close to or double that found with the full-width method. The two methods that use fewer peaks (individual and alternative) have much larger errors. The difference is much larger than the difference found in the WH method (strain values), where there was little difference in the deviation from the fitted trend when using less peaks. Considerable errors were also found with the log-ALL method. The main reason for this appears to be due to the difficulty the method had in separating dipole character and dislocation density values. However, it should be noted that the errors were large for both the FCC and Ti-6Al-4V samples, so it is not just a feature of the quality of peaks.

The methods give systematically different values to each other but the differences are different for the different metals (Figure 6-27). The exception to this is the alternative method, which has the lowest dislocation density values for all the metals. These differences are considered in more detail in the next chapter.

The variations in the errors of the size value of different methods are much smaller than for the dislocation density. The deviation varies from less than 0.1 to around 0.3 (with the exception of the alternative method for nickel). The largest errors are for those methods that use the fewest peaks (individual and alternative). In comparison to the WH method these methods are not prone to produce unrealistic negative or too high values. Unlike the dislocation density values, the errors in the size values of the log-ALL method are comparable to the log-INDI and lin-INDI methods.

The different WA methods show the same trends in the change size values, but with systematic errors between them (Figure 6-26). The log-ALL method gives the highest size values, which may be because this method has a different function to describe size or the difference of the ALL approach. If the former were the case then it would suggest that the use of the simplified Cauchy size function gives a systematic error to give lower size values. The log-INDI, lin-INDI and individual

give similar values of the size, within the error of the measurement. Which, suggests the use of the contrast factor does not give a big additional systematic error to the size values. The alternative method provides the largest size values, which are at or close to the upper fitting limit for SS-316 and Ti-6Al-4V, which is probably due to the differences in the separation of size and strain in this method in comparison to the WA methods.

The following recommendations are made by me for use of Fourier methods, based on the errors found and the analytical approach taken:

- The INDI method is recommended, and in particular the log-INDI method. The method has less errors and is less prone to difficulties in separating dislocation density and arrangement. This is especially the case if the quality of peaks is lower, for example if a laboratory x-ray is used.
- The individual method is not recommended unless there are at least two peaks with a relatively good quality. That is better quality than the 222 peak measured here.
- The ALT method could be considerably improved by inclusion of the more peaks, possibly by using the contrast factor.

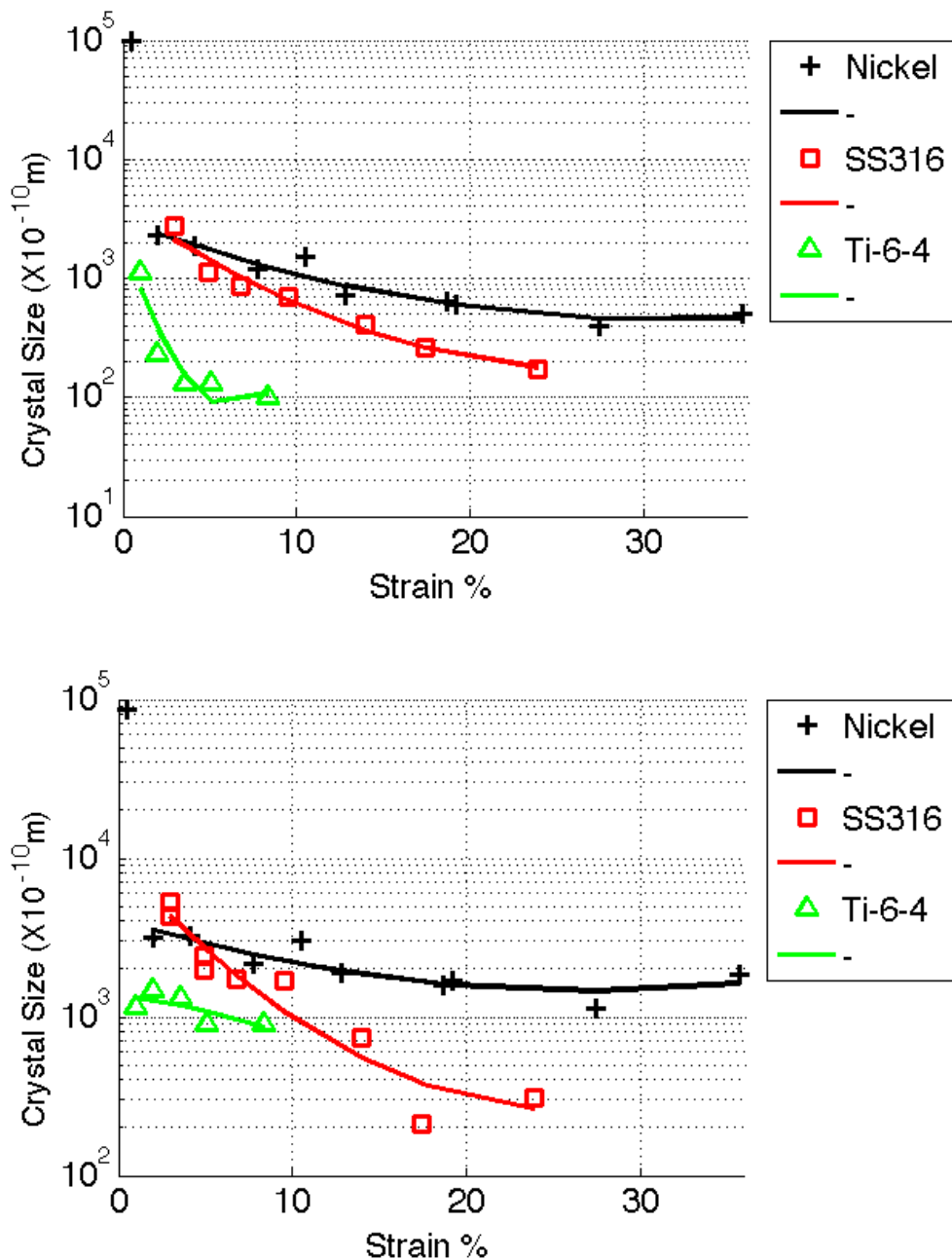


Figure 6-24. The change in crystal size values (in Å), for the log-INDI (top) and log-ALL (bottom) methods. The lines represent a fit of the values to a 2nd order polynomial (see text Section 6.2).

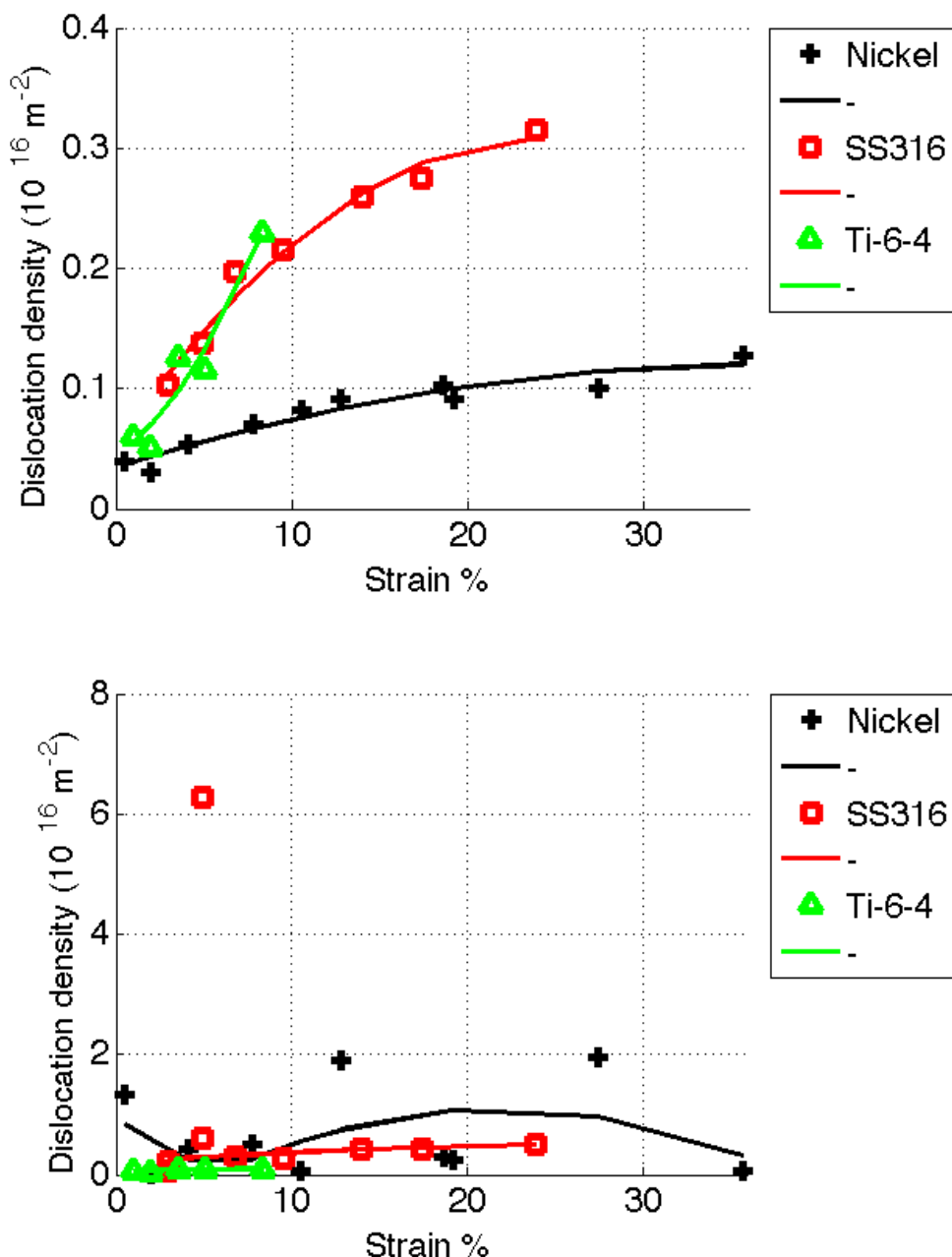


Figure 6-25. The change in dislocation density values, for the log-INDI (top) and log-ALL (bottom) methods. The lines represent a fit of the values to a 2nd order polynomial (see text Section 6.2).

Table 6-11. Errors associated with dislocation density and size values from the Warren-Averbach methods, for Ni, SS-316 and Ti-6Al-4V. The fractional deviation from a polynomial fit of the data, and the percentage of results that are used in this fit, because they are assessed to be part of a trend, are shown.

	log-INDI	lin-INDI	log-ALL	individual	alternative
Size- Ni	0.12	0.063	0.13	0.30	2.0
Size- SS-316	0.13	0.14	0.24	0.16	0.14
Size- Ti	0.28	0.095	0.12	0.29	0.0004
Size % Reliable FCC	95	95	95	95	95
Dis. Dens. Ni	0.095	0.16	0.90	0.55	0.23
Dis. Dens. SS-316	0.047	0.075	0.29	0.53	0.40
Dis. Dens. Ti	0.16	0.084	0.19	0.16	0.06
Dis dens % Reli. FCC	100	100	95	95	100

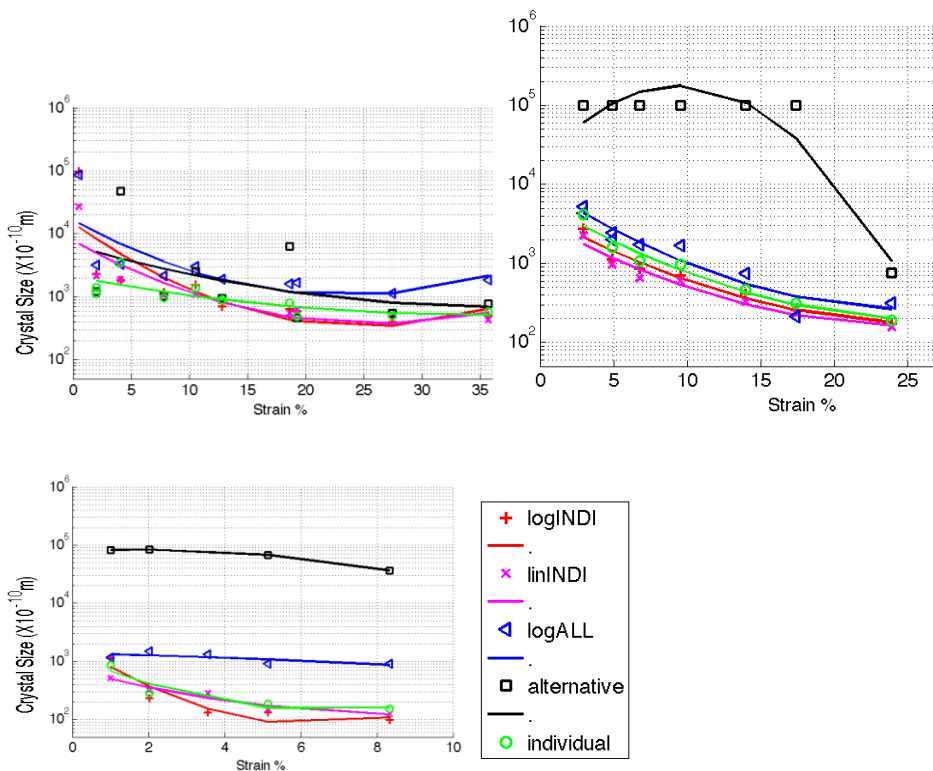


Figure 6-26. The change in the crystal size values (in Å) found from different Fourier methods. The changes are shown for Nickel-200 (top left), SS-316 (top right) and Ti6Al-4V (bottom). The lines represent a fit of the values to a 2nd order polynomial (see text Section 6.2).

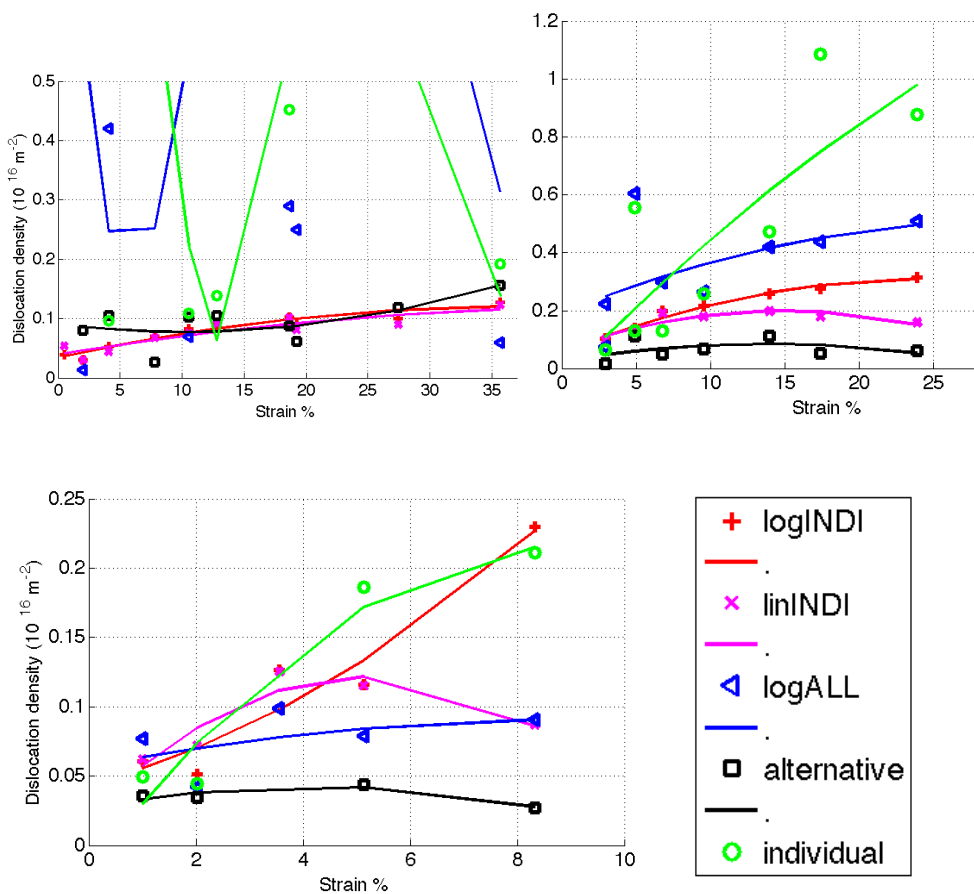


Figure 6-27. The change in the dislocation density values found from different Fourier methods. The changes are shown for Nickel-200 (top left), SS-316 (top right) and Ti6Al-4V (bottom). The lines represent a fit of the values to a 2nd order polynomial (see text Section 6.2).

6.10 Conclusion

In this chapter, details of how different DPPA methods work and how they are implemented have been presented. Details of the best practise in their use and a qualitative understanding of the errors involved have been discussed.

The use of the full-width is the simplest method and the one with the least errors. The more complicated methods, that try to use the shape of the peaks to quantify details of the microstructure in more detail, increase the magnitude of the errors.

The single line methods that use the analytical pseudo-Voigt fit, integral breadth and Variance-A methods, were shown to be unreliable for analysing the FCC samples, because they produced large errors and unreliable results. This suggests either that the underlying assumptions in these methods are flawed, or the use of a pseudo-Voigt to fit the data cannot be determined accurately enough.

The use of the Variance-B method involved a complicated fitting method that only worked on some peaks. The reason that the method only worked on a limited number of peaks was not determined, but adds an uncertainty to the validity of the underlying formula. The method is also prone to large systematic errors because of the complicated fitting procedure.

For FCC samples, the use of the Williamson-Hall methods compared to the use of the full-width, gives errors 3-5 times higher for strain values, and up to 7 times higher for size values. There are particular problems found in determining the size values, where unreliable values are often observed. The use of the contrast factor produces less of these unreliable results, but with similar random errors. The mWH-3 method has the lowest errors and of the two standard approaches, WH-2 has the lowest errors.

The errors vary widely for different Fourier methods and in general are smaller for the dislocation density values. The Fourier methods do not have the same problem, as the WH methods, with unreliable crystal size values and also have lower errors. The use of the contrast factor reduces the errors in both size and dislocation density values and consequently the alternative and individual methods give the largest errors. The log-ALL method has higher errors in the

dislocation density values, which is probably due to problems in separating dislocation density and dislocation arrangement values. The INDI methods have the lowest errors overall, and in particular the log-INDI has the lowest errors being around two times higher than the full-width errors.

Based on these findings, it is recommended that the full-width is always used as a first step to characterise a deformed metal. If more detail is required, it is recommended that the mWH-3 and log-INDI methods are used because of their lower errors.

7 Application of DPPA Methods

7.1 Introduction

In this chapter I will evaluate the meaning of the results from diffraction peak profile analysis (DPPA) methods. This is done to find out the usefulness of these methods to study deformed metals.

To achieve this aim I will study a number of different popular DPPA methods (how these methods are implemented are described in Chapter 6), using lab x-ray and synchrotron diffraction measurements (described in Section 3.4). These methods are applied to different metals, which are chosen because they have different deformation microstructures. The alloys studied are SS-316, SS-304, nickel-200 and Ti-6Al-4V, details of these metals are found in Section 3.2 and 5.1. These metals are deformed by uni-axial tension and compression (see Section 3.3). To evaluate the DPPA methods, the results from the different methods at different applied strains are compared to knowledge about the deformation of these alloys.

The following details are considered:

- The full-width change in the different alloys;
- The meaning of crystal size;
- How different methods separate size and strain broadening;
- Whether the dislocation density values and slip system population predictions are representative of the alloys;
- The meaning of the dipole character and whether it can be used to characterise a metal and
- The use of the contrast factor equation to describe full-width broadening heterogeneity

7.2 Full-width Analysis Method

The diffraction peak full-width is the easiest DPPA parameter to determine and as shown in the last section has the lowest error. It is mainly used in situations where the quality of the diffraction peak is low, or there is a limited number of diffraction peaks available (Quinta da Fonseca et al. 2006, Wang et al. 2005, Frankel 2008, Evans et al. 2005).

In this section, we will examine how the full-width can be used to characterise a deformed metal. In addition, this discussion will be useful to evaluate whether there is any benefit in using more complicated methods.

In Figure 7-1, the change in the full-width with applied strain is shown for the different metals. When a strain is applied to these metals there is an accumulation of dislocations and dislocations can arrange to split crystals apart into smaller crystals. Both of these contribute to increase the full-width of a particular peak and hence the increases found for all metals is expected. From the figure, it appears that if the full-width values are extrapolated to zero-strain there is minimum full-width value of 0.002 found for all metals (the full-width has been corrected for instrumental broadening).

Figure 7-1 also shows that the relationship between the flow stress and the full-width is not linear for all alloys. It is apparent that there is a big difference between Ti-6Al-4V and the other metals but is not apparent why there is such a difference. In addition, whereas it would be expected that the two stainless steel metals should behave the same, the figure shows that the full-width of SS-304 is closer to nickel than SS-316.

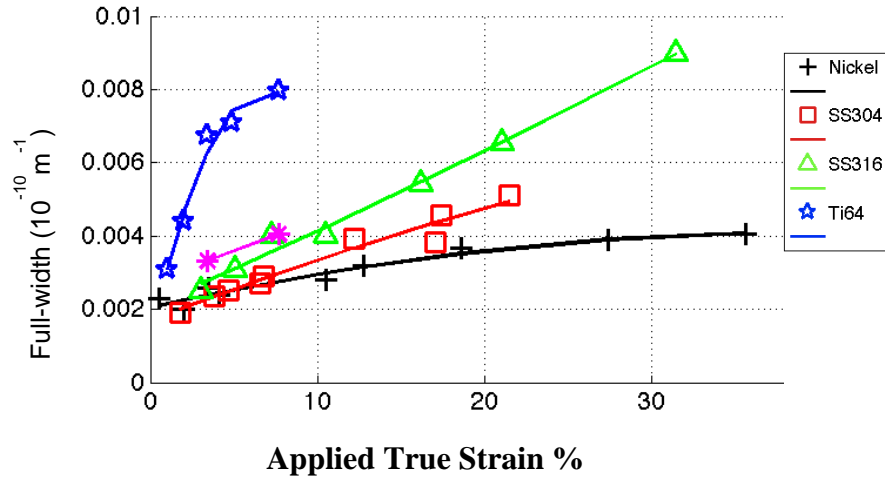


Figure 7-1. The change in the full-width of the different metals with true strain. The lines represent a fit of the values to a 2nd order polynomial (see text Section 6.2).

It is often beneficial to plot against DPPA parameters against stress instead of strain, as is done in Figure 7-2.

In order to understand this figure more, it is helpful to re-introduce concepts from the background section (Section 2.4). A description of how the full-width (β) may change with changes in the crystal size ($\langle D_V \rangle$) and dislocation density (ρ), is given by the modified Williamson-Hall equation (mWH-3) (Ungar, Gubicza et al. 2001).

$$\beta(g) = K / \langle D \rangle_v + \sqrt{\rho} f_M^2 g^2 \bar{C}_{hkl} \quad (7.1)$$

Where, K is the Scherer constant, f_M is related to the parameter M and gives information about the dislocation structure and g is the reciprocal of the d-spacing.

It has also been shown that the flow stress varies linearly with the square root of the dislocation density of a metal (Kocks and Meckig 2003) (and directly proportional to the work-hardening stress, that is the stress minus the yield stress), and the yield stress is proportional to the reciprocal of the dislocation cell size (Abson and Jonas 1972, Barrett et al. 1972, Lee and Lin 2001). Hence, based on Equation 7.1 it would be expected that the stress would be proportional to the full-width. Consequently, the intersection of this line with the x-axis should occur at

the yield point if dislocations are the dominant form of broadening and at zero if size broadening by dislocation cells is dominant.

From Figure 7-2 it can be seen that the two stainless steels do behave in a similar manner, that is distinctly different to nickel. The full-width increases at the same rate with stress for the two metals but with a slight offset in the stress. This is expected since the dislocation density might be expected to increase with the same rate with stress for the two metals. In these metals the crystals do break up due to deformation but defined dislocations structures are not expected to form (Section 5.1, Byun et al. 2003, Feaugus 1999) and so broadening by dislocations is expected to be dominant. The difference in the offset between the two curves of the full-width may be explained by the higher yield stress for SS-316. The yield stress of SS-304 is approximately 175MPa and for SS-316 is 250MPa. If the full-width values are extrapolated to zero strain, the yield stress at zero strain is found to be around 80MPa for SS-304 and 120MPa for SS-316. These extrapolated values are smaller than the yield stresses, which would not be expected based on the expected relationship between the flow stress and full-width. A possible explanation is that plastic deformation may be occurring before the macroscopic yield.

When the full-width of Ti-6Al-4V is extrapolated to zero strain, the stress (of around 860MPa) is found to be close to the yield stress (880MPa).

In contrast to the other metals, when Ni-200 is extrapolated to zero strain in Figure 7-2 the stress is found to be negative (around -400MPa). In addition, the rate of increase of the full-width with flow stress is lower than the other metals. Both these factors may be related to the higher stacking fault energy of this metal and the greater recovery it experiences. These differences mean that nickel accumulates less dislocations- and hence a smaller increase in full-width with stress. It also means that they develop a cell structure at low strains (Keller 2010), hence the full-width is related to the cell size as well as the dislocation density, which may cause the negative value of stress when the full-width is extrapolated to zero.

The full-width values increase approximately linearly with stress in Figure 7-2. The relationship is not exactly linear, particularly for SS-316, but Ti-6Al-4V and to a lesser extent Ni-200 (if the first point is ignored) are more linear than when plotted against strain. The reason that the full-width of the former two metals have a more linear relationship when plotted against stress, is because they both have a curved stress-strain curve, with a fall in the rate of work-hardening with increased strain. Hence, based on these results, a good approximation is that the work-hardening stress is directly proportional to the full-width, for those metals with low SFE. Since the work-hardening stress is the stress minus the stress at which plastic deformation starts this may differ and be lower than the 0.2% offset macroscopic yield. However, for nickel this relationship does not hold and may be a feature of its higher SFE.

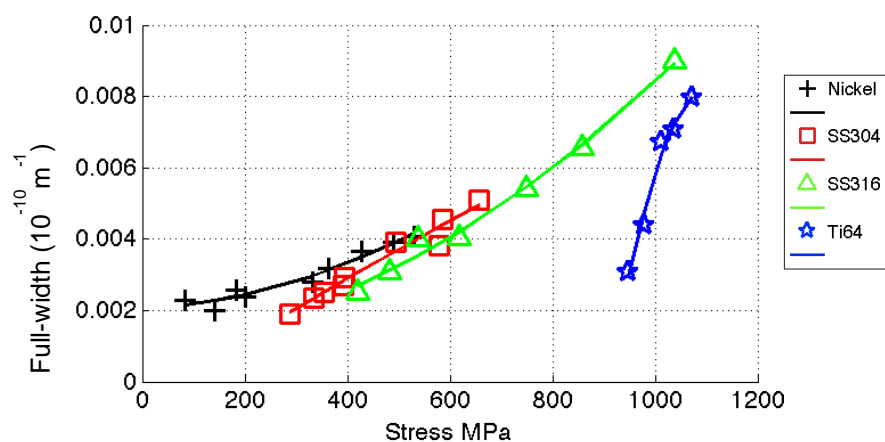


Figure 7-2. The change in full-width of the different metals plotted against the flow stress. The lines represent a fit of the values to a 2nd order polynomial (see text Section 6.2).

7.3 Size And Strain Broadening

Crystal size and micro-strain values are important parameters obtained by DPPA methods. In general, the crystal size represents the size of a domain that diffracts coherently (and incoherently with the rest of the sample) and the micro-strain is the micro-strain caused by the distortion of the lattice within these domains. The problem with the parameters is that they are different from the size and strain values that can be measured by other methods, such as TEM or EBSD.

In deformed metals there is, most often, a contribution to both size and strain broadening. Furthermore, these two values are interrelated, because they are both predominantly caused by the presence of dislocations. When no micro-strain is present, the use of DPPA methods has been found to be effective in determining the size of crystals (Kuzel 2007, Ungar 2003). However, when both size and strain broadening are present there is an ambiguity over what the parameters actually represent (van Berkum et al. 1994).

The aim of this section is to examine how different methods separate size and strain components and to try to better understand what size and strain broadening represent in the different methods.

Crystal Size

The size in DPPA is the length of a region in the metal that diffracts incoherently (or diffracts independently) with respect to all other regions. A region would diffract incoherently with another region if it were separated by a grain boundary, because of the difference in orientation. However, in metals with high SFE that develop a dislocation structure, it is often found that there is a discrepancy between TEM (or optical, or EBSD) size values of the dislocation structure and those found using DPPA (Ungar 2003, van Berkum et al. 1994, Kuzel 2007). This difference could be caused by a number of different factors, which include:

- Ungar (2003) argued that discrepancies are partly due to the fact that size values occur in a distribution. The different methods have different distributions and hence give different values when averaged.
- Ungar (2006) suggested that the walls of dislocation cells, with no misorientation across them can cause a break in coherency. Hence, it is argued that DPPA size results represent the size of undistorted regions of a crystal, whereas TEM results represent the size of regions misorientated from each other.
- The presence of planar faults can cause systematic reductions in the size values (Warren 1969).

- Alternatively, van Berkum et al. (1994) suggested the discrepancy could be due to systematic errors due to the mathematics involved in the separation of size and strain values. They also suggested that only high angle boundaries and small angle boundaries that had very large local strain concentrations would result in a break of coherency.

In order to understand which if any of these explanations are valid in our case, the changes in the crystal size values for the different methods and metals are considered.

7.3.1 Crystal Size in Nickel

Nickel, due to its high SFE (see Table 3.2), is the only sample that develops a dislocation cell structure, under the conditions tested at (see Section 2.1.6). Hence, it is the only sample whose crystal size component (from DPPA methods) can be compared with other measurements.

It has also been shown that when a cell structure develops, the dislocation cell size falls with increasing applied strain and flow stress. The flow stress and the dislocation cell size have been found to be almost inversely proportional (Abson and Jonas 1972, Barrett et al. 1972, Lee and Lin 2001, Raj and Pharr 1986). The change with the crystal size for different DPPA methods, for nickel are shown in Figure 7-3. The absolute size values and the rate the size falls are different for the methods. The crystal values variations are large, and can vary by a factor of around 100.

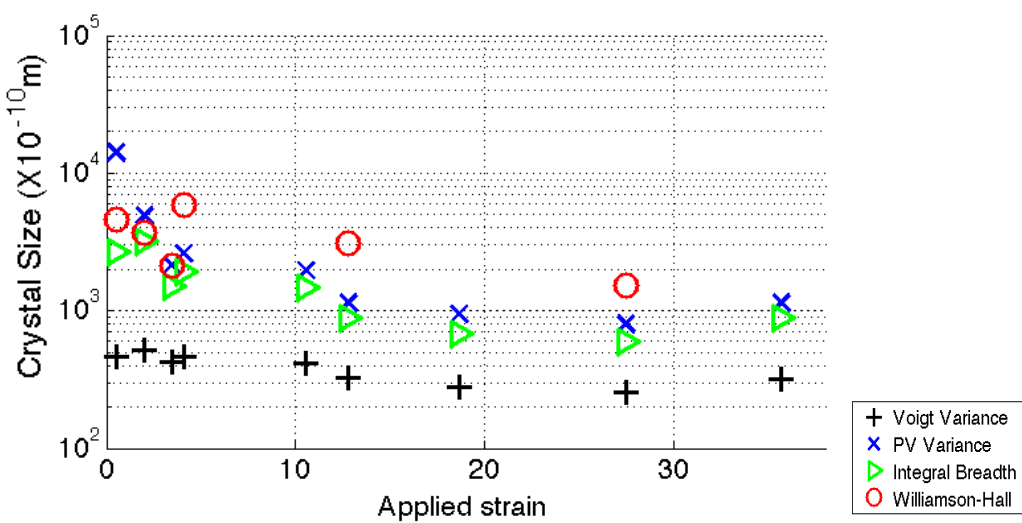
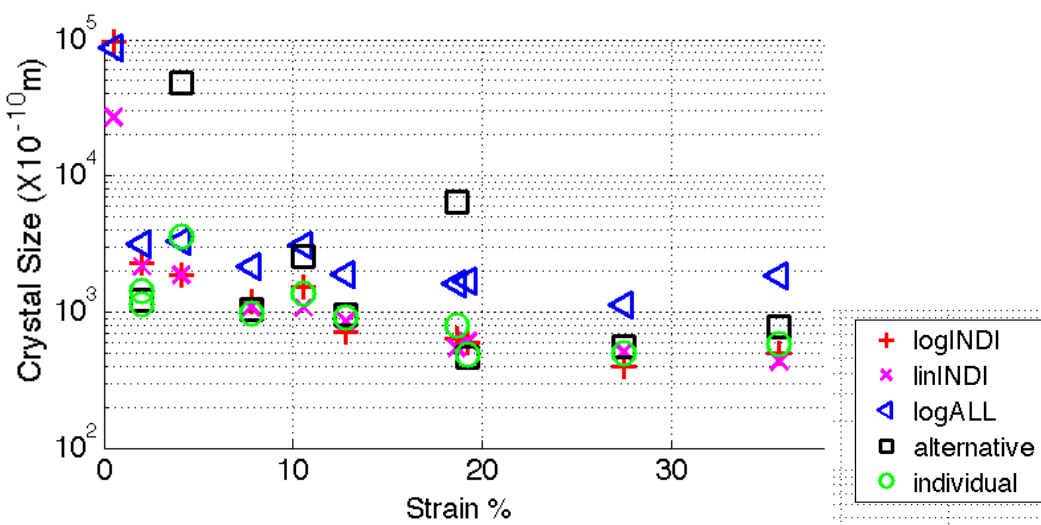


Figure 7-3. The change in crystal size plotted against true strain for nickel and different methods. The lines represent a fit of the values to a 2nd order polynomial (see text Section 6.2).

In order to quantify these differences and compare them with experimentally determined TEM results, the equation between dislocation cell size (D) and stress (σ) proposed by (Raj and Pharr 1986) is used (Equation 7.2). Where, b is the magnitude of the Burgers vector and G the shear constant. K and m are constants that are different for different materials.

$$D = Kb \left(\frac{G}{\sigma} \right)^m \quad (7.2)$$

Two different sets of TEM measurements are used to compare with the DPPA results. TEM data on aluminium (with a high SFE and hence deformation microstructure close to that of nickel) from Raj and Pharr (1986) and Mehta and Varma (1992) wire drawing of nickel-200. I have re-fitted the TEM data of Mehta and Varma (1992), to obtain the K and m values.

Equation 7.2, was fitted to the crystal size results of the different DPPA methods (shown in Figure 7-3) using the stress-strain curve of nickel (shown in Section D.2.2) to determine the values of K and m, which are shown in Table 7-1 alongside the TEM results on aluminium and nickel. Two different estimates of m and K are shown, those on the left are found by allowing both m and K to change, and those on the right when only K is allowed to change, with a value of m between the two expected values.

Table 7-1. The change in parameters K and m (found from fitting data to equation 7.2), used to show how the crystal size changes with flow stress, for different DPPA methods. These parameters are determined allowing both to change and only allowing K to change. The expected values are compared with TEM data on aluminium (Raj and Pharr 1986)* and nickel-200 (Mehta and Varma 1992).**

Method	M	K	m	K
log-INDI	1.33	0.25	0.96	1.8
log-ALL	0.67	20.6	0.96	4.2
lin-INDI	1.28	0.3	0.96	1.8
individual	0.85	3.4	0.96	1.8
ALT	0.59	14.9	0.96	2.0
mWH-3	0.72	23	0.96	6.2
IB	1.3	0.35	0.96	2.7
var PV	1.1	1.1	0.96	3.0
var V	0.46	11	0.96	1.0
Expected- Al*	0.95	25		
Expected- Ni**	0.98	13.7		

The change in crystallite size values with stress, represented by m, is different for the different methods varying from approximately 0.5 to 1.3. The TEM results from Raj and Pharr (1986) and Mehta and Varma (1992), suggest the value is just less than 1, which is approximately the mean of these different values.

A comparison of the absolute values is possible by comparing the K values on the right hand side, when the m value is kept constant. In all cases the DPPA results are smaller than the TEM results. The ratio in the values from the TEM and DPPA methods varies from around 1:2 (for mWH-3) to 1:10 (for Variance Voigt). However, most values are around 2, which give a ratio of 1:7 with the nickel TEM results. These values are consistent with comparison between TEM and DPPA. Ungar (2006), compiled data on plastically deformed metals and showed that the ratio of sizes from TEM to DPPA varied from around 3 times at a size of 750Å, using DPPA, to 7 times at 5000Å.

From Figure 7-3 it can be seen that the two methods with the highest crystallite size values are the modified Williamson-Hall and Warren-Averbach log-ALL methods. These methods have different interpretations of the crystal size than the other methods, based on the assumed size distribution. Hence, this may suggest that consideration of the size distribution may partly explain the discrepancy in results. The mWH-3 method gives the highest size values. The crystallite size value from the WH method represents the volume weighted crystal size, whereas the other methods give the area weighted crystal size. The volume-weighted size should always be more than or equal to the area-weighted value, depending on the distribution (Ungar 2003). The log-ALL method gives the 2nd highest size values. As described in Section 6.9, this method is the only one that doesn't assume the size distribution but instead finds the size values by fitting to the lognormal distribution, with parameters for the mean size and the standard deviation.

In this part it has been showed that for nickel there is a discrepancy with DPPA size results in Table 7-1 and those obtained of the dislocation cell size from TEM, for all the methods studied. The results show that the discrepancy may in part be

due to the differences in the distribution of crystallite size values. However, it is not clear whether any of the other causes (listed at the start of Section 7.3.1) of differences also need consideration. In order to help understand this in the next section, the change in size values for the other alloys are shown.

7.3.2 Crystal Size in metals with low SFE

Unlike, nickel that has a well-developed dislocation cell structure after small amounts of applied strain (Keller et al. 2010), the higher stacking fault energy of Ti-6Al-4V and stainless steel means that their dislocation structure is very different. Instead, the microstructure is dominated more by dislocation tangles and dislocation walls, which lie along the dominant slip planes (Feaugas 1999, Byun et al. 2003, Zaehlerer 2003). In some cases, particularly after larger amounts of strain, dislocation cell structures can develop but are not as well defined as those in nickel.

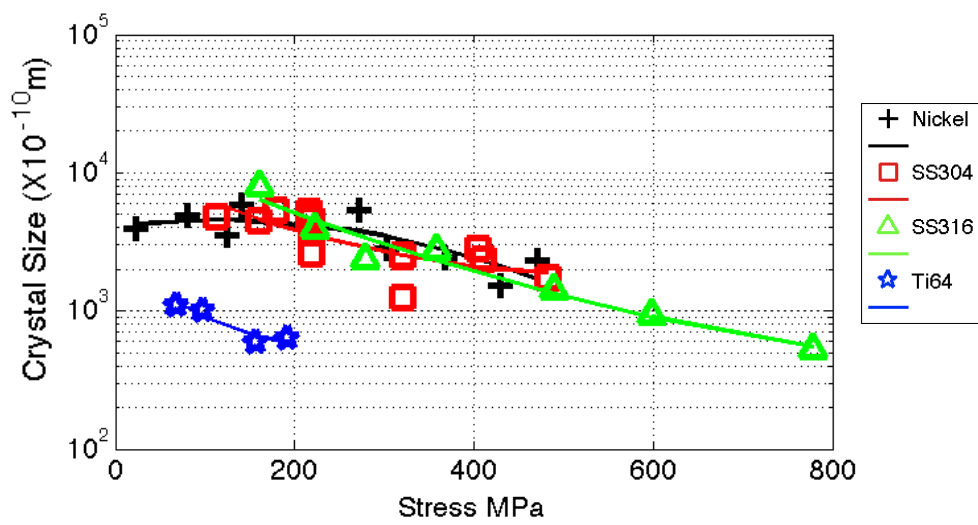
Hence, it may be expected that the crystallite size values from DPPA of stainless steel and Ti-6Al-4V, would be different from those for nickel. In particular, if the crystal size values are the result of regions misorientated from each other, it would be expected that the size values would be lower in nickel than the other alloys. In Figure 7-4 and Figure 7-5 the change in the crystal size values for the different metals are shown, plotted against stress. From these figures it can be seen that, with the exception of the alternative method (described in Section 2.4.3), the crystallite size values for the lower SFE metals, are either comparable or lower than those found for nickel. In the alternative method, the crystal size values, for the low SFE metals, are either at the upper fitting boundary (for the stainless steel sample) or just below it (for Ti-6Al-4V). Van Berkum et al. (1994), who developed the alternative method, suggested that this method was less prone to systematic errors in over-estimating size broadening, than other methods. They showed that for metals where there was expected to be an increase in dislocation density but a relatively large crystal size (which would not cause considerable broadening), the alternative method showed size broadening comparable with the size of the crystals (see van Berkum et al. 1994, Section A and B pg. 351-353), but the WA log-INDI method gave considerably smaller crystal sizes.

For the other methods it is found in Figure 7-4 and Figure 7-5 that the crystal size values of the different FCC metals are very close, particularly for the mWH-3 and WA log-indi methods. In addition, the crystal size values for nickel, found using the WA log-INDI and integral breadth methods, are close to those found using the alternative method.

These results suggest that the discrepancy between size values obtained by most DPPA methods and those determined experimentally are a result of the mathematics involved in the separation of crystallite size and (micro) strain, which result in an overestimation of size broadening. However, it is still not clear whether these derived crystal size values can be attributed to anything physically observable within the sample or are just due to incorrect size and strain separation. It could be that these values represent the size of regions bounded by dislocations, that do not cause any change in orientation, as suggested by Ungar (2006). The closeness between the size values of nickel found using the log-INDI and alternative methods, and in addition the closeness between the size values of the different FCC metals in the log-INDI method suggest the explanation by Ungar may have some validity for our data.

This issue of size broadening is considered further in Chapter 7. In the next part, how the strain broadening changes for different metals and how this compares to the size broadening is shown.

mWH-3



Integral Breadth method

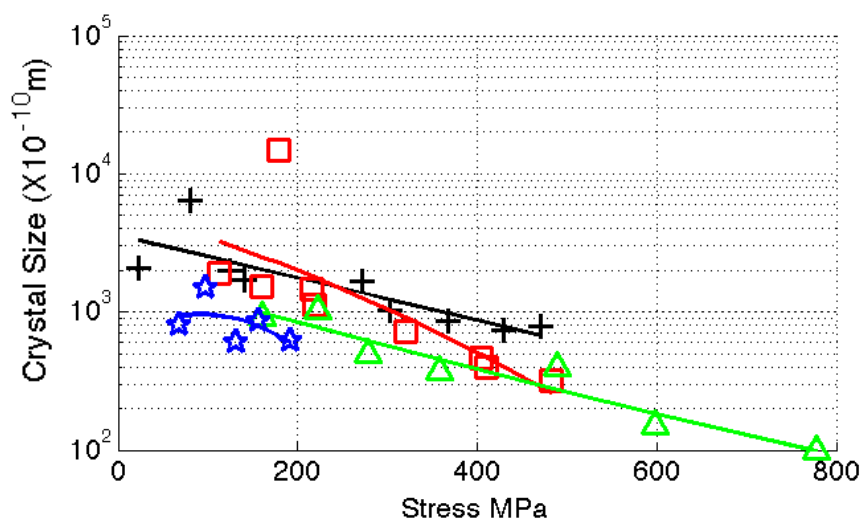
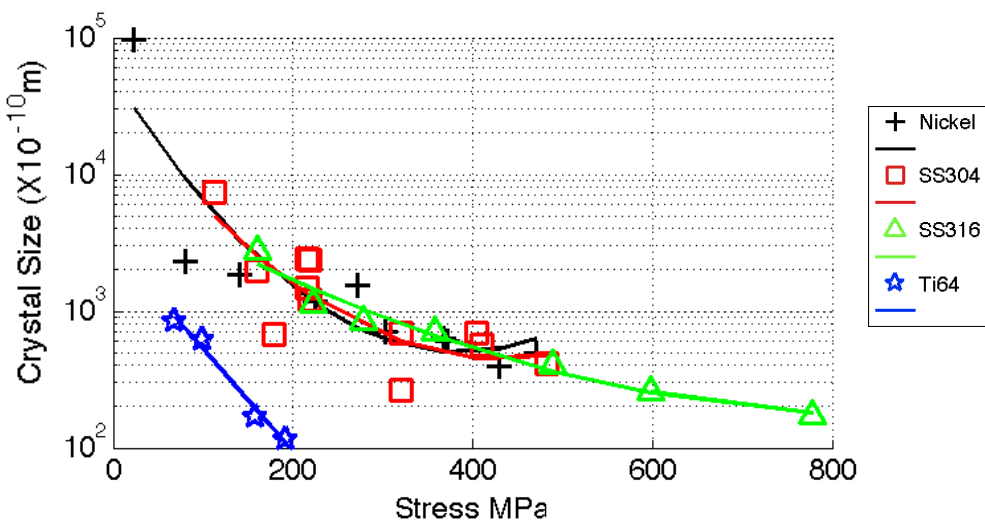


Figure 7-4. The change in crystal size (in Å) for nickel, plotted against work-hardening stress. The results are for the mWH-3 (top) and Integral Breadth (bottom) methods. The lines represent a fit of the values to a 2nd order polynomial (see text Section 6.2).

WA log-INDI



alternative

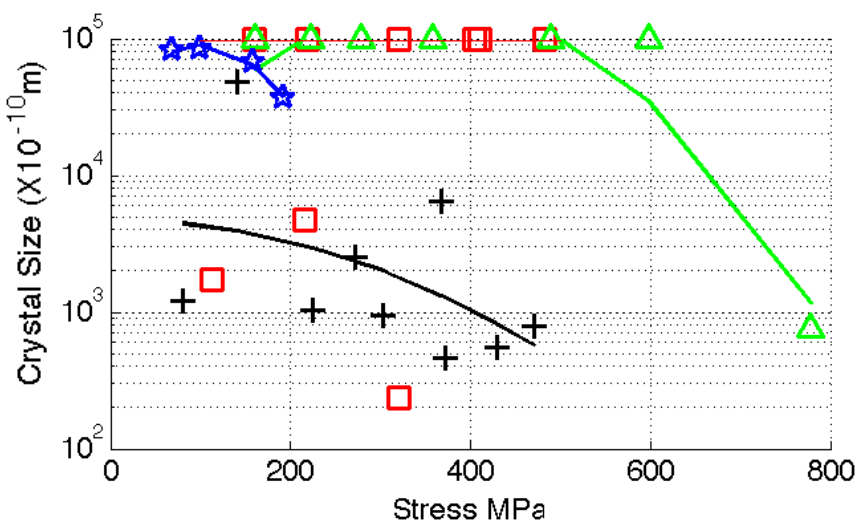


Figure 7-5. The change in crystal size (in Å) for nickel, plotted against work-hardening stress. The results are for the WA log-INDI (top) and alternative (bottom) methods. The lines represent a fit of the values to a 2nd order polynomial (see text Section 6.2).

7.3.3 Micro-strain and Size Broadening

Strain broadening is a quantity that is difficult to verify with other methods. In this way it is similar to size broadening, however the difference is that size values can in theory be compared with TEM measurements. In order to verify strain measurements it is necessary to separate it into its different components. These are the dislocation density, arrangement and population. These values can then in turn be compared, at least qualitatively, with TEM or other measurements. This is dealt with in Section 7.4. In this part the relative broadening from size and strain components of the different methods and metals are identified. The aim is to further understanding of how different methods separate size and strain broadening, and determine whether this separation could introduce systematic errors.

The size and strain broadening for different methods and the different metals are shown in Figure 7-6, Figure 7-7 and Figure 7-8. To calculate the strain broadening in the WH methods the strain component of the equation is used with $g=1$. For the WA methods the strain component is found using the calculated dislocation density and arrangement values, with the Wilkens equation (Wilkens 1970b), and the size Fourier coefficients using the size value and the Cauchy size equation (de Keijser et al. 1982), both these terms are described in Section 6.9. The Fourier coefficients ($A(L)$) are converted to integral breadth measurements (β) using the following equation (Kuzel 2007):

$$\beta = \frac{1}{2 \int_0^{\infty} A(L) dL} \quad (7.3)$$

Since different peaks have different contrast factor values, C , (see Section 6.10) and hence strain values, an average contrast factor value is used to allow comparison of modified and standard approaches.

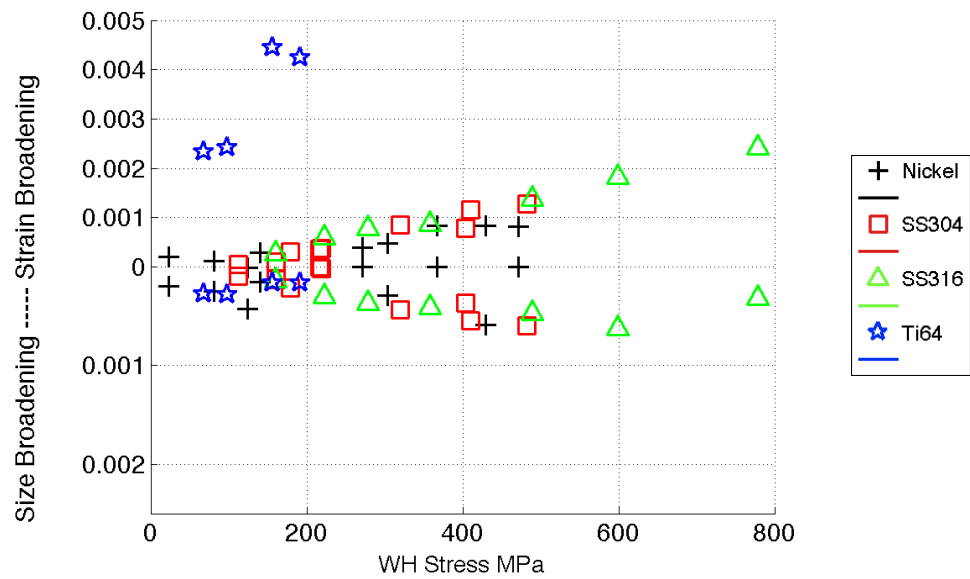
In general, all methods show an increase in micro-strain broadening with applied strain, or work-hardening stress (see Figure 7-6, Figure 7-7, Figure 7-8 and Figure

7-9). The exceptions to this are the lin-INDI (Figure 7-9) and integral breadth methods (Figure 7-8) at higher applied strains. The different methods give different relative contributions of size and strain broadening. The WH and alternative methods attribute most of the broadening to strain broadening, relative to size. Whereas, the integral breadth attributes most of the broadening to size broadening and the WA methods attribute almost equal amounts to the two contributions. There are also differences in the combined magnitude of size and strain broadening. For example, WH methods have a smaller total broadening contribution than WA methods, because of the way size and strain broadening are combined.

There are differences in the way the different overall broadening of nickel and Ti-6Al-4V, relative to the stainless steel samples, is divided into size or strain broadening components (in Figure 7-6, Figure 7-7, Figure 7-8 and Figure 7-9). Ti-6Al-4V's higher total broadening is split between both size and strain components for most methods. However there are exceptions, for the WH-2, integral breadth and alternative method the size contributions are comparable to other metals, but the strain broadening is much larger. For nickel the lower overall broadening, mainly results in lower strain broadening than for the stainless steel alloys. However, for the WH-2 and integral breadth methods the opposite occurs.

It is apparent, in Figure 7-6, Figure 7-7, Figure 7-8 and Figure 7-9 that most methods show an increase in size and strain broadening with applied strain. However, the large differences in size and strain broadening for the different methods add to the uncertainty as to the physical significance of these inferred parameters.

WH-2



mWH-3

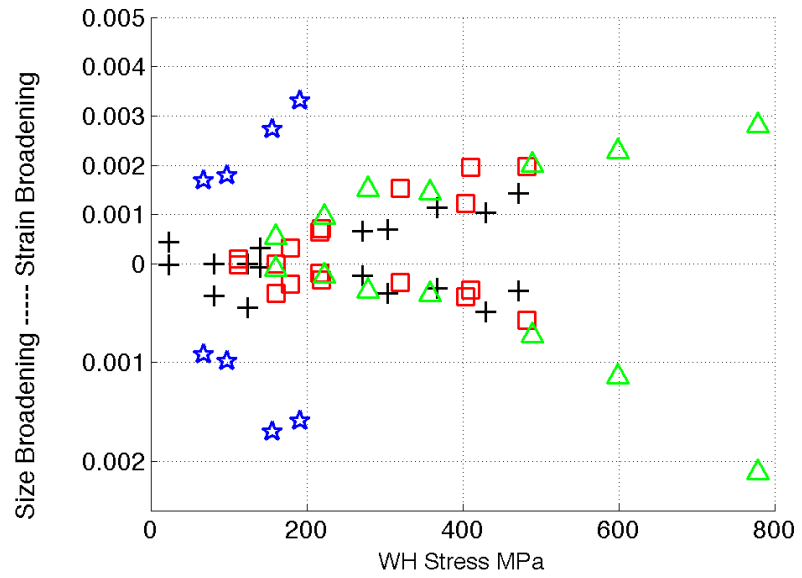
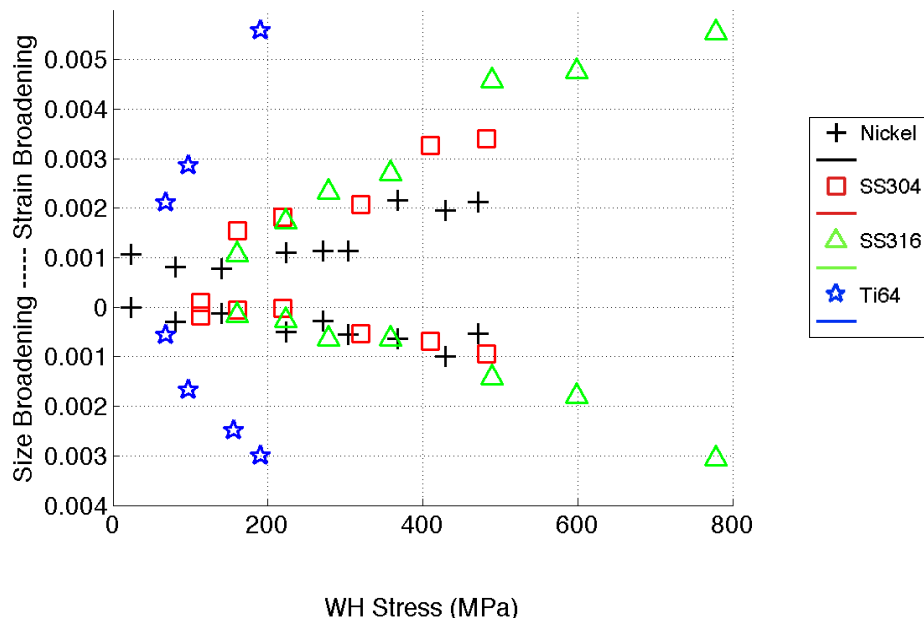


Figure 7-6. The change in the relative size and strain broadening for the different metals using the standard (top) and modified (bottom) Williamson-Hall methods. Values are plotted against WH stress.

WA individual



WA log-INDI

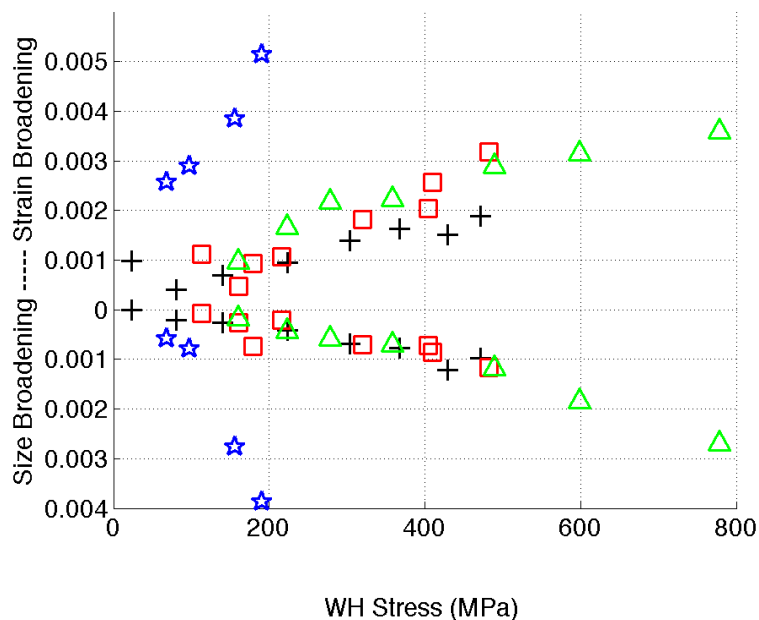
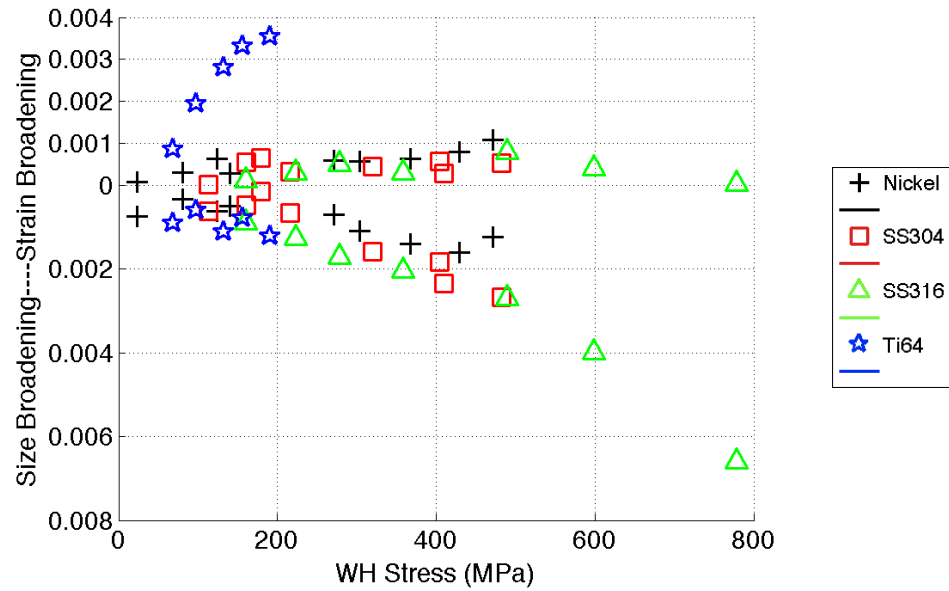


Figure 7-7. The change in the relative size and strain broadening for the different metals using the standard (top) and modified (bottom) Warren-Averbach methods. Values are plotted against WH stress.

Integral Breadth Method



Alternative method

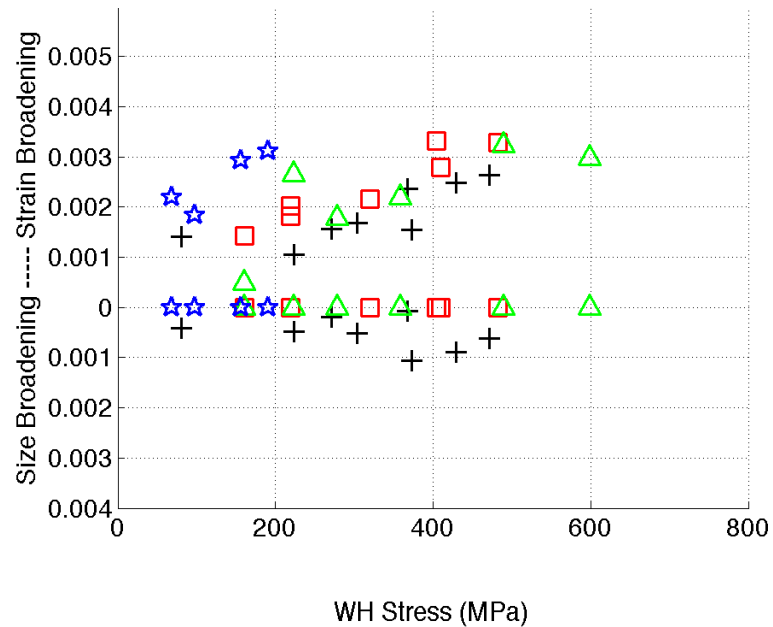
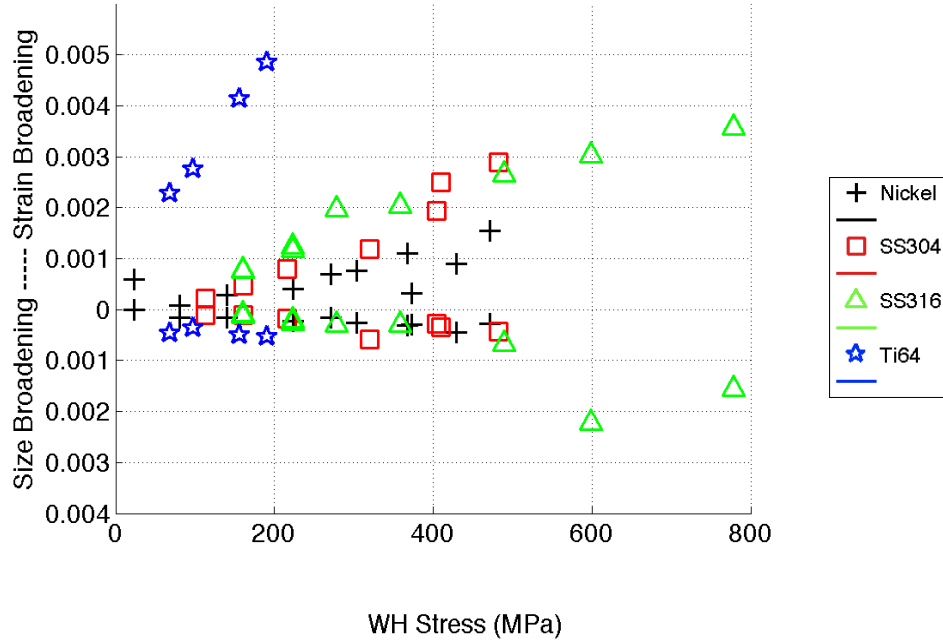


Figure 7-8- The change in the relative size and strain broadening for the different metals using the integral breadth methods (top) and alternative method (bottom). Values are plotted against WH stress.

log-ALL Method



lin-INDI Method

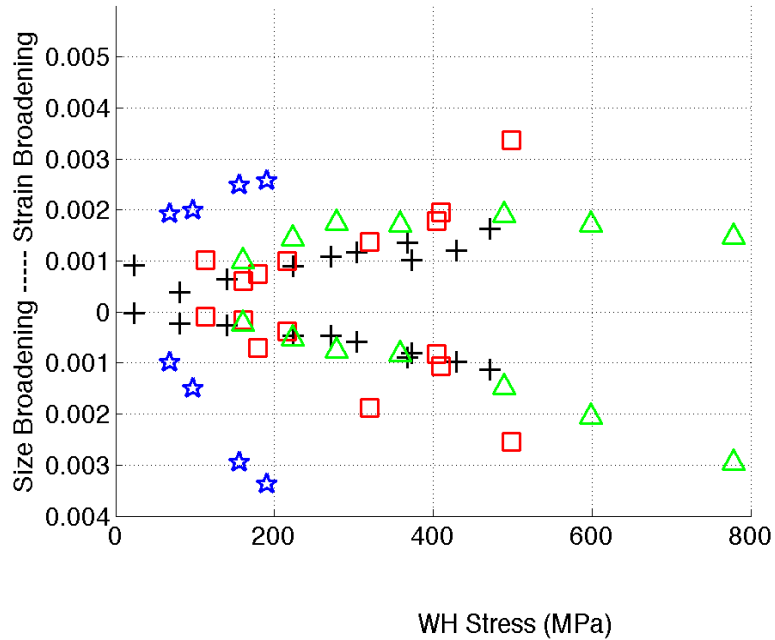


Figure 7-9. The change in the relative size and strain broadening for the different metals using the log-ALL (top) and lin-INDI (bottom) methods. Values are plotted against WH stress.

7.4 Components of Strain Broadening

The amount of strain broadening, present in a metal increases with the number of dislocations, but the manner in which these dislocations contribute to broadening is dependent on what dislocations are present and how they arranged (see for Section 2.4.5). In this section, the three different components of the strain broadening, (a) the dislocation density (ρ), (b) the dislocation arrangement (indicated by M) and (c) the dislocation population are considered in turn.

7.4.1 Dislocation Density

In this part the dislocation density values (ρ) obtained from the different Fourier methods and the Variance-B method are presented, and compared with values obtained on similar alloys by TEM.

It has been found that for metals that work-harden, the dislocation density increases with the flow stress (e.g. Mecking and Kocks 1981, Conrad 1981). All the metals studied here significantly work-harden and as expected the dislocation density increases for all the methods and metals (see for example Figure 4.25). However, the magnitude of the dislocation density and how they change with applied strain (or the flow stress) are different for the different methods.

In order to compare different methods, and metals, the Taylor equation (Equation 7.4), which relates dislocation density (ρ) to flow stress (σ), is used. The equation has shown to be valid for a wide range of metals irrespective of the dislocation structure that develops or the crystal structure (Mecking and Kocks 1981, Conrad 1981).

$$\sigma = \sigma_0 + \alpha' G b \sqrt{\rho} \quad (7.4)$$

Where, G is the shear modulus and b the magnitude of the Burgers vector of dislocations and σ_0 is the friction stress, or the yield stress of an annealed sample. The value α' is a constant that is found to change depending on the material studied. From the TEM results of Lee and Lin (2001) a value of 0.48 was found for SS-316. For comparison with the nickel results, a value of 1 was found by Gubicza et al. (2006) using DPPA on nickel. Whereas, for copper (a metal with a

relatively high SFE like nickel) Mecking and Kocks (1981) obtained a value of 0.5 from TEM and 1 using an etch pit technique. For titanium it has been found (Conrad and Wang 1978, Biswas et al 1973, Conrad 1981) that the value of α' are independent of interstitial content, temperature, dislocation structure or grain size and vary between 0.34 and 0.9.

The calculated dislocation density values were fitted to Equation 5.4, for the different DPPA methods and are presented in Table 7-2, along with the expected values from the literature. The magnitude of the Burgers vector, b , used for Ti-6Al-4V was for $\langle a \rangle$ dislocations because they are expected to be the dominant dislocation. An example of the fit for the WA log-INDI method is shown in Figure 7-10. In the table two values of α' are presented. For the top value the value of the yield stress and α' are allowed to change (the fitted yield stress value found is presented below the value of α' in the table), and for the lower value, the measured yield is used and only α' is allowed to change.

It is found that the dislocation density varies linearly with the stress in most cases (Figure 7-10), but it is found that in many cases this linear relationship when extrapolated to zero dislocation density gives a negative work-hardening stress. This can also be seen in Table 7-2, where the fitted values of the yield stress (σ_0 in Equation 7.4) are lower than the measured yield stress, and in many cases are also negative. This behaviour is suggestive of a systematic error in the results, which gives higher than expected values of the dislocation density at low values of stress, relative to high values of stress. This behaviour is particularly noticeable in nickel and SS-316 metals, although it does occur to a lesser extent for the other metals. The behaviour is largest in the alternative and lin-INDI methods, then the log-INDI and log-ALL methods and for the individual method is lowest, and doesn't arise for SS-316.

The behaviour has not to the author's knowledge been observed in either DPPA or TEM measurements. Hence, there are a number of possible causes for the behaviour, the most probable of these are either errors caused by separating the instrumental broadening, or systematic errors separating the different DPPA parameters. In the next two parts the possibility that the behaviour is due to the separation of dislocation arrangement and dislocation population are considered.

There is an alternative explanation for the behaviour which is not due to errors. Although, it has been shown that the Taylor equation describes the relationship between the dislocation density and the flow stress (see Section 2.1.5 and Figure 2.7), it has been stated (Mecking and Kocks 1981) that there may be cases when the equation needs to be modified. Such a modification would be included to account for things such as lattice resistance, solution hardening and grain size effects and would result in an additive term added to the right hand side of equation 7.4 (Mecking and Kocks 1981). Of these the grain size effect (often called a Hall-Petch contribution see Equation 2.2) could explain the observed behaviour. For a particular flow stress the presence of this contribution would reduce the value of the dislocation density. As can be seen by including the extra term in the Taylor equation and re-arranging, $\sqrt{\rho} = \frac{1}{\alpha' G b} (\sigma - \sigma_0 - \sigma_{GS})$. This contribution would increase with the flow stress as the crystal size falls (see Equation 2.2), therefore producing the observed behaviour- a lower than expected dislocation density at high stress.

The values of α' found when this behaviour is observed are much larger than the expected values. However, the values of α' found when the measured yield stress is used are close to those expected. For the stainless steel metals the mean of the WA values is 0.53 for SS-304 and 0.59 for SS-316 (or 0.51 if the higher lin-INDI value is ignored), which is close to the expected value of 0.48. For Ti-6Al-4V the mean of the WA values is 0.49, which is within the range of values observed by TEM, although at the lower end. However, the mean value of α' for nickel is 0.67, which although higher than for the other metals, as is expected, is a third less than the expected value.

There is range of α' values for the different WA methods and no obvious trend to suggest which would give the highest or lowest values. These differences are significant and are a reflection of both random and systematic errors that result from applying the different methods. For example in Ti-6Al-4V, the difference between log-ALL and individual methods represents a dislocation density two times higher in the individual than the log-ALL method. The alternative method provides the largest value of α' of all the methods and in most cases these values are larger than expected. It ranges from providing similar values for nickel to

twice those observed in SS-316. These higher values of α' correspond to lower values of the dislocation density, for a given stress. This shows that even though the alternative method gives a smaller contribution to size broadening, for the low SFE metals, this does not equate to higher values of the dislocation density. The main cause for the larger value of α' for the alternative method, is due to the different size and strain separation, in the alternative and Warren-Averbach methods. From comparison of the strain broadening in the WA individual (Figure 7-7) and alternative methods (Figure 7-8), it is apparent the strain broadening is lower for the alternative method (as described in Section 6.9 these methods can be compared because both these methods use the same diffraction peaks). The Variance-B method, which was only performed for Ti-6Al-4V, provides similar values to the other methods and close values to the expected value of α' . The Variance-B method is a single peak method, but the values presented are the average of four peaks (10T0) and (10T2) in the two directions.

This behaviour can also be observed in the other methods. By comparison of the fitted value of α' (when only α' is allowed to change) in Table 7-2, with the strain values, shown in Figure 7-6, Figure 7-7, Figure 7-8 and Figure 7-9, the different dislocation density values for the different methods are mainly due to the differences in strain values.

Overall, the dislocation density values found by the Warren-Averbach methods are close to the measured TEM results of similar metals, although there is considerable spread in the different results. In contrast, those found by the alternative method are lower than expected. In some of the metals, the results show a systematic error from the expected values. This systematic error causes higher than expected dislocation density values at values of low strain.

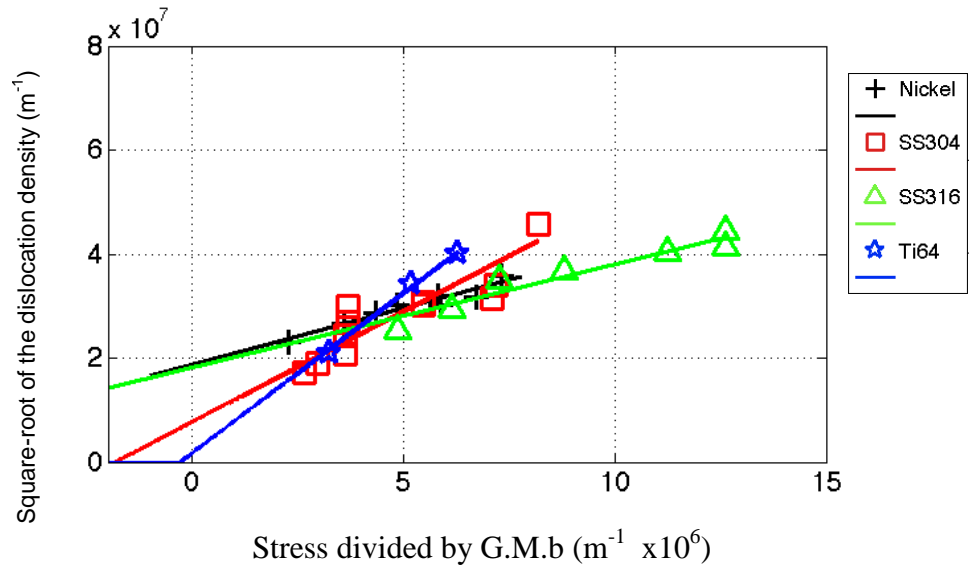


Figure 7-10. Fit of WA log-indi method dislocation density values against work-hardening stress used to determine α' (and in this case also the yield stress). The value $(\sigma - \sigma_0)/(GMb)$ is plotted against the square-root of the dislocation density. Where $\sigma - \sigma_0$ is the work-hardening stress, G the shear modulus, b the magnitude of the Burgers vector and M a constant equal to 3.

Table 7-2. The change in parameters α' and σ_0 (found from fitting data to equation 7.4), used to show how the dislocation density changes with flow stress, for different DPPA methods. These parameters are determined allowing both to change and only allowing α' to change. The expected values are compared with TEM data (details in body of text).

Method		LOGindi	LINindi	LOGall	ALT	individ.
Nickel	α'	1.63	1.71	0.36	2.38	1.40
Yield from stress-strain curves = 60MPa	yield	-460	-480	-450	-900	-380
	α' (yield=60)	0.68	0.69	0.14	0.66	0.63
	Expected α'	1.0				
SS304	α'	0.70	0.61	0.50	1.11	0.83
Yield from stress-strain curves = 175MPa	yield	65	110	120	-16	-18
	α' (yield=175)	0.56	0.54	0.43	0.75	0.57
	Expected α'					
SS316	alpha	1.56	2.88	0.77	4.5	0.42
Yield from stress-strain curves = 260MPa	yield	-530	-1200	-240	-1200	300
	α' (yield=260)	0.65	0.81	0.42	1.29	0.46
	Expected α'	0.48				
Ti-6AL4V	α'	0.49	1.35	0.76	8.70	0.40
Yield from stress-strain curves = 880MPa	yield	870	610	820	-620	880
	α' (yield=880)	0.45	0.53	0.57	0.91	0.40
	Expected α'	0.62				
Ti-6AL4V-Variance-B method	α'	054				
	yield	879				
	α' (yield=880)	0.54				

7.4.2 The Arrangement of Dislocations

The strain field around a group of dislocations are different than the strain field of individual dislocations, because the strain field of the dislocations interact. This interaction can mean that the same dislocation density can cause more or less broadening depending on how the dislocations are arranged. In DPPA methods, the dipole character, M, (See section 2.4.5) is used to explain this arrangement. This section will consider whether the dipole character has physical meaning, or is just a fitting parameter, and whether its use may introduce systematic errors.

The value of the dipole character varies considerably with each WA method (see Figure 7-11), and there is a greater scatter than other parameters previously discussed. In general though, the value of M increases with applied strain and then saturates. For Ni, the values increase and then level off, the exceptions are log-ALL and the individual method where the results are too scattered to determine any relationships. For the stainless steel and Ti-6Al-4V samples the behaviour of the dipole character is in general the same as for nickel, but there are instances when the values increase throughout. The magnitudes of the values are highest for the Alt method, at ~7 for Ti-6Al-4V, then the log methods and then the lin methods, for lin-INDI Ti-6Al-4V has a value of ~1. It is evident from Figure 7-11 that Nickel has the lowest value for all methods, the value of the stainless steel alloys are similar and that of Ti-6Al-4V is either comparable to stainless steel or higher depending on the method.

The general behaviour of M, increasing and then levelling off, is in agreement with the expectations and the results of Zehetbauer et al. (1999) on copper polycrystals. They observed an increase in M up to a strain of around 0.2, followed by a plateau. The increase in M was explained as being due to regions with low and high dislocation density developing, with increasing applied strain. The plateau was explained as being due a transition in the type of dislocations present, from those with a higher value of M, which are dominant at low strains, to those with a lower value of M, which become dominant at higher strains. However, this behaviour was explained for a high SFE metal, and it is not clear whether the same behaviour occur for metals with lower SFE. For low SFE metals

(such as stainless steel), with more applied strain the dislocation arrangement becomes more organized. For example in stainless steel it has been found that the dislocation arrangement is related to the flow stress (Feaugas 1999, Byun et al. 2003). At lower stresses the dislocations were mainly organized as tangles, whilst at higher stresses dislocation cells were observed. Hence, for all metals there should be two competing influences on the value of M. One that causes an increase with applied strain due to increases in dislocation density and a one that causes a reduction due to a more organised dislocation structure. The problem is that it is difficult to quantify these two effects and hence quantify what changes in M would be expected.

If changes due to variations in dislocation density are ignored, then the lower the value of M the greater the screening of the dislocations by their neighbours, which is what happens when dislocations become organised into cell structures. Hence, an inverse relationship might be expected between the stacking fault energy and the value of M. The absolute values of M found for nickel and stainless steel are in agreement with this (Figure 7-11). The value of M for nickel, with the highest SFE, is the lowest, and the two stainless steel metals with close values of SFE are close. There is no relationship between the values of the dipole character for the two titanium metals and values of the FCC metals. For WA-log methods and Alt method Ti-6Al-4V has a larger value of M than the FCC metals, but for the lin-INDI method the values are lower than the stainless steel metals. It may be the case that the differences in diffraction source have an influence on the value of M and consequently makes comparison between the titanium and FCC metals difficult. However, the values of Ti-6Al-4V are higher than Ni-200, which would be expected because dislocation cell structures are less frequent in Ti-6Al-4V.

As discussed in Section 6.9, and shown in Figure 6.22, systematic errors can result from the separation of the dislocation density and dipole character, M. In that section it was shown that a particular set of strain coefficients can be described by different values of the dislocation density and dipole character, depending on how they are fitted. The coefficients can be described by a higher dislocation density and lower dipole character or a lower dislocation density and

higher dipole character. If the changes observed for the dipole character, in this section, are not real changes of the microstructure, but are instead artifacts, then this could cause systematic changes in the dislocation density. In particular it would cause there to be a higher dislocation density at low applied strains, where the value of M is lowest. Hence, a systematic error in M may explain (at least partly) the reason for the systematic differences between the dislocation density results and the Taylor equations, found in the previous section. For the log-ALL method this problem of separating dislocation density values from its arrangement, appears to be more of a problem. This is particularly noticeable for Ni-200, where the dipole character tends to very low values.

There is some justification that the values and trends seen for the dipole character represent the metals. The behaviour of the dipole character follows a trend found and explained by other researchers, and the difference in its magnitude between steel and nickel samples is expected, given the differences in the deformed microstructure. However, there are still some un-answered questions. Why does the value of M change depending on the method used? What exact values and trends are expected and how can the value be compared to TEM results? Without an understanding of these questions, the dipole character becomes just a fitting parameter that may cause systematic errors.

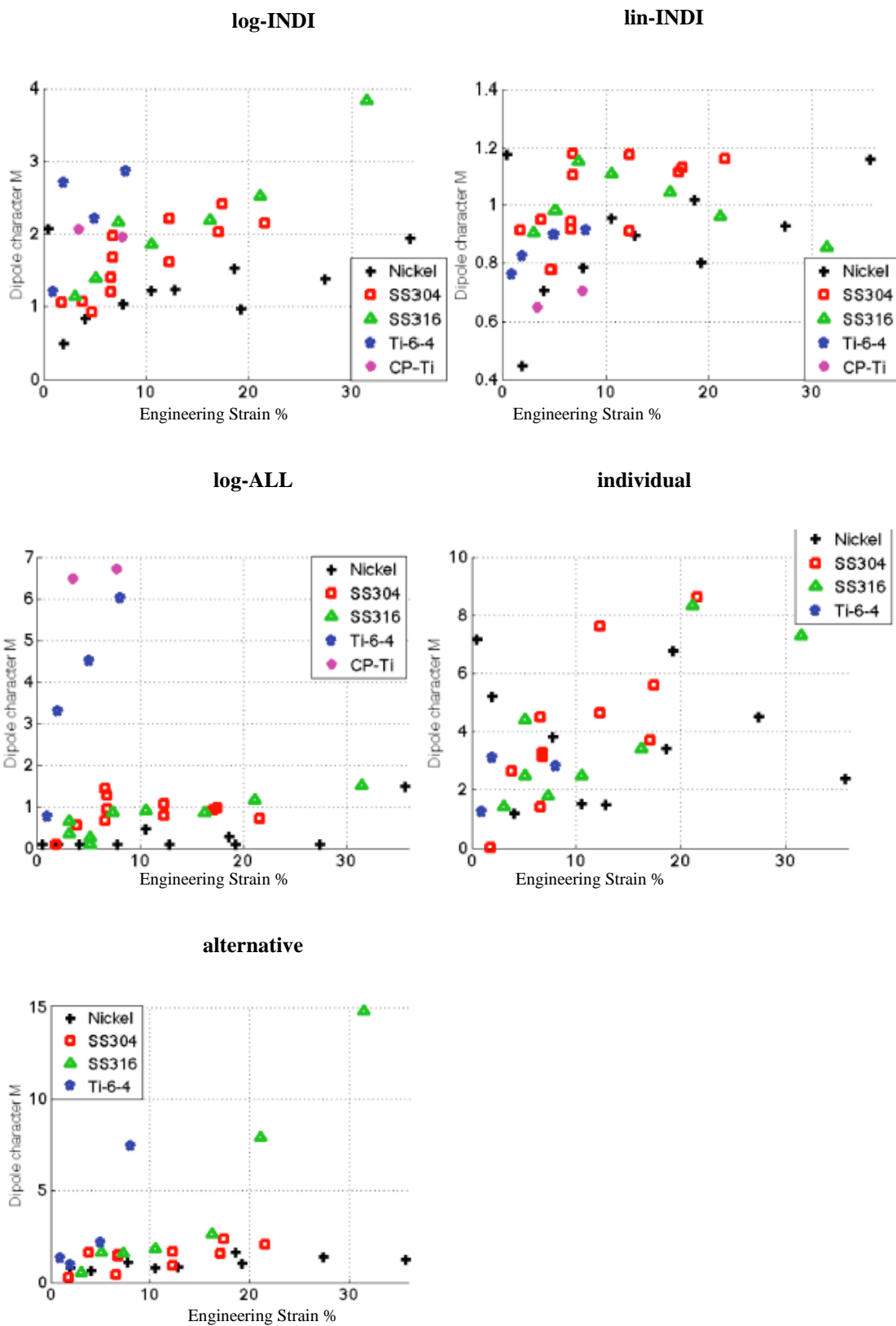


Figure 7-11. Results of the dipole character M, for the different Fourier methods applied to the different metals.

7.4.3 Dislocation Population and the Contrast Factor

The dislocation population is a term used to reflect the nature of the Burgers vector, slip plane normal and slip line, relative to the diffraction vector, of a metal sample. In FCC metals, with only one slip system, the dislocation population is most often used to refer to the relative quantities of edge and screw dislocations. Whereas, in HCP metals it is also used to represent the relative amounts of the different types of dislocations, for example $\langle a \rangle$ and $\langle c+a \rangle$. The reason why the dislocation population is important is that depending on the relationship between these three vectors and the diffraction vector the broadening of a dislocation can vary considerably. For example, in the extreme case, an edge dislocation with a Burgers vector perpendicular to the diffraction vector, will not contribute to the broadening of a diffraction peak.

In order to determine the dislocation population, the contrast factor term, C, is often used (see Section 2.4.5). This term is useful in that it allows multiple peaks, of different families, to be used when using DPPA methods (Ungar and Borbely 1996). However, the term is not only a fitting parameter but should in theory provide information about the dislocation population. This section seeks to understand whether the values obtained from the contrast factor are in agreement with the expected changes in the dislocation population for FCC and titanium alloys and what if any systematic errors may result because of its use.

7.4.4 Slip system population in FCC metals

The dislocation population is reflected by the q-value. In FCC metals the value is most often used to reflect whether the ratio of edge and screw dislocations present in a sample. As discussed in Section 6.7 a large q-value is representative of screw dislocations and a small value representative of edge dislocations.

In Figure 7-12, the changes in the q-value with applied strain are shown for different methods. As has been observed before there are variations with the different methods. For the log-INDI method (Figure 7-12a) the q-value falls for all FCC metals, from values close to the screw values to close to the edge values at strains near 20%. For larger strains the q-values increases. The Williamson-

Hall results in Figure 7-12b display the same trends for nickel, but for the stainless steel metals a different trend is observed. For the stainless steel metals the q-values increase from values close to edge values to values close to screw values at higher strains.

The two other WA methods have slightly different trends to the log-INDI method (Figure 7-12 c and d). The lin-INDI q-values are in many cases close to the lower fitting boundary. For nickel the q-values are at these values for most strains, whereas for the stainless steel the q-values fall to these values with increasing strain. For the log-ALL method the q-values show similar trends to log-INDI but with higher values.

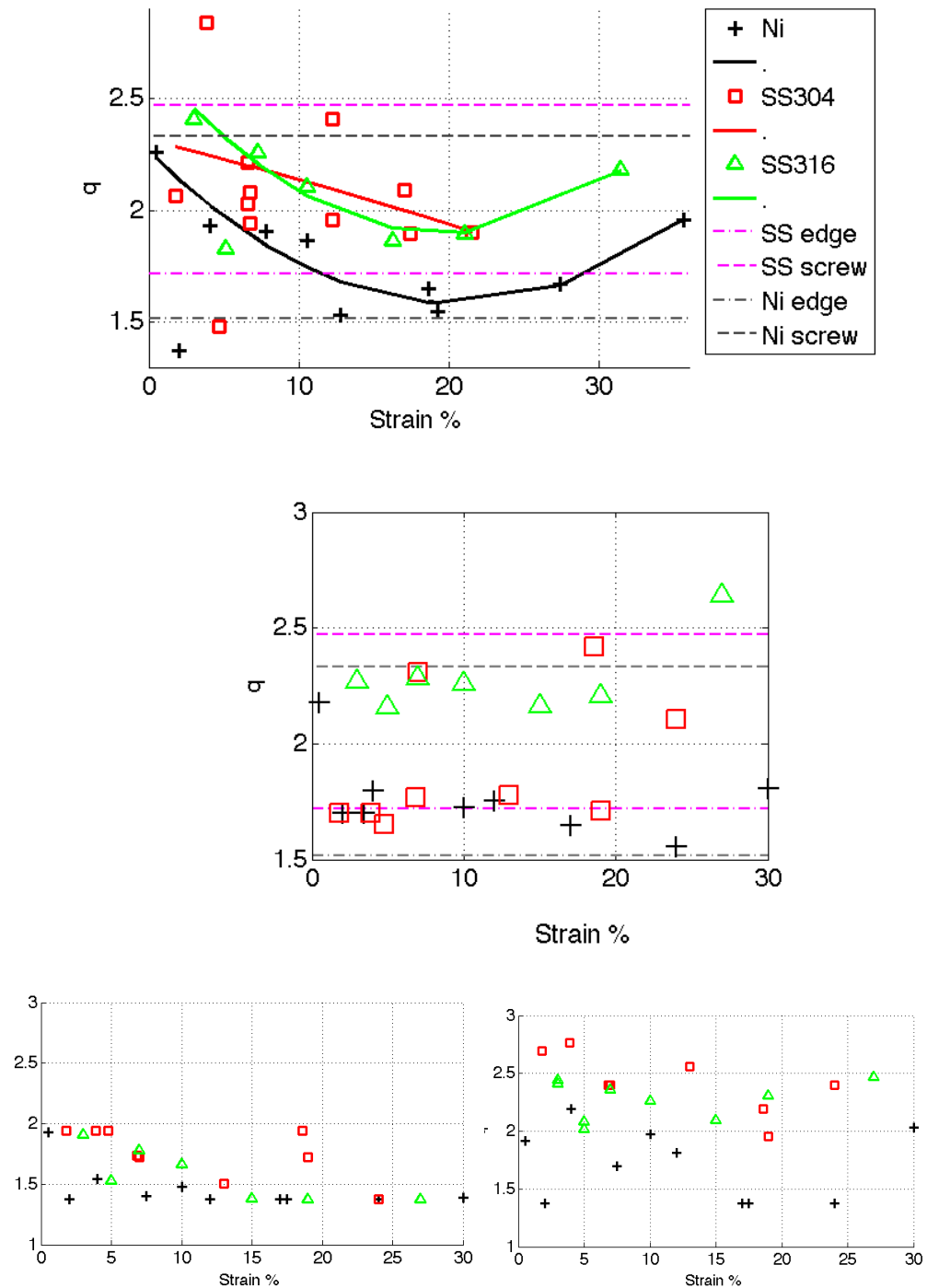


Figure 7-12. Results of the q -values for FCC samples found using the WA log-INDI method (a, top), mWH-3 method (b, middle), lin-INDI (c, bottom left) and log-ALL (d, bottom right). The lines represent a fit of the values to a 2nd order polynomial (see text Section 6.2).

Discussion of FCC slip system predictions

In FCC metals, differences in the dislocation population, found from the contrast factor, are due to differences in the relative amounts of edge and screw

dislocations. However, there has been no systematic study undertaken to display these changes with different amounts of deformation, in the different FCC metals studied. Nonetheless it is possible to make certain assessments of how these parameters may change.

The general trend observed for the metals is a transition from high q-values to lower values. There are reasons that would explain this transition for metals with high and low SFE. For low SFE metals such as stainless steel, at low amounts of plastic strain there can be more screw dislocations because of the greater mobility of edge dislocations (Hull and Bacon 2001). With increased plastic deformation, there is an activation of secondary slip systems and interactions of dislocations that can cause the ratio of screw to edge dislocations to fall. For high SFE metals, such as nickel, the initiation of stage III, can occur at low amounts of deformation (Keller et al. 2010, Hansen & Ralph 1982 and Feaugas and Haddou 2007). This stage is accompanied by annihilation of screw dislocations and the arrangement of dislocations in low-angle boundaries consisting of edge dislocations. Zehetbauer (1993) made predictions of the amount of edge and screw dislocations, based on the dynamics of cross-slip, for high SFE metals. The same trend was found, with an almost equal amount of edge and screw dislocations up to a shear strain of around 1, and then an increasing dominance of edge dislocations. Hence, a general reduction in the percentage of screw dislocations may be expected for these metals but the precise changes are difficult to quantify.

Alternatively, the results may indicate a transition from full dislocations to partials, as this would also cause a fall in the q-value. This trend would also be expected with increased plastic deformation. However, it would be expected to occur more for stainless steel, because of its lower SFE.

7.4.5 Systematic Errors in the use of contrast factors for FCC metals

In this part, systematic errors that can be introduced by the use of the contrast factor equation, and C, are considered. In Section 5.3.4, it was shown that there were differences in the broadening from size and strain, for methods that used the

contrast factor (modified approaches) and those that didn't (standard). Hence, systematic errors can be introduced by the use of the contrast factor, but it is not clear how these errors are introduced. Another problem that has been shown in the previous section, is that different q-values are obtained for different methods and for the two stainless steel metals, that are expected to be the same, different q-values are found. This section aims to understand these issues.

Comparison of standard and modified results

Figure 7-13 shows a comparison of the size and strain broadening from the WH and WA modified and standard methods. For both DPPA methods there are differences between the results of the standard and modified approaches, but for the FCC metals, the difference is largest in magnitude for SS-316. For nickel there is a larger contribution in the strain broadening in the modified than the standard approach for the WA method, but this trend is reversed for the WH method. The size contribution is closer for the two approaches, but is larger in the modified approach for the WA method. In SS-316, the behaviour is approximately the same as nickel. The main difference, other than the difference in the approaches being larger, is that the size broadening is larger in the modified WH method than the standard WH method.

The strain broadening values is a component that includes contributions due to the dislocation density (ρ), dislocation arrangement (M) and dislocation population (through C). C is included as the average value of the first 5 FCC peaks, for both modified and standard approaches using equation 6.4, for the results in Figure 7-13. However, this C value is different for the two approaches. The value of C is constant for the standard approach (q is set at half way between the edge and screw values) and changes based on the fit of the data for the modified approach. So if this were accounted for it would cause a fall in the strain broadening of the standard approach relative to the modified approach, when the fitted q-values are nearer to the edge value (Since from Table 7-3, the value of C is larger for edge dislocations than screw dislocations). However, this would only partly explain the discrepancies between the SS-316 results in the Warren-Averbach method, since the q-values are in general closer to screw values, except at 15 and 18%. It would also not explain the differences in the size results, for either method.

Table 7-3. Contrast factor values for different FCC planes, for edge and screw dislocations, calculated for Nickel-200 and stainless steel.

Peak	111	200	220	311	222
C-Screw Nickel	0.064	0.29	0.12	0.18	0.064
C-Edge Nickel	0.14	0.28	0.17	0.21	0.14
C-Screw SS	0.057	0.32	0.12	0.20	0.057
C-Edge SS	0.13	0.31	0.18	0.23	0.13

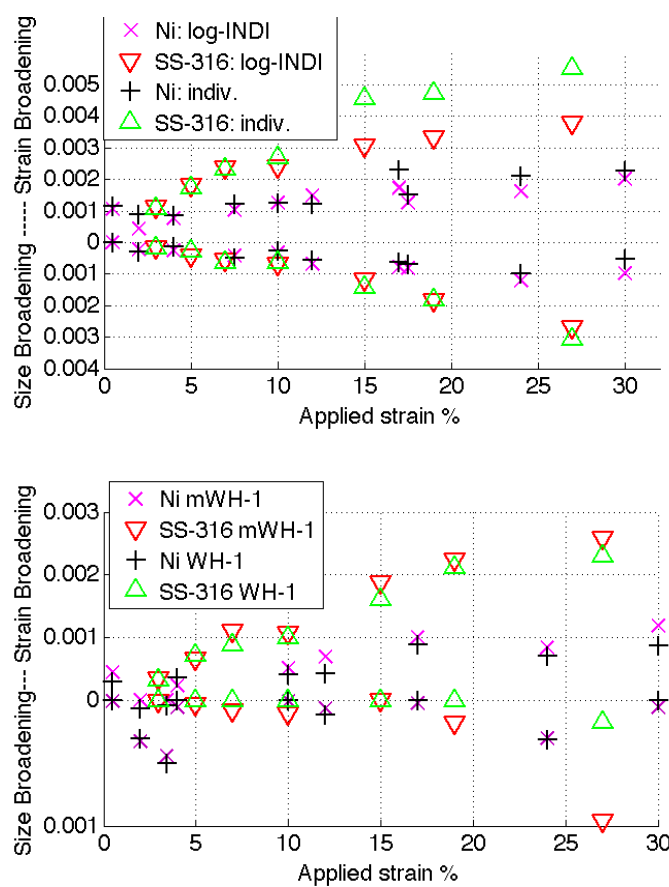


Figure 7-13. Comparison of size and strain broadening for modified and standard approaches for different metals plotted against strain. The Williamson-Hall (top) and Warren-Averbach (bottom) methods are shown.

The heterogeneity of full-width for different hkl

To help understand the contrast factor in more detail, this part considers the broadening of different peaks in more detail.

In Figure 7-14 to Figure 7-16, the change in the full-width of the individual peaks, for the different metals, are shown. From the figure it can be seen that the relative magnitude of the full-widths of the different peaks is different for the different metals. For a particular metal the relative broadening of different peaks stays approximately the same with applied strain. The main exception to this are the {111}/{222} peaks in nickel, which increase in magnitude, relative to the other peaks, at around 12% strain before falling at 30%. The expected transition to more edge dislocations would cause an increase in the {111}/{222} and {220} full-widths relative to the others (see the contrast factor values in Table 7-3). But this doesn't happen for any of the metals, only in nickel is part of this behaviour observed.

In Figure 7-14 to Figure 7-16, are selected modified Williamson-Hall plots for the different metals. The plots show that the contrast factor does not fully explain the heterogeneity observed. On the mWH plots, the full-width should increase linearly with $gC^{0.5}$, but in many cases the full-width values lie above or below the best-fit line. Of the plots shown the SS-304 full-width heterogeneity is best explained by the fit. The inability of the contrast factor to explain the heterogeneity probably explains why different contrast factor values are found for different methods and why the results are so scattered.

The presence of planar faults also causes different peaks to broaden by different amounts. When planar faults were inserted into WA and WH methods, by using the $W(g)$ function (see Section 2.4.6), the twin probability was found to be negligible for all metals and strain except for SS-316 at the two highest strains, where a twin probability of around 0.001 was found. Hence, planar faults would not explain the discrepancy.

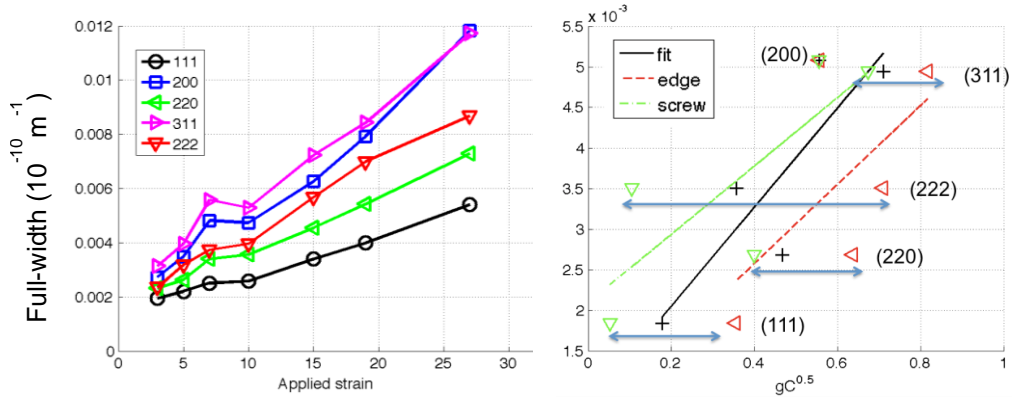


Figure 7-14. The change in the full-width of different FCC peaks for SS-316 with applied strain (left) and a modified WH plot at 27% strain (right). On the mWH plot the fit of the data is shown as well as fits when the q-values are set at edge and screw values.

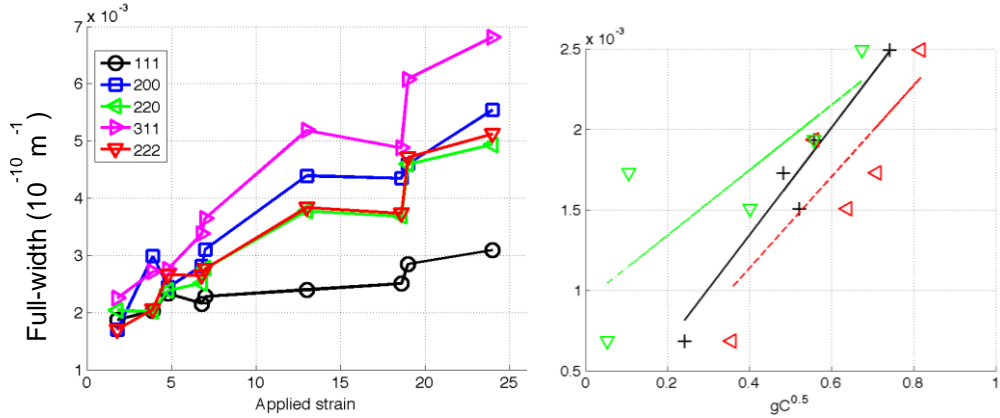


Figure 7-15. The change in the full-width of different FCC peaks for SS-304 with applied strain (left) and a modified WH plot at 24% strain (right). On the mWH plot the fit of the data is shown as well as fits when the q-values are set at edge and screw values.

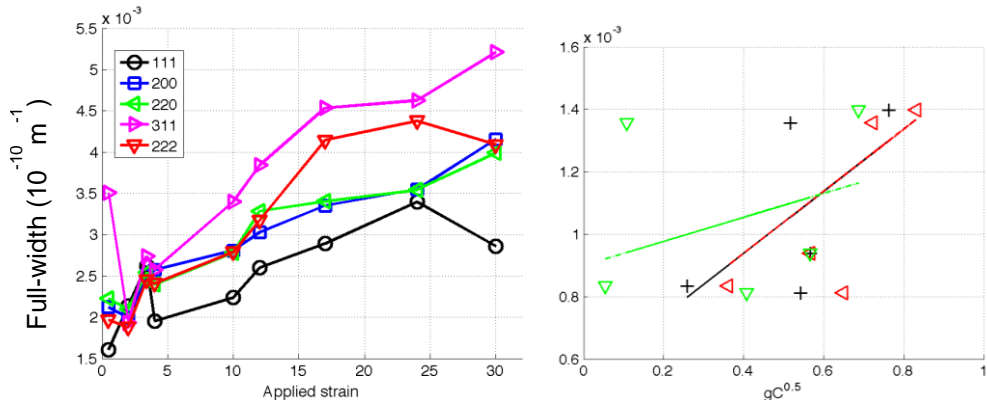


Figure 7-16. The change in the full-width of different FCC peaks for Ni-200 with applied strain (left) and a modified WH plot at 24% strain (right). On the mWH plot the fit of the data is shown as well as fits when the q-values are set at edge and screw values.

7.4.6 Conclusion: Contrast Factors in FCC alloys

In the previous sections, the use of the contrast factor in FCC metals has been investigated. It has been shown that in general, the q-value parameter of the contrast factor falls with applied strain. This change was shown to be consistent with the changes in dislocation population that are expected based on the deformation of these metals.

However, this section has also shown that there are problems with the use of the contrast factor equation. The contrast factor equation does not adequately explain the observed full-width heterogeneity, and hence different q-values are found for different methods. In addition, the q-values for the two stainless steel alloys, which should be expected to be the same, are different. These issues place considerable uncertainty on the measured q-values, and on whether the use of the contrast factor equation can be used to represent the dislocation population. Perhaps more problematic are the systematic differences between the results found with and without the use of the contrast factor. This is because these differences show that the use of the contrast factor could introduce errors to all other DPPA results.

There is another possible explanation to explain the heterogeneity, that the differences are due to inherent heterogeneities of deformation and different peaks represent different texture components. This explanation may explain the apparent discrepancy between stainless steel samples, which are measured in different directions. It could also explain the differences between the standard and modified approaches, since the different peaks represent different texture components. This is investigated further in Chapter 8.

7.4.7 Slip systems in Titanium alloys

In HCP metals the dislocation population represents the edge or screw nature of dislocations, but also represents the types of dislocation slip systems present. This additional factor means that the contrast factor can have more importance in HCP metals.

The q-values

The q-values for Ti-6Al-4V are found using the modified Williamson-Hall method (see Section 6.7.2 and 6.8). The q-values found for the three different mWH methods were found to be approximately the same and so only the q-values from the mWH-1 method are used. The q-values are different for the transverse and axial directions and different depending on which planes are used (see Figure 7-17). Hence in order to minimise these differences, the q-values used to calculate the slip system are the average of mWH fits of peaks using different plane combinations in the two measurement directions. The plane combinations are: the first ten HCP peaks (in increasing 2θ , g, or 1/d) (labelled 1:10), the first fifteen peaks (1:15), the first twenty (1:20), and the first twenty-five (1:25).

The q-values in Figure 7-17 follow a clear trend. The value of q_1 starts (at 1% strain) at just under 0, and with increasing amounts of applied strain the value falls, to around -1 at 8%. The value of q_2 starts at a similar value to q_1 , but increases with applied strain to a value of around 0.5 at 8%. The difference between the two measurement directions is markedly different for the 5% and 8% samples. In the transverse direction the q_1 are more negative and the q_2 values more positive in the transverse direction.

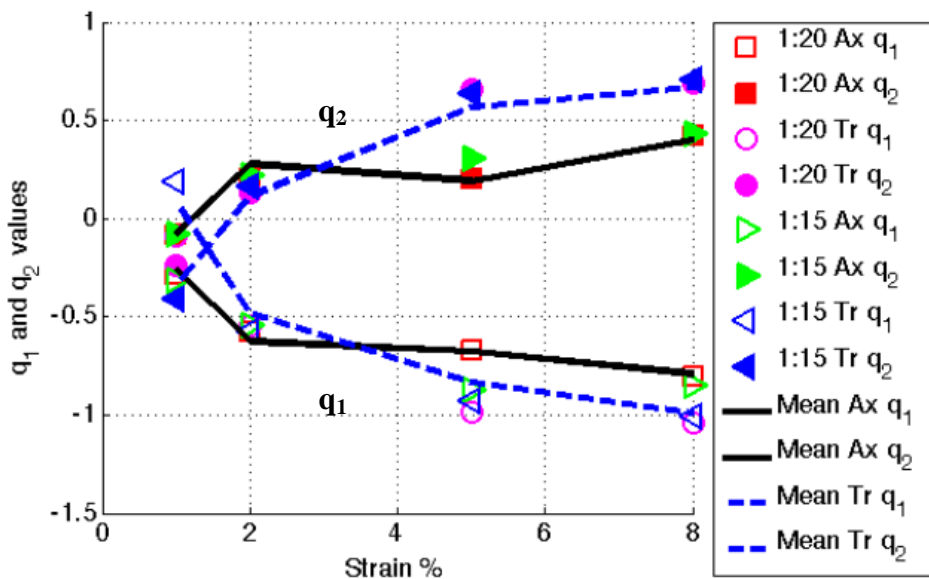


Figure 7-17. The q-value results from the mWH-1 method for Ti-6Al-4V. The results shown are for the fit of the first 15 and 20 HCP peaks measured in the axial and transverse direction.

The Ungar approach

Different slip systems broaden different peaks differently, and it has been found that for all slip systems there is a relationship between the broadening contribution and the value of x (for x , see equation 2.64) (Klimanek P, Kuzel 1988, Dragomir and Ungar 2002). Hence, it is possible to convert these q -values into slip systems. To do this a method similar to that used by Ungar et al. (2007), and described in Section 6.7.2, is used. The Ungar-type method can give a range of slip system results depending on the q -values, as shown in Figure 7-18.

Using the average q -values, the Ungar-type method predicts the slip systems shown in Figure 7-19, for Ti-6Al-4V. The individual slip systems are shown as well as the values of the different dislocation Burgers vector types. The $\langle a \rangle$ type dislocations are dominant with around 85%, then $\langle c+a \rangle$ with on average just over 10% and $\langle c \rangle$ with just under 10%. There are changes in these values with strain, but other than the increase in $\langle c \rangle$ between 1% and 2% strain, are within the expected random error. Prismatic and pyramidal $\langle a \rangle$ are the dominant slip systems at about 25% each, then basal and screw $\langle a \rangle$ which are on average just under 20%. From the literature (Biswas 1973, Zaefferer 2003, Partridge 1967) it would be expected that the dominant slip systems would be prismatic and basal $\langle a \rangle$, and so the dominance of pyramidal $\langle a \rangle$ would not be expected. There are no contributions from the non $\langle a \rangle$ screw slip systems and the dominant $\langle c+a \rangle$ slip system is $\text{Py}2\langle c+a \rangle$, with 5% slightly more than the expected dominant $\langle c+a \rangle$ slip system $\text{Py}4\langle c+a \rangle$ with 3.5%.

In order to compare CP-Titanium with Ti-6Al-4V, a different combination of peaks are used, which leads to different q -values and consequently different slip system prediction for Ti-6Al-4V than shown elsewhere. The results of the slip system analysis for Ti-CP 3.5% and the Ti-6Al-4V samples nearest in strain, 2% and 5%, are shown in Table 7-4. Both metals have large values of $\langle a \rangle$ dislocations, 100% for Ti-CP 3.5% and Ti-6Al-4V 5%, and 90% for Ti-6Al-4V 2%. The main difference between the metals is that for Ti-CP the dislocations are all $\text{Pr}\langle a \rangle$, whereas for Ti-6Al-4V there is a mix of $\langle a \rangle$ types.

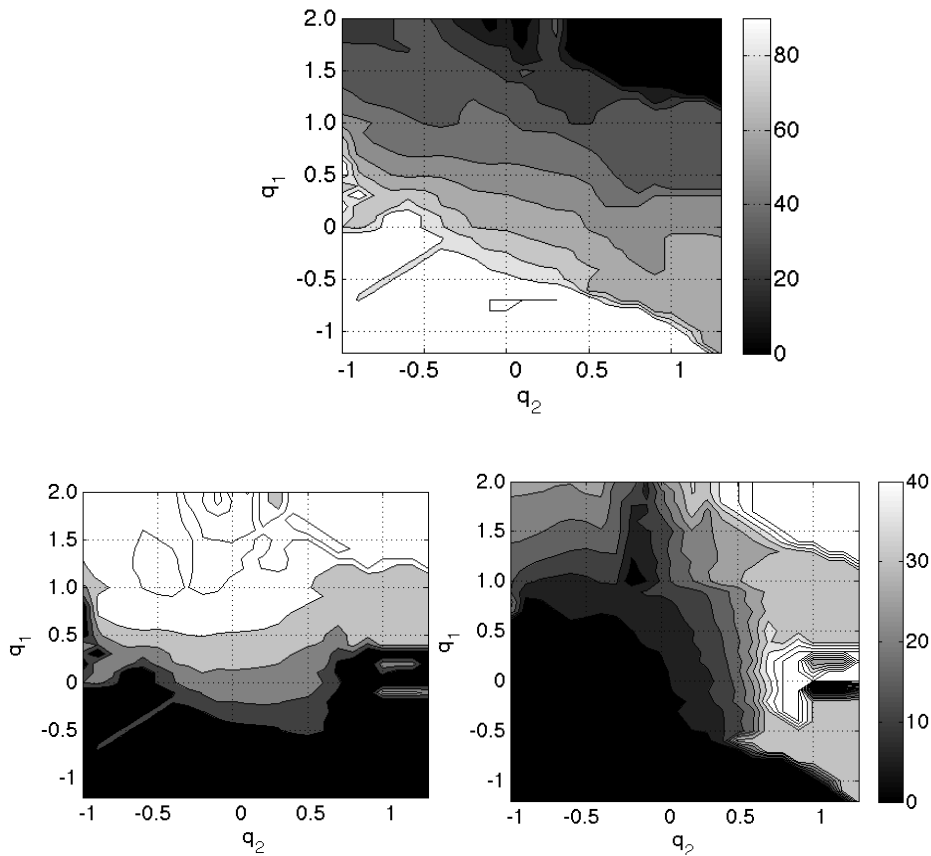


Figure 7-18. The change in the percentage of $\langle a \rangle$ (top), $\langle c+a \rangle$ (bottom left) and $\langle c \rangle$ (bottom right) slip systems, with different q -values, found using the Ungar-type method.

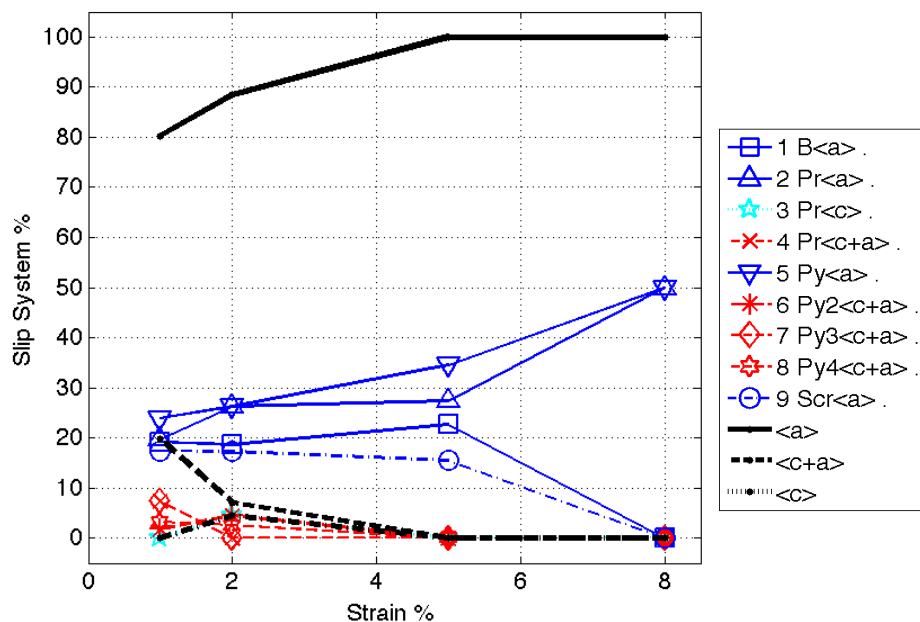


Figure 7-19. Inferred slip systems in Ti-6Al-4V using an Ungar-type method based on the q -values shown in Figure 7-17. The planes of the slip systems are given in Table 6.8.

A Modified Contrast Factor Approach- The individual method

A possible problem with the Ungar-type method is that it views all slip systems as being equally likely, when in reality some slip systems are expected to exist and others are not. Hence, based around this idea an alternative approach to calculate the dislocation population is used.

This method, which will be called, the individual method, works in the same way as the Ungar-type method, but limits the slip systems. From the literature review it was found that the most commonly observed slip systems in Ti-6Al-4V are prismatic $\langle a \rangle$, basal $\langle a \rangle$, pyramidal $\langle a \rangle$ and pyramidal $\langle c+a \rangle$ most commonly on the $\{10\bar{1}1\}$ plane (Py4). For this reason the following combination of slip systems were used.

A: Prismatic $\langle a \rangle$, Pyramidal $\{10\bar{1}1\} \langle c+a \rangle$, Screw $\langle a \rangle$, Screw $\langle c+a \rangle$

B: Basal $\langle a \rangle$, Prismatic $\langle a \rangle$, Pyramidal $\{10\bar{1}1\} \langle c+a \rangle$, Screw $\langle a \rangle$,
Screw $\langle c+a \rangle$

C: Pyramidal $\{10\bar{1}1\} \langle a \rangle$, Basal $\langle a \rangle$, Prismatic $\langle a \rangle$, Pyramidal $\{11\bar{2}2\}$
 $\langle c+a \rangle$, Screw $\langle a \rangle$, Screw $\langle c+a \rangle$

The values of the screw dislocations used in the Ungar-type method were calculated as an average of the different slip systems. The values for $\langle a \rangle$ dislocations are the same regardless of the slip plane but those for $\langle c+a \rangle$ are not. If we are to assume that the $\langle c+a \rangle$ screw dislocations are on the same pyramidal plane $\{10\bar{1}1\}$ used for the edge dislocations the values are very different. The value of C_{hk0} is approximately one third smaller and whereas the average values are negative for q_2 and positive for q_1 , the $\{10\bar{1}1\}$ q -values are the opposite. Both screw $\langle c+a \rangle$ values are used in the calculations of slip systems but are done so separately.

The slip system predictions for the individual methods are shown in Figure 7-20, using the average screw $\langle c+a \rangle$ values, as used in the Ungar-type method. The values of the two approaches are similar at low strains (1% and 2%), but at higher strains (5% and 8%) they are not. At the higher strains the individual method does
251

not have 100% $\langle a \rangle$ dislocations. Instead, the values of $\langle a \rangle$ and $\langle c+a \rangle$ slip systems, are approximately constant with applied strain. There is an overall fall in screw $\langle a \rangle$ and basal $\langle a \rangle$ systems. The $\text{Pr}\langle a \rangle$ is the dominant slip system and its percentage increases with applied strain. This is even the case when $\text{Py}\langle a \rangle$ slip system is included, which had the same activity as $\text{Pr}\langle a \rangle$ in the Ungar-type method. The $\langle c+a \rangle$ dislocations are almost all of edge character. The addition of more slip systems does not change the trends or relative percentages of the different slip systems but it does reduce the magnitude of the slip systems.

The slip system predictions for the individual methods using the screw $\text{Py}\langle c+a \rangle$ values are shown in Figure 7-21. There is a large difference between these values and those using the average values, particularly due to the change in screw $\langle c+a \rangle$ values. The quantity of screw $\langle c+a \rangle$ is close to zero for the average values but is the second most dominant slip system when the $\text{Py}\langle c+a \rangle$ screw values are used, and the values of screw $\langle c+a \rangle$ and $\text{Pr}\langle a \rangle$ are close to each other up to 5%. Unlike the other individual method, in this one the percentage of $\langle a \rangle$ slip systems falls and the percentage of $\langle c+a \rangle$ dislocations increases.

The results of the slip system analysis for Ti-CP 3.5% and those nearest in strain Ti-6Al-4V sample of 2% and 5% are shown in Table 7-4. The slip systems predicted for Ti-CP, using the different individual methods, are similar to those found for Ti-6Al-4V, particularly the Ti-6Al-4V 5% sample. The main difference between the Ti-6Al-4V 5% and Ti-CP, for the individual methods, is the larger activity of the pyramidal $\langle c+a \rangle$ slip system for the Ti-6Al-4V 5% sample. This is also seen for the Ti-6Al-4V 2% sample and on average the Ti-6Al-4V samples predicts higher pyramidal $\langle c+a \rangle$ slip activity by around 5%. For the Ti-6Al-4V 2% sample the predictions also suggest a larger activity of basal $\langle a \rangle$ and screw $\langle a \rangle$.

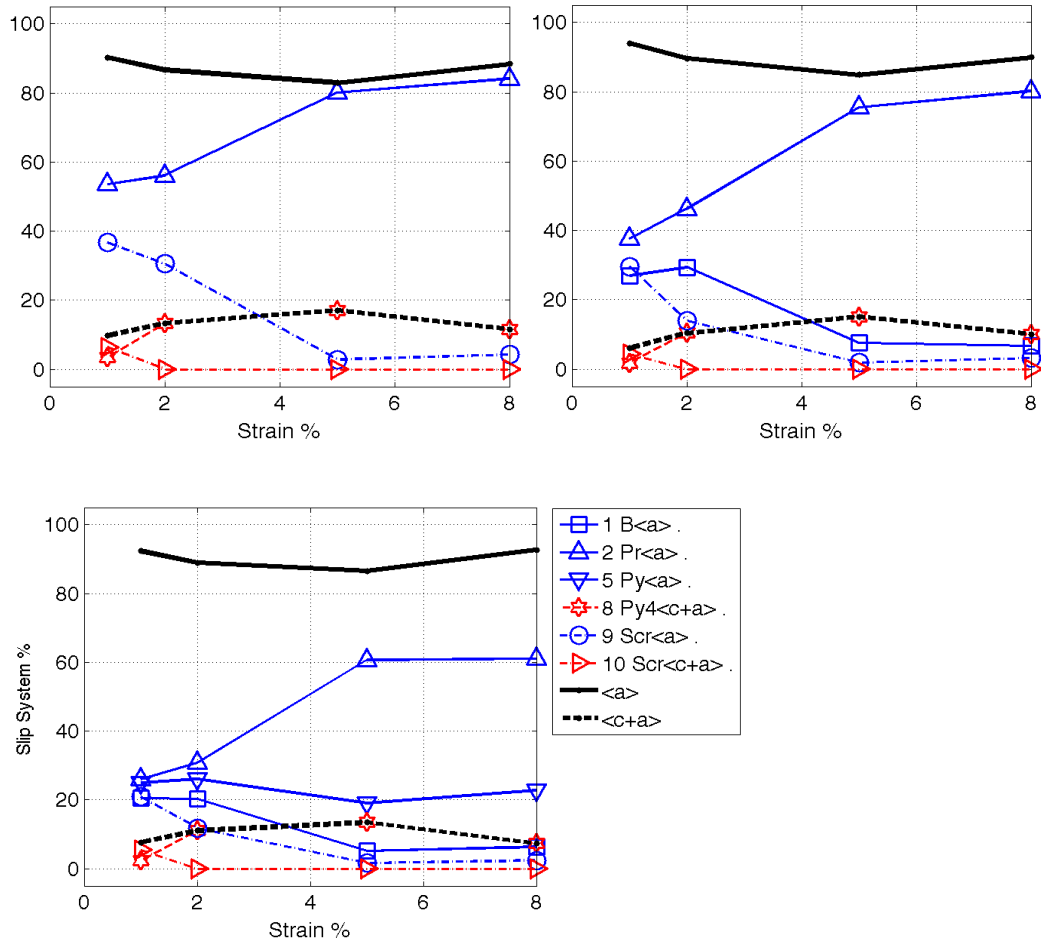


Figure 7-20. Results of the individual slip system predictions using the average $\langle C+a \rangle$ screw values for Ti-6Al-4V. For $Pr\langle a \rangle$, $Py\langle c+a \rangle$, $Scr\langle a \rangle$, $Scr\langle c+a \rangle$ (top left), $Ba\langle a \rangle$, $Pr\langle a \rangle$, $Py\langle c+a \rangle$, $Scr\langle a \rangle$, $Scr\langle c+a \rangle$ (top right) and $Ba\langle a \rangle$, $Py\langle a \rangle$, $Pr\langle a \rangle$, $Py\langle c+a \rangle$, $Scr\langle a \rangle$, $Scr\langle c+a \rangle$ (bottom left). Found using q-values from Figure 7-17.

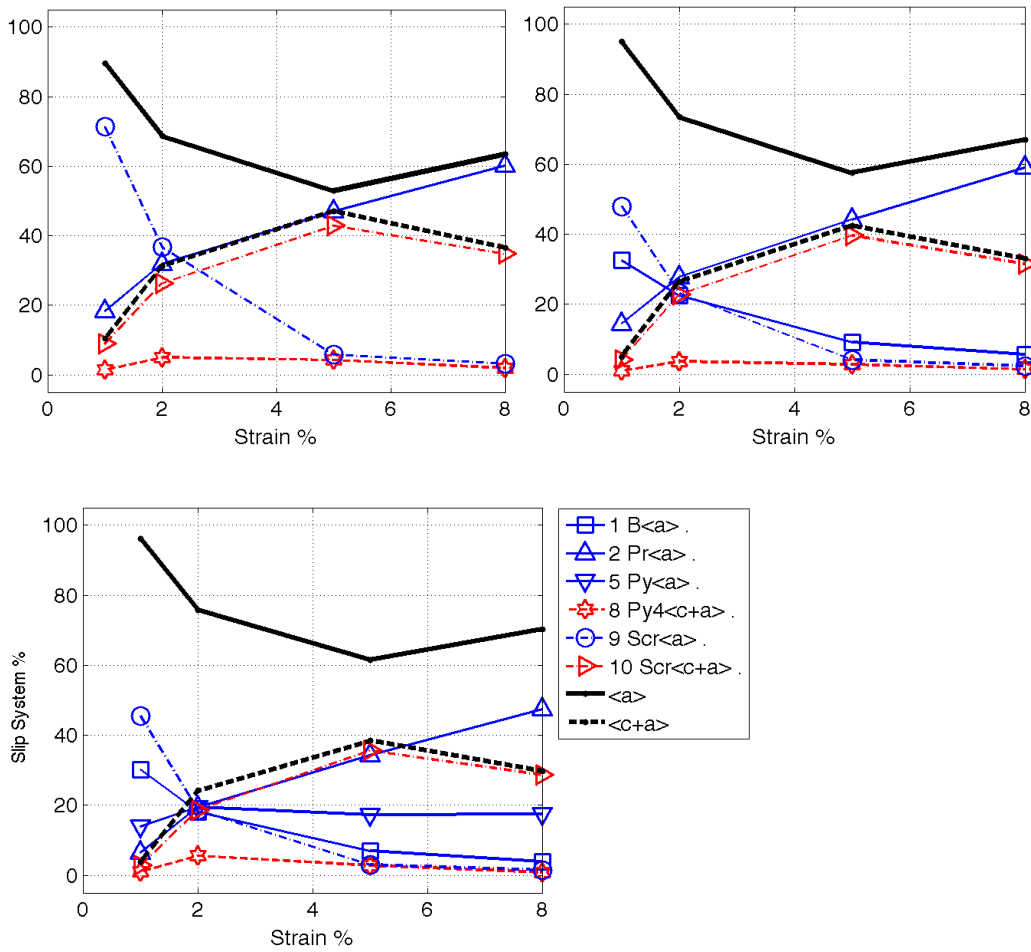


Figure 7-21. Results of the individual slip system predictions using the $\text{Py} \{10 \bar{1}1\} <\text{c+a}>$ screw values, for Ti-6Al-4V. For $\text{Pr} < \text{a}>$, $\text{Py} < \text{c+a}>$, $\text{Scr} < \text{a}>$, $\text{Scr} < \text{c+a}>$ (top left), $\text{Ba} < \text{a}>$, $\text{Pr} < \text{a}>$, $\text{Py} < \text{c+a}>$, $\text{Scr} < \text{a}>$, $\text{Scr} < \text{c+a}>$ (top right) and $\text{Ba} < \text{a}>$, $\text{Pr} < \text{a}>$, $\text{Py} < \text{c+a}>$, $\text{Scr} < \text{a}>$, $\text{Scr} < \text{c+a}>$ (bottom left). Found using q-values from Figure 7-17.

Table 7-4.The predicted slip systems for Ti-CP at 3.5% and Ti-6Al-4V at 2% and 5%. Results are based on the average q-values obtained from modified Williamson-Hall fits for the axial and transverse direction and using different peaks. For details of the methods see the body of the text. The planes of the slip systems are given in Table 6.8.

	1 B[a]	2	3	5 Py [a]	6 Py2 [c+a]	8 Py4 [c+a]	9 Scr [a]	[a]	[c+a]	[c]
CP-3.5%										
PrPyCA	0.0	82.8	0.0	0.0	0.0	11.3	5.9	88.7	11.3	0.0
BaPrPyCA	6.8	79.4	0.0	0.0	0.0	9.9	3.9	90.1	9.9	0.0
PyBaPrPyCA	5.7	58.9	0.0	25.0	0.0	7.5	2.8	92.5	7.5	0.0
SS-Ungar	0.0	100.0	0.0	0.0	0.0	0.0	0.0	100.0	0.0	0.0
Ti-6-4 2%										
PrPyCA	0.0	59.2	0.0	0.0	0.0	15.8	25.0	84.2	15.8	0.0
BaPrPyCA	25.6	50.5	0.0	0.0	0.0	12.8	11.2	87.2	12.8	0.0
PyBaPrPyCA	18.0	34.3	0.0	26.4	0.0	13.2	8.2	86.8	13.2	0.0
SS-Ungar	20.1	25.7	4.9	25.7	4.9	0.0	18.8	90.3	4.9	4.9
Ti-6-4 5%										
PrPyCA	0.0	80.1	0.0	0.0	0.0	17.1	2.9	82.9	17.1	0.0
BaPrPyCA	7.6	75.7	0.0	0.0	0.0	15.2	1.4	84.8	15.2	0.0
PyBaPrPyCA	5.2	61.1	0.0	18.9	0.0	13.5	1.3	86.5	13.5	0.0
SS-Ungar	20.8	29.2	0.0	41.7	0.0	0.0	8.3	100.0	0.0	0.0

Discussion on titanium dislocation population calculations

In titanium the dominant slip systems are, in order of activity, are prismatic $\langle a \rangle$, basal $\langle a \rangle$, first order $\{10\bar{1}1\}$ pyramidal $\langle a \rangle$ and first order pyramidal $\langle c+a \rangle$ (Biswas 1973, Zaefferer 2003, Partridge 1967). All methods are in agreement that $\langle a \rangle$ slip is the most active, as would be expected. As can be seen in Figure 7-18, there are q-values that would give $\langle c+a \rangle$ or $\langle c \rangle$ as the dominant slip system, but those that are found correspond to $\langle a \rangle$ dislocations being dominant. The slip system expected to be the most active, Prismatic $\langle a \rangle$, is also found to be the dominant slip system in most methods, especially at high strain. The second most active slip system is found to be pyramidal $\langle a \rangle$ and then the third basal $\langle a \rangle$ at low strains and pyramidal $\langle c+a \rangle$ at high strains. Whereas, it is expected that the order of these slip systems would be basal $\langle a \rangle$, then pyramidal $\langle a \rangle$. However, this discrepancy may be explained by the observation that basal dislocations tend to be of screw type (Biswas 1973, Zaefferer 2003). It has been found that at low strains, dislocations tend to be close to screw character in CP titanium and Ti-6Al-4V, and with an increasing amount of deformation there is an increase in edge dislocations (Conrad and Jones 1953, Biswas 1973, Zaefferer 2003, Castany et al 2007, Zaefferer 2003). The results show a decrease in $\langle a \rangle$ screw dislocations, from being one of the most dominant slip systems at 1%, to being almost non-

existent at 8%, so the results are in some agreement with the observations of $\langle a \rangle$ screw dislocations. A large difference found between the different approaches is the amount of $\langle c+a \rangle$ slip systems. In the Ungar-type method, there are no $c+a$ dislocations calculated at 5% and 8%, whereas for the individual method, using pyramidal $\langle c+a \rangle$ screw dislocations, there are 30-40% at these strains. An indication of the relative quantities of prismatic $\langle a \rangle$ to pyramidal $\langle c+a \rangle$ slip, is given by the resolved stresses needed to initiate them (CRSS). The smaller the CRSS, the more active a slip system is expected to be. However, for Ti-6Al-4V the calculated or measured values can vary widely, the ratio of the CRSS of $\langle c+a \rangle$ to the CRSS of $\text{Pr}\langle a \rangle$ has been found to vary from around 1.3 (Yapici et al. 2006) to 12 (Fundenberg et al. 1997). Although difficult to quantify by TEM, the TEM analysis of Zaefferer (2003), on Ti-6Al-4V deformed by 5%, provides a qualitative idea of the relative amount of $\langle c+a \rangle$ slip. Zaefferer found that of grains with a specific or dominant glide system, approximately 20% of these the dominant slip system was pyramidal $\langle c+a \rangle$. However, they also noted that in these grains the dislocation density was lower than in those with $\langle a \rangle$ dislocations. Hence, based on this discussion it is suggested that the amount of $\langle c+a \rangle$ dislocations is closest to the values obtained in the individual method with the average $\langle c+a \rangle$ screw value (Figure 7-20).

The differences between CP titanium and Ti-6Al-4V are difficult to evaluate because of the limited number of strain increments measured for CP titanium. However, the main difference is a lower percentage of $\langle c+a \rangle$ slip in CP titanium. It is expected that twinning is more active in Ti-CP than in Ti-6Al-4V, hence twinning is easier to activate relative to $\langle c+a \rangle$ in Ti-CP. Therefore, it may be expected that if these two systems compete there would be a higher percentage of $\langle c+a \rangle$ in Ti-6Al-4V and a higher percentage of twins in Ti-CP. However, this would not be in full agreement with the TEM analysis of Zaefferer (2003), who found the quantity of $\langle c+a \rangle$ dislocations in the alloy that twinned was comparable or more than that found in the other alloys. If the average of 2% and 5% Ti-6Al-4V results are compared with Ti-CP, then there is less activity of basal $\langle a \rangle$ in Ti-

CP. Zaefferer (2003) showed that there is greater activity of basal $\langle a \rangle$ in Ti-6Al-4V than Ti-CP, which is in agreement with the DPPA results.

7.4.8 Systematic Errors from the use of the contrast factor for titanium

There are two main causes of systematic errors that may result from the use of the contrast factor in HCP metals. Errors can result because of incorrect calculations of the dislocation population, and as a result of the use of the contrast factor equation. These possible errors are discussed next.

Systematic Error from calculating the dislocation population

One of the main reasons that a method is needed to calculate the slip systems in HCP metals is to be able to calculate the value of Cb^2 , so that the correct micro-strain and dislocation density values are found. As shown in Section 2.4.5, in FCC metals, the active slip systems, assuming they are equally distributed, do not have a large effect on the value of the contrast factor and Cb^2 , since there is only one active slip system. However, for HCP metals, with many more possible slip systems, the value of Cb^2 can change by significant amounts. This can be seen in Table 7-5, where it is shown that values of Cb^2 range from close to 0, for screw $\langle c \rangle$ to almost 13 for screw $\langle c+a \rangle$. The differences are also large between the different slip systems for the dominant $\langle a \rangle$ Burgers vector. The lowest values are for screw $\langle a \rangle$ and then basal $\langle a \rangle$, at 1.26 and 1.76 respectively, are approximately half that of prismatic $\langle a \rangle$ at 3.08, the dominant slip system in titanium. To put these values into perspective the root-mean-square-strain using the WH-1 method changes between about 2×10^{-3} and 4.5×10^{-3} from 1% to 8% applied strain. These changes are smaller than those between prismatic $\langle a \rangle$ edge and screw $\langle a \rangle$.

The values that are obtained from the different methods, at the different applied strains, are shown in Figure 7-22. The values of Cb^2 vary between around 10^{-6} to over 12, for the different slip systems. The changes in the calculated values are less than these changes but are still significant, varying by about 20% between the maximum and minimum predictions. The differences between the predictions

from the individual methods and the Ungar-type method are significant for values below 8%, with differences between the two of around 20% at 1% and 5% applied strains. It should be noted that the C_b^2 values are calculated based on the individual slip systems, and not the average $\langle a \rangle$, $\langle c+a \rangle$ and $\langle c \rangle$ values as done by Ungar and colleagues (2007). There are benefits to both approaches, the approach used by Ungar et al. (2007) is probably best used if there is uncertainty in the slip systems calculations, and the approach used here if the slip systems are known.

The problem is that the change in the dislocation population is not known, yet different dislocation populations can have a large change in the results. Hence, the use of the contrast factor, with a method to use the slip system activity, could be adding large systematic errors to the results.

Table 7-5. The parameters used to find the contrast factor for the eleven slip systems of titanium (Dragomir and Ungar 2002). The planes of the slip systems are given in Table 6.8.

	Ba[a]	Pr[a]	Pr[c]	Pr [c+a]	Py[a]	Py2 [c+a]	Py3 [c+a]	Py4 [c+a]	Scr[a]	Scr	Scr[c] [c+a]
q1	-0.101	-1.193	3.616	2.017	-0.894	1.299	1.894	1.527	0.595	1.257	1.7E+05
q2	-0.103	0.356	1.226	-0.617	0.183	0.397	-0.366	0.146	-0.710	-0.940	-9.9E+04
Cslip	0.202	0.354	0.049	0.102	0.312	0.092	0.098	0.093	0.144	0.419	3.6E-06
b	2.95	2.95	4.68	5.53	2.95	5.53	5.53	5.53	2.95	5.53	4.68
C_b^2	1.76	3.08	1.06	3.14	2.71	2.82	3.00	2.85	1.26	12.82	7.9E-05

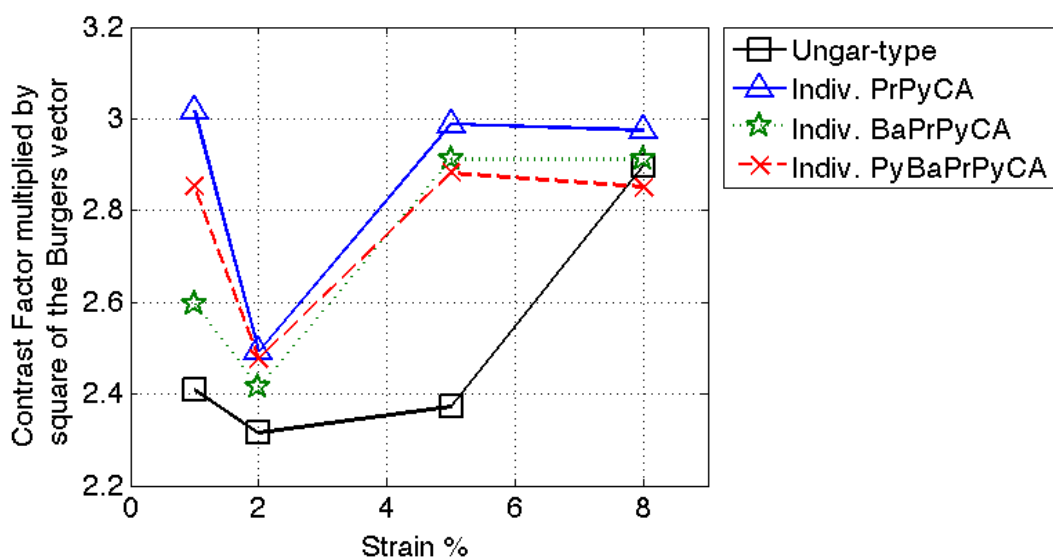


Figure 7-22. Predicted C_b^2 values calculated based on the different slip system predictions.

Systematic errors due to the use of the contrast factor equation

The systematic error due to the use of the contrast factor equation can be thought of as consisting of two parts. Firstly, the formula, and the underlying assumptions it uses, could be incorrect and secondly, the q-values obtained from fitting could be incorrect. Unlike the error in dislocation population, both of these will contribute to errors in the size and strain results. However, it may not be possible to separate the two contributions. To investigate this the transverse results are considered.

When using the WH-1 and mWH-1 method it is found that there are differences in both size and strain contributions depending on which peaks are chosen and whether the modified method is used, as shown in Figure 7-23. Part of the discrepancy between the modified and standard approached may be due to the dislocation population and how this influences the q-values, and hence the contrast factor (as was discussed for FCC metals). In general, for a given peak the higher the q-values the higher its contrast factor (except for peaks with an 'l' index equal to 0, such as {2000}). Different peaks have different contrast factor values and should also have different strain contributions.

$$\bar{C}_{hk,l} = \bar{C}_{hk,0}(1 + q_1x + q_2x^2) \quad x = \frac{2l^2}{3(ga)^2} \quad (7.5)$$

In order to investigate this, the strain contribution is adjusted based on calculated contrast factor values, which use the q-values found from the m-WH fit of the first 15 peaks. This is shown in Figure 7-24. The strain for the {2020} peak is unchanged because its contrast factor value is independent of the q-values, however the values of the {0002} and {1121} peaks do change based on the change in the value in the bracket in Equation-7.5. For the {0002} peak, the value in the bracket increases with applied strain from 0.17 to 1.4, whereas the {10T1} peak falls slightly from 0.84 to 0.73. This adjustment brings the strain contribution values of the {0002} and {10T1} peaks closer to the {2020} peak, in most cases. However, it doesn't explain why there are differences in the size values and there is still a significant difference between the different values. The differences between strain values may be due to how size and strain contributions are separated. In order to investigate this and see how effective the contrast factor

is in describing the heterogeneity of full-width, it is helpful to consider modified WH plots of the metal.

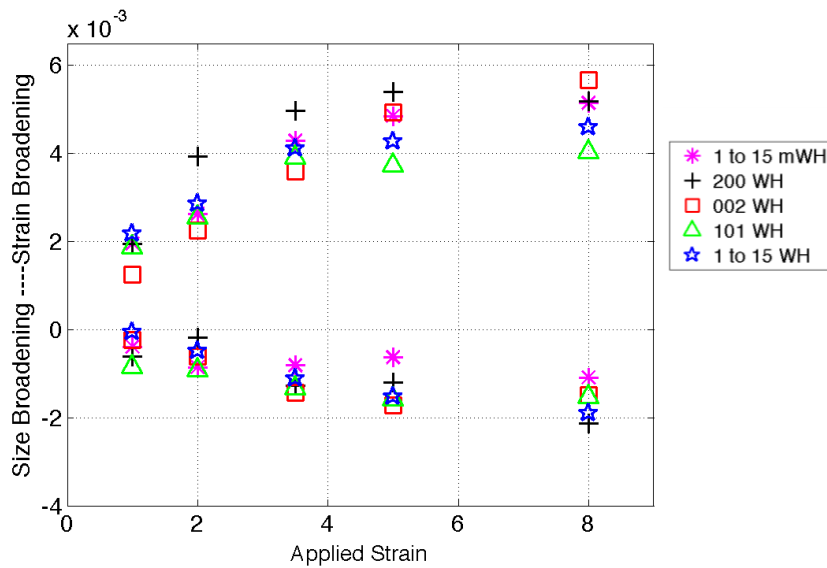


Figure 7-23. Comparison of size and strain broadening for modified and standard approaches of the Williamson-Hall method, for Ti-6Al-4V plotted against strain. Only the hkl indices of the hkil notation are shown.

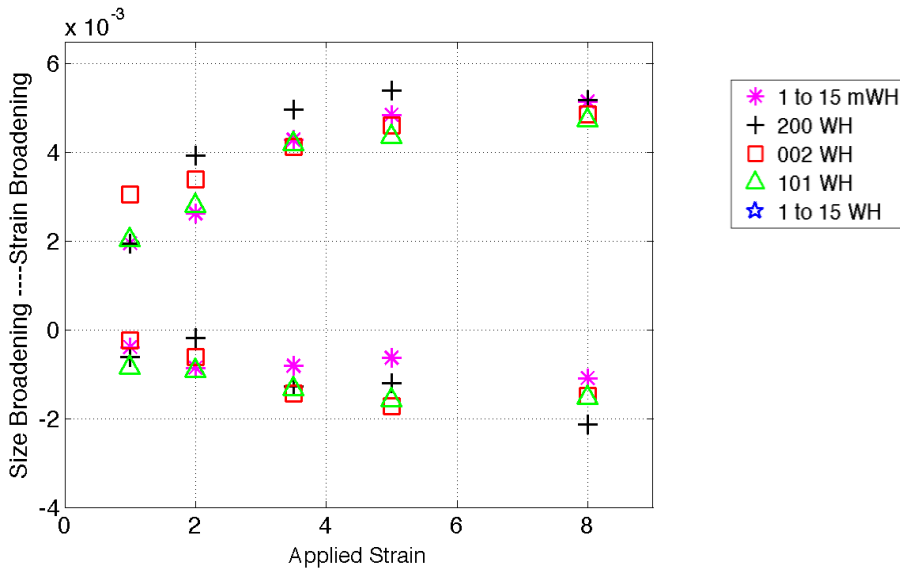


Figure 7-24. Comparison of size and strain broadening for modified and standard approaches of the Williamson-Hall method, for Ti-6Al-4V plotted against strain. The strain values are adjusted by using the q-values found from the modified WH method, to adjust the contrast factor value. i.e. if a peak has a larger contrast factor then the strain broadening is reduced. Only the hkl indices of the hkil notation are shown.

In Figure 7-25, example modified Williamson-Hall (mWH-1) plots for 2% and 8% applied strain are shown. In general, the contrast factor does reasonably well in describing the hkl heterogeneity in full-width. The fit is comparable with that seen for SS-304 and better than Ni-200 and SS-316. However, there is a problem with the fits at strains of 5% and 8%. The problem is that the q-values are not possible from any combination of slip systems. At 8% strain q_1 is approximately -1 and q_2 approximately 0.6. Both values are possible individually, but together are not (see Table 4.8). The slip system that is closest to these q-values is prismatic $\langle a \rangle$ slip, and a plot of the full-width at 8% against $gC^{0.5}$, for contrast values found using this slip system, is shown in Figure 7-25. This value of the contrast factor leads to a very poor fit of the data. In addition, to unrealistic q-values there is also the problem that the full-widths are different in the two measurement directions, and consequently give different q-values.

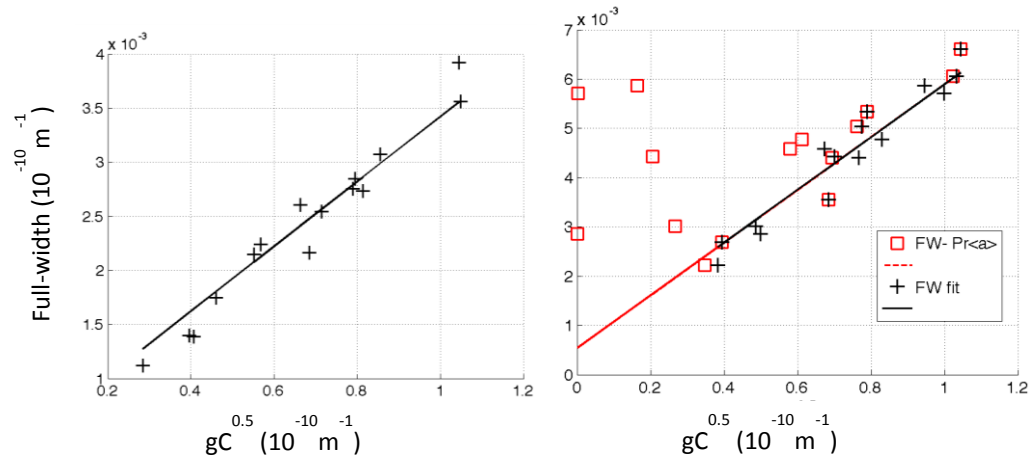


Figure 7-25. Example modified Williamson-Hall plots for Ti-6Al-4V at a strain of 2% (left) and 8% (right). For the 8% mWH plot the change in $gC^{0.5}$ if all dislocations are $Pr\langle a \rangle$ is shown.

7.4.9 Contrast Factor in titanium: Conclusions

In the previous sections the use of the contrast factor equation in titanium, and how it can be used to provide information about the dislocation population have been investigated.

Three different approaches were used to find the dislocation population, from the fitted q-values. There is a difficulty in evaluating these methods because of the uncertainty of what the dislocation population is. However, based on the TEM results of other researchers, it was found that the results of the three methods qualitatively agree with the expected dislocation population in titanium alloys, such as the dominance of $\langle a \rangle$ and particularly prismatic $\langle a \rangle$ slip systems. There are also cases when the results are in disagreement with the expectations, such as the 100% $\langle a \rangle$ dislocations found for the Ungar-type method. The use of the individual method (where only those slip systems expected to exist) should be advantageous to the Ungar-type method, if the active slip systems are known. However, in its full form (when the expected pyramidal $\langle c+a \rangle$ plane is used for screw dislocations) the method gives higher values of $\langle c+a \rangle$ dislocations than expected. Overall, based on the results presented here, it is not clear how reliable the results of these methods are in providing information about the dislocation population.

The dislocation population is needed to calculate the dislocation density, and differences in the dislocation population can result in large differences in the dislocation density. Hence, it is important that the uncertainty surrounding the calculation of dislocation population is resolved, for the DPPA methods to be used in HCP metals.

It was also shown in the previous sections that there are problems with the use of the contrast factor equation, which could in turn produce errors. The use of the equation does well in explaining the broadening heterogeneity of different hkl peaks. The problem is that it does so with q-values that are not representative of any possible slip system and there is a difference in different measurement directions. A different approach to the contrast factor, and a discussion on the possible causes of discrepancies with its use is presented in Chapter 8.

7.5 Comparison of Diffraction Sources

In this section the influence that the diffraction source has on the results of DPPA methods are considered. In this thesis three different diffraction sources are used (see Section 3.4), and of these two have been used to study the same material-laboratory x-ray and neutron. To quantify the influence of the diffraction source on DPPA results, one metal is used nickel-200, using neutron and lab x-ray sources. To be consistent, the same five FCC peaks are used for both sources, even though for neutron diffraction more peaks are measured.

In Figure 7-26, the average full-width of the first five diffraction peaks are shown for the two sources. The full-width values for neutron source are close to the lab x-ray values, and within the scatter of the lab x-ray results. The results of the PV variance method (Figure 7-27) are also close for the two diffraction sources. The neutron results also exhibit the same problems with the micro-strain values being negative. These two features are also found with the Voigt Variance method, and integral breadth method, and may be a feature of the similar full-width and PV mixing parameter values of the instrumental of the two sources (as shown in Figure 3.1). Larger differences are found with the modified and standard Williamson-Hall methods (Figure 7-28 and Figure 7-29). The differences for the crystal size values using the WH method are probably further evidence of the unreliability of the crystal size values found using this method. The differences in the micro-strain values using the modified WH method may be partly explained by the different q-values obtained for the two sources. The results of the Warren-Averbach method (Figure 7-30) from the two sources are closer than the WH methods, but show some differences. The crystal size values from the two methods are close above around 5%, but the dislocation density values are lower in almost all cases for the neutron source.

The results of this section show that the diffraction source can introduce additional uncertainty to DPPA results. The way that the results are changed by the different sources is different depending on the DPPA method. This makes quantification of the influence of a diffraction source on results difficult. In addition, it is not clear how the differences shown here would relate to the differences between lab x-ray and synchrotron x-ray (the sources used in Chapter

7). The main difference between the two sources is the size of the diffracting volume, which is much larger for neutron samples. The similarity in the instrumental samples of lab x-ray and neutron sources, in contrast to synchrotron x-ray which has lower full-width and mixing parameter values (Figure 3.1), may mean that the differences between lab x-ray and synchrotron sources are larger.

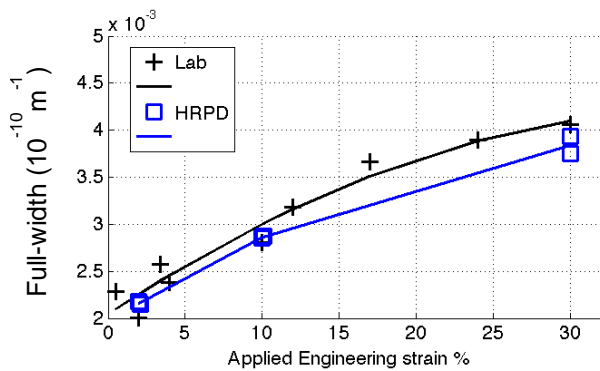


Figure 7-26. The change in the Full-width (average of first 5 peaks, with instrumental accounted for) found from laboratory x-ray and neutron sources (HRPD). The lines represent a fit of the values to a 2nd order polynomial (see text Section 6.2).

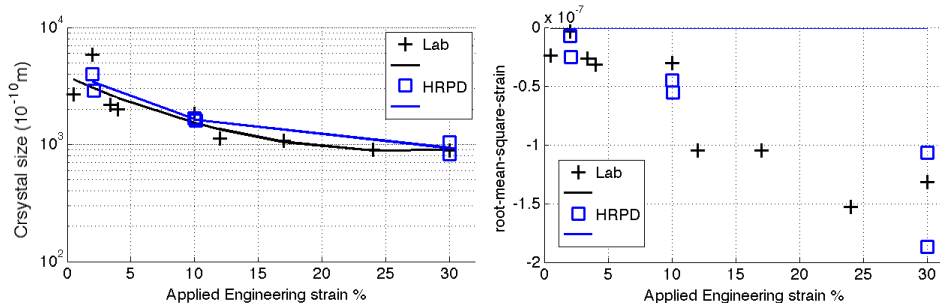


Figure 7-27. The change in the crystal size (left) and rms strain (right) found from laboratory x-ray and neutron sources (HRPD), using the PV Variance method. The lines represent a fit of the values to a 2nd order polynomial (see text Section 6.2).

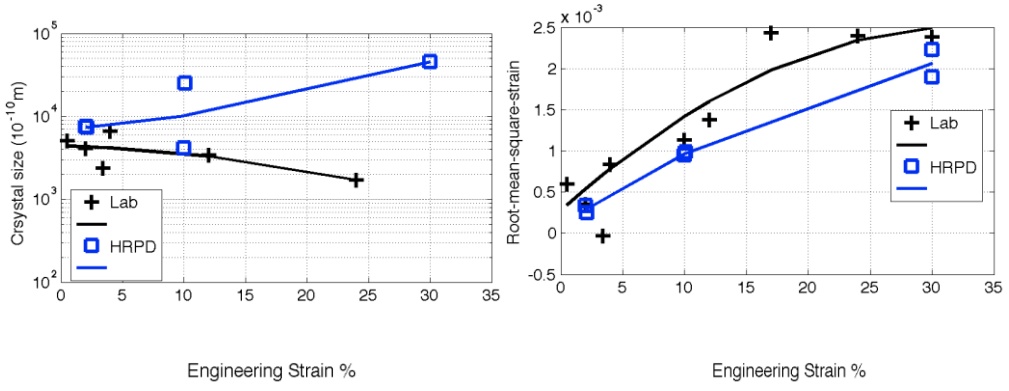


Figure 7-28. The change in the crystal size (left) and rms strain (right) found from laboratory x-ray and neutron sources (HRPD), using the WH-2 method. The lines represent a fit of the values to a 2nd order polynomial (see text Section 6.2).

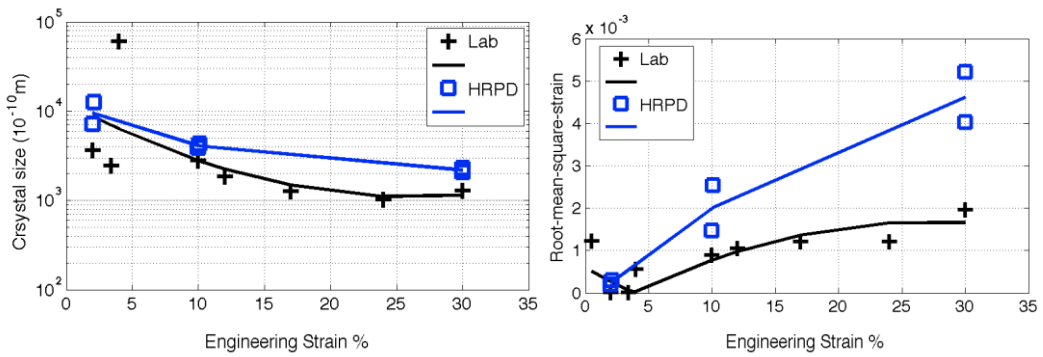


Figure 7-29. The change in the crystal size (left) and rms strain (right) found from laboratory x-ray and neutron sources (HRPD), using the mWH-3 method. The lines represent a fit of the values to a 2nd order polynomial (see text Section 6.2).

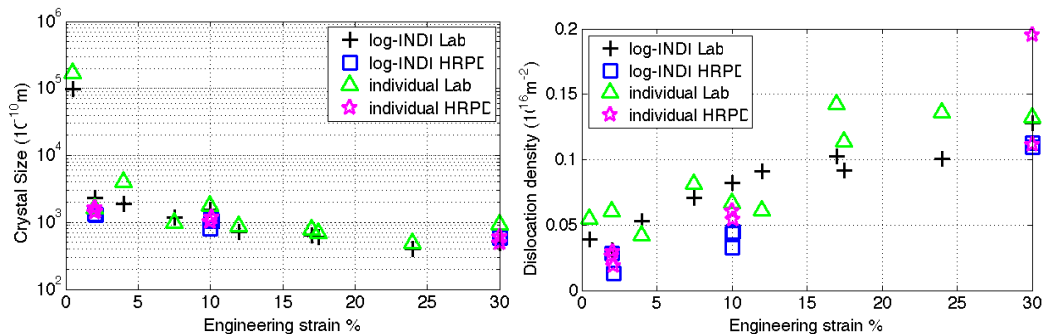


Figure 7-30. The change in the crystal size (left) and dislocation density (right) found from laboratory x-ray and neutron sources (HRPD), using the WA log-INDI method. The lines represent a fit of the values to a 2nd order polynomial (see text Section 6.2).

7.6 Conclusion

In this Chapter I examined different Diffraction Peak Profile Analysis (DPPA) methods, to establish their usefulness in characterising the deformed state of a metal. The results highlighted the difficulty in evaluating a particular DPPA method and in turn the effectiveness of its use.

The main problems are that -

- most of the parameters obtained by the DPPA methods cannot be evaluated by other methods (e.g. TEM).
- the differences between the DPPA results of different metals are smaller than expected given the differences in their deformed microstructure

7.6.1 Crystal Size and Micro-strain

The problem of evaluation is best represented by the crystal size and micro-strain parameters. For most methods, the micro-strain increases and the crystal size falls with increasing applied strain. It would be expected that the micro-strain would increase for all metals, because they all work-harden and hence accumulate strain and dislocations within grains. The problem is that it is not possible to establish whether the micro-strain values have any quantifiable meaning or even qualitatively compare different metals, because they can't be verified by other methods (e.g. TEM). Hence, it is not possible to verify, or otherwise, a method based on the micro-strain values it produces.

This is also the case for crystal size. The traditional view of crystal size is that it is the size of a region that diffracts incoherently with all other parts of a crystal. This is because it has a different orientation to neighbouring regions. However, the results of this chapter show that this description is not correct. In the metals studied those that are not expected to consist of small crystals misorientated from each other (Ti-6Al-4V and stainless steel) and have DPPA crystal size values of similar magnitude to those that do (nickel). Hence, the crystal size can be thought of as either, being due to an error from size and strain separation or, the size of an undistorted part of a crystal. This undistorted size component can be thought of as

being caused by dislocations, that do not necessarily have a misorientation across them.

I have tried to demonstrate in this chapter that the second description is the more likely. This description of the crystal size means that the value cannot be verified, and the obscure definition also means that the value has little use. The exception to this obscure definition of crystal size is found with the alternative method, which gives a falling crystal size value for nickel, but no size broadening for the low SFE metals. Hence, the alternative method is the only one that gives a description of crystal size that can be verified.

Based on these findings, I conclude that the use of most DPPA methods to provide crystal size and micro-strain information, is of little value since they add additional errors (as shown in Chapter 6) without providing additional information about the sample. However, there may be benefits for studying different type of metals than those used in this thesis which were deformed metals that work-harden and have a medium sized grain size.

7.6.2 Comparison of methods that give crystal size and micro-strain values

Despite these problems it is still worthwhile to consider the results of methods that provide crystal size and micro-strain values.

Based on the results in this and chapter 6, I would not recommend the use of the variance-A method for deformed metals. The methods attribute the majority of broadening to size broadening, and give negative strain values for all the FCC metals, using both lab x-ray and neutron diffraction sources. The problems are smaller for Ti-6Al-4V, but it still provides strain values that are over 10 times lower than other methods (e.g. the Williamson-Hall method WH-1). The problem may be due the fundamental assumptions in the method, which are not based on strain being due to dislocations.

The integral breadth method is based on similar assumptions to the variance-A methods. However, the values obtained are not as problematic. It produces un-

expected negative strain values for some FCC peaks, but in general the micro-strain and crystal size values are similar to other methods, albeit slightly lower. A possible indication that the method may not be adequately separating micro-strain and crystal size, is found by comparing the results of nickel with other metals. It is found that for similar strains nickel has higher strain broadening than other metals. This would not be expected given that it has a lower overall broadening compared to other metals, and most other methods give nickel a lower strain broadening than the other metals.

The Williamson-Hall method attributes more of the broadening of the metals to strain broadening than size broadening, in comparison other methods. It could be argued that the higher crystal size values found are due to the method providing a different, and bigger, definition of size than the other methods, because it gives the volume-weighted crystal size when other methods give the area weighted value. It could also be argued that it may be because of the separation of size and strain. The crystal size values found have a significant uncertainty (as shown in Chapter 6). This may be because the g^2 term (shown in equations 2.17-2.20) was not used and may be significant. The problem with the use of this term is that if there are limited peaks (as with the FCC samples) it adds more uncertainty and problems. Other problems may be due to the poor quality (222) peak in FCC samples, or the simplistic description to remove instrumental broadening.

The Warren-Averbach methods attribute almost equal amounts to crystal size and strain broadening. They give lower crystal size values than WH methods but similar size to the integral breadth method. The size values, as shown in Chapter 6, have a smaller uncertainty than found for the WH method, even with the use of just the (111) and (222) peaks.

The alternative method is different to all the other methods because it does not provide crystal size broadening for the low SFE metals. For nickel the crystal size values are similar to other methods. This behaviour makes the method very useful, and its use is recommended to determine crystal size values of regions that have different orientation.

The variance-B method was found to give similar crystal size values to the WA methods. However, because of the way it was implemented the accuracy of these values was very low.

7.6.3 Methods that give dislocation density values

The Warren-Averbach methods, the alternative method and the variance-B method can all be used to provide values of the dislocation density. This makes these methods more useful, since they can provide the value of a useful quantity, dislocation density, which can be used to define the state of a material, e.g. its flow stress, or stored energy. In addition, they are also more valuable because the dislocation density is the only component that can easily be verified by other method (e.g. TEM).

It was shown in this chapter that all methods produce dislocation density values that are close to those found for similar alloys, using TEM. The DPPA results are closest for Ti-6Al-4V and the stainless steel alloys, but for nickel the values are significantly higher than expected for all methods. Some of the results did not follow the expected change of dislocation density with flow stress and gave much higher dislocation density values at low strain values. The exact cause of this is not clear. As discussed in Section 7.4.1, the behaviour may be due to the organisation of dislocations into cell walls and subgrain boundaries that produces a Hall-Petch hardening. However, since it was not observed with Ti-6Al-4V and has not been observed by other researchers, I believe it to be due to instrumental effects from the use of a lab x-ray, with higher instrumental broadening, for the FCC samples.

The dislocation density values, found with the alternative method, are in many cases significantly lower than other methods and also further from the expected values. Based on the strain coefficients of the different methods, I would say that this method has strain coefficients that least match the Wilkens and Krivoglaz description of dislocation broadening. These factors combined with the greater

uncertainty in the results of this method (shown in Chapter 6), make it, in my opinion, the least useful for obtaining dislocation density values.

The results of the variance-B method, which was only used for Ti-6Al-4V, provided dislocation density and crystal size values close to other methods and the expected values. This shows that it is a useful method, especially since in comparison to other methods it should only require one diffraction peak. However, the method is difficult to implement because of the number of fitting parameters and the need for two equations. There is also uncertainty in its use, because I found different dislocation density values for the two equations it uses, when they should be the same, and most diffraction peaks gave variance values that were not well fit by the equations.

Of the Warren-Averbach methods there is no obvious trend to say one method provides the maximum dislocation density and another the minimum. However, I believe the best method is the INDI approach and in particular the log-INDI method (or the individual method if the contrast factor is not used). As shown in Chapter 6, the method has lower errors than the other WA methods. However, the reason I believe the INDI approach is better than the ALL approach is because it uses Fourier length values (L) that are least affected by background effects (low L) and limitations of the separating of size and strain (high L). In turn it can also account better for the ‘hook-effect’, which there is reason to believe may not just be due to instrumental effects, and has less problems separating dislocation density from dipole character. The lin-INDI method appears less valid because the strain coefficients less match the dislocation description of Krivoglaz and Wilkens.

When using Fourier methods to obtain dislocation density values, a parameter known as the dipole character (M) is also obtained. M is potentially a useful value as it can provide information about the nature of the dislocation arrangement, i.e. whether dislocations are arranged in cells or tangles. The changes in M , shown in this chapter, were found to behave in a similar way to that found by other researchers (Zehetbauer et al. 1999), the changes of which they justified based on

a description of the change in the dislocation structure with applied strain. The value of M was also found to be different, and lower, for nickel, which would be expected given the dislocation cell structure nickel develops which the other alloys do not. However, there are problems with the dipole character term. It is found with greater uncertainty than other parameters and it has different values for different methods. The biggest problem with the dipole character is that until it can be defined with respect to the dislocation structure, and hence measured by another way, its use remains limited to being a fitting parameter. In addition, if the parameter were better understood it would allow dislocation density values to be obtained by methods that only provide micro-strain values.

7.6.4 The contrast factor

In this chapter the use of equations (contrast factor equations) to describe the heterogeneity of broadening have been investigated. These equations may be used to find the slip system population, and the results of this analysis have been presented. It was shown that in both FCC and HCP metals the slip system predictions agreed qualitatively with their expected changes. However, an understanding of the exact slip system population in the metals is lacking, due to the difficulty in obtaining these values.

It has been shown that for both FCC and HCP alloys there are problems with its use. In HCP metals, in some cases, the broadening of different hkl peaks can only be explained by using fitting parameters (the q-values) that would not represent any possible slip system. Furthermore, different slip system populations would be found depending on the measurement direction used. In FCC metals, the contrast factor equation does not provide a good fit to the broadening heterogeneity of different hkl peaks. Different slip system populations are predicted depending on the method used and the two stainless steel samples are predicted to have different dislocation populations. These results put in doubt the use of the contrast factor and the slip system population predictions. These issues are significant because when used the contrast factor affects all other DPPA results. They affect how size and strain is separated and how the dislocation density value is separated from the strain value. It was shown that the errors that can result from the use of the

contrast factor are significant and that these errors are especially large for HCP metals.

7.6.5 The full-width analysis methods

It has been shown in this chapter that there is an approximate proportional relationship between the work-hardening (WH) stress and the full-width, for the stainless steel alloys and Ti-6Al-4V. Hence, since the dislocation density can also be related to the work-hardening stress, the full-width could be used to evaluate the dislocation density. This approach would be beneficial to more complicated methods, which add errors to the results. The WH stress does not have the same relationship in nickel changes but instead varies linearly with the full-width and when extrapolated to zero stress has a non-zero full-width.

Based on the results in this chapter I would recommend that the full-width is the most important DPPA parameter that can be obtained. The reason for this is partly due to the ambiguity in the meaning of the different results of the DPPA methods, but also because the results can vary between different methods. The use of the full-width is also beneficial because it has the least error.

8 The use of polycrystal plasticity models to predict peak shape in different texture components

8.1 *Introduction*

In Chapter 7 it was shown that there are problems with the use of contrast factor equation. This equation assumes that all grains deform in the same manner, whereas in reality deformation is expected to be heterogeneous. In this chapter the influence that this heterogeneity in deformation has on the broadening of diffraction peaks is considered. The aim is to better understand DPPA methods and how systematic errors may be introduced. Furthermore, the chapter seeks to understand whether DPPA methods can be used to verify or otherwise a polycrystal plasticity model.

To achieve these aims polycrystal plasticity models are used to explain the heterogeneity of deformation. The predictions of these models are then compared with two different sets of peak profile measurements. Three different deformed alloys are studied, nickel-200, SS-316 and Ti-6Al-4V. For FCC metals, neutron diffraction measurements were made on compression samples at different angles (Section 3.4.4). For Ti-6Al-4V, synchrotron measurements were made on tensile samples at two measurement directions over a wide range of peaks (Section 3.4.3). The different peaks at different measurement directions represent different texture components, and they should consequently deform in different ways that can be characterised by the plasticity models. These measurements will be used to understand whether the heterogeneity of broadening is due to variations in slip system population, and hence changes in the contrast factor, or whether other causes of broadening are also orientation dependent. Furthermore, the results and predictions will be used to try to understand what size and strain broadening actually represent.

8.2 Polycrystal Plasticity Modelling Approach

In order to understand the manner in which different texture components may deform in different ways, two different polycrystal plasticity models are used, one for the FCC metals and one for titanium alloys. The methods calculate the same thing, differences in the activity of different slip systems, but the underlying assumptions are slightly different. The Taylor model (1934), is used for the FCC predictions, and is based on the assumption that all grains have the same strain as the bulk material. Whereas, for the titanium metals, a model based on the Schmid factor is used, which is based on the assumption that all grains are under the same stress state.

For both methods it is assumed that the texture is random and that there are not significant texture changes during deformation so that only one strain increment is used for the results. The metals, particularly titanium, have a slight texture but these differences shouldn't be significant, especially since the predictions are only qualitative. For the quantity of applied strains studied in this section there is not expected to be significant changes in texture, so the second assumption is expected to cause relatively small errors in the results.

8.2.1 FCC: Polycrystal Plasticity Modelling Approach

The Taylor model is one of the most widely used polycrystal plasticity models, and has been shown to successfully predict different features of the deformation of various metals (Dilamore and Katoh 1974, van Houtte 1978, Philippe et al. 1995, Bate and Fonseca 2004).

For the Taylor model the slip systems used are the twelve most common slip systems in FCC metals [110](111). Each slip system produces a shear, and the Taylor model works by finding which combination of slip systems produces the same strain as the externally imposed strain. It is assumed that a particular slip system combination consists of five active slip systems. Of all these possible slip system combinations, the active slip systems are those that minimise the energy. The energy dissipated M^T (also known as the Taylor factor) for a particular slip system combination, is the sum of the critically resolved shear stress, τ^C , and the

increment of strain $|\gamma_s|$ of its constituent slip systems (s) (see equation 2.4). The Taylor model can lead to multiple solutions, in order to solve this the average of these solutions is taken.

For the FCC results 6 different peaks are used: {111}, {200}, {220}, {311}, {222} and {400}. These peaks are measured at different angles between the tensile direction and diffraction vector, where the diffraction vector is parallel to the plane normal of the planes being measured. A given plane at a given angle represents a particular texture component and different angles and planes are different texture components.

As an example of how the activity of the different slip systems change with orientation, the slip activity of different texture components that contribute to the {111} peak at different angles between the tensile and diffraction vector are shown in Figure 8-1, where the slip systems have been divided based on their contrast factor, because of the symmetry.

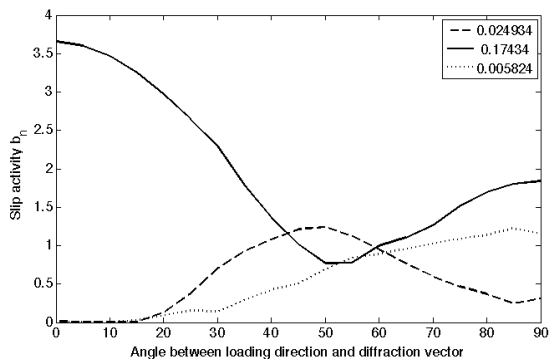


Figure 8-1. The slip activity of different slip systems, for different texture components. The slip systems are separated based on their contrast factor (See section 2.4.5) into three different values. The texture components represent the grains that correspond to the (111) reflection at the different angles between the loading and diffraction vectors.

8.2.2 Titanium: Polycrystal Plasticity Modelling Approach

A polycrystal plasticity model that uses the Schmid factor is used to describe titanium. The use of models that use the Schmid factor, or that are based on the assumption that the stress state is the same in all grains, are a popular method used to describe the deformation of HCP metals, particularly at low strains

(Zaefferer 2003, Bridier et al 2005, Battaini et al. 2007, Liu and Hansen 1995, Winther 2001). The Sachs model (Sachs 1928) is a model that uses the Schmid factor to find the active slip systems. The model used in this Chapter for titanium, is different to the Sachs model because in that model only the slip system(s) with the highest Schmid factor is active, whereas in the model used here all slip systems can be active, unless the Schmid factor is zero.

The applications of polycrystal plasticity models is more difficult in HCP metals than FCC metals because of the greater number of slip systems. In HCP metals it is necessary to specify which slip systems are present and the relative ease with which these slip systems occur, which was not necessary for the FCC approach. These choices can have large differences on the results of polycrystal plasticity models, hence the model is only used to qualitatively describe broadening behaviour.

In the model used here, the slip activity (γ) of a slip system (l) is found by resolving the stress onto the slip system, the larger the resolved stress the more active the slip system. Since different slip systems have different ease with which they are activated, this is accounted for by variations in the critically resolved shear stress (τ_{CRSS}) of the slip systems. To account for the fact that $< a >$ slip systems has less symmetrical variants than $< c+a >$ slip, the average slip activity of these variants is taken (i.e. $(10\bar{1}0)[T2\bar{T}0]$, $(01\bar{1}0)[2\bar{T}T0]$ are different variants of prismatic $< a >$). The activity of a particular slip system in the model used for titanium is given by:

$$\gamma^l = \frac{\sin \chi^l \cos \varpi^l}{\tau^l_{CRSS}} \quad (8.1)$$

Where, χ is the angle between the slip plane and tension axis and ϖ the angle between slip direction and tension axis, and the product of the sine and cosine terms is the Schmid factor.

The method is very simple and would not allow homogeneous deformation, since grains with their c-axis parallel to the tensile direction would have much less strain than other grains with the c-axis perpendicular to the tensile direction.

However, there is some justification for the use of the model particularly at low levels of deformation.

In titanium, the order of the relative activity of slip systems is prismatic $\langle a \rangle$, basal $\langle a \rangle$, pyramidal $\langle a \rangle$ and finally slip systems with $\langle c+a \rangle$ dislocations (Lutjering and Williams 2007, Partridge 1967). The activity is dependent on the alloy composition (Biswas 1973, Zaefferer 2003, Partridge 1967), temperature of deformation (Lutjering and Williams 2007, Conrad 1981) and the direction of an applied load, i.e. whether compression or in tension (Yapici et al. 2006, Fundenberger et al. 1997). The way in which CRSS values are commonly found is by the use of plasticity models to predict a property of the material such as texture. CRSS values found by others for Ti-6Al-4V are shown in Table 8-1, which were used to obtain the values that will be used in this work. The slip system pyramidal $\langle a \rangle$ is ignored because its inclusion was found to have little influence on the broadening predictions. Two different sets of CRSS values were used, one where the CRSS values are close to each other, Model-A, and one where the CRSS values are further apart, Model-B.

Table 8-1. CRSS values for different slip systems in Ti-6Al-4V from literature [1]- Yapici et al. 2006, [2]- Fundenberger et al. 1997, [3]- Philippe et al. 1995 and those used in this work.

Source	Prismatic $\langle a \rangle$	Basal $\langle a \rangle$	Pyramidal $\langle a \rangle$	Pyramidal $\langle c+a \rangle$
[1]	1	1.08-3.6	1.35-4.5	1.32-4.6
[2]	1	3-5	3-9	4-12
[3]	1	3	-	7
This work				
A	1	1.3	1.5	1.6
B	1	3	5	7

In contrast to the FCC metals, where there are over ten measurement directions, for titanium there are only two. Instead, to compare different texture components different peaks in one measurement direction are compared to each other. This is done by plotting the results and predictions against x. The value of x being related

to how close a peak is to the basal plane, (0002) at high x, or the prism planes, (2020) at x=0.

$$x = \frac{2l^2}{3(ga)^2} \quad (8.2)$$

Where, g is the reciprocal of the d-spacing, a is a lattice parameter, and l is the 4th index of a plane.

This choice of axis is used because, as has been shown in Chapter 7 and Section 2.4.5, the contrast factor of different slip systems changes smoothly with x, and x is used to help determine the slip activity in the methods shown in Chapter 7. The problem with this choice of axis is that different values of x also have different values of g.

The predictions of the dislocation density for Model A, plotted against x are shown in Figure 8-2, and the total dislocation density of both models in Figure 8-3. The absolute values here (as with the predicted full-width values) are arbitrary, and it is only the relative changes that are being considered. The main differences between the two directions are – i) a decrease in the density of prismatic $\langle a \rangle$ dislocations with increasing x (closer to basal plane) in the transverse but not the axial direction and ii) an increase in the density of $\langle c+a \rangle$ dislocations at high x in the axial but not in the transverse direction. Both models show the same trends in the individual slip systems, the only difference being is the relative weights, as given by the differences in CRSS values. The changes in the total slip activity are different in the two measurement directions, in the axial direction the slip activity falls, whereas in the transverse direction the values fall and then increase.

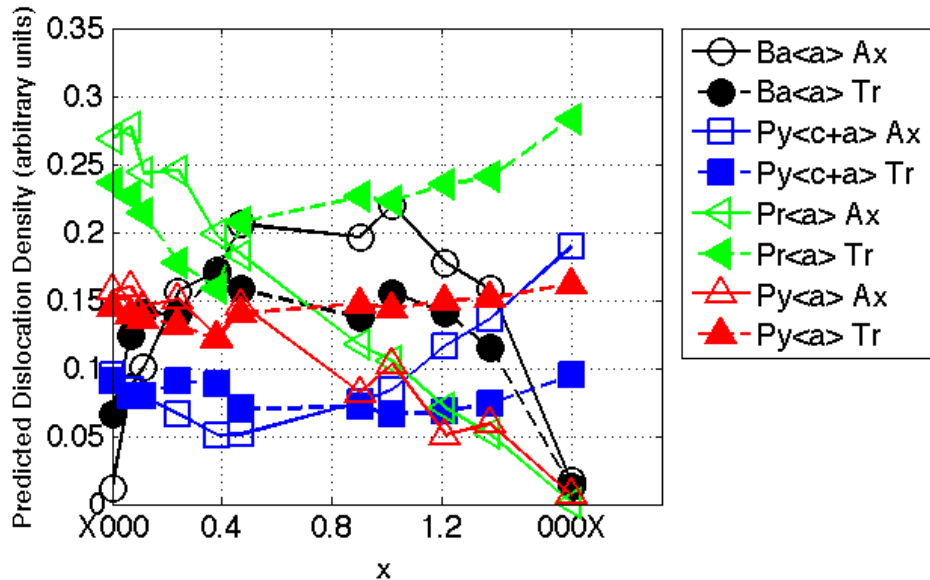


Figure 8-2. Dislocation density predictions found using the Schmid model. Model A, left, and Model B, right. Model B has higher CRSS values for the secondary slip systems basal $\langle a \rangle$, pyramidal $\langle a \rangle$ and pyramidal $\langle c+a \rangle$. The two measurement directions transverse (Tr) and axial (Ax) are shown.

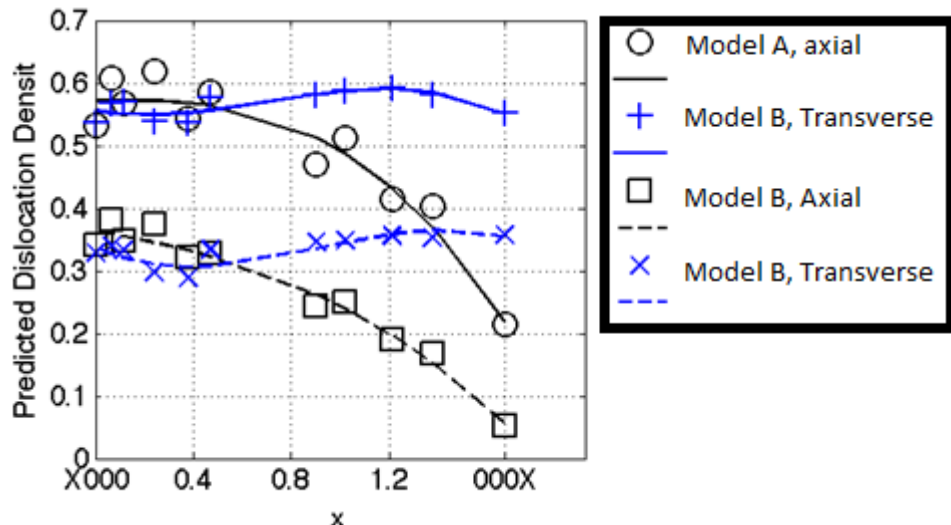


Figure 8-3. The changes in the predicted total dislocation density plotted against x for the two different models in the measurement directions.

8.3 Comparisons of Measured Broadening with Predicted Contrast Factor

In the previous section, it was shown that different diffraction peaks represent different texture components, and that these have different slip system activities. In this section it will be shown how these differences, can change the broadening of diffraction peaks. Furthermore, it is necessary to examine whether the differences explain the observed heterogeneity of broadening in the FCC and titanium metals.

8.3.1 Modelling Approach

In this section (Section 8.3), what is being examined is whether the slip system population predictions from polycrystal plasticity models can be used to describe the heterogeneity of broadening of hkl peaks. Hence, the assumption that is being made is that the only cause of differences in broadening of different diffraction peaks is a result of differences in the slip system population. Therefore, the crystal size $\langle L \rangle_v$, the arrangement of dislocations $f(M)$ and the dislocation density ρ , are assumed to be constant for a particular sample.

The slip system population changes the contrast factor (see Section 2.4.5); therefore what will be predicted is the square root of the contrast factor and only the changes not the exact magnitudes are being considered. This relationship can be seen from the modified Williamson-Hall equation (Equation 6.4).

$$FW(g) = \frac{1}{\langle L \rangle_v} + f(M)g\sqrt{(\rho b^2 \bar{C}_{hkl})} \quad (8.3)$$

The polycrystal plasticity models predict shear of a given slip system but what is required is the amount of dislocations of these slip systems. It is assumed that the shear values of a slip system are proportional to the dislocation density on that system, and that the proportionality constant is the same for all slip systems. Therefore, it is also assumed that there is no cross-slip, dislocation annihilation or dislocation interaction. This is sometimes called Orowan's equation. (see Equation 8.4) (Ungar, Gubicza et al. 2001)

$$\gamma^l = \rho_m^l b^l V^l \quad (8.4)$$

Where, the slip activity (γ) of a slip system, l , is proportional to the mobile dislocation density (ρ_m) multiplied by the slip systems Burgers vector (b) and the speed it moves (V).

A particular diffraction peak consists of a number of grains, representing different texture components that have diffraction plane normals that are parallel to the diffraction vector. For each of these grains (j) the contrast factor (C_{ij}) is found for all of the possible slip systems (i) using the program ANIZC (Borbely et al 2003). These are combined with the shear values, from the polycrystal plasticity model, to give an average value for each grain of the contrast factor multiplied by the Burgers vector (b).

$$\langle bC \rangle_{\text{grain}} = \frac{1}{\sum_i \gamma_i} \sum_i (\gamma_i b_i C_i) \quad (8.5)$$

These values are then found for all grains that contribute to a particular peak (subscript j). The predicted full-width is then proportional to the average of the square root of these values. This is shown in Equation 8.6, where k_1 is a constant. The predictions are performed for edge and screw dislocations.

$$FW^{hkl} = k_1 g_{hkl} \left(\frac{1}{j} \right) \sum_j \left(\langle bC \rangle_j \right)^{0.5} \quad (8.6)$$

The plasticity models predict different total slip activity for a particular grain and so the model would predict different dislocation densities in different grains. Therefore, two variations exist (1) the dislocation density changes in different grains in proportion to the total slip activity in that grain and (2) the dislocation density is assumed to be the same for all grains.

8.3.2 FCC Metals

The fitted full-width divided by g (FW/g), without instrumental broadening, measured at different angles to the compression direction, are shown in Figure 8-4 and Figure 8-6, and for rolled samples in Figure 8-7 and Figure 8-8. The FW/g

values are not constant across different angles, but instead the FW/g values change with angle, and is different for the different diffraction peaks. The changes are significant, for example the {200} peak of stainless steel at 10% strain falls by ~20% over the range of angles measured. The results show that deformation is not homogeneous for these samples. The different peaks at different angles represent different texture components, hence the results show that these texture components deform in a different manner to each other. To investigate whether these differences are due to changes in the dislocation population, we must compare these results with the calculated contrast factor values.

Compression Samples

The changes in the measured FW/g values in the compression samples are considered first and in the next part the rolled samples.

From the FW/g values for the compression samples, shown in Figure 8-4, the following changes are observed. There are differences between the two metals and with the amount of deformation applied. The differences are largest between the 2% samples than the other strains, however the error in these values is also the greatest because the variations in FW/g values is the smallest and close to the errors involved in measuring the full-width. In contrast, the differences between the higher strained samples, of a particular metal, are much smaller, and the systematic changes of the full-widths are similar.

The full-width of the {111} / {222} peaks fall for both nickel and steel with angle between the tensile direction and diffraction vector. But whereas the FW/g values in nickel increases from 45° to 90°, this is either not seen or is much smaller in steel than nickel. Most of the {200} / {400} peaks have a minimum at around 45°. This is better observed in the steel samples, since for the nickel samples the behaviour is not seen in the {200} peaks but only in the 400 peaks at 2% and 10% strain. Instead for nickel, the {200} peak displays a gradual fall between 0° and 90°. The {311} peak also shows similar trends in both metals, with very little change. The FW/g values of the {220} peaks are similar for both metals. They both have a maximum at around 45° and the FW/g values is the same at 0° and 90° (the case for most nickel samples) or increases slightly (the case for most steel samples).

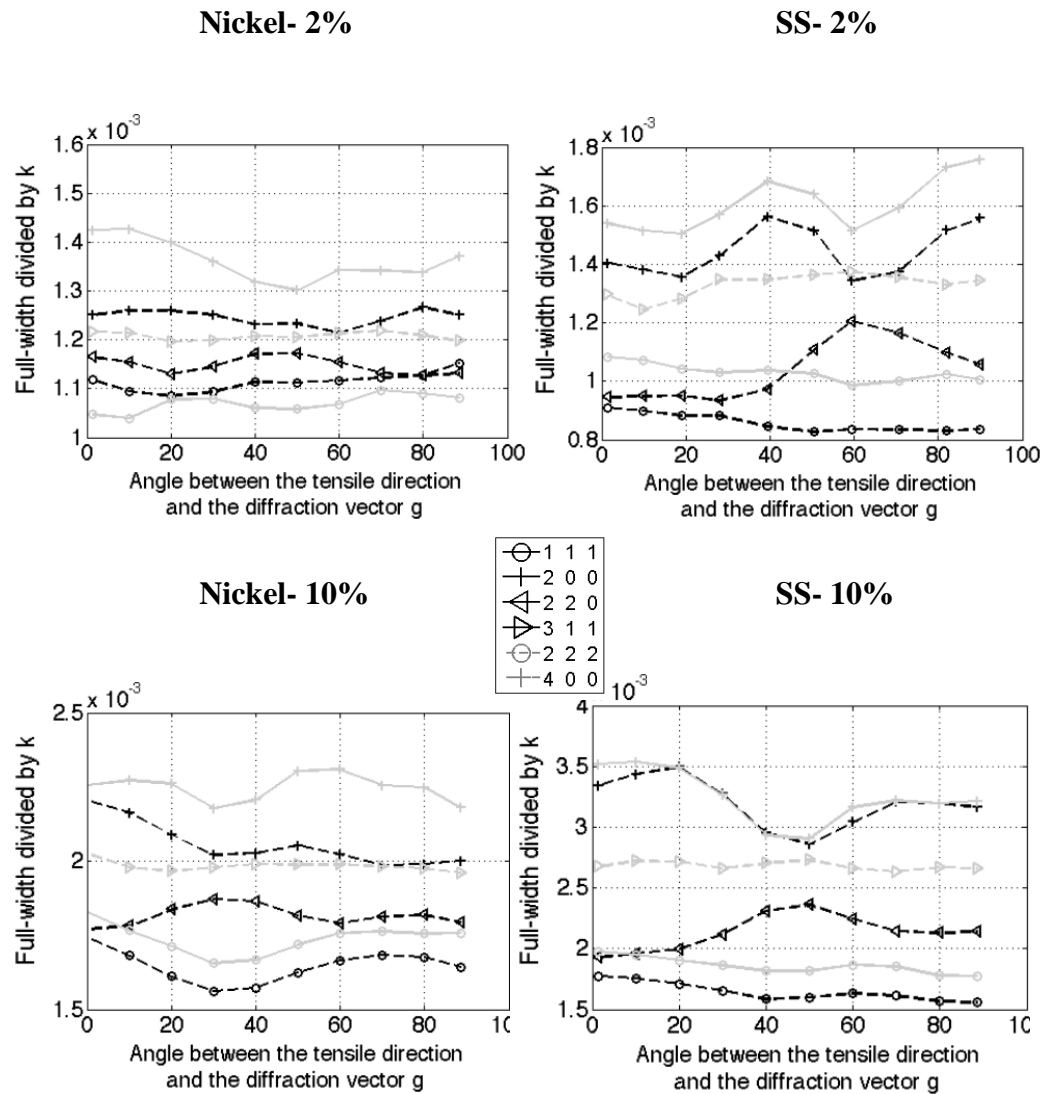


Figure 8.4. Measured and fitted full-width values divided by g ($g=1/d$) at different angles between the tensile direction and the diffraction vector. These measurements are for nickel-200 and stainless steel 316. The fatigue sample is from the work of Wang et al. (2005).

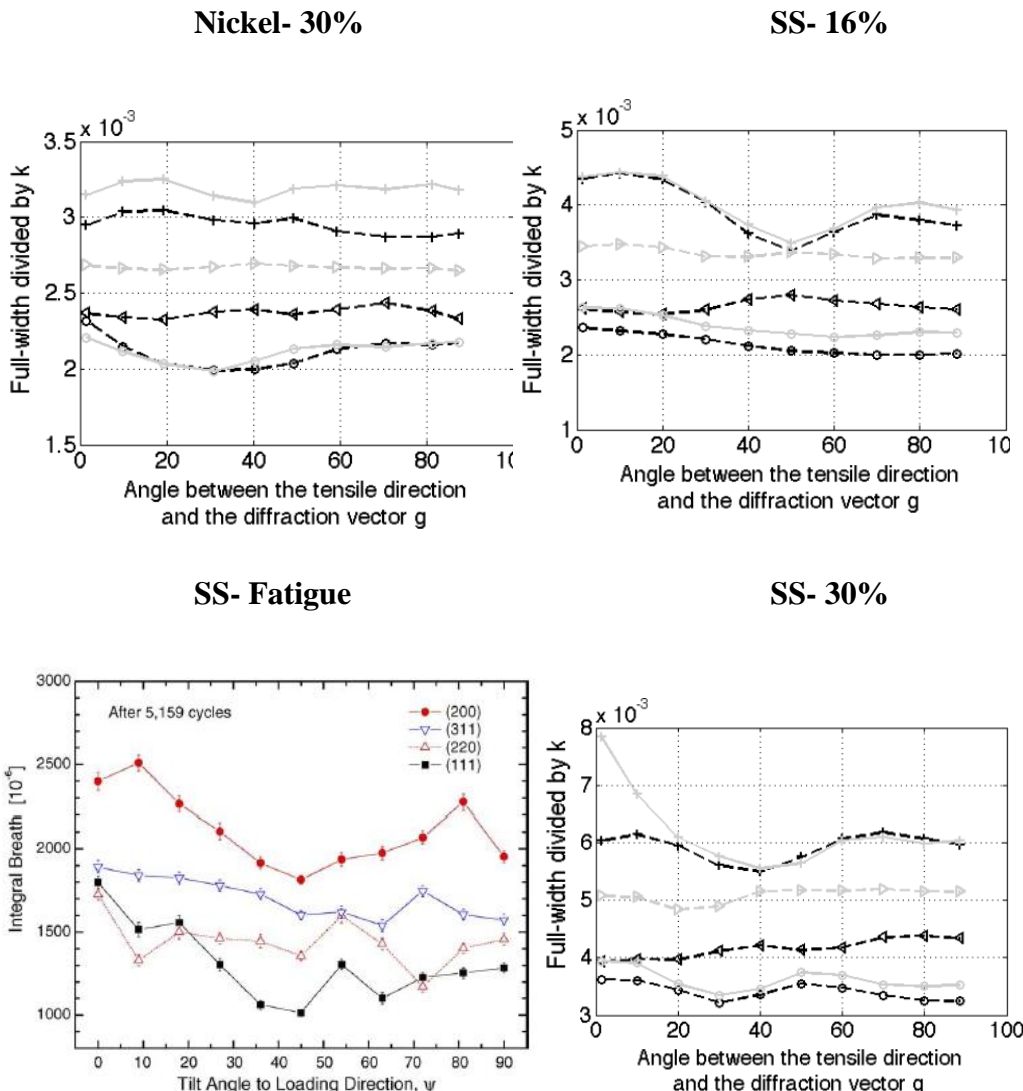


Figure 8-4. Measured and fitted full-width values divided by g ($g=1/d$) at different angles between the tensile direction and the diffraction vector. These measurements are for nickel-200 and stainless steel 316. The fatigue sample is from the work of Wang et al. (2005).

The predicted contrast factor values are shown in Figure 8-5 for compression tests. The predictions show that there are differences depending on whether the dislocations are of edge or screw type and are different depending on whether we assume that the dislocation density is the same in each grain, or each grain has a different dislocation density proportional to the Taylor factor in that grain. To compare the predictions with the measured values, the 10% samples are used. By comparison with the different predictions it can be seen that the stainless steel results best matches the edge predictions, with all grains having the same

dislocation density and the nickel results best match the edge predictions with grains having variations in dislocation density proportional to M^T , these comparisons can be seen in Figure 8-6. Both metal results show a maxima at $\sim 45^\circ$ for the {220} peak, this is a feature of the edge results, suggesting that both samples consist mainly of edge dislocations. The reason that the two metals are closer to the different approaches can be seen by the differences in the {111}/{222} and {200}/{400} peaks. The nickel has a bigger minimum in the {111}/{222} peaks and a flatter {200}/{400} peak than the stainless steel, in the same way as the M^T predictions show the same differences compared with the equal predictions. There are discrepancies between results and predictions. For steel the {111}/{222} FW/g values increases from $40-60^\circ$ but then falls, whereas in the predictions it increases up to 90° . For nickel the {200}/{400} FW/g values does not have a maxima at $\sim 45^\circ$. For both metals the {311} and {220} FW/g values do not fall between 0 and 90° . In addition the relative magnitudes of the different peaks are not well explained by the predictions.

Wang et al. (2005) performed high cycle fatigue tests on austenitic stainless steel 316 and measured diffraction peaks at different angles to the tensile direction. The results, shown in Figure 8-4 and Figure 8-6, are close to the stainless steel results we measured. However, their results follow a better correlation with the mixed edge and screw predictions, whereas the 10% compression results better match the edge predictions. The dip of the {111} and {200} peaks and their lower values at 90° than 0° , the overall fall of {220} and its slight increase in its middle and the relative magnitudes of the FW/g values of the different peaks are all observed in both their results and our predictions. In contrast to the compression tests, the contrast factor values match the relative broadening of the different peaks to a greater extent.

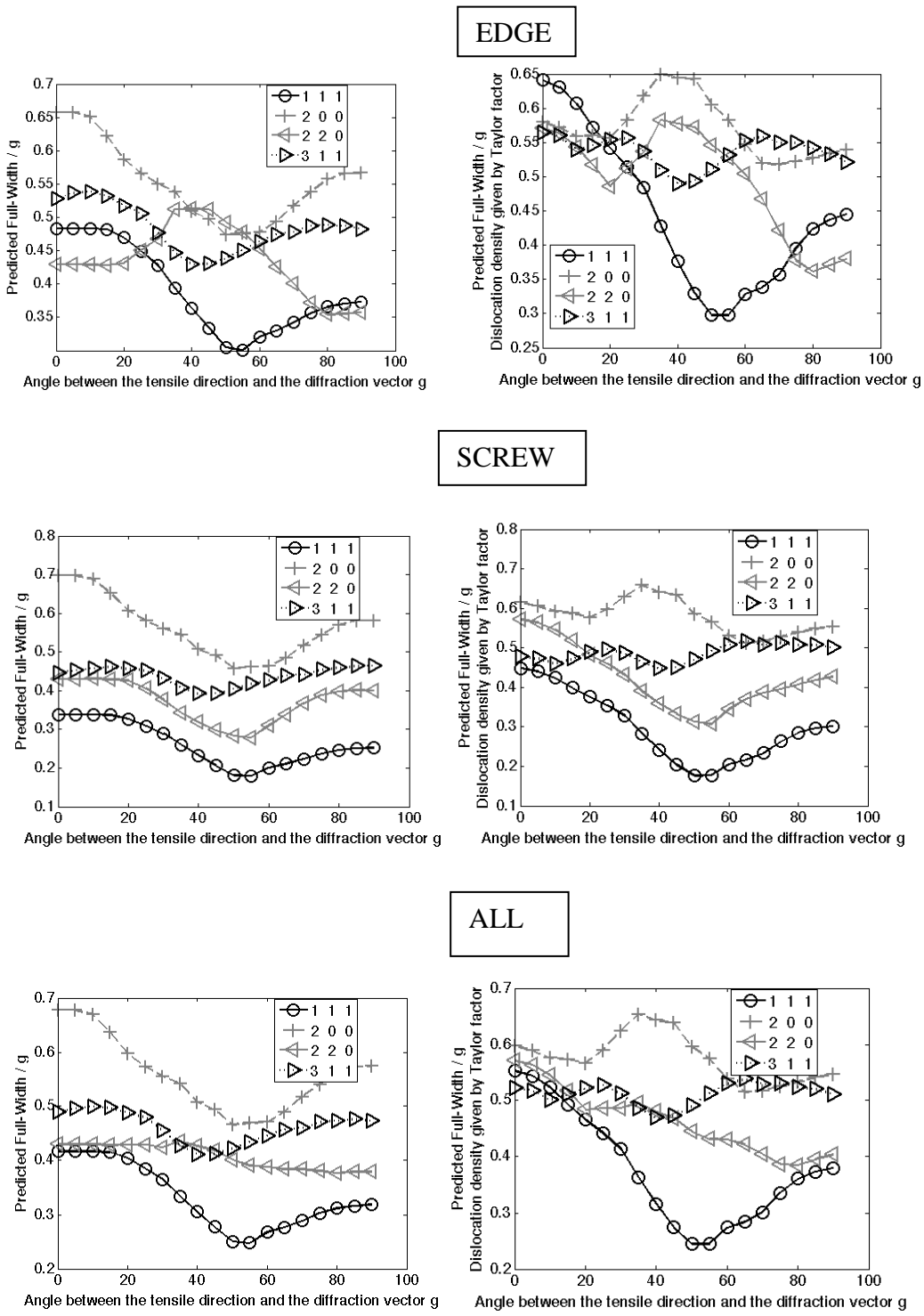


Figure 8-5. The full-width divided by g ($k=g=1/d$) predictions for uni-axial tension test. These values are found from the square root of the contrast factor, found the use of the Taylor model. The predictions on the left assume all grains have the same dislocation density, and those on he right that the relative dislocation densities are given by the Taylor factor.

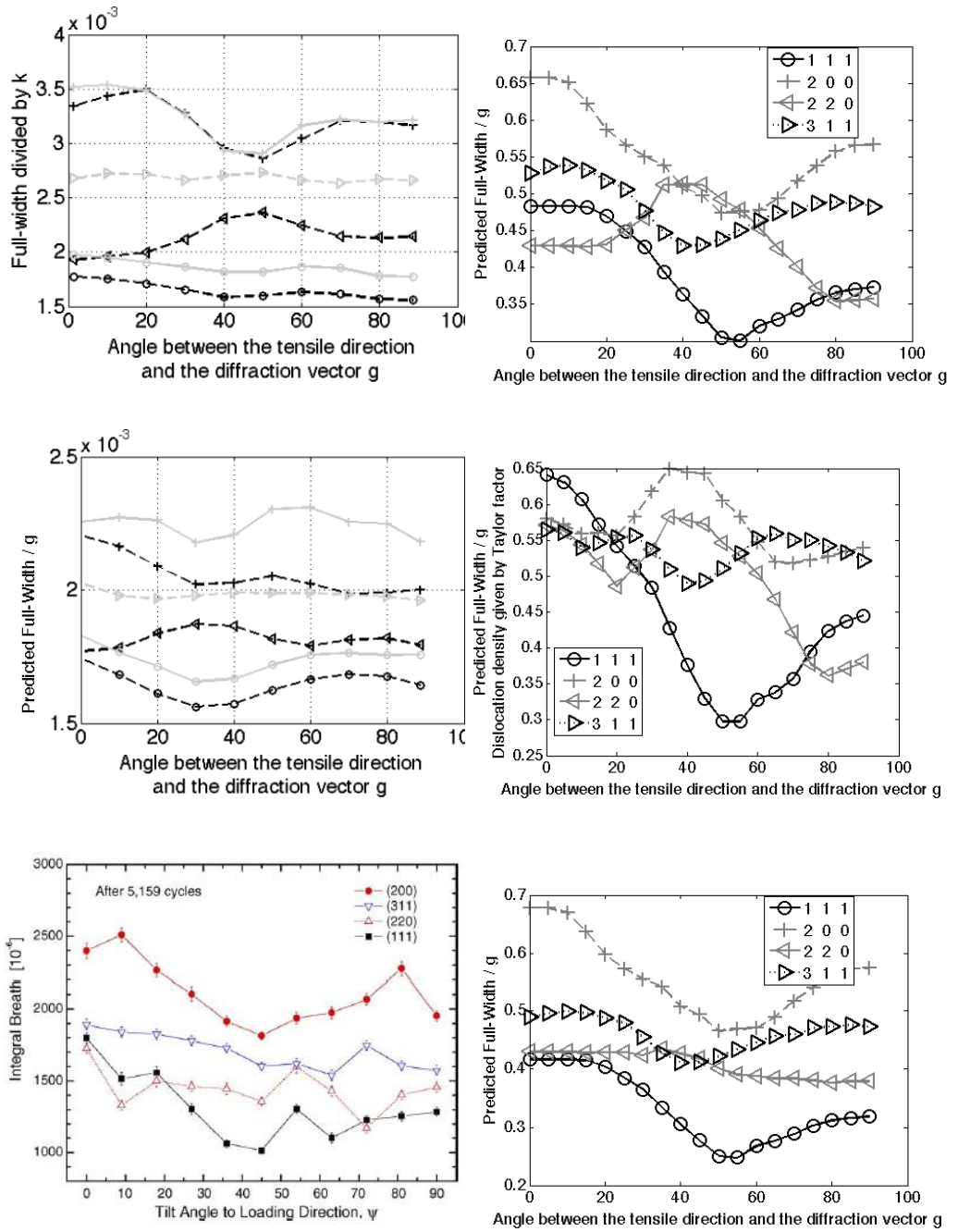


Figure 8-6. A comparison of measured (left) full-width (or integral breadth) divided by g results at different angles, and the corresponding best matched predictions. For stainless steel 10% (top), the results best match the edge predictions with equal dislocation density. For nickel 10%, the results best match the edge predictions with variable dislocation density. For stainless steel fatigue sample the results best match the 50:50 edge to screw, equal dislocation density predictions.

Rolled Samples

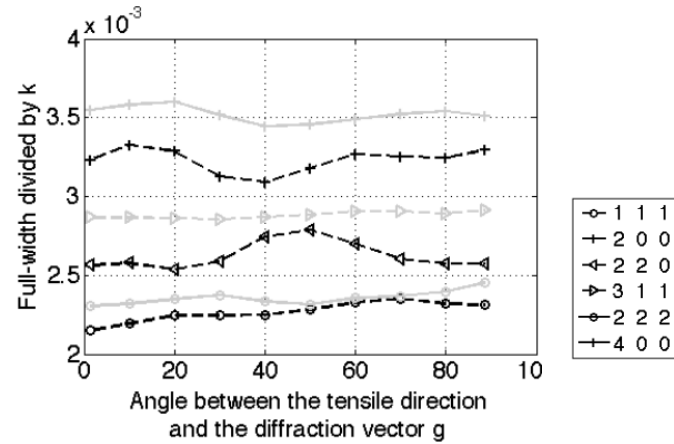
The change in the FW/g values for the rolled nickel samples are shown in Figure 8-8, for angles between the rolling and normal direction (RD-ND) and between the rolling and transverse direction (RD-TD) in Figure 8-9. The contrast factor predictions for RD-ND and RD-TD measurements are also shown in these figures. The predictions are for edge dislocations, since the edge results best matched the compression samples, and the two variations depending on whether there are any changes in the dislocation density are shown.

There are some similarities between the results and predictions, but unlike the compression samples the rolled results are better matched to the equal dislocation density predictions. For the RD-ND nickel sample (Figure 8-8), the similarities between predictions and results are: (1) the {200} and {400} peaks both have minima's at around 45° and maximum values at 0° and 90°, (2) the {220} peak has a maxima at 45° and minimum values at 0° and 90°, (3) the {111} and {222} peaks have a maximum at 90° and falls to 45°, however whereas for the predictions the values increase between 0° and 45°, the measured values fall for {111} peak or increase then fall for the {222} peak. The {311} peak results show no correlation with the predictions, the FW/g values are constant across all angles but the values are predicted to be a minima at 45°.

For the RD-TD nickel sample (Figure 8-9), all FW/g values fall between 0° and 90°, which is the same as the predictions. However, the predictions do not predict the increase in the FW/g values before 90°, or the different rate at which the FW/g values fall with angle. The RD-TD FW/g values for stainless steel share some similarities with nickel, since most values fall between 0° and 90°. However, there are differences, the {220} FW/g values increases between 0° and 90° and the {111} / {222} peak's dull-width only falls after 50°.

It is possible that discrepancies in the rolling results and predictions, which are larger than those found for the compression sample, are due to not accounting for the texture changes, since these would be larger than those found in the compression samples

Nickel RD-ND



RD-ND, Equal dislocation density

RD-ND, Variable dislocation density

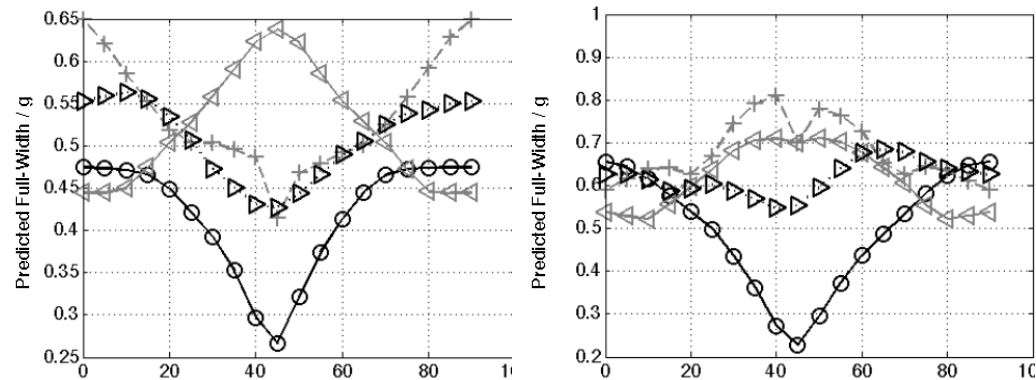


Figure 8-7. Measured and fitted full-width values divided by g ($g=1/d$) at different angles between the rolling direction and the diffraction vector (top). For RD-ND sample. These measurements are for nickel-200. The full-width divided by g predictions for this plane is shown for edge dislocations with equal (left bottom) and variable (right bottom) dislocation density in different grains.

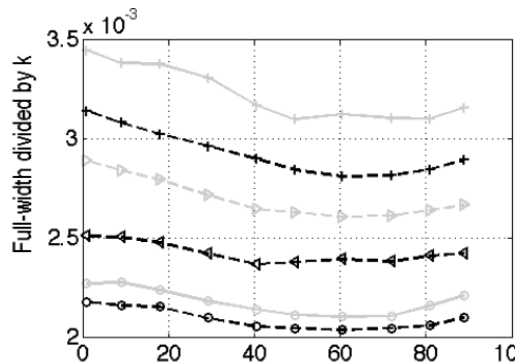
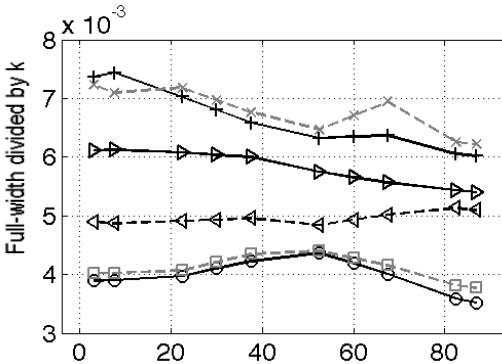
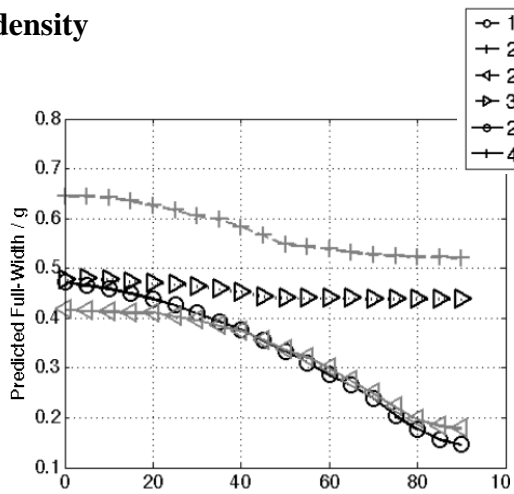
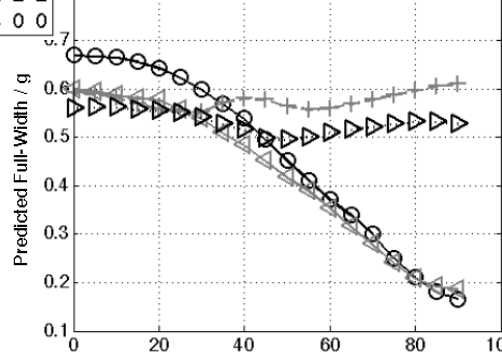
Nickel RD-TD**St. Steel RD-TD****RD-TD, Equal dislocation density**
density**RD-TD, Variable dislocation**

Figure 8-8. Measured and fitted full-width values divided by g ($=1/d$) at different angles between the rolling direction and the diffraction vector (top). For RD-TD samples. These measurements are for nickel-200 and stainless steel 304. The full-width divided by g predictions for this plane is shown for edge dislocations with equal (left bottom) and variable (right bottom) dislocation density in different grains.

Conclusion

In this section it has been shown that the full-width vary considerably in different texture components for both nickel and stainless steel, deformed by compression and rolling. These changes were shown to be described qualitatively by the slip system predictions from the use of the Taylor model.

The differences between nickel and steel compression results add an uncertainty to the method used to predict the full-width values. They would be the same if differences between different orientations were only due to changes in the dislocation population. Hence, the difference suggests that the dislocation population is not the only difference between grains in different orientations. This difference has been accounted for by allowing the dislocation density in nickel to change in proportion to the Taylor factor. In Section 8.4.1 this difference will be examined in more detail, to establish if there is any justification for this based on the differences in the metals.

8.3.3 Titanium

The full-width divided by g (FW/g), plotted against x, for different strains in both measurement directions (transverse and axial) are shown in Figure 8-9. The FW/g values change smoothly with x for both directions, which provides justification for the use of x. The change in the FW/g values with x is different at different applied strains, and also in the two measurement directions. The difference between the two directions increases with applied strain, and at 8% is significantly different. If deformation were homogeneous, that is all grains deform in the same way, then the differences between the measurement directions would not be observed. To compare whether these differences are due to differences in dislocation population within grains, we compare the results with the contrast factor predictions.

At low values of applied strain (1% and 2%), the changes in FW/g values in the two directions are similar (Figure 8-9). The FW/g values fall with x, the fall is largest between x=1 to x=1.6, and almost constant from x=0 to x=0.8. The exception to this is the 2% transverse sample, because of the large FW/g value at x=1.6. There is a difference in magnitude between the FW/g values in the two directions. At 1% strain, the FW/g values are larger in the axial direction, whereas at 2% strain the opposite is the case.

At the higher values of strain (5% and 8% in Figure 8-9), the greatest fall in the FW/g values is now found at low values of x, between x=0 and x=0.8. At higher values of x, there is a clear difference between the two measurement directions. In the axial direction, the FW/g values either fall (5%) or is approximately constant (8%) between x=0.8 to x=1.6. Whereas, in the transverse direction the FW/g values increases to values close to those found at x=0. The FW/g values are larger in the transverse direction at high and low values of x at 8% strain, but just at high values of x at 5% strain.

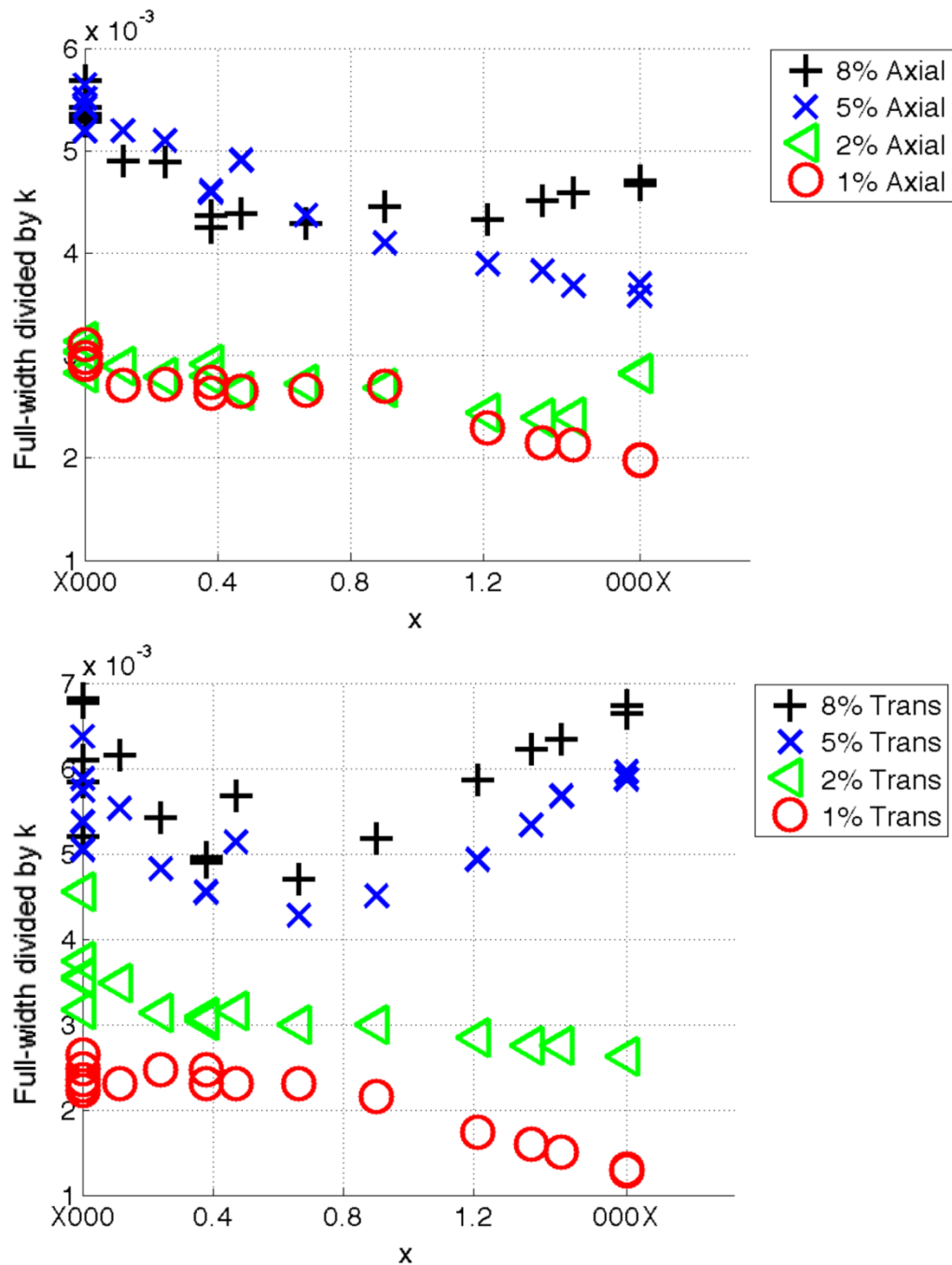


Figure 8-9. The change of FW/g values at different x-values and at different strains, for axial (top) and transverse (bottom) directions.

The measured FW/g values for 1% and 8% strain and the predicted FW/g variations with x are shown in Figure 8-10. In the predictions it is assumed that the dislocation density is constant for different grains. Both models show an overall decrease in the FW/g values with x, with higher FW/g values in the axial direction than the transverse. These predictions are qualitatively what is observed

in the 1% full-width results. However, the almost constant FW/g values between $x=0$ and 0.8 is not observed in either model, nor is the increase in the predicted FW/g values in the axial direction at high x , observed in Model A. Although, this is observed at 2% strain in the axial direction.

The changes in the measured FW/g values at 8% are very different to those seen at 1% and in this case the models completely fail to explain the behaviour. In particular the FW/g values are larger in the transverse direction and the FW/g values in the transverse direction increases significantly after $x=0.8$.

In order to understand why the models fail to explain the observed behaviour at the high strains it is worthwhile to consider how the contrast factors of the different slip systems change with x , as shown in Figure 8-11. The contrast factor of all $\langle a \rangle$ slip systems fall with increasing x , and other than edge basal dislocations the values fall to 0, for the maximum x -value. However, the contrast factor of the $\langle c+a \rangle$ dislocations increases with x , after 0.8. The models predict that the quantity of basal $\langle a \rangle$ dislocations fall from $x \sim 0.8$, hence the main contribution to the predicted full-width at high x is due to $\langle c+a \rangle$ dislocations. Hence, if the problem is due to the Schmid model then either basal slip or $\langle c+a \rangle$ slip should be higher in the transverse than axial direction at high x (close to basal plane). Neither of these seems likely, instead another possibility is that there is another contribution to broadening not accounted for.

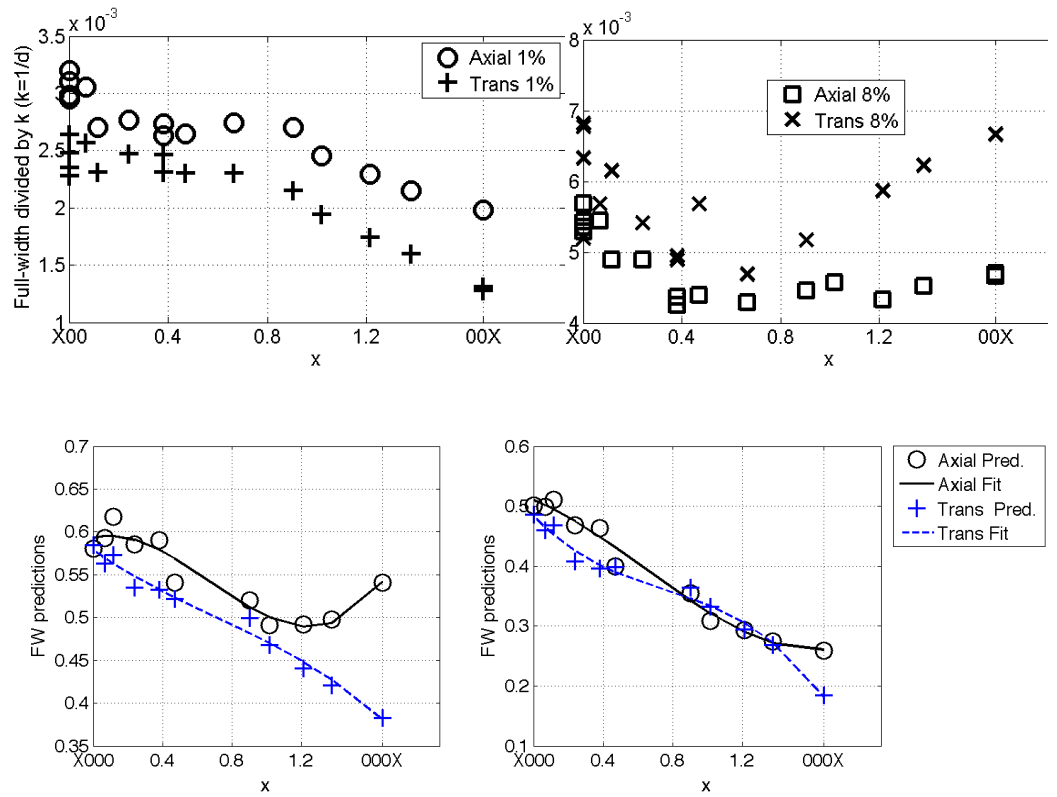


Figure 8-10. Measured FW/g values data plotted against x, for 1% strain (top left) and 8% strain (top right) and the predicted FW/g values using Model A (bottom left) and Model B (bottom right).

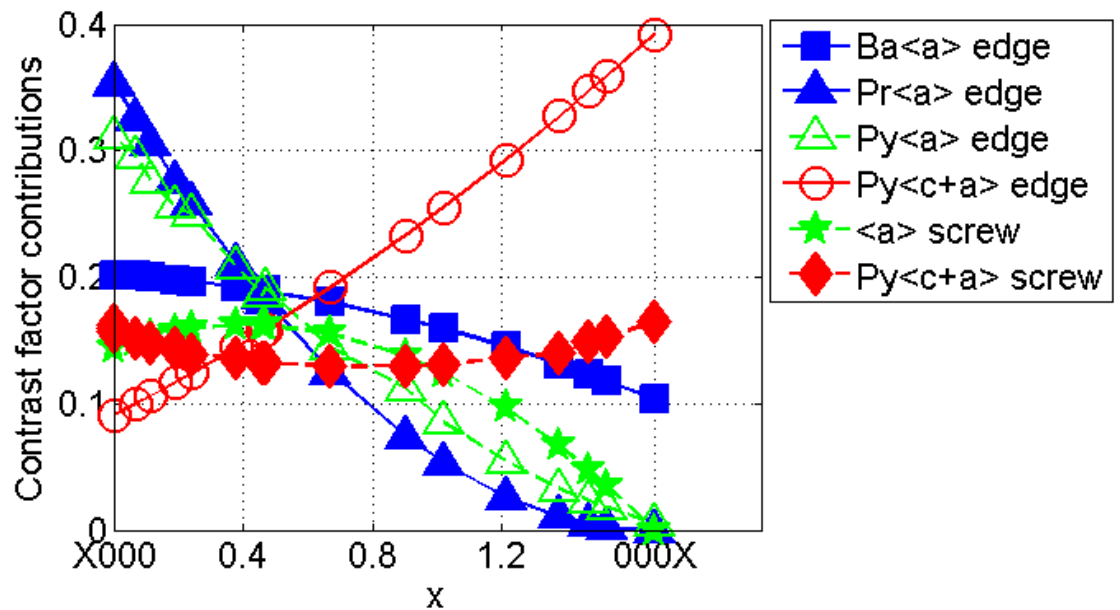


Figure 8-11. Calculated average contrast factor values found using the program ANIZC (Borbely et al 2003), for the different slip systems used in the model.

8.4 Additional Causes of Peak Broadening Heterogeneity

In Section 8.3 it was shown the full-width predictions, from the models that used changes in the dislocation population, could in some cases explain the measured changes in broadening in different texture components. However, there was some problems with the predictions for both FCC and titanium metals. This chapter investigates whether other possible causes of broadening may be orientation dependent to help explain these discrepancies. There are numerous possibilities and to help to investigate this in detail the changes in the shape of the fitted peaks and the Warren-Averbach method are used.

8.4.1 FCC Metals

In Section 8.3.2, the full-width changes in different texture components was found to be different for nickel and stainless steel compression samples. The differences were shown to represent different variations of the predictions. Those for stainless steel best matched predictions where the dislocation density was constant for all grains, whereas for nickel the best matched predictions had dislocation density that varied in different grains and was proportional to the Taylor factor. In this section the shape of peaks are used to understand the differences between the metals and to try to determine if the differences are due to variations in the dislocation density.

Changes in the Shape of Peaks

In Figure 8-12, the mixing parameter from the pseudo-Voigt fit, a feature of the shape of a peak, are shown for the FCC compression samples. Only the changes of the {111}, {200}, {222} and {400} peaks are shown, because of the error in the values and to help explain trends. The errors in the mixing parameter are larger than for the full-width. However, even with the large error there are systematic changes in the values for different angles. These changes are different for the different peaks and show similar trends in the different samples, which suggest these changes are not just due to instrumental effects.

For nickel, most of the samples show a trend for the {200} and {400} peaks mixing parameter. They have a maxima at around 45° and minimum values at 0°

and 90°. This is particularly noticeable at 2%, but is also noticeable at other strains, however the exact behaviour is not always observed. The {111} and {222} peaks also show a trend. This trend is an overall fall in the mixing parameter between 0° and 90°, with an increase between ~60° and 90°.

For stainless steel these same trends are sometimes observed. This is particularly noticeable for the {111} and {222} peaks at 10% and to a lesser extent at 16% strain. However, the changes in the {200} and {400} mixing parameter show different trends for all samples. For example, for 16% strain sample the peaks have maximas at 45°, at 10% the values fall between 0° and 90° and at 2% there is a minima at 45°.

The changes in the mixing parameter for rolled samples are shown in Figure 8-13. The RD-ND sample of nickel has similar changes in the mixing parameter to those observed for the rolled samples. There is a minima in the {111} / {222} peaks (although the {222} values do fall at high angle after initially increasing) and a maxima for the {200} / {400} peak at around 45°. For the rolled samples some of the other peaks are shown. The {220} and {311} peaks both have minimum values at around 45 degrees. In contrast to the RD-ND sample, the RD-TD sample for nickel shows different changes in the mixing parameter compared to the compression samples. The mixing parameter falls with angle for {111}, {222} and {220} but increases for {200}, {400} and {311}. The values obtained for the RD-TD stainless steel sample shows different changes to the other samples. The average of {111}/{222} and the average of the {200}/{400} have a minima at 45°, {220} falls with angle and {311} doesn't change.

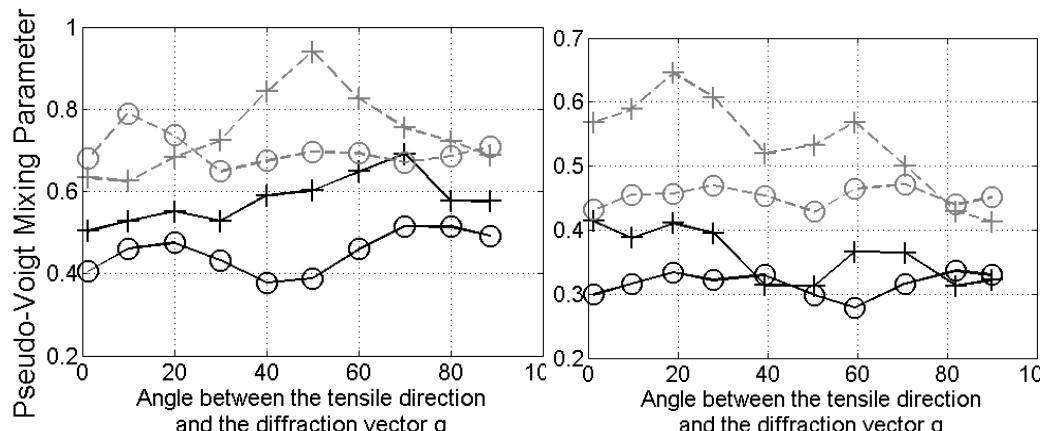
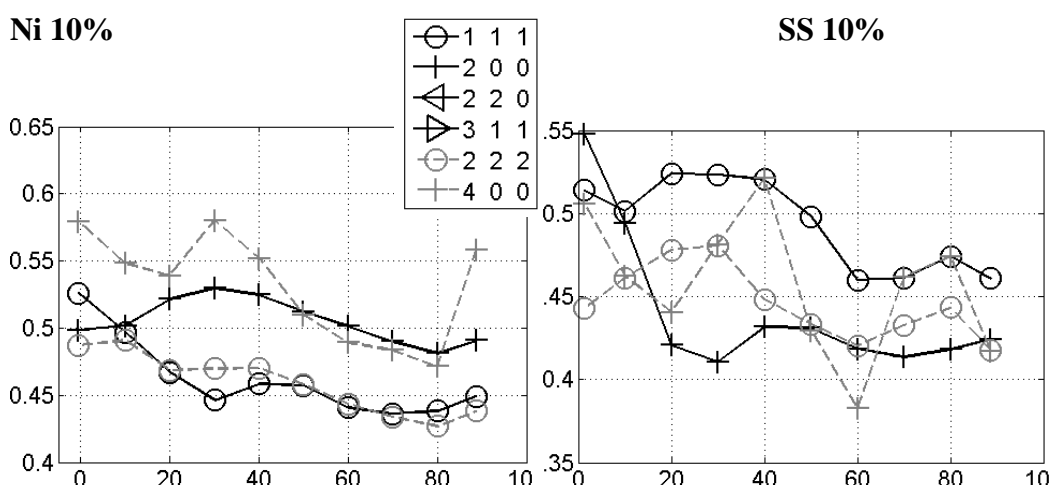
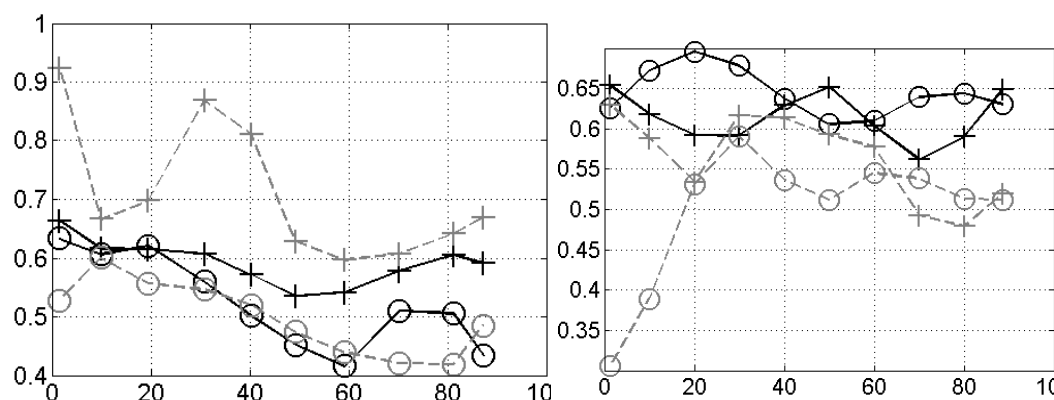
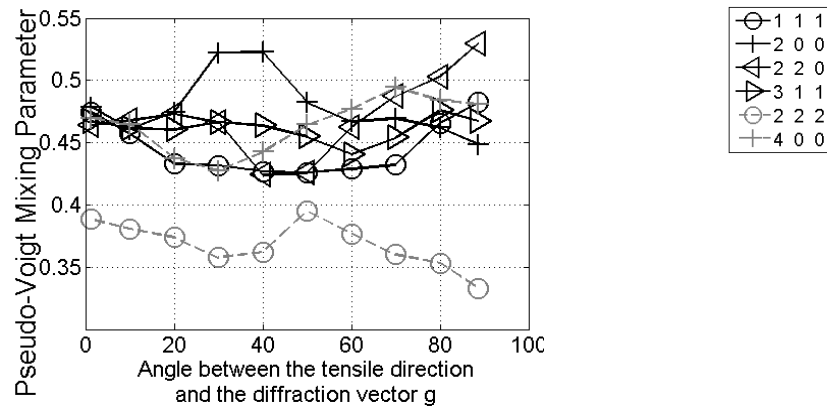
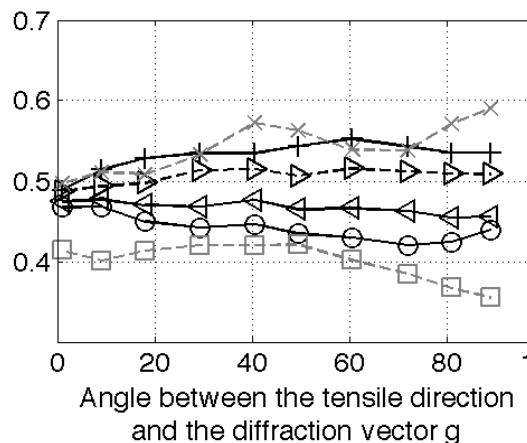
Ni 2%**SS 2%****Ni 10%****SS 10%****Ni 30%****SS 16%**

Figure 8-12. The changes in the measured fitted pseudo-Voigt mixing parameter for deformed nickel at 2%, 10% and 30% (left) and stainless steel at 2%, 10% and 16% (right) measured at different angles between the tensile and diffraction vector. The values are the fitted values that are not corrected based on the instrumental broadening.

Nickel RD-ND



Nickel RD-TD



St. Steel RD-TD

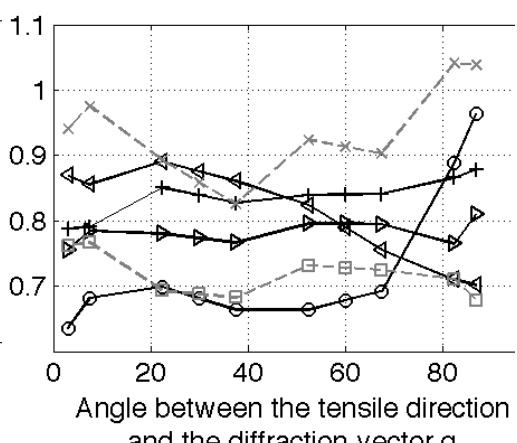


Figure 8-13. Measured and fitted pseudo-Voigt mixing parameter values at different angles between the tensile direction (or rolling direction) and the diffraction vector g. The values are the fitted values that are not corrected based on the instrumental broadening.

Peak Shape Changes due to Contrast Factor Predictions

Differences in the contrast factor and dislocation density would both change the full-width of a peak, but they would also change the mixing parameter. In order to calculate the effect of changes of the contrast factor and the dislocation density on the shape of a diffraction peak the log. Warren-Averbach (WA) method with the Wilkens model for dislocations is used to simulate diffraction peaks (see Section 6.9). In Figure 8-14, the changes in the mixing parameter caused by changes in

the predicted contrast factor are shown for the {111} and {200} peaks of compression samples. The changes are the opposite of the changes in the contrast factor, a maxima is observed at ~45 degrees for the mixing parameter of both peaks, instead of a minima as observed for the contrast factor. Consequently, if the only differences were those predicted by the two methods (described in last section) then the shape of the peaks (given by the mixing parameter) would have the opposite behaviour to the predicted full-widths, i.e. maximas in {111} & {200} mixing parameter values. However, this is not what is observed for most samples, instead in many cases we see a maxima in {200} but a minima in {111} and {222} peaks. This is also the case for the rolled samples, for example the minima in the {111}/{222} peaks, when a maxima would be expected and the fall in the {111}, {222} and {220} values, when an increase would be expected.

Therefore, these results suggests that the dislocation population and dislocation density are not the only things that vary for grains with different orientations. They also suggest that the explanation that the difference between nickel and steel full-width values being due to nickel having variations in dislocation density values is not valid.

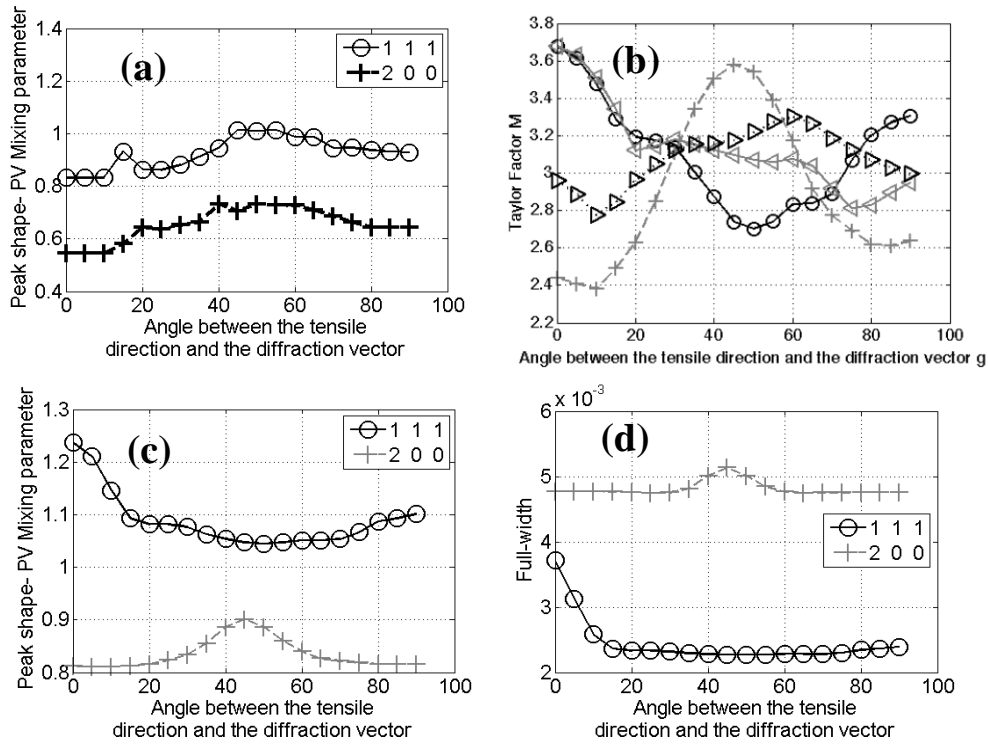


Figure 8-14. The calculated pseudo-Voigt mixing parameter of diffraction peaks due to variations in the slip systems (a). The change in the Taylor factor for the grains contributing to the different orientations (b). The calculated shape of diffraction peaks due to a cell structure, where dislocation arrangement and crystal size are orientation dependent, for the full-width (c) and pseudo-Voigt mixing parameter (d).

Peak Shape Changes due to a Dislocation Cell Structure

If the differences between stainless steel and nickel are not due to variations in the dislocation density in different grains, then it is necessary to investigate what other causes of broadening may be texture dependent, for nickel in particular.

It has been shown (Dilamore et al. 1972) that the dislocation structures that develop in high stacking fault energy metals, like nickel, are heterogeneous, and can be related to the Taylor factor (M^T). Grains with larger values of M^T have a more cell-block structure, with larger misorientation across cell walls and a smaller cell size. The dislocations are arranged such that their strain fields are more screened by their neighbours and consequently have a lower value of the dislocation dipole character, M . To model how the heterogeneity in the dislocation structure would affect the shape of the peaks, a Warren-Averbach analysis was conducted.

In the WA analysis, it is assumed that only the parameters M and the crystal size (GS) change in different grains. Secondly, it is assumed that there is a linear relationship between the Taylor factor and the two parameters. When the Taylor factor is at 3.7- M= 1 and GS= 100Å and when the Taylor factor is at 2.4- M= 2 and GS= 3000Å. These values were chosen because M was found to vary between 0.5 and 2 between applied strains of 2% to over 30% and the crystal size was found to fall from 3000Å to 400Å over the same range. A dislocation density value of $0.07 \times 10^{16} \text{m}^{-2}$ (approximately the value found at 10% strain in nickel) and the contrast factor using a description where it is assumed that dislocations are half edge and screw and equally distributed were used (i.e. constant in different texture components). The WA analysis predictions were converted to intensity values and fitted to a pseudo-Voigt peak. The changes in the full-width and pseudo-Voigt mixing parameter, caused by how the Taylor factor changes the dislocation structure are shown in Figure 8-14. The full-width increases with increasing Taylor factor values, whereas the mixing parameter falls with increasing Taylor factor values.

The changes in the predicted mixing parameter, or the Taylor factor, are the same trends that are observed in the compression nickel samples mixing parameter. Furthermore, the trends observed for the mixing parameter in the rolled nickel samples also show a correlation with the Taylor factor of these samples (Figure 8-15). In contrast, the trends observed in the mixing parameter for the stainless steel samples, do not show a good correlation with the Taylor factor, or with changes that would be predicted by changes in the contrast factor. There are some cases when they correlate, but also many cases when they don't. In addition to this, for the compression samples the trends change with different strains. Hence, the changes in the mixing parameter in nickel can be explained by changes in the cell structure in different texture components, but the cause for the changes in stainless steel is unknown.

A change in the crystal size and dislocation arrangement would also cause changes in the full-width. The change in the full-width predicted by the WA analysis, for compression samples, is shown in Figure 8-14. The full-width contribution to the {111}/{222} peak is a maximum at 0°, a fall to a minimum at

$\sim 45^\circ$ and then an increase. The $\{200\} / \{400\}$ full-width contribution has a maximum at 45° , and falls to a minimum at 0° and 90° . These changes are the same as the changes in the Taylor factor. Hence, the discrepancy between the contrast factor predictions and full-width values, of the nickel compression samples, can be explained by the presence of a dislocation cell structure, rather than a variation in dislocation density.

The two values allowed to change for the dislocation cell structure predictions, crystal size and dislocation arrangement, would have different contributions to the full-width. An increase in the Taylor factor would give a smaller crystal size and dipole character, but only the small crystal size would cause an increase in the full-width. Therefore, it is the heterogeneity of crystal size caused by a dislocation cell structure that is the cause for the differences between stainless steel and nickel results.

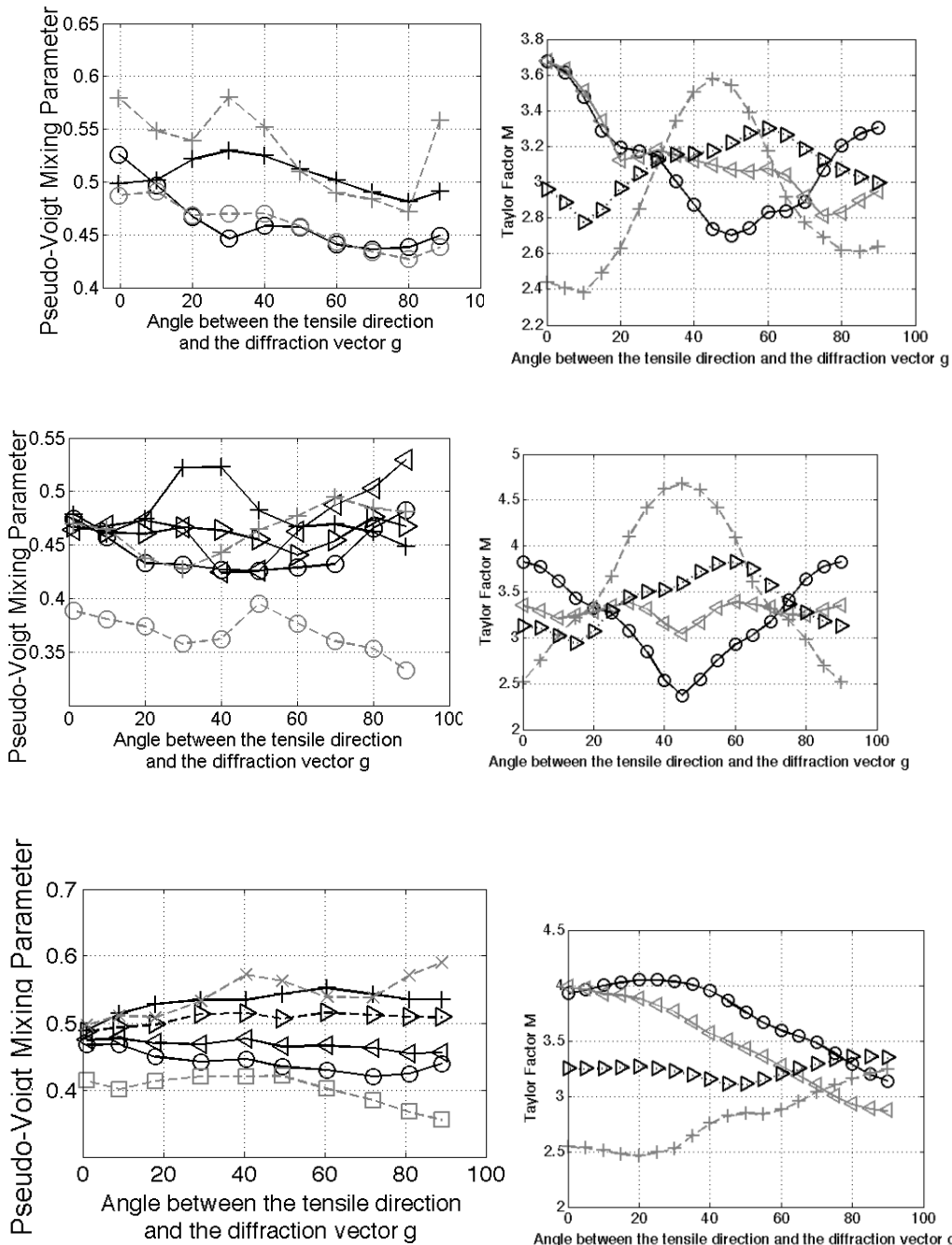


Figure 8-15. Taylor factor for uni-axial tension (top) and rolling between the rolling and normal directions (bottom-left) and between rolling and transverse directions (bottom-right).

8.4.2 Titanium

In Section 8.3.3, it was shown that the slip system population predictions could qualitatively explain the changes in the full-width at low strain, but at the higher strains the predictions failed. This section investigates what the possible cause may be for the discrepancy. This is done by considering the changes in the shape of the peaks and by conducting a Warren-Averbach analysis on selected peak families, to determine if the cause is due to heterogeneities in different DPPA parameters.

Changes in the Shape of Peaks

The change in the mixing parameter (representative of the shape of a peak) plotted against x , for the different applied strains and directions are plotted in Figure 8-16. It can be seen that the mixing parameter changes with x . For the axial direction, the mixing parameter falls up to $x=0.8$ and then increases to $x=1.6$, whereas in the transverse direction the same behaviour occurs at 1% strain but at higher strain the values fall from $x=0$ to $x=1.6$.

As discussed for FCC metals, the contrast factor will change the full-width, but it will also change the shape of the peak. In order to investigate how changes in the contrast factor will change the mixing parameter, the Warren-Averbach method was used. Appropriate values of the crystal size, dipole character and dislocation density were used and the contrast factor was allowed to vary for each peak, based on the predictions of Model-A. In Figure 8-17, the changes in the mixing parameter due to changes in the contrast factor from Model-A's predictions are shown. It can be seen that there is not a good relationship between the mixing parameter and x , this is because the parameter is also dependent on the position of the peak (g), and instead a good relationship between the mixing parameter and $gC^{0.5}$ is found. It should be noted that there are difficulties in fitting pseudo-Voigt curves from the simulated diffraction peaks, because the peaks are not exactly given by pseudo-Voigt curves.

The figures suggest that the changes in the mixing parameter are not due to changes in the contrast factor. Furthermore, they suggest that the changes in the

mixing parameter are due to a cause of broadening that is independent of g . This suggests that there is heterogeneity in size broadening, in different texture components, that is in some way related to x .

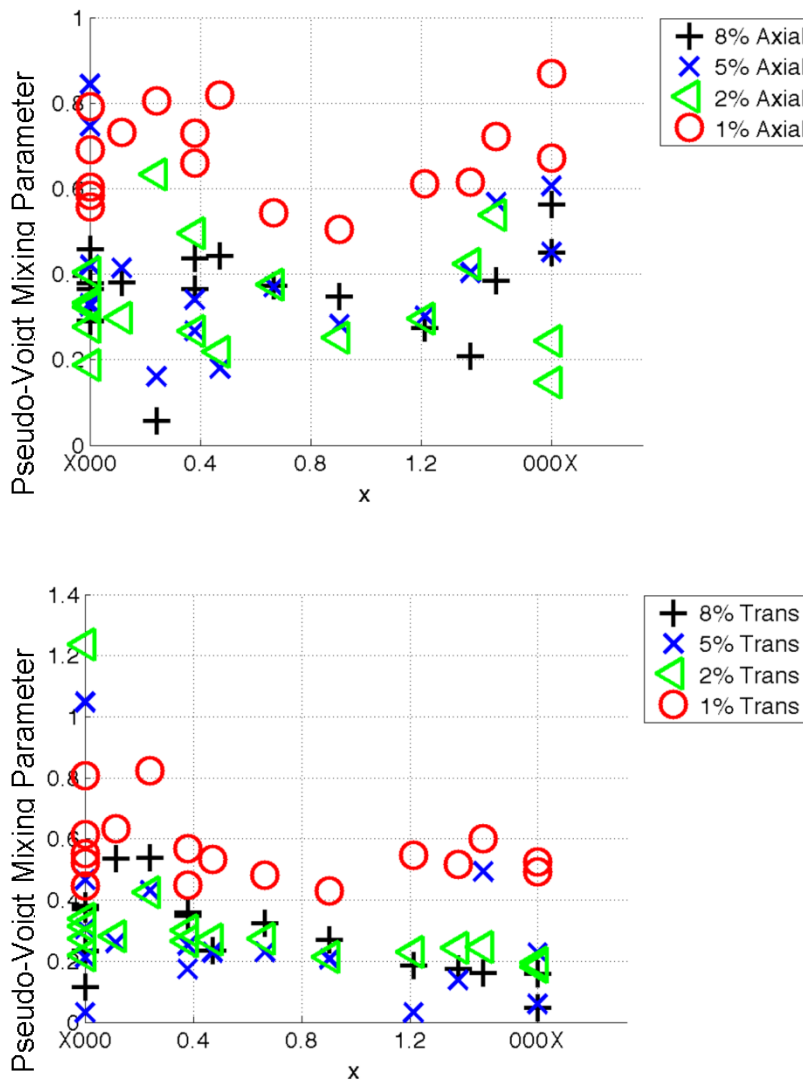


Figure 8-16. The measured pseudo-Voigt mixing parameter values for Ti-6Al-4V samples deformed to different applied strains. The values are plotted against x . The values are the fitted values that are not corrected based on the instrumental broadening.

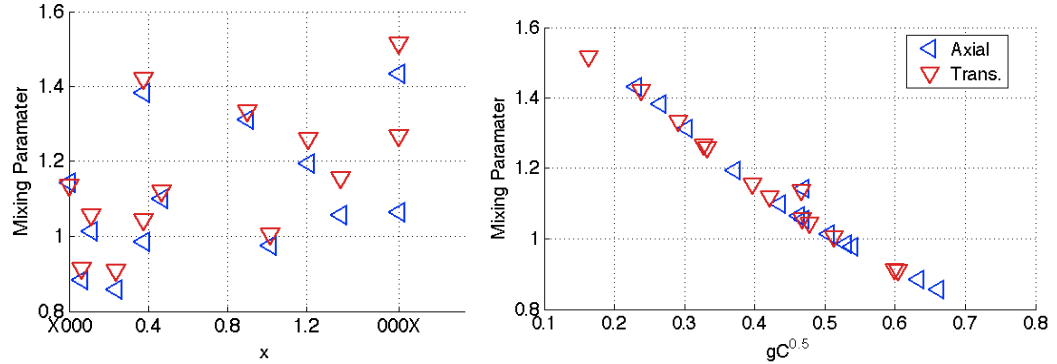


Figure 8-17. WA prediction of mixing parameter from model A.

Warren-Averbach Analysis

To investigate in more detail what DPPA parameters may be orientation dependent a Warren-Averbach (WA) analysis was conducted, on selected diffraction peaks. The method was carried out separately on the first two orders of the following peaks: $\{10 \bar{1}0\}$, $\{00 02\}$, $\{10 \bar{1}1\}$. The log-INDI method was used for all strain values, but to reduce statistical errors, the average values of 1% and 2% (low), and the average values of 5% and 8% (high) are used. The results of the WA analysis, a measure of the dislocation density, the reciprocal of the crystal size and the extent of the hook effect, are shown in Figure 8-18, plotted against x .

In the Warren-Averbach method it is not possible to separate the dislocation density from the contrast factor, hence $\rho b^2 \bar{C}$ is plotted in Figure 8-18. Which is the same as what is predicted by the model, since it has been assumed that the dislocation density is constant for different grains. The model predictions (Figure 8-10) qualitatively agree with the WA analysis $\rho b^2 \bar{C}$ values. In particular, (1) the value of $\rho b^2 \bar{C}$ falls with increasing x values, (2) $\rho b^2 \bar{C}$ is on average higher in the axial directions and (3) there is a smaller fall in $\rho b^2 \bar{C}$ in the axial direction and even an increase between 0.4 and 1.6. The WA analysis therefore suggests that the model predictions are qualitatively correct in giving the dislocation population at all strains. They do not however predict the measured full-width, so there must be another contribution to the broadening.

In the model, it was assumed that the crystal size is constant with orientation, but the WA analysis shows that there are systematic changes with orientation. The reciprocal of the crystal size falls between prismatic ($x=0$) and basal ($x\sim 1.6$) planes, for all measurements except the transverse measurement at high strain. It is the high strain transverse full-width values that showed a large discrepancy between the full-width measurements and predictions, and this discrepancy would be explained (at least in part) by the variations in size broadening. The changes in the size broadening at high strain are qualitatively the same as the predicted total dislocation density. That is the reciprocal of the crystal size falls in the axial direction but falls and then increases in the transverse direction.

The hook-effect is most often believed to be caused by inaccurate Fourier coefficients due to an overestimation of the background, but it has also been shown (Wilkens 1979) that it can be caused by the presence of small-angle grain boundaries. The size Fourier coefficients of all peaks display a hook-effect, and the extent of this is highest in the transverse direction at high x . In Figure 8-18, this hook effect is displayed as the position on the y -axis that the Fourier coefficients would intersect if they were extrapolated backwards from a point after the hook. The hook-effect is larger in the transverse direction, and increases (averaged over all strains) between the prismatic and the basal plane. Whereas, in the axial direction the opposite is the case, the hook-effect falls with increasing x between prismatic and basal planes. These changes in the hook-effect are similar to those of the crystal size at high strain, but unlike the crystal size the hook-effect increases at both low and high strains in the transverse direction.

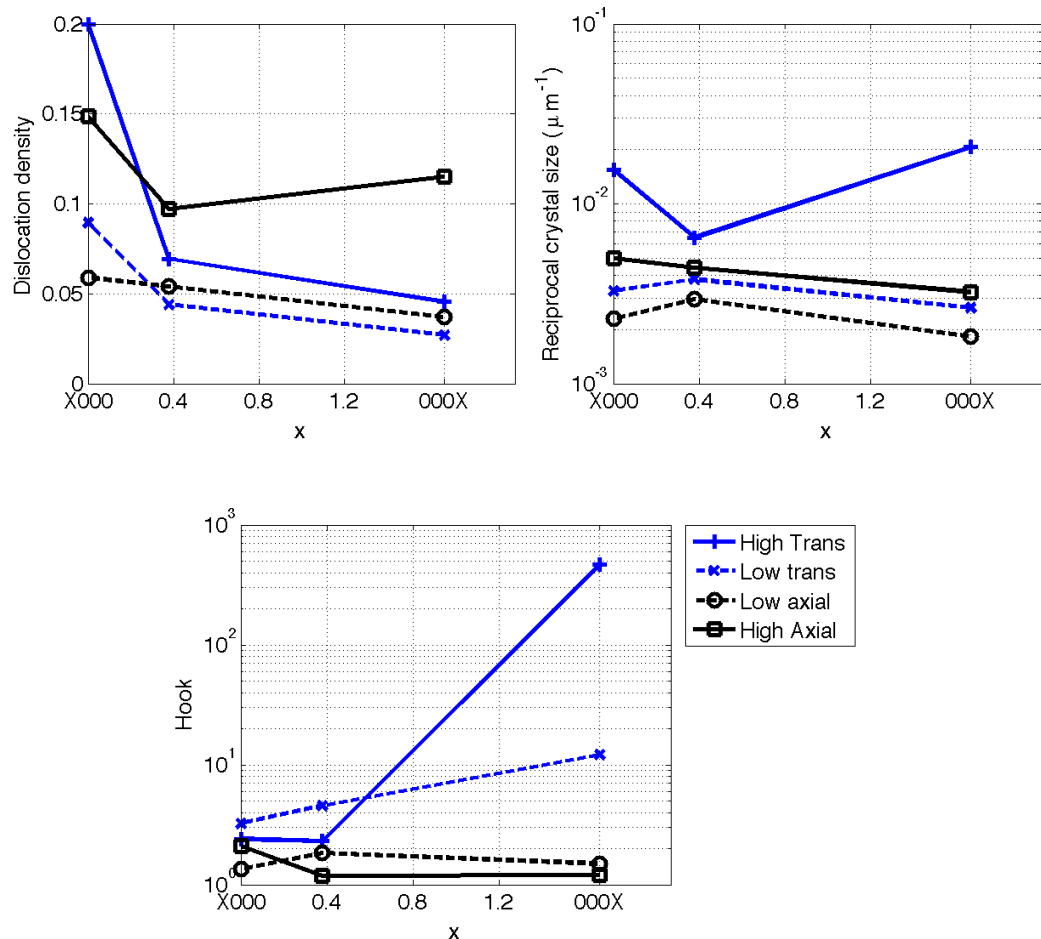


Figure 8-18. Warren-Averbach analysis results. The change in dislocation density assuming b and C are zero, which is actually $\rho b^2 \bar{C}$. The change in the reciprocal of the crystal size and the extent of the hook effect.

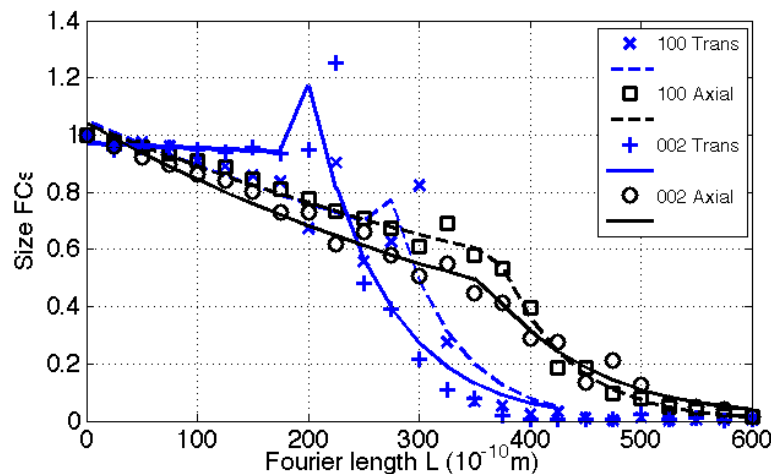


Figure 8-19. Size Fourier coefficients at 8% strain. There is a clear hook effect for all planes, such that the size coefficients can be thought of consisting of two parts.

The WA analysis results suggest that there is some validity in the Schmid factor predictions. But instead of these predictions being used to explain changes in strain values they also need to be used to explain changes in crystal size values. However, there are some problems with this idea. The changes in the size Fourier coefficients (Figure 8-19) appears to consist of two parts, the hook and after the hook. The size part after the hook is used to get the crystal size results in Figure 8-18, but if the hook part was instead used the trends in crystal size values would be very different. This is a problem because the hook extends to such large values of L. In addition, although the change in crystal size values with x in the different directions is consistent with changes in slip activity (or dislocation density), the changes between the directions are not. In particular, the prism plane (100) has similar slip system predictions but the crystal size is very different. There is also an uncertainty in some of the dislocation density results. The lower dislocation density in the transverse direction at high strain values for the basal plane, which has been used to suggest the validity of the contrast factor predictions, is found with a correspondingly very high value of the dipole character of $\sim 10^7$.

Additional Causes of Broadening in titanium

There are a number of different reasons that may explain why the plasticity models failed. The differences in the two directions may be due to instrumental effects. However, the low instrumental broadening suggests this is not the case. Another possibility is that there may additional broadening by variations in intergranular strains. The sample is small in the transverse direction and it is possible that sample preparation may have caused changes in the intergranular strains near the surface. However, care was taken to avoid this and the problem would most likely affect both directions. Alternatively, the difference could be caused by variations in intergranular strains due to plastic deformation. However based on the work of Quinta da Fonseca and colleagues (2006) on IF steel this contribution is not expected to be significant. They found that the broadening from predicted variation in intergranular strains, found using a CPFEM model, are only a fraction of the measured full-width (around $1/7^{\text{th}}$). These values are found when the sample is under load, where the variations in intergranular strains may

be larger than when un-loaded as discussed in this work. This work was carried out on a BCC metal and further investigation would be needed to quantify this contribution in titanium alloys.

The main problem with the models appears to be that they all predict higher $\langle c+a \rangle$ slip activity in the axial direction than in the transverse from $x=0.8$ to $x=1.7$. This is because pyramidal $\langle c+a \rangle$ dislocations are the main contributor to the broadening at high x , because of the low contrast factors of prismatic $\langle a \rangle$ and screw dislocations and the low predicted activity of basal $\langle a \rangle$ slip. It is sometimes found that the amount is lower than would be expected in Ti-6Al-4V (Zaefferer 2003), and it has been suggested that this may be due to deformation by the second phase or grain boundary sliding (Zaefferer 2003) or alternatively by the activation of twinning (Prakash et al. 2010). Alternatively, the amount of $\langle c+a \rangle$ dislocations may be lower than the predictions because although we have assumed the Orowan equation to have the same proportionality constants for the different slip systems this may not be the case. However, a reduction in the overall quantity of $\langle c+a \rangle$ dislocations would not explain the results. Instead, the results could be explained if the predicted quantity of $\langle c+a \rangle$ dislocations in the axial direction at high x , near the basal plane, is reduced relative to the amount in the transverse direction. This effect could be caused by a directional $\langle c+a \rangle$ slip, which means the slip system has different CRSS or activity depending on whether it is in compression or tension. It has been observed in titanium alloys that the CRSS of $\langle c+a \rangle$ slip is higher in compression than tension (Yapici et al. 2006, Fundenberger et al. 1997). The deformation of the second phase or grain boundary sliding could also in theory explain the discrepancy in predictions and results (Lutjering and Williams 2007, Zaefferer 2003). This could occur if these two mechanisms contribute to a shear in the direction of the tensile direction more than in the transverse direction. This would be expected and if this occurs instead of $\langle c+a \rangle$ slip then this could explain the differences.

A final possible explanation for the observed differences is the presence of twinning. However, twinning is not expected in Ti-6Al-4V under the deformation conditions tested at (Liu et al. 2003, Karaman et al. 2005, Yappici 2006). Its

contribution to Ti-CP, which is expected to twins, is considered in the next section.

Of these possible additional causes of broadening none of them appear to fully explain the discrepancies between the Schmid model predictions and full-width values. They may have some influence on the results, but further investigation is needed to quantify this. Instead, the best explanation for the observed changes in peak shape in Ti-6Al-4V is due to changes in slip system population calculated by the Schmid model, and variations in crystal size due to changes in the dislocation density in different orientations.

8.5 Twinning in titanium alloys

In this thesis two different titanium alloys were chosen to be investigated, Ti-6Al-4V and Ti-CP. The main reason for this choice was to investigate the presence that twinning has on peak profile methods, since Ti-CP is expected to twin (Glavicic et al. 2004, Battaini et al. 2007, Bozzolo et al. 2010, Mullins and Patchett 1981) and Ti-6Al-4V is not (Liu et al. 2003, Karaman et al. 2005, Yappici 2006). In this section, the differences between the shape of the diffraction peaks in Ti-6Al-4V and Ti-CP are investigated, without the consideration of particular peak profile methods. The reason for this is that twinning should cause different hkl peaks to broaden by different amounts, because twinning like slip (discussed in previous sections) should vary in different texture components, and hence different hkl peaks. In addition, the presence of twins in DPPA methods is often introduced by a function that changes with different hkl diffraction peaks (see Section 2.4.6).

The change in three parameters of the shape of a peak are considered: (1) the full-width divided by g (FW/g), (2) the Pseudo-Voigt mixing parameter and (3) a measure of the asymmetry of the peak (ASY). The value of ASY is defined as:

$$ASY = \frac{FW_R - FW_L}{FW_R} \quad (8.7)$$

Where, FWR is the full-width at high values of g and FWL the value at low values of g. These are found from the split Pseudo-Voigt fits of the peaks.

In Figure 8-20, the fitted FW/g values for the different Ti-CP samples measured are shown plotted against x. By comparison with this figure and Figure 8-9, it can be seen that the FW/g values follow similar trends seen in Ti-6Al-4V at the higher strains (5% and 8%). The main difference is the greater relative increase in FW/g at high x values in Ti-CP. The pseudo-Voigt mixing parameter values are shown in Figure 8-21, for Ti-CP. As with the FW/g values, the mixing parameter values for Ti-CP follow the same trends as those found in Figure 8.16 for Ti-6Al-4V.

In Figure 3.1 it was shown that the instrumental peaks found from synchrotron x-ray diffraction at ID-31, are almost symmetrical. However, as can be seen in Figure 8-22, both metals have asymmetric peaks. The asymmetry is largest for Ti-6Al-4V at 1% strain and for Ti-CP in the transverse direction at high x. In contrast to the full-width and mixing parameter, the ASY values are markedly different for the two metals. For Ti-6Al-4V, the value of ASY is positive in the axial direction with a smaller magnitude at the highest and lowest x values. Whereas for Ti-CP in the axial direction, the ASY value is approximately zero for most peaks and at high and low x is negative. In the transverse direction, the ASY value of Ti-6Al-4V is negative for most peaks, but has a zero or positive value at high x. However, for Ti-CP the ASY value is positive for most peaks, it is almost zero from x=0 to x=0.8 after which it increases gradually. In general, the magnitude of ASY value falls with strain.

In the same way that the activity of different slip systems are expected to be orientation dependent, so is the activity of different twin systems (Philippe et al. 1995, Honeycombe 1968, Wang et al. 2010). To investigate how the activity of a twin may vary in different orientations (and hence different hkl peaks) the Schmid model, presented in Section 8.2.2, is used. To do this the most common twin system in titanium (Glavicic et al. 2004, Battaini et al. 2007, Bozzolo et al. 2010),

the (10T2) tensile twin is used. A tensile twin cannot be activated if the c-axis is under compression (Honeycombe 1968). To account for this, the CRSS of the twin is set at zero if the c-axis is under compression and otherwise positive and non-zero (in the same way as done by van Houtte 1968). Using the Schmid model, the twin activity was calculated (and shown in Figure 8-23) to give an indication of the amount of grains that have twinned (labelled parent) and the amount of twins (labelled twin) that contribute to different diffraction peaks. The orientation of the twins were found by the method shown by Marshall and colleagues (Marshall et al. 2010). From Figure 8-23, it can be seen that the quantity of twins changes significantly with x. In the axial direction, at x=0 (the prismatic planes) no grains twin, since the c-axis would be under compression, whereas at the maximum x (basal plane) there is large activity of twin, since the c-axis is in tension and the Schmid factor of the (10-12) twin are high. In the transverse direction, the trend is the reverse.

There are a number of possible ways in which a twin may contribute to the broadening of a diffraction peak. These may be separated into contributions from the parent grain and the twin.

The parent of a twin may contribute to broadening in the following ways:

- A.1. Crystal size broadening from the reduction in size of the grain, because part of it twins.
- A.2. Broadening due to the twin boundary (twin broadening see Section 2.4.6).

The twin may contribute to broadening in the following ways:

- B.1. Crystal size broadening because of the size of the twins.
- B.2. Differences in the dislocation density (and arrangement and population) in the twin relative to non-twinned regions.
- B.3. Differences in the intergranular strains in twin and non-twinned regions.
- B.4. Broadening due to the twin boundary (as A.2).

Changes in the dislocation density and crystal size in grains contributing to a particular peak (A.1, B.1 and B.2), could explain differences in the changes of the full-width and mixing parameter of Ti-6Al-4V relative to Ti-CP. For example, twins break up grains resulting in a smaller crystal size, and twin have different dislocation densities as shown by the results of Salem et al. (2006), who showed that the hardness (micro and nano) in newly formed twins was always larger than in non-twinned regions. However, it is not clear how they would also explain the differences in asymmetry. Broadening due to twin boundaries (A.2 and B.4) can cause changes in the asymmetry of a peak (Balogh et al. 2006). However, the large size of twins (Glavicic et al. 2004) may mean the amount of twin boundaries is too low to have a significant contribution. In addition, it is not clear whether this description could explain the different changes in asymmetry in the two directions and with x .

Differences in the intergranular strains in twinned and non-twinned regions could explain the differences in full-width and asymmetry between the two titanium alloys. The intergranular strains are expected to vary considerably in different grains, because of the way they accommodate the imposed deformation (Quinta da Fonseca et al. 2006). The intergranular strains in twinned regions may also be different to non-twinned regions due to the way they are formed. Brown et al. (2005), explained changes in the measured full-width of magnesium samples as being due to lower intergranular strains in twinned regions relative to non-twinned regions. Hence, the larger full-width in the transverse direction at high x , could be due to the greater predicted quantity of twins (seen in Figure 8-23). However over the range $x=0$ to $x=0.8$ in the axial direction, the full-width is constant for both alloys, even though the quantity of twins increases towards $x=0$.

If the twinned regions have a different intergranular strain to the non-twinned regions and there are differences in the quantity of twinned and non-twinned regions, then this would produce an asymmetric peak. This would occur in the same way as shown in nickel single crystals, due to differences in the intergranular strains in cell walls and interiors (Ungar et al. 1984). The increase in ASY in the transverse direction from $x=0.8$ and the lower value of ASY in the

axial direction at low values of x , could be explained by the high presence of twins at these values.

The changes in the asymmetry of the Ti-6Al-4V peaks, may also be due to variations in intergranular strains. However, instead of being caused by the presence of twins these changes could be caused by differences in the way grains accommodate the imposed strain. Since planes in the axial direction are in tension and those in the transverse are in compression (when deformed), this could explain why the asymmetry is positive and negative in the two directions. The largest values of ASY are found at 1% strain, which may be indicative of some grains plastically deforming and others not. Furthermore, the presence of broadening by intergranular strains in Ti-6Al-4V may explain the relatively high broadening of this alloy when compared to the others studied that was shown in Section 7.2.

In this section, it has been shown that there are differences in the shape of diffraction peaks in Ti-CP and Ti-6Al-4V. The differences are not significant for the full-width or mixing parameter, but are for the asymmetry of the peaks. Since Ti-CP is expected to twin and Ti-6Al-4V is not, the difference were examined based on the contribution that twinning may have. The possible ways that a twin may contribute to the broadening were discussed, and it was shown that of these the best explanation for the differences between the two alloys is a result of differences in intergranular strains in twinned and non-twinned regions. Furthermore, it was shown that the changes in the asymmetry in Ti-6Al-4V may be due to variations in intergranular strains without the presence of twinning.

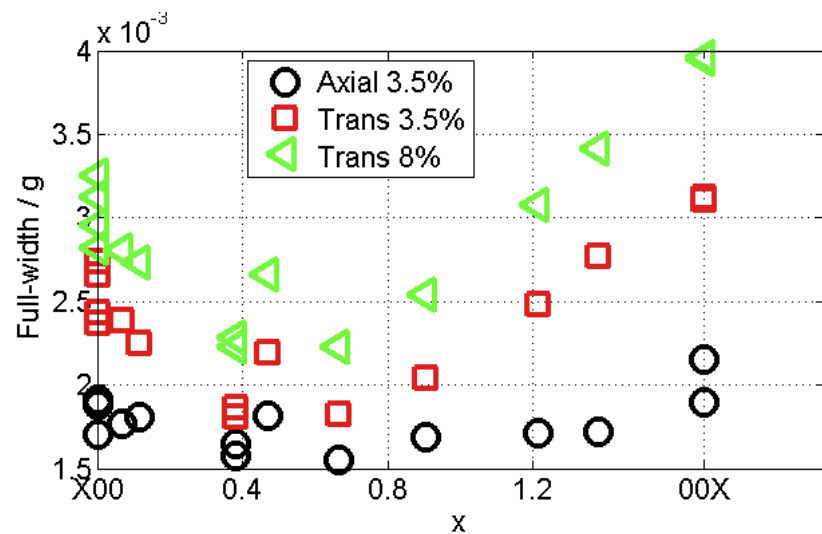


Figure 8-20. Full-width divided by g plotted against x , for Ti-CP.

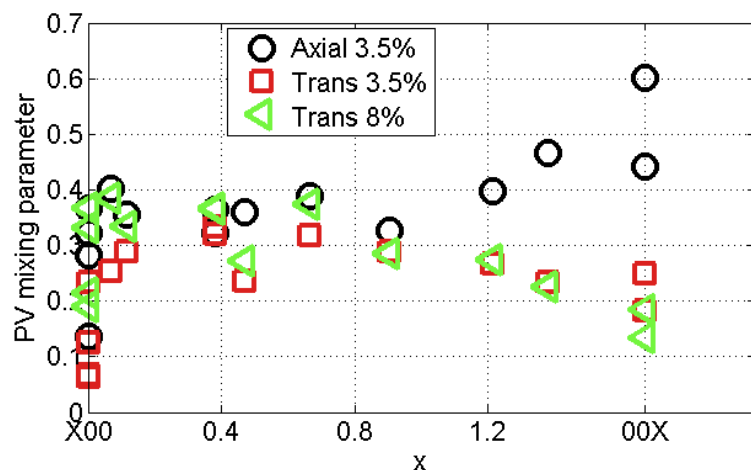
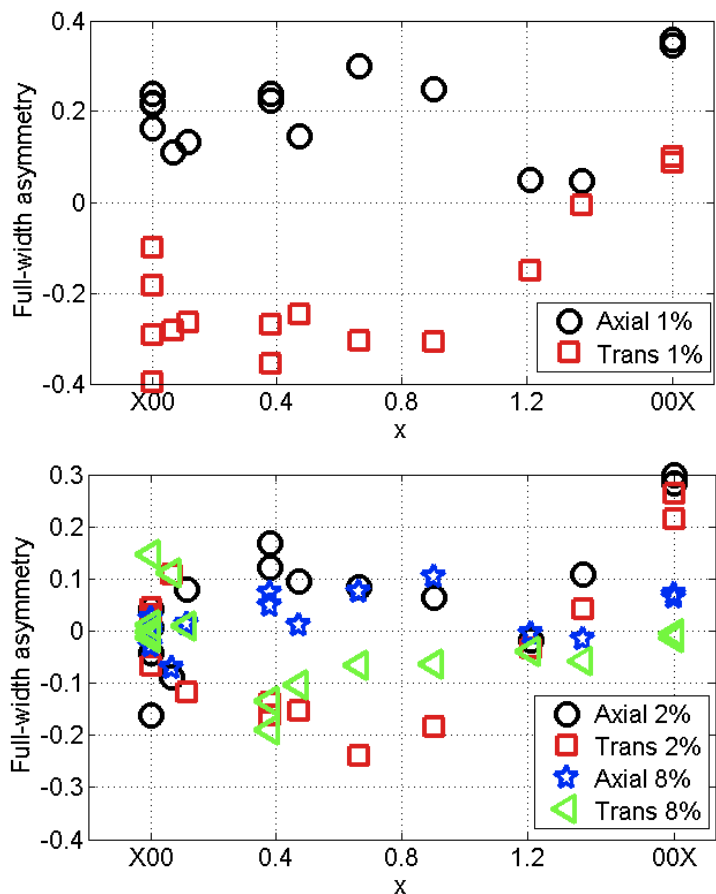


Figure 8-21. PV mixing parameter values for Ti-CP. Values are the fitted values from the diffraction pattern.

Ti-6Al-4V



Ti-CP

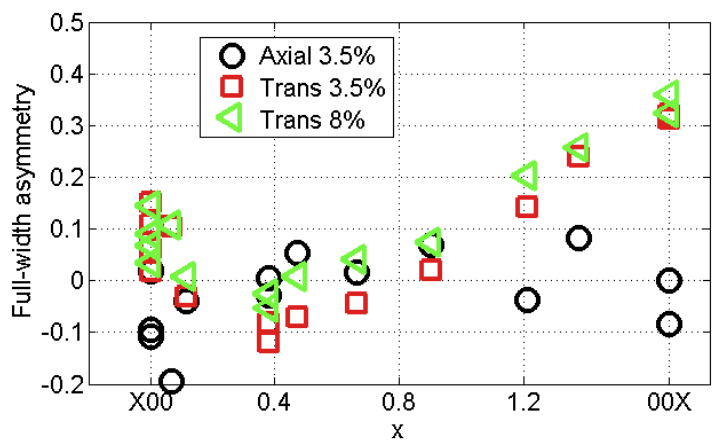


Figure 8-22.Full-width asymmetry, ASY, (see text for definition) of Ti-6Al-4V (top at 1% strain and middle at 2% and 8%) and Ti-CP (bottom) plotted against x.

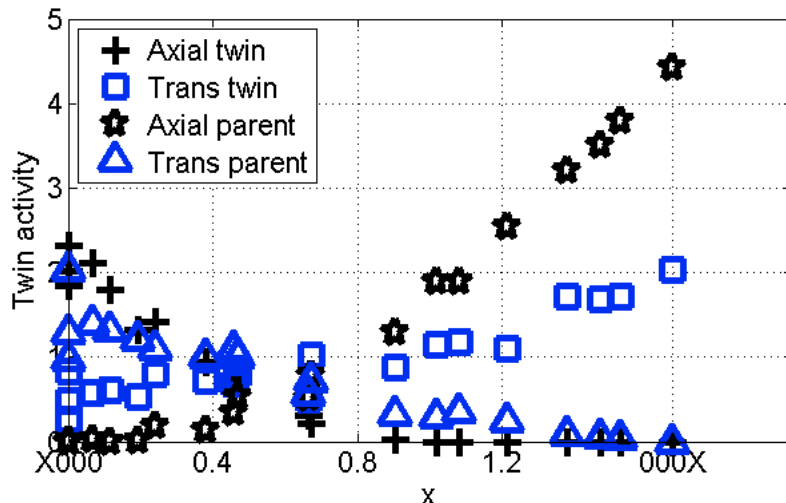


Figure 8-23. The predicted activity of (10.12) twins using the Schmid model presented in Section 8.2.2. The peaks See text for difference between twin and parent values.

8.6 Conclusions

In this chapter it has been shown that there are significant differences in the full-widths in different texture components, in both FCC and titanium alloys. This could not be explained if grains deformed homogeneously, as assumed with the use of the contrast factor equation. Instead, it was shown that these differences could be partly explained by predicted variations in the dislocation population of different texture components, in a manner similar to that used by Borbely and colleagues on cubic metals (Borbely et al. 2000, Guiglionda et al. 2004). It was shown that the discrepancy with these predictions was small for stainless steel and Ti-6Al-4V, at low strains; but larger for nickel, Ti-6Al-4V at higher strains and Ti-CP. For nickel the additional broadening heterogeneity was shown to be most likely caused by the heterogeneity of the dislocation structure, which means the crystal size varies for different texture components. For Ti-6Al-4V, the additional broadening heterogeneity was also shown to be caused by a heterogeneity in the crystal size, but instead of being related to a dislocation structure was shown to be due to changes in dislocation density (and in particular dislocation density of $\text{Pr}\langle a \rangle$), which in turn cause a size effect. It was shown that there was a difference in the shape of diffraction peaks in different texture components in the two titanium alloys, Ti-CP and Ti-6Al-4V. This difference was shown to be most

likely due to the presence of twinning, in Ti-CP, which changes the shape of the peaks because of variations in intergranular strains in twinned and un-twinned regions.

Hence, the results show that different texture components, in a deformed metal, have different slip system populations, dislocation densities, dislocation arrangements, crystal sizes and intergranular strains. These results are in contradiction to the commonly used approach in diffraction peak profile methods. In this approach all grains, measured in a particular direction, are thought of as being the same (Ungar and Tichy 1999, Dragomir and Ungar 2002), i.e. they have the same q -values. This is the approach taken in Chapter 7. In this approach any differences in broadening of different hkl peaks is due to how the same dislocation population broadens different hkl peaks, by the use of the contrast factor equation. Hence, these results show that this approach can result in errors being produced.

One of the aims of this chapter was to establish whether DPPA methods could be used to verify polycrystal plasticity models. I believe that the technique could become a valuable technique in this field, but there are a number of issues that need addressing. A greater understanding is needed of what the DPPA parameters represent and how they may change, in particular the crystal size and dipole character values. The results suggest that changes in the crystal size in different orientations are just as important as changes in the slip system population. But without a good understanding of what the crystal size represents the use of this technique to verify polycrystal plasticity models would be limited. The way that dislocation density can be related to the slip activity (the Orowan equation) may have an important implication particularly in HCP metals, and so this would also need to better understood. The results in this chapter also suggest that broadening by intergranular strains in HCP metals occurs. A model of HCP metals would therefore need to incorporate this.

9 Conclusions

The aim of this work was to investigate the usefulness of diffraction peak profile analysis (DPPA) method when applied to the understanding of the deformation of metals. From the results of Chapters 6, 7 and 8 the following conclusions are made about their use.

DPPA Methods

- The full-width is the most important DPPA parameter. It is the simplest method with the least uncertainty and is not prone to systematic errors that may result based on assumptions in more complicated DPPA methods (Section 7.2).
- The use of the variance-A method is not recommended, because it gave values (particularly the micro-strain) that are not expected.
- The integral breadth method and the different Williamson-Hall method were found to be more useful. However, a large drawback of these methods is the ambiguity in crystal size and micro-strain, and the additional errors their use produces.
- The alternative method has the advantage over other methods, because it was able to differentiate crystal size values in high and low SFE metals (Section 7.3.2 and Section 7.3.3). However, the dislocation density values were found to have a large error and gave in many cases lower dislocation density values than expected from TEM results (Section 7.4.1).
- The Fourier methods were found to give dislocation density values at approximately the same values as expected from TEM results (Section 7.4.1). Of the different approaches I would recommend the log-INDI approach because of the lower errors and because it uses the Fourier coefficients that are least prone to errors from instrumental effects and limitations in the equations that separate crystal size and micro-strain.
- The variance-B method was found to give similar dislocation density values to those expected (Section 7.4.1), and similar crystal size values to the Fourier methods (Section 7.3.3). It has the advantage that it is a single peak method but there were found to be difficulties in implementing it.

DPPA parameters

- Based on the results of Section 7.3 and Chapter 8, I believe that the crystal size can be thought of as being the size of an undistorted region of a metal, which can be caused by the presence of defects such as dislocations that have no misorientation across them.
- The exception to this is the alternative method where it can be thought of as the size of a region which is misorientated with respect to neighbouring regions.
- In Section 8.4, it was found that the crystal size can vary significantly in different texture components. This can be due to either variations in the amount of dislocations, or variations in the arrangements of dislocation in different grains. These differences can cause comparable changes in the broadening of different peaks as caused by the dislocation population.
- Almost all methods show an increase in crystal size and micro-strain broadening with applied strain (7.3.4). Different methods attribute size and strain broadening in different ways.
- The dislocation density values found by different Warren-Averbach methods and the variance-B method (Section 7.4.1), were shown to be approximately the same as found by TEM measurements on similar alloys. The alternative method was found to give similar values but in many cases gave values that were significantly lower.
- The dislocation density values found for nickel were higher than expected (Section 7.4.1).
- The dislocation density values found in many cases for FCC metals were higher than expected at low strain. I believe the cause of this is due to instrumental effects (Section 7.4.1).
- The dipole character showed changes with applied strain for all metals which were in agreement with the expectations and the results of others (Zehetbauer et al. 1999) (Section 7.4.2). The differences between the values of nickel and other alloys also suggests that the value of those results represent how dislocations are arranged in a metal. However, variations in the magnitude of the parameter for different methods and

because it cannot be measured by other methods, mean the parameter is in most cases limited to being a fitting parameter.

- Dislocation population calculations, using the contrast factor equation, were found to be consistent with expected changes for both FCC and HCP alloys (Section 7.4.4 and 7.4.7). However, based on the results of Chapter 8, I believe that the assumption behind the approach taken are not valid. This is because I believe the relative broadening of different peaks can better be described by differences in the slip system population and crystal size in different texture components.

Additional Considerations

- A method which uses polycrystal plasticity models to explain the changes in the shape of diffraction peaks in different texture components was applied to nickel, stainless steel and titanium alloys. The method was shown to qualitatively describe the changes in the shape of the peaks for all metals. It was shown that unlike the previous work using this method (Borbely et al. 2000, Guiglonda et al. 2004), differences in the dislocation population in different orientations could only partly explain changes in the shape of the peaks. To fully explain the changes, differences in crystal size and variations in intergranular strains must be accounted for. To explain the nickel results, it was shown that differences in the cell structure in different texture components needs to be accounted for. For titanium alloys, it was shown that differences in the dislocation density, which would contribute to a crystal size broadening must be accounted for. To explain the differences between the two titanium alloys it was shown that the presence of twins that cause variations in intergranular strains needs to be accounted for.
- In this thesis three different diffraction sources have been used. Based on the results of Section 7.5, there are some differences in the results of DPPA methods depending on the diffraction source. The differences are small for the full-width but larger for other methods.
- The use of the contrast factor equations was found to be useful in providing more consistent results. However, there was found to be

problems with its use in adequately describing the broadening of different hkl peaks for both FCC and HCP alloys. It was also shown that large errors could result in its use. Furthermore, the results of Chapter 8 showed that a different approach to describe the broadening of different peaks, which accounted for the heterogeneity of deformation, could describe changes in the broadening of different peaks. This second approach suggests that the assumptions of the contrast factor are not valid for the alloys studied. Based on this I would still use the contrast factor equations for both FCC metals, especially if limited diffraction peaks were available. But I would also recommend that an approach not using the contrast factor but using peaks of the same family (e.g. 111 and 222) are also used. However, for HCP metals I would not recommend its use, as I believe the errors in its use could be large.

Further Work

The results presented in Chapter 8 on HCP metals gave un-answered questions as to the causes of broadening of different peaks in HCP metals. The use of the contrast factor equation for HCP metals (Dragomir and Ungar 2002) would not explain the differences in the full-width of different diffraction peaks, and its use would produce errors. However, the use of the Schmid model could only partly explain the differences. The problem is that not enough different hkl peaks in different texture components were measured and there are too many possible parameters to explain broadening, to fully understand what is happening. This problem could be greatly reduced with an experiment similar to the HRPD experiment, where diffraction patterns are obtained at a number of different angles between the tensile direction and the diffraction vector. This could be done at HRPD, if for example a zirconium alloy was used, but would have to be conducted at a synchrotron source such as ESRF, if using a titanium alloy. It would also be beneficial to use two HCP metals with notably different active slip system are compared- e.g. magnesium (basal $\langle a \rangle$ dominates) and titanium ($\text{Pr}\langle a \rangle$ dominates). The differences between the metals could be then used to understand what is happening.

A further problem identified with the HCP alloys was broadening by intergranular strains. To fully establish the influence this would have on peak profiles would require a two-part approach. A model would need to be used that could provide information as to the intergranular strains, such as CPFEM. In order to verify this model an in-situ diffraction experiment could be conducted. In this experiment a sample would be loaded and un-loaded, and the movement and shape of the peaks would be measured and compared with the CPFEM results.

A big problem that was identified was the ambiguity of different DPPA results, in particular the crystal size and dipole character. A systematic TEM study combined with results from the DPPA methods, could be performed that would enable a better understanding of what these parameters represent.

References

- Abson D J, Jonas J J; Journ. Nuc. Mat.; Vol. 42, Issue 1; 73-85; (1972)
- Agnew S R, Duygulu O; ‘Plastic anisotropy and the role of non-basal slip in magnesium alloy AZ31B’; International Journal Of Plasticity; 21; 1161-1193; (2005)
- Allison S K; Phys. Rev.; 44; 63-72; (1933)
- Akhtar A; Metall. Trans. A; vol. 6A; 1105–13; (1975)
- Balogh L, Ribárik G, Ungár T; ‘Stacking faults and twin boundaries in fcc crystals determined by x-ray diffraction profile analysis’; Journal of Applied Physics; 100; 023512; (2006)
- Balzar D, Ledbetter H; J. Appl. Cryst.; 26; 97-103; (1993)
- Balzar D; ‘7: Voigt function model in diffraction-line broadening analysis’; pg. 94; Editors Snyder R L, Fiala J, Bunge H; ‘Defect and Microstructure Analysis by Diffraction’; IUCR Monographs on Crystallography 10; Oxford University Press; Oxford; (1999)
- Balzar D, Audebrand N, Daymond M R, Fitch A, Hewat A, Langford J I, Le Bail A, Louer D, Masson O, McCowan C N, Popa N C, Stephens P W, Toby B H; Jour. Appl. Cryst.; 37; 911-924; (2004)
- Barrett C R, Muehleisen E C, Nix W D; Mat. Sci. and Eng.; Vol. 10; 33-42; (1972)
- Barnett M R; Metall. And Mater. Trans. A; 34A; 1799-1806; (2003)
- Barnett M R, Keshavarz Z, Beer A G, Atwell D; Acta Mat.; 52; 5093-5103; (2004)
- Bate P; Phil. Tran.:Math. Phys. And Eng. Sci.; vol 357; No 1756; pp 1589-1601; (1999)
- Battaini M, Pereloma E V, Davies C H J; Metal. And Mat. Trans. A; 38A; 276-285; (2007)

Bay B, Hansen N, Hughes D A, Kuhlmann-Wilsdorf A; ‘Evolution of FCC deformation structures in polyslip’; Acta metall, Mater; Vol. 40, No. 2; 205-219; (1992)

Bertaut F; C. R. Acad. Sci; Paris 228; 187; (1949)

Bearden J A, Shaw C H; Phrs. Rev.; 48; 18-30; (1935)

Bhadeshia H K D H, Honeycombe R; ‘Steels Microstructure and Properties’; 3rd edition; Butterworth-Heinemann; Oxford; (2006)

Biswas C P; PhD thesis; Massachusetts Institute of Technology; (1973)

Bocher L, Delobelle P, Robinet P, Feaugas X; International Journal of Plasticity; 17; 1491–1530; (2001)

Borbely A, Driver J H, Ungar T; ‘An X-ray Method for the determination of stored energies in texture components of deformed metals; Application to cold worked ultra high purity iron’; Acta Mater. 48 2005±2016; (2000)

Borbely A, Groma I; ‘Variance method for the evaluation of particle size and dislocation density from x-ray Bragg peaks’; Applied Physics Letters; Vol 79; Number 12; 1772; (2001)

Borbely A, Dragomir-Cernatescu J, Ribarik G, Ungar T; ‘Computer program ANIZC for the calculation of diffraction contrast factors of dislocations in elastically anisotropic cubic, hexagonal and trigonal crystals’; J. Appl. Cryst.; 36; 160–162; (2003)

Borbely A, Revesz A, Groma I; ‘Momentum method applied to evaluation of size and strain in ball-milled iron’; Z. Kristallogr. Suppl.; 23; 87–92; 2006

Bozzolo N, Dewobroto N, Wenk H R, Wagner F; J Mater Sci; 42; 2405–2416; (2007)

Bozzolo N, Chan L, Rollett A D; Applied Crystallography; 43; 596-602; (2010)

Bridier F, Villechaise P, Mendez J; Acta Mater.; 53; 555-567; (2005)

Brown D W, Agnew S R, Bourke M A M, Holden T M, Vogel S C, Tome L C N; Mater. Sci. Eng. A; 399; 1-12; (2005)

Bunge H J, Leffers T; Scripta Metall.; 5; 143; (1971)

Byun T S, Lee E H, Hunn J D; Jour. Of Nuc. Mat.; 321; 29-39; (2003)

Byun T S; Hashimoto N; Farrell K; Jour. Of Nuc. Mat.; 351; 303-315; (2006)

Capeletti T L, Jackman L A, Childs W J; Metal. Trans.; Vol. 3 April; 789-796; (1972)

Callister W; Materials Science and Engineering: An Introduction, 5th Edition; pg 140;
Wiley and Sons Inc.; New York; (2000)

Castany P, Pettinari-Sturmel F, Crestou J, Douin J, Coujou A; Acta Materialia; 55;
6284–6291; (2007)

Chescoe D, Goodhew P J; The Operation of transmission and scanning electron
microscopes- Royal Microscopy Society Handbooks; Oxford Science
publications; Oxford; (1990)

Christian J W, Mahajan J; Prog. In Mat Sci.; 39; 1-157; (1995)

Conrad H, Jones R; Trans. AIME; 45; 57; (1953)

Conrad H; Progress in Materials Science; 26; 123-40; (1981)

Cowley J M; Diffraction Physics; 388-400; New York and London: North-Holland;
(1981)

Cullity.B D; Elements of X-Ray Diffraction; Addison-Wesley Publishing Co.;
Reading, Mass.; (1978)

de Keijser Th H, Mittemeijer E J, Vogels A B P; J. Appl. Cryst.; 15; 308-315; (1982)

De M, Sen Gupta P; J. Phys. D: Appl. Phys.; 3; (1970)

Delhez R, de Keijser Th. H, Mittemeijer E J; Fresenius Z Anal Chem; (1982); 312:1-
16

Diehl J; Z Metallkde; 47; 331; (1956)

Dilamore I L, Morris P L, Smith C J E, Hutchinson W B; Proc. R. Soc. Lond. A.; 329;
405-420; (1972)

- Dilamore I L, Katoh H; Met. Sci. J.; 8; 21; (1974)
- Dong Y H, Scardi P; J. Appl. Cryst.; 33; 184-189; (2000)
- Dragomir I, Ungar T; ‘Contrast factors of dislocations in hexagonal crystal system’; J. Appl. Cryst; 35; 556–564; (2002)
- Dragomir I C; PhD thesis; Eotvos University Budapest, Hungary; (2002)
- Dragomir I S, Li D S, Castello-Branco G A, Garmestania H, Snyder R L, Ribarik G, Ungar T; Materials Characterization; 55; 66– 74; (2005)
- Edwards H J, Toman K; J. Appl. Cryst.; 4; 319; (1971a)
- Edwards H J, Toman K; J. Appl. Cryst.; 4; 472; (1971b)
- Evans A, S-B. Kim S-B, Shackleton J, Bruno G, Preuss M, Withers P J; International Journal of Fatigue; 27; 1530-1535; (2005)
- Feaugas X; Acta Mater.; Vol. 47, No. 13; 3617-3632; (1999)
- Feaugas X, Haddou H; Phil. Mag.; Vol. 87, No. 7; 989-1018; (2007)
- Fitch, A.N; Journal of Research of the National Institute of Standards and Technology; 109(1); 133-142; (2004)
- Franciosi P; ‘The concepts of latent hardening and strain hardening in metallic single crystals’; Acta metal; Vol. 33. No. 9; 16014612; (1985)
- Frankel P G; EngD thesis; University of Mancheseter; (2008)
- Fundenberger J J, Philippe M J, Wagner F, Esling C; Acta mater.; Vol. 45, no. 10; 4041-4055; (1997)
- Furu, T, Nes E; ‘Recrystallization’92’; eds. Fuentes and Sevillano, San Sebastian, Spain, 311; (1992)
- Gil Sevillano J, van Houtte P, Aernoudt E; Progress in Materials Science; Vol. 25; 69-412; (1981)
- Glavicic M G, Salem AA, Semiatin S L; Acta Materialia; 52; 647–655; (2004)

Glavicic M G, Semiatin S L; 'X-ray line-broadening investigation of deformation during hot rolling of Ti–6Al–4V with a colony-alpha microstructure'; *Acta Materialia*; 54; 5337–5347; (2006)

Gloaguen D, Francois M, Guillen R, Royer J; *Phys. Stat. Sol. (a)*; 193, No. 1; 12-25; (2002)

Groma I, Ungar T, Wilkens M; *J. Appl. Cryst.*; 22; 26; (1988)

Groma I; *Phys. Rev. B*; 57; 7535; (1998)

Gubicza J, Chinh N Q, KraLllics G, Schiller I, Ungar T; *Current Applied Physics*; 6;194–199; (2006)

Guiglionda G, Borbely A, Driver J H; 'Orientation-dependent stored energies in hot deformed Al–2.5%Mg and their influence on recrystallization'; *Acta Materialia* 52, 3413–3423; 2004

Gupta R K, Anantharaman T R; *Z. Metall.*; 62; 732 735; (1971)

Gutierrez-Urrutia I and Raabe D; 'Dislocation density measurement by electron channeling contrast imaging in a scanning electron microscope'; *Scripta Materialia*; 66; 343-346; (2012)

Hadji M, Badji R; *Journal of Materials Engineering and Performance*; 11; 145-151; (2002)

Hahner P; *Script. Mat.*; 47; 415-421; (2002)

Halder N C, Wagner C N J; *Adv. X-ray Anal.*; 9; 91-102; (1966)

Hansen N, Ralph B; *Acta. Metall.*; 30; 411–417; (1982)

Hansen N, Huang X, Pantleon W, Winther G; Vol. 86, Nos. 25–26;; 3981–3994; (2006)

Hendricks S, Teller E; 'X-ray interference in partially ordered layer lattices'; *J. Chem Phys.*; 10; 147-167; (1942)

Hill R; *J. Mech. Phys. Solids*; 13; 89; (1965)

Holt D L; J. Appl. Phys.; 41; 3197; (1970)

Holzer G, Fritsch M, Deutsch M, Hartwig J, Forster E; Physical Review A; Vol. 56; No. 6; 4555; (1997)

Honeycombe, R W K; ‘The Plastic Deformation of Metals’; Edward Arnold; London; (1968)

Houska C R, Kuzel R; ‘6: Classical treatment of line profiles influenced by strain, small size, and stacking faults’; IUCR monographs on crystallography, Defects and microstructure analysis by diffraction; edited by Snyder R L, Fiala J, Bunge H J;264-317; International Union of crystallography; Oxford University Press; Oxford; (1999)

Hull D, Bacon D J; ‘Introduction to dislocations’; 4th Ed; Butterworth-Henemann; Oxford; (2001)

Humphreys F J; Review, Grain and subgrain characterisation by electron backscatter diffraction’; Journal of Materials Science; 36; 3833-3854; (2001)

Humphreys F J, Hatherly M; ‘Recrystallization and related annealing phenomena’; Elsevier; Oxford; (2004)

Humphreys F J, Bate P S; Acta Mat.; 54; 817-829; (2006)

Hutchings M T, Withers P J, T.M Holden T M, and T. Lorentzen T; ‘Introduction to the characterization of residual stress by neutron diffraction’; Taylor and Francis; (2005)

Ibberson R M, David W I F and Knight K S; ‘The High Resolution Powder Diffractometer (HRPD) at ISIS – A User Guide’; Report RAL 92±031; Rutherford Appleton Laboratory, Chilton, Didcot, England; (1992)

Jorge-Badiola D, Iza-Mendia A, Gutierrez I; ‘EBSD characterization of a hot worked 304 austenitic stainless steel under strain reversal’; Journ. Of Microsc.; Vol. 235 Pt 1; 36-49; (2009)

Joy D C, Newbury D E, Davidson D L; Rev. Phys. Appl.; 53; 81; (1982)

Kad B K, Schoenfeld S E, Burkins M S; Mater. Sci. Eng. A; 322; 241–251; (2002)
332

Kakinoki J, Tomura Y; 'Intensity of x-ray diffraction by a one-dimensionally disordered crystal I the intensity equation; *Acta Cryst.*; 19; 137-147; (1965)

Kapoor K, Lahiri D, Rao S V R, Sanyal T, Kashyap B P; *Bull. Mater. Sci.*; Vol. 27, No. 1; 59-67; (2004)

Karaman I, Yapici G G, Chumlyakov Y I, Kireeva I V; *Mater. Sci. Eng. A*; 410–411; 243-247; (2005)

Keller C, Hug E, Retoux R, Feaugas X; *Mechanics of Materials*; 42; 44–54; (2010)

Kesavan Nair P, Vasudevan R; *J. Appl. Cryst.*; 10; 401-404; (1977)

Klimanek P, Kuzel R; *J. Appl. Cryst.*; 21; 59±66; (1988)

Klug, H. P & Alexander, L. E; 'X-ray Diffraction Procedures', 2nd ed; Wiley Interscience; New York; (1974).

Kocks U F; *Philos. Mag.*; 13:541; (1966)

Kocks U F, Mecking H; *Progress in Materials Science* 48; 171–273; (2003)

Krivoglaz M A; 'Theory of X-ray and Thermal Neutron Scattering by Real Crystals'; Plenum Press; New York; (1969)

Krivoglaz M A; 'X-ray and Neutron Diffraction in Nonideal Crystals'; Springer-Verlag; Berlin; (1996)

Kubin L P, Canova G; *Scrpts Metal. Et Mater.*; Vol 27; pp 957-962; (1992)

Kuhlmann-Wilsdorf D. *Trans Met Soc AIME* ; 218:962; (1962)

Kuhlmann-Wilsdorf D; *Mat. Re. Innovat.*; 1; 265-297; (1998)

Kiran Kumar M, Vanitha C, Samajdar I, Dey G K, Tewari R, Srivastava D, Banerjee S; *Materials Science and Technology*; vol. 22, no. 3; (2006)

Kuzel R, Klimanek P; *J. Appl. Cryst.*; 21; 363-368; (1988)

Kuzel R; 'Kinematical diffraction by distorted crystals – dislocation X-ray line broadening'; *Z. Kristallogr.* 222; 136–149; (2007)

- Ladell J, Zagofsky A & Pearlman S; *Appl. Cryst.*; 8; 499; (1975)
- Landau L; *Phys. Z. Sowjetunion*; 12; 579; (1937)
- Langford J I; Wilson A J C; ‘Crystallography and Crystal Perfection’ edited by Ramachandran G N; pp. 207-222; Academic Press; London; (1963)
- Langford J I; *J. Appl. Cryst.*; 11; 10-14; (1978).
- Langford J I, Wilson AJ C; *J. Appl. Cryst.*; 11; 102-113; (1978)
- Langford J I; *J. Appl. Cryst.*; 15; 315-322; (1982)
- Langford J I, Louer D; *Rep. Prog. Phys.*; 59; 131-234; (1996)
- Langford J I; ‘5: Use of pattern decomposition or simulation to study microstructure: theoretical considerations’; pg. 59; Editors Snyder R L, Fiala J, Bunge H; ‘Defect and Microstructure Analysis by Diffraction’; IUCR Monographs on Crystallography 10; Oxford University Press; Oxford; (1999)
- Lebensohn R A, Tome C N; *Acta. Metal. Mater.*; vol 41; no 9; pp 2611-2624; (1993)
- Ledbetter H M; *Phys. Stat. Sol.*; A85; 89–96; (1984)
- Lee W, Lin C; *Mat. Sci. and Eng.*; A308; 124–135; (2001)
- Lehockey E M, Lin Y, Lepik O E; *Electron Backscatter Diffraction in Materials Science*; edited by Schwarts, A.J., et al.; ‘Mapping residual plastic strain in materials using electron backscatter diffraction’; 247–264; Kluwer Academic/Plenum Publishers; (2000)
- Leineweber A, Mittemeijer E J; ‘Anisotropic microstrain broadening due to compositional inhomogeneities and its parametrisation’; *Z. Kristallogr. Suppl.* 23; 117-122; (2006)
- Lifshitz I M; On the theory of scattering of x-rays by crystals of variable structure; *Phys. Z. SowjUn.*; 12; 491-511; (1937)
- Liu Q, Hansen N; *Phys. Stat. sol. (a)*; 149; 187; (1995)
- Liu Q, Juul Jensen D, Hansen N; *Acta Mater.*; Vol 46; No. 16; 5819; (1998)

- Liu Y, Yang D Z, He S Y, Wu W L; Materials Characterization; 50; 275– 279; (2003)
- Lutjering G, Williams J C; ‘Titanium’ 2nd edition; Springer; New York; (2007)
- Malygin G A; ‘Kinetic Mechanism of the Formation of Fragmented Dislocation Structures upon Large Plastic Deformations’; Physics of the Solid State; Vol. 44; No. 11; 2072–2079; (2002)
- Marshall P E, Proust G, Rogers J T, McCabe R J; Journal of Microscopy; Vol 238 Pt3; 218-229; (2010)
- Mecking H, Kocks U F; Acta Metall; 29; 1865; (1981)
- Mitra G B, Giri A K; Journal of Materials Science; 22; 1573-1579; (1987)
- Mughrabi H; ‘Deformation-induced long-range internal stresses and lattice plane misorientations and the role of geometrically necessary dislocations’; Philosophical Magazine; Vol. 86; Nos. 25–26, 1–11; 4037–4054; (2006a)
- Mughrabi H; ‘Dual role of deformation-induced geometrically necessary dislocations with respect to lattice plane misorientations and/or long-range internal stresses’; Acta Materialia; 54; 3417–3427; (2006b)
- Mullins S, Patchett B M; Metal. Trans. A; 12A; 853-863; (1981)
- Nandi R K, Sen Gupta S P; J. Appl. Cryst.; 11; 6-9; (1978)
- Needleman A, Gil Sevillano J; Scripta Mat.; 48; 109-111; (2003)
- Partridge PG; Metall. Rev.; 12; 169; (1967)
- Perlovich Yu, Bunge H J, Isaenkova; ‘Textures & Microstructures’; 29; 241-266; (1997)
- Philippe M J, Serghat M, Van Houtte P, Esling C; Acta metal. Mater.; Vol. 43, No. 4; 1619-1630; (1995)
- Prakasha D G Leo, Ding R, Moat R J, Jones I, Withers P J, Quinta da Fonseca J, Preuss M; Materials Science and Engineering A; 527; 5734–5744; (2010)

Quinta da Fonseca J, Oliver E C, Bate P S, Withers P J; Materials Science and Engineering A; 437; 26-32; (2006)

Rachinger W A; J. Sci. Instrum; 25; 254-255; (1948)

Raj S V and G. M. Pharr G M; Mater. Sci. Engng; 81; 217; (1986).

Ribarik G, Ungar T, Gubicza J; ‘MWP-fit: a program for Multiple Whole Profile fitting of diffraction peak profiles by ab-initio theoretical functions’; Appl. Cryst; 34; 669–676; (2001)

Rietveld, H.; J. Appl. Cryst.; 2; 65–71; (1969)

Rohatgi A, Vecchio K S, Gray G T; ‘Chapter 3: A systematic study of the role of stacking fault energy (SFE) on shock-hardening in Cu and Cu-Al alloys’; Fundamental Issues and Applications of Shock-Wave and High-Strain-Rate Phenomena; edited by Staudhammer K P, Murr L E, Meyers M A; Elsevier Science Ltd.; Oxford; (2001)

Sachs, G Z; VDI; 12; 734; (1928)

Salem A A, Kalidindi S R, Doherty R D, Semiatin S L; Metall. And Mat. Trans. A; Volume 37A January; 259; (2006)

Sanchez-Bajo F, Cumbre F L; J. Appl. Cryst.; 30; 427-430; (1997)

Sanchez-Bajo F, Ortiz A L, Cumbre F L; J. Appl. Cryst.; 39; 598–600; (2006)

Sarkar A, Mukherjee P, Barat; Mat. Sci. and Eng. A; 485; 176-181; (2008)

Sarkar A, Bhowmik A, Suwas S; Appl Phys A; 94; 943–948; (2009)

Scardi P, Leoni M; ‘Diffraction line profiles from polydisperse crystalline systems’; Acta Cryst; A57; 604–613; (2001)

Scardi P, Leoni M, Delhez R; ‘Line broadening analysis using integral breadth methods: a critical review’; J. Appl. Cryst; 37; 381±390; (2004)

Schafler E, Simon K, Bernstorff S, Hanak P, Tichy G, Ungar T, Zehetbauer M J; ‘A second-order phase-transformation of the dislocation structure during plastic

deformation determined by in situ synchrotron X-ray diffraction'; *Acta Materialia*; 53; 315–322; (2005)

Scherrer P; *Nachr. Ges. Wiss. Gottingen*; September 26; 98-100; (1918)

Seefeldt M; *Rev. Adv. Mater. Sci.*; 2; 44-79; (1999)

Seeger A, Diehl J; *DIEHLJ*, .., D E RS.,, and REBSTOCHK.,, 1957, *Phil. Mag.*, 2,323

Snyder R L, Fiala J, Bunge H; 'Defect and Microstructure Analysis by Diffraction'; *IUCR Monographs on Crystallography* 10; Oxford University Press; Oxford; (1999)

Soleimanian V, Aghdaee S R; *Powder Diffraction*; Vol. 23, No. 1, March; 41-51; (2008)

Staker MR, Holt DL. *Acta Metall*; 20:569; (1972)

Stokes A R, Wilson A J C; 'The diffraction of X-rays by Distorted crystal Aggregates-I'; *Proc Phys Soc*; London; 61; 174-181; (1944)

Taylor GI. *Proc Roy Soc*;A145; 362; (1934)

Tournarie, M; *C. R. Acad. Sci. Paris*; 242; 2161; (1965)

Treacy M M J, Newsam J M, Deem M W; *Proc. Math. And Pys. Sc.*; Vol 433; No 1889; pp 499-520; (1991)

Ungar T, Mughrabi H, Ronnpagel D, Wilkens M; *Acta. Metall.*; Vol. 32, No. 3; 333-342; (1984)

Ungar T, Biermann H, Mughrabi M; 'Dislocation distributions as seen by X-ray line profiles'; *Materials Science and Engineering*; A 164; 175-179; (1993)

Ungar T, Borbely A; 'The effect of dislocation contrast on x-ray line broadening: A new approach to line profile analysis'; *Appl. Phys. Lett.*; 69; 21; (1996)

Ungar T, Ott S, Sanders P G, Borbely A, Weertman J R; 'Dislocations, grain size and planar faults in nanostructured copper determined by high resolution X-ray

diffraction and a new procedure of peak profile analysis'; *Acta Mater.*; Vol. 46; No. 10; 3693-3699; (1998)

Ungar T, Tichy G; 'The effect of dislocation contrast on X-ray line profiles in untextured polycrystals'; *Phys. Stat. Sol.*; 17; 42-43; (1999)

Ungar T, Gubicza J, Ribarik G and Borbely A; *J. Appl. Cryst.*; 34, 298±310; (2001)

Ungar T; 'The Meaning of Size Obtained from Broadened X-ray Diffraction Peaks'; *Advanced Engineering Materials*; 5; 323; (2003)

Ungar T; 'Microstructural parameters from X-ray diffraction peak broadening'; *Scripta Materialia*; 51; 777–781; (2004)

Ungar T; 'Subgrain Size-Distributions, Dislocation Structures, Stacking- and Twin Faults and Vacancy Concentrations in SPD Materials Determined by X-ray Line Profile Analysis'; *Materials Science Forum*; Vols. 503-504; 133-140; (2006)

Ungar T, Castelnau O, Ribarik G, Drakopoulos M, Bechade J L, Chauveau T, Snigirev A, Snigireva A, Schroer C, Bacoux B; 'Grain to grain slip activity in plastically deformed Zr determined by X-ray micro-diffraction line profile analysis'; *Acta Materialia*; 1117–1127; (2007)

Ustinov A I; *IUCR monographs on crystallography* 10, Defects and microstructure analysis by diffraction; edited by Snyder R L, Fiala J, Bunge H J; 264-317; International Union of crystallography; Oxford University Press; Oxford; (1999)

van Berkum J G M, Vermeulen A C, Delhez R, de Keijser Th H, Mittemeijer E J; 'Applicabilities of the Warren-Averbach Analysis and an Alternative Analysis for Separation of Size and Strain Broadening'; *J. Appl. Cryst.*; 27; 345-357; (1994)

van Berkum J G M, Delhez R, de Keijser Th H; Mittemeijer E J; 'Diffraction-line broadening due to strain fields in materials: Fundamental aspects and methods of analysis'; *Acta Cryst.*; A52; 730–747; (1996)

van Houtte P; *Acta Metal.*; 26; 591-604; (1978)

Vaughan D; *Phil. Mag.*; 22, 179; 1003-1011; (1970)

Wang L, Yang Y, Eisenlohr P, Bieler T R, Crimp M A, Mason D E; Metal. And Mat. Tran. A; 41A Feb; 421; (2010)

Wang X L, Wang Y D, Stoica A D, Horton D J, Tian H, Liaw P K, Choo H, Richardson J W, Maxey E; ‘Inter- and intragranular stresses in cyclically-deformed 316 stainless steel’; Materials Science and Engineering A 399, 114–119; (2005)

Warren B E; ‘X-Ray Diffraction’; Addison-Wesley; Reading; (1969)

Warren BE; Progr Metal Phys; 8:147; (1959)

Wertheim G K, Butler M A, West K W, Buchanan D N E; Rev. Sci. Instrum.; Vol. 45; No. 11; (1974)

Wilkens M, Bargouth M O; Acta Metall; 16; 465; (1968)

Wilkens M; ‘The determination of density and distribution of dislocations in deformed single crystals from broadened X-ray diffraction profiles’; Phys. Stat. Sol.; A2; 359–370; (1970a)

Wilkens M; Fundamental Aspects of Dislocation Theory; Vol. II; edited by Simmons J A, de Wit R, Bullough R; 1195-1221; Natl. Bur. Stand. (US)Spec. Publ. No. 317; Washington DC USA; (1970b)

Wilkens M; Broadening of X-Ray Diffraction Lines of Crystals Containing Dislocation Distributions’; Kristall und Technik; 11; 1159-1169; (1976)

Wilkens M; J. Appl. Cryst.; 12; 119-125; (1979).

Wilkens M; Phys. Sta. Soli. A; 104; K1; (1987)

Wilkinson A J, Anstis G R, Czernuszka J T, Long N J, Hirsch P B; Philos. Mag. A; 68; 59; (1993)

Williams D B and Carter C B; ‘Transmission Electron Microscopy, A textbook for materials science’; Springer; New York; (2009)

Williamson G K, Hall W H; Acta. Metall.; 1; 22-31; (1953)

Wilson A J C; Imperfections in the structure of cobalt II. Mathematical treatment of proposed structure; Proc. R. Soc. Lond. A; 180; 277-285; (1942)

Wilson A J C; The reflection of x-rays from the 'anti-phase nuclei' of AuCu3; Proc. R. Soc. Lond. A; 181; 360-368; (1943)

Wilson, A. J. C; 'X-Ray Optics'; Methuen; London; (1962a)

Wilson A J C; Proc. Phys. Soc.; 80; 286; (1962b)

Wilson A J C; Proc. Phys. Soc.; 81; 41-46; (1963a)

Wilson A J C; Proc. Phys. Soc.; 82; 986-991; (1963c)

Winther G; Mat. Sci. and Eng.; A309-310; 486-489; (2001)

Winther G; 'Effect of grain orientation dependent microstructures on flow stress anisotropy modelling'; Scripta Materialia; 52; 995–1000; (2005)

Withers P J; Journal of Applied Crystallography; 37; 607-612; (2004)

Withers P J, Bhadesia D H; Residual stress, Part 1 – Measurement techniques; Materials Science and Technology; April; Vol 17; 355; (2001)

Wu E, Gray E Mac A, Kisi E H; J Appl Crystallogr; 31:356; (1998a)

Wu E, Kisi E H, Gray E Mac A; J Appl Crystallogr; 31:363; (1998b)

Yapici G G, Karaman I, Luo Z P; Acta Mater.; 54; 3755–3771; (2006)

Yoo M H and Wei C T; J. Appl. Phys. 38; 4317–4322; (1967)

Zaefferer S; Materials Science and Engineering; A344; 20-30; (2003)

Zehetbauer M; Acat metal. Mater.; Vol. 41, No. 2; 589-599; (1993)

Zehetbauer M, Seumer V; Acat metal. Mater.; Vol. 41, No. 2; 577-588; (1993)

Zehetbauer M, Ungar T, Kral R, Borbely A, Schafler E, Ortner B, Amenitsch, Bernstorff; 'Scanning X-ray diffraction peak profile analysis in deformed Cu-poly-crystals by synchrotron radiation'; Acta Mater; Vol. 47; No. 3; 1053±1061; (1999)

